

<http://researchspace.auckland.ac.nz>

ResearchSpace@Auckland

Copyright Statement

The digital copy of this thesis is protected by the Copyright Act 1994 (New Zealand).

This thesis may be consulted by you, provided you comply with the provisions of the Act and the following conditions of use:

- Any use you make of these documents or images must be for research or private study purposes only, and you may not make them available to any other person.
- Authors control the copyright of their thesis. You will recognise the author's right to be identified as the author of this thesis, and due acknowledgement will be made to the author where appropriate.
- You will obtain the author's permission before publishing any material from their thesis.

To request permissions please use the Feedback form on our webpage.

<http://researchspace.auckland.ac.nz/feedback>

General copyright and disclaimer

In addition to the above conditions, authors give their consent for the digital copy of their work to be used subject to the conditions specified on the [Library Thesis Consent Form](#) and [Deposit Licence](#).

Global effects of Pyragas time-delayed feedback control

Anup S. Purewal

March 2015

A THESIS SUBMITTED IN FULFILLMENT OF THE REQUIREMENTS FOR THE DEGREE OF
DOCTOR OF PHILOSOPHY IN MATHEMATICS, THE UNIVERSITY OF AUCKLAND, 2015.

Abstract

Pyragas time-delayed feedback is a control scheme designed to stabilize unstable periodic orbits, which occur naturally in many nonlinear dynamical systems. The control scheme targets a specific unstable periodic orbit by adding a feedback term with a delay chosen as the period of the unstable periodic orbit. In this thesis we consider the global effects of applying Pyragas control to a nonlinear dynamical system near a subcritical Hopf bifurcation. We start by considering the standard example of the Hopf normal form subject to Pyragas control, which is a delay differential equation that models how a generic unstable periodic orbit is stabilized. We find that the addition of feedback induces infinitely many Hopf bifurcation curves and possibly infinitely many stable periodic orbits in addition to the target periodic orbit. Therefore, the controlled system could follow one of these periodic orbits rather than the target periodic orbit. As such, we find that to ensure successful implementation of the control scheme, one must consider the global dynamics of the system. Furthermore, we consider the effect of a delay mismatch in the system, where the delay is set close to but not equal to the period of the target periodic orbit. We find that the delay must be set as at least a linear approximation of the period of the target periodic orbit. To verify the predictiveness of the normal form analysis, we consider the global dynamics of the Lorenz system subject to Pyragas control. We find that the addition of feedback induces further Hopf bifurcation curves and further stable periodic orbits, showing that the Hopf normal form with feedback is indeed predictive of the observed global dynamics and the effect of a delay mismatch in the system. Finally, we consider the subcritical complex Ginzburg–Landau equation subject to a modified Pyragas control scheme, which includes a spatial feedback term. We find that traveling wave solutions of the system cannot be stabilized with either spatial or temporal feedback.

Acknowledgements

First, I would like to thank my supervisors Claire Postlethwaite and Bernd Krauskopf for the opportunity to spend the last few years working in a truly amazing place. This PhD would not have been possible without their support, guidance and most of all their patience. I am also grateful for the doctoral scholarship from the Faculty of Science.

I would like to thank my fellow PhD students and, in particular, those who have resided in room 512 at some point; Mike, Kate, Pete, Andrew, Pun and Rebecca. All of the office tomfoolery helped to put a smile back on my face when the rest of life was getting me down. Thank you!

Finally, I would like to thank my family for their continuous support and encouragement. Special love and thanks go to Divya for putting up with me every day!

Contents

Abstract	iii
Acknowledgements	v
1 Introduction	1
1.1 The OGY control scheme	2
1.2 The Pyragas control scheme	3
1.2.1 Delay differential equations	4
1.2.2 Determining the target period	6
1.3 Motivation and aims	7
1.4 Outline of thesis	8
2 A global bifurcation analysis of the subcritical Hopf normal form subject to Pyragas time-delayed feedback control	11
2.1 Notation & Background	13
2.2 The (λ, b_0) -plane near the point b_0^c	15
2.3 A more global view of the (λ, b_0) -plane	17

2.3.1	Families of Hopf bifurcations and bifurcating periodic orbits	18
2.3.2	Torus bifurcations and the domain of stability of Γ_P	23
2.3.3	Other regions of stable periodic orbits	25
2.4	The effect of the 2π -periodic feedback phase β	29
2.4.1	The effect on the domain of stability	30
2.4.2	The effect of β on the delay-induced Hopf bifurcation curves	35
2.5	The effect of the parameter γ	47
2.6	Conclusion	53
3	Effect of delay mismatch in Pyragas feedback control	55
3.1	The exact-period case	59
3.2	The constant-period case	62
3.3	The linear-period case	65
3.4	The variable-slope case	68
3.5	Conclusions	71
4	The Lorenz system subject to Pyragas time-delayed feedback control	73
4.1	Background and local bifurcation analysis	77
4.1.1	The period as a function of ρ	77
4.1.2	Stabilization of Γ_P near the point b_0^c	78
4.2	A more global view of the (ρ, b_0) -plane	81
4.2.1	Families of Hopf bifurcations	82

4.2.2	Overall domain of stability of Γ_P	84
4.2.3	Other regions of stability in the (ρ, b_0) -plane	86
4.3	The effect of the 2π -periodic feedback phase η	90
4.3.1	Best match for η	97
4.4	Investigation of delay mismatch	101
4.4.1	The constant-period case	102
4.4.2	The linear-period case	105
4.5	Conclusions	109
5	The complex Ginzburg–Landau equation subject to Pyragas feedback control	110
5.1	Introduction	110
5.2	Linear stability analysis	114
5.3	Spatial feedback in one-dimension	118
5.4	Temporal feedback with real feedback gain	119
5.5	Temporal feedback with complex feedback gain	122
5.6	Conclusions	129
6	Discussion and future work	132
A	Parametrization of the delay-induced Hopf bifurcation curves	136
B	The double Hopf bifurcation points in the set HH_K	138
	Bibliography	140

List of Figures

1.1	Pyragas time-delayed feedback control schematic	4
1.2	Initial function of a DDE	5
2.1	One-parameter bifurcation diagram of (2.0.1)	16
2.2	Bifurcation set in the (λ, b_0) -plane of (2.0.1) near the point b_0^c	18
2.3	Bifurcation set in the (λ, b_0) -plane of (2.0.1).	20
2.4	Bifurcation set in the (λ, b_0) -plane of (2.0.1) showing further bifurcation curves.	22
2.5	Bifurcation set in the (λ, b_0) -plane of (2.0.1) showing the domain of stability of Γ_P	24
2.6	Bifurcation set in the (λ, b_0) -plane of (2.0.1) showing other regions of stability	27
2.7	Bifurcation set in the (τ, b_0) -plane of (2.0.1).	28
2.8	The effect of an increase in β on the domain of stability of Γ_P	31
2.9	The effect of a decrease in β on the domain of stability of Γ_P	33
2.10	The compactified $(\hat{\lambda}, \hat{b}_0)$ -plane.	36
2.11	The curve H_L transforming into the curve H_J^1	38
2.12	The curve H_J^1 transforming into the curve H_J^2	41

2.13	Formation of the curves H_R^2 and H_R^1	43
2.14	Formation of the curve H_L	46
2.15	The effect of an increase in γ on the domain of stability of Γ_P	48
2.16	Transition of the curve H_L in the $(\hat{\lambda}, \hat{b}_0)$ -plane as γ is increased.	50
2.17	The stability boundary $S(\beta)$	52
3.1	One-parameter bifurcation diagram for the exact-period case.	60
3.2	Bifurcation set for the exact-period case.	61
3.3	One-parameter bifurcation diagram for the constant-period case	63
3.4	Bifurcation set for the constant-period case.	64
3.5	One-parameter bifurcation diagram in the constant-period case for $b_0 = 0.02$	65
3.6	One-parameter bifurcation diagram for the linear-period case.	66
3.7	Bifurcation set for the linear-period case.	67
3.8	The overall domain of stability in the variable slope case.	70
4.1	One-parameter bifurcation diagrams of (4.0.5).	79
4.2	Bifurcation set in the (ρ, b_0) -plane of (4.0.5) near the point b_0^c	80
4.3	Bifurcation set in the (ρ, b_0) -plane of (4.0.5).	83
4.4	The overall domain of stability of Γ_P in (4.0.5).	85
4.5	A chaotic attractor of (4.0.5).	87
4.6	Period-doubling bifurcations of (4.0.5).	89
4.7	The overall domain of stability of Γ_J in (4.0.5).	90
4.8	The effect of a decrease in η on the domain of stability of Γ_P in (4.0.5).	93

4.9	Transition of the Hopf bifurcation curve H_R^1 in the (ρ, \hat{b}_0) -plane as η is decreased.	94
4.10	The effect of an increase in η on the domain of stability of Γ_P in (4.0.5). . .	96
4.11	One-parameter bifurcation diagram in ρ for $\eta = 2.8$ of (4.0.5).	98
4.12	Bifurcation set in the (ρ, b_0) -plane of (4.0.5) for $\eta = 2.8$	100
4.13	One-parameter bifurcation diagram in ρ of (4.0.5) for the constant-period case.	103
4.14	Bifurcation set in the (ρ, b_0) -plane of (4.0.5) for the constant-period case. .	104
4.15	One-parameter bifurcation diagram in ρ of (4.0.5) for the linear-period case.	106
4.16	Bifurcation set in the (ρ, b_0) -plane of (4.0.5) for the linear-period case. . . .	108
5.1	The real part of the two eigenvalues of (5.2.18) without feedback.	117
5.2	The real part of the two eigenvalues of (5.2.18) with purely spatial feedback.	119
5.3	The purely real eigenvalue of (5.2.18) for temporal feedback with real feedback gain.	121
5.4	The real part of the leading complex conjugate pair of eigenvalues of (5.2.18) for temporal feedback with complex feedback gain.	122
5.5	The real part of the leading complex conjugate pair of eigenvalues of (5.2.18) for temporal feedback with complex feedback gain for $0 < \beta < 2\pi$.	124
5.6	The real part of the leading eigenvalue and the number of unstable eigenvalues of (5.2.18) against b_0 for complex temporal feedback gain.	125
5.7	The real part of the leading eigenvalue and the number of unstable eigenvalues of (5.2.18) against b_1 for complex temporal feedback gain.	127
5.8	The real part of the leading eigenvalue and the number of unstable eigenvalues of (5.2.18) against b_3 for complex temporal feedback gain.	128

5.9 The real part of the leading eigenvalue and the number of unstable eigenvalues of (5.2.18) against k for complex temporal feedback gain. 130

List of Tables

2.1	Description of the effect of an increase in the parameter β on the domain of stability of $\Gamma_{\mathcal{P}}$. To accompany Fig. 2.8	30
2.2	Description of the effect of a decrease in the parameter β on the domain of stability of $\Gamma_{\mathcal{P}}$. To accompany Fig. 2.9	34
2.3	Description of the transformation of the curve H_L into the curve H_J^1 as the parameter β is increased by 2π . To accompany Fig. 2.11.	37
2.4	Description of the curve H_J^1 transforming into the curve H_J^2 as the parameter β is increased by 2π . To accompany Fig. 2.12.	40
2.5	Description of the formation and transition of the curves H_R^1 and H_R^2 in the $(\hat{\lambda}, \hat{b}_0)$ -plane, as the parameter β is increased. To accompany Fig. 2.13.	42
2.6	Description of the formation of the curve H_L , as the parameter β is increased. To accompany Fig. 2.14.	45
2.7	Description of the effect of an increase in the parameter γ on the domain of stability of $\Gamma_{\mathcal{P}}$. To accompany Fig. 2.15	49
2.8	Description of the curve H_L as the parameter γ is increased. To accompany Fig. 2.16.	51
4.1	Description of the effect of a decrease in the parameter η on the domain of stability of $\Gamma_{\mathcal{P}}$. To accompany Fig. 4.8	91

4.2	Description of the effect of an increase in the parameter η on the domain of stability of $\Gamma_{\mathcal{P}}$. To accompany Fig. 4.10	95
-----	----------------------------------------------------------------------------------------------------------------------------------------------------------	----

Co-Authorship Form

This form is to accompany the submission of any PhD that contains research reported in published or unpublished co-authored work. **Please include one copy of this form for each co-authored work.** Completed forms should be included in all copies of your thesis submitted for examination and library deposit (including digital deposit), following your thesis Acknowledgements.

Please indicate the chapter/section/pages of this thesis that are extracted from a co-authored work and give the title and publication details or details of submission of the co-authored work.

The content of sections 1.1, 1.3.1, chapter 2 and appendices A and B are extracted from: A. S. Purewal, C.M. Postlethwaite and B. Krauskopf, A global bifurcation analysis of the subcritical Hopf normal form subject to Pyragas control, SIAM Journal of Applied Dynamical Systems, to appear

Nature of contribution by PhD candidate	Lead author. Performed analysis and investigation, generated all figures, wrote, proofread and edited manuscript
Extent of contribution by PhD candidate (%)	85


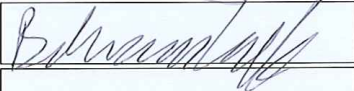
CO-AUTHORS

Name	Nature of Contribution
Claire Postlethwaite	Supervision of work. Proofreading and editing of text
Bernd Krauskopf	Supervision of work. Proofreading and editing of text

Certification by Co-Authors

The undersigned hereby certify that:

- ❖ the above statement correctly reflects the nature and extent of the PhD candidate's contribution to this work, and the nature of the contribution of each of the co-authors; and
- ❖ in cases where the PhD candidate was the lead author of the work that the candidate wrote the text.

Name	Signature	Date
Claire Postlethwaite		27/11/14
Bernd Krauskopf		27/11/14

Co-Authorship Form

This form is to accompany the submission of any PhD that contains research reported in published or unpublished co-authored work. **Please include one copy of this form for each co-authored work.** Completed forms should be included in all copies of your thesis submitted for examination and library deposit (including digital deposit), following your thesis Acknowledgements.

Please indicate the chapter/section/pages of this thesis that are extracted from a co-authored work and give the title and publication details or details of submission of the co-authored work.

The content of sections 1.3.2 and chapter 3 are extracted from: A. S. Purewal, C.M. Postlethwaite and B. Krauskopf, Effect of delay mismatch in Pyragas control, Physical Review E, 90(5), 2014, 052905.

Nature of contribution by PhD candidate	Lead author. Performed analysis and investigation, generated all figures, wrote, proofread and edited manuscript
Extent of contribution by PhD candidate (%)	85


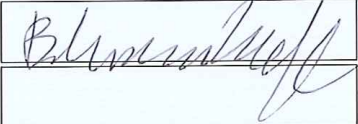
CO-AUTHORS

Name	Nature of Contribution
Claire Postlethwaite	Supervision of work. Proofreading and editing of text
Bernd Krauskopf	Supervision of work. Proofreading and editing of text

Certification by Co-Authors

The undersigned hereby certify that:

- ❖ the above statement correctly reflects the nature and extent of the PhD candidate's contribution to this work, and the nature of the contribution of each of the co-authors; and
- ❖ in cases where the PhD candidate was the lead author of the work that the candidate wrote the text.

Name	Signature	Date
Claire Postlethwaite		27/11/14
Bernd Krauskopf		27/11/14

1

Introduction

The control of unstable dynamics is an area of significant interest in engineering [3], biotechnology [28, 59, 78], chemistry [60] and other scientific disciplines. The motivation for controlling unstable behavior stems from applications where stable periodic motions or equilibrium solutions are favored over the unpredictability associated with unstable or chaotic dynamics. For instance, in [41] the unstable motion of a cutting tool, known as machine chatter, is undesirable as it results in an imperfect cut. The majority of available control methods, such as gain scheduling [51] and feedback linearization [36], focus on controlling an equilibrium solution of a nonlinear system. In this thesis we are interested solely in the control of unstable periodic orbits, these are also called UPOs [13, 24, 63]. An unstable periodic orbit is a periodic solution of a dynamical system that has at least one Floquet multiplier outside of the unit circle in the complex plane. The motion of the unstable periodic orbit may be desirable from an experimental point of view, but to make this motion observable it must be stabilized or controlled. For example, in [28] a stable periodic motion of the cardiac system is required, but the addition of a drug into the system makes the desired periodic orbit unstable; these authors apply a control scheme to stabilize the unstable periodic orbit.

Our starting point is a system of (autonomous) ordinary differential equations (ODEs)

$$\dot{x}(t) = f(x(t), \mu), \tag{1.0.1}$$

where $x \in \mathbb{R}^n$, $f : \mathbb{R}^n \times \mathbb{R}^m \mapsto \mathbb{R}^n$ is a smooth function and $\mu \in \mathbb{R}^m$ is a vector of scalar parameters. Here \mathbb{R}^n is the phase space of the ODE, meaning that an initial condition $x_0 \in \mathbb{R}^n$ uniquely defines the solution of the initial value problem (IVP). Suppose that system (1.0.1) has an unstable periodic orbit Γ , which we would like to stabilize. Unstable periodic orbits such as Γ can arise in system (1.0.1) in a number of ways. In particular, a periodic orbit may bifurcate from an equilibrium solution at a Hopf bifurcation; the bifurcating periodic orbit may be unstable depending on the eigenvalues at the equilibrium and the criticality of the Hopf bifurcation. Moreover, unstable periodic orbits (of saddle type) can be found as part of chaotic attractors, where they are dense. In both cases it may be desirable to find and stabilize an unstable periodic orbit. Two of the most successful methods designed to control and stabilize an unstable periodic orbit Γ are that by Ott, Grebogi and Yorke (OGY) [58] and that by Pyragas [70]. Both of these methods are non-invasive, that is, when the target periodic orbit Γ has been stabilized the control force vanishes.

1.1 The OGY control scheme

The method by Ott, Grebogi and Yorke [58] was one of the first control schemes suggested to stabilize an unstable periodic orbit Γ . The method is mainly used for the control of periodic orbits that lie within a chaotic attractor. It is defined for maps of dynamical systems, which are in discrete time. For a continuous time dynamical system such as that in (1.0.1), the user can take a Poincaré section of the system. For this map the periodic orbit Γ gives rise to a periodic point γ . When a trajectory passes within a predefined fixed neighborhood of γ , it is given a small perturbation towards its stable direction. If the trajectory visits this neighborhood often enough, the unstable periodic orbit Γ is stabilized. That is, the trajectory requires a sufficient number of perturbations towards its stable direction in order to stabilize Γ . Once the periodic orbit Γ is stabilized the trajectory will receive no further perturbations. Thus, as the control force, which is in the form of small perturbations, has disappeared the OGY method is non-invasive. However, the method has a few disadvantages. One disadvantage of the original OGY method is that the time taken for a trajectory to visit the fixed neighborhood can be large. This waiting time can be minimized through more advanced processes of targeting, such as those described by Shinbrot et al. [84]. For example, one technique is to continually adjust the size of the perturbation parameter. This pushes the trajectory nearer to the desired state

more quickly. Both the original and targeted OGY methods require quite some detailed knowledge of the system. In particular, the user must know the linear stable and unstable directions of the target unstable periodic orbit Γ . Thus, this method has sometimes proved difficult to implement in experiments, especially where detailed analytical information on the system is unavailable. In addition, if the attractor in the system is not chaotic but is a stable periodic solution, or if the user would like to stabilize multiple orbits, then revisions to the original method are required to achieve stabilization of a desired unstable periodic orbit [58]. This is because small parameter perturbations will only change the periodic orbit slightly, not enough to stabilize it, and the system will continue to follow the behavior of the stable periodic orbit. The system behavior can, however, be changed by altering the time taken before returning to the fixed neighborhood. Furthermore, to stabilize multiple periodic orbits the user can switch between different return times. Despite these difficulties the OGY method has been successfully implemented in a number of applications, most notably in laser [77] and chemical [60, 61] experiments.

1.2 The Pyragas control scheme

The method introduced by Pyragas [70] applies a continuous time-delayed feedback term that forces the system towards the desired periodic dynamics. Suppose system (1.0.1) has an unstable periodic orbit Γ with period $T(\mu)$. The Pyragas control scheme is then

$$\dot{x}(t) = f(x(t), \mu) + K[x(t - \tau) - x(t)], \text{ with } \tau = T(\mu). \quad (1.2.1)$$

Here K is a $n \times n$ feedback gain matrix [13, 63, 65], coupling the feedback term to the original system of ODEs (1.0.1). Pyragas control targets the unstable periodic orbit Γ by setting the delay equal to its period $T(\mu)$. The control force depends on the difference between the signals $x(t - T(\mu))$ and $x(t)$ in (1.2.1); when the control is successful (that is, K is chosen suitably) system (1.2.1) converges toward the target state, which is the periodic orbit Γ . As Γ is approached the difference in the control term becomes smaller. When the target periodic orbit Γ has been stabilized, the system follows the desired periodic motion effectively with zero control force. Hence, the Pyragas control method is indeed non-invasive. Figure 1.1 shows a schematic that describes Pyragas control.

Pyragas time-delayed feedback control [69] was first developed as a method to control chaotic systems and was initially tested on the Rössler system. Since then it has been implemented successfully in a number of applications, most notably in laser [9, 80], elec-

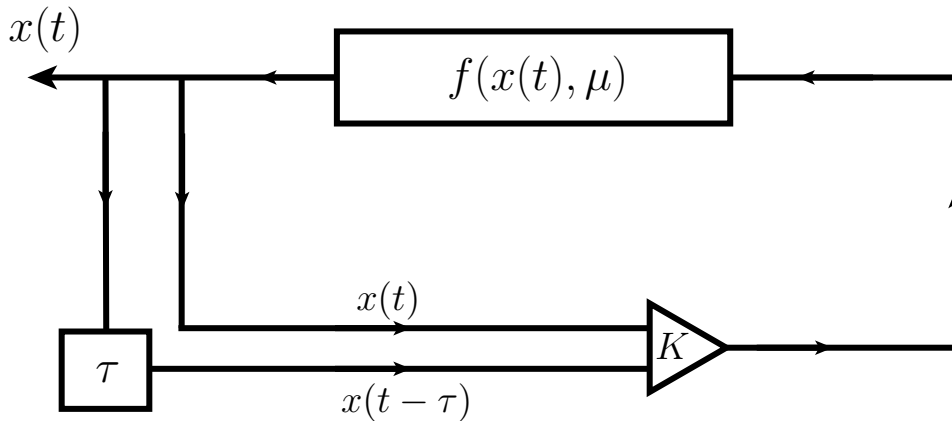


Figure 1.1: A schematic of the Pyragas control scheme. The difference between the signals $x(t - \tau)$ and $x(t)$ is fed back into the system via the feedback gain K .

tronic [29] and engineering [27, 81] systems. There have also been several modifications to the original method; for example, to stabilize high-period orbits [62, 92] and to extend the control scheme to include spatial feedback [53]. This combination of spatial and temporal feedback has led to the Pyragas control scheme being successfully used to control pattern formation [43, 56, 64]. The control scheme has also been adapted to control synchronization in coupled systems, such as synchronized firing in coupled neuron systems [82]. An overview of the method and many of its extensions and applications can be found in [83].

1.2.1 Delay differential equations

A result of implementing the Pyragas scheme is that the controlled system (1.2.1) is a delay differential equation (DDE) with a single fixed delay τ . A DDE describes a system where the time evolution of a state is dependent on past states. DDEs are particularly useful for modeling systems that have an inherent time-lag such as those that involve some transportation of information and also systems that are highly dependent on past states such as predator-prey models.

One of the main differences between the analysis of a DDE and an ODE is the nature of the phase space. For a DDE with a fixed delay, an initial condition takes the form of a continuous function $\phi(t)$ on the interval $[-\tau, 0]$; see, for example, [21, 32, 91]. In other words, to determine how (1.2.1) will evolve, the user must define a history of length τ . This means that the phase space of the DDE is the infinite-dimensional space $C([-\tau, 0]; \mathbb{R}^n)$ of continuous functions from $[-\tau, 0]$ to \mathbb{R}^n ; here \mathbb{R}^n is referred to as the physical space. A schematic of the initial function $\phi(t)$ on the interval $[-\tau, 0]$ is shown in Fig. 1.2.

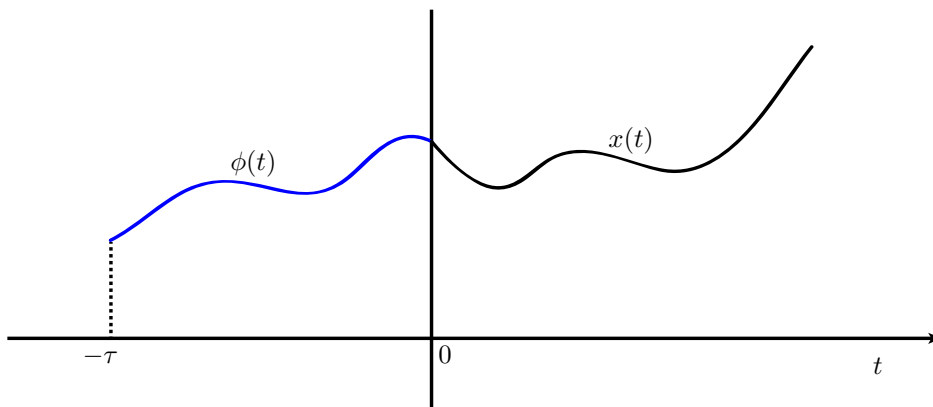


Figure 1.2: An initial function $\phi(t)$ of a DDE defines a history of length τ .

As with ODEs the stability of an equilibrium point of a DDE is determined by the roots of the characteristic equation of the system. However, the characteristic equation of a DDE is quasi-polynomial, that is to say, it contains terms of the form $e^{\lambda t}$ (for eigenvalues λ) [32]. Hence, it has infinitely many roots in the complex plane. For an equilibrium solution of a DDE to be stable, all of these roots must have a negative real part. It has been shown that the equilibrium solution of a DDE only has a finite number of roots with positive real part [21, 32]. Therefore, one need only consider the root (or complex conjugate pair of roots) with the largest real part to determine stability. This means that standard bifurcation theory (i.e. that for ODEs) applies to a system such as (1.2.1); for example, a Hopf bifurcation occurs when a pair of complex conjugate eigenvalues have zero real part [21].

A periodic orbit Γ is a solution of (1.2.1) such that after time $T(\mu)$, where $T(\mu)$ is the parameter-dependent period of Γ , a function section of length τ is repeated. The stability of Γ is determined by its Floquet multipliers. A periodic orbit Γ has a countable number of Floquet multipliers with only a finite number outside of the unit circle in the complex plane [32]. Therefore, when a parameter is changed in a DDE such as (1.2.1), one can find the same bifurcations of periodic orbits as in ODEs, including saddle-node of limit cycles or fold bifurcations, Hopf bifurcations and period-doubling bifurcations.

Although DDEs are generally more difficult to study analytically than ODEs, there are several computational tools available for the study of DDEs. The routine `dde23` implemented in Matlab [55] is a numerical integrator that solves IVPs for DDEs with constant time-delays. `DDE-Biftool` [22] is a software package, implemented in Matlab [55], that is capable of continuing equilibria, periodic orbits and bifurcations of equilibria. We use `DDE-Biftool` in its extended form (version 3.0) developed by Sieber [85] to compute the bifurcation curves presented in this thesis, including those of periodic orbits.

1.2.2 Determining the target period

It is often stated that the Pyragas control scheme is easy to implement [9, 26, 82], as the user requires only knowledge about the period $T(\mu)$ of the target unstable periodic orbit Γ ; setting the system delay τ equal to $T(\mu)$ provides an in-built targeting mechanism. However, there are two major questions that must be answered to ensure successful implementation of the Pyragas control scheme. The first is the practical question of how to determine the parameter-dependent period $T(\mu)$ of an unknown target unstable periodic orbit Γ . The second is the more theoretical question of how close the chosen delay τ must be to the target period $T(\mu)$ for the control scheme to still produce a stable periodic orbit that is sufficiently close to Γ .

Of course one could simply choose an arbitrary period, fix the delay τ at this value, and observe what happens. This is a particularly useful approach when there is a chaotic attractor in the system. A chaotic attractor is densely filled with unstable periodic orbits and, therefore, it is likely that, even with an arbitrary choice of period, the system will converge to some periodic orbit [31].

However, this approach is of little use when the system has only one unstable periodic orbit of interest, as it is highly unlikely that the user will guess its (parameter-dependent) period correctly. Therefore, to run Pyragas control in a parameter dependent setting, a scheme is required that determines the period $T(\mu)$ of the target periodic orbit for all μ . In this way, a specific periodic orbit can be targeted and tracked in parameter space.

In [79, 80] Schikora et al. implement Pyragas feedback control for a multisection semiconductor laser near a subcritical Hopf bifurcation. The complexity of the system in question makes an analytic determination of the period difficult. Instead, a constant value for the period was chosen and set as the delay τ of the Pyragas control term. This chosen value was found via independent experiments before the periodic orbit becomes unstable. As long as a periodic orbit is stabilized and the residual control force in the system is below a predetermined threshold, the control scheme is considered successful. As parameters are changed the residual control force grows, and when it reaches the threshold the target period and, hence, the delay τ is adjusted [79, 80]. In an iterative procedure τ is adjusted in accordance with parameter changes to ensure the system is at a stable periodic orbit and there is low residual control force. This procedure has the disadvantage that it is operator intensive, that is, as parameters are changed the operator must manually change the delay in the control term.

A solution to finding the parameter-dependent period of a target unstable periodic orbit

is provided by the method developed by Sieber and Krauskopf [88, 89]. Their approach is to embed Pyragas control into a continuation scheme, which automatically determines the period of the target periodic orbit as part of the continuation procedure. Moreover, the local control scheme allows them to drive the system to a reference target ensuring with a Newton step that the control force goes to zero when a parameter is changed slightly. This results in the next point where the reference signal and output of the system agree. This approach has the advantage that the user need not specify an equation for the right-hand side of the system (1.2.1). The method was demonstrated with proof of concept computer experiments of an injection laser and a dry-friction oscillator; it was also demonstrated in an actual experiment of a vertically forced pendulum [87, 89]. Subsequently, the method was used by Barton et al. in an energy-harvester [5, 6] and by Bureau et al. in an experimental bifurcation analysis of a harmonically forced impact oscillator [15]. A disadvantage of this method is that the process of embedding Pyragas control into a continuation scheme adds complexity and computational effort.

Pyragas et al. [74] developed an adaptive algorithm that determines the period through the use of a state-dependent delay. The algorithm adapts the delay time continuously, which results in exact convergence to the period of the targeted periodic orbit. As such, no switching of the control force is required. The method was implemented in proof of concept computer experiments of the Rössler and Mackey-Glass systems. A disadvantage of this method is the presence of a state-dependent delay. The theory of state-dependent delays is not as well developed as that of fixed delays; for example the Hopf bifurcation theorem for state-dependent delay equations was only proved recently [86]. As such, the analysis of systems with state-dependent delays is, in general, more difficult than that of systems with fixed delays.

1.3 Motivation and aims

The principal aim of this thesis is to understand the global or overall dynamics that may arise when Pyragas time-delayed feedback control is implemented. Here, the term global is used with respect to the parameter space. To understand these dynamics, we aim to answer the following questions. Can stabilization of the target periodic orbit be achieved for all values of system parameters? Does the addition of feedback induce further stable periodic orbits that are not the target? As we will see, even in a simple setting, successful implementation of Pyragas control is actually quite challenging.

In this thesis, we start by considering the subcritical Hopf normal form subject to Pyragas

control. Brown [14] found that close to a subcritical Hopf bifurcation the same local dynamics are induced if feedback is added to a full system as when feedback is added to the system reduced to the subcritical Hopf normal form. Here, we consider whether the same is true of the global dynamics. That is, can the global dynamics of the subcritical Hopf normal form subject to Pyragas control predict the global dynamics of other systems with feedback near a subcritical Hopf bifurcation?

Furthermore, this thesis aims to answer the question of how precisely the delay must be set in the Pyragas control scheme. The scheme is simple to setup, but determining the exact period can be difficult. As previously discussed, there are several methods that can be used to automatically determine the period, such as the iterative procedure of Schikora et al. [79, 80], the continuation procedure of Sieber and Krauskopf [88] and the adaptive algorithm developed by Pyragas [74]. However, all of these methods add complexity and computational effort. Thus, in this thesis we consider whether the Pyragas control scheme is successful when the delay is set as a simpler functional form of the exact period of the target periodic orbit. In other words, we consider the effect of a delay mismatch.

We also consider the effectiveness of Pyragas control on a spatially extended system near a subcritical Hopf bifurcation. Specifically, we consider stability of traveling wave solutions of the subcritical cubic complex Ginzburg–Landau equation in one complex spatial variable subject to Pyragas control. Here, our aim is to understand whether or not Pyragas control can be successfully applied to spatially extended systems near a subcritical Hopf bifurcation.

1.4 Outline of thesis

The thesis is organized as follows. Chapter 2 considers the global effect of applying Pyragas control to a nonlinear dynamical system. Specifically, we consider the standard example of the subcritical Hopf normal form subject to Pyragas control. Our aim is to study how this model depends on its different parameters, including the phase of the feedback and the imaginary part of the cubic coefficient, over their entire ranges. We show that the delayed feedback control induces infinitely many curves of Hopf bifurcations, from which emanate infinitely many periodic orbits that, in turn, have further bifurcations. Moreover, we show that, in addition to the stabilized target periodic orbit, there are possibly infinitely many stable periodic orbits. We compactify the parameter plane to show how these Hopf bifurcation curves change when the 2π -periodic phase of the feedback is varied. In particular, the domain of stability of the target periodic orbit changes in this

process and, at certain parameter values, it disappears completely. Overall, we present a comprehensive global picture of the dynamics induced by Pyragas control in the subcritical Hopf normal form.

In chapter 3 we consider how precisely the delay must be set in Pyragas control. The control scheme targets a specific unstable periodic orbit by adding a feedback term with a delay chosen as the period of the unstable periodic orbit. However, in an experimental or industrial environment, obtaining the exact period or setting the delay equal to the exact period of the target periodic orbit may be difficult. This could be due to a number of factors, such as incomplete information on the system or the delay being set by inaccurate equipment. We again consider Pyragas control applied to the prototypical generic subcritical Hopf normal form but now when the delay is close to but not equal to the period of the target periodic orbit. Specifically, we consider two cases: firstly a constant and, secondly, a linear approximation of the period. We compare these two cases to the case where the delay is set exactly to the target period, which serves as the benchmark case. For this comparison, we construct bifurcation diagrams and determine any regions where a stable periodic orbit close to the target is stabilized by the control scheme. In this way, we find that at least a linear approximation of the period is required for successful stabilization by Pyragas control.

In chapter 4 we consider the famous Lorenz system subject to Pyragas time-delayed feedback control. Our aim is to show that the global dynamics induced when Pyragas control is added to the subcritical Hopf normal form (presented in chapter 2) are relevant for other systems with Pyragas control near a subcritical Hopf bifurcation. We perform a detailed bifurcation analysis of the Lorenz system with feedback and show that the global dynamics agree closely with those of the Hopf normal form with feedback. In particular, the domain of stability of the target periodic orbit in the Lorenz system closely resembles that for the Hopf normal form. Moreover, for a suitable value of the 2π -periodic feedback phase, we find that the stability domain in the Lorenz system is topologically the same as in the Hopf normal form. That is, in both systems the stability domain is bounded by the same bifurcation curves and these curves start and end at the same points. Similarly to the Hopf normal form with feedback, we also find further delay-induced Hopf bifurcation curves and stable delay-induced periodic orbits. We also consider the effect of a delay mismatch in the controlled Lorenz system, and again find that our results closely correlate with those for the Hopf normal form. In particular, we again find that the delay must be set as at least a linear approximation of the period of the target periodic orbit for the control scheme to be considered successful. Overall, we find that the dynamics of the Lorenz system subject to Pyragas control are accurately predicted by the subcritical Hopf normal form subject to Pyragas control.

In chapter 5 we aim to stabilize traveling wave solutions of the subcritical complex Ginzburg–Landau equation (CGLE) through the application of the modified Pyragas control scheme developed by Lu. et al [53]. The modified Pyragas method involves spatial feedback as well as temporal feedback. We perform a linear stability analysis of the traveling wave solutions by considering small-amplitude perturbations for some perturbation wavenumber. The spatial shifts are chosen according to the wavelength of the targeted traveling wave and the temporal delay term is set as its period. We find that spatial feedback is not sufficient in stabilizing the traveling wave solution. We also show analytically that stabilization is not possible with a purely real temporal feedback gain. Lastly, we provide numerical evidence to support our observation that stabilization is not possible with a complex temporal feedback gain.

A discussion of the analysis presented in this thesis and possible future directions of research is given in chapter 6.

2

A global bifurcation analysis of the subcritical Hopf normal form subject to Pyragas time-delayed feedback control

The results in this chapter have been published in [67]. The aim of this chapter is to understand the global dynamics that arise when Pyragas time-delayed feedback control is implemented. To this end, we analyze the generic subcritical Hopf normal form subjected to Pyragas feedback control, as first proposed by Fiedler et al [24], and given by

$$\dot{z} = (\lambda + i)z(t) + (1 + i\gamma)|z(t)|^2z(t) + b_0e^{i\beta}[z(t - \tau) - z(t)]. \quad (2.0.1)$$

Here $z \in \mathbb{C}$ and $\lambda, \gamma \in \mathbb{R}$; the complex number $b_0e^{i\beta}$ is the feedback gain K ; $b_0 \in \mathbb{R}$ is the control amplitude; and β is the phase of the feedback. We use the convention that $b_0 \geq 0$ and $\beta \in [0, 2\pi]$. As the feedback gain of the Pyragas control is dependent on both b_0 and β , and as $b_0e^{i\beta} = -b_0e^{i(\beta \pm \pi)}$, a reflection of the same dynamics as those presented in this chapter can be achieved for a negative b_0 through a shift of π in the 2π -periodic feedback phase β .

We consider system (2.0.1) because the period of the target periodic orbit and the local mechanism of stabilization can be understood by analytical work, which is rare for non-linear time-delay systems. System (2.0.1) has been well studied in [13, 24, 38] near the Hopf bifurcation point; a summary of this work is given in section 2.1. On the other hand, the global dynamics resulting from the addition of feedback have not been fully considered yet.

The generic subcritical Hopf normal form is given by the ODE part of (2.0.1), which is

$$\dot{z} = (\lambda + i)z(t) + (1 + i\gamma)|z(t)|^2z(t). \quad (2.0.2)$$

As in (2.0.1), system (2.0.2) is written in the complex variable $z \in \mathbb{C}$. There is a subcritical Hopf bifurcation at $\lambda = 0$, which we denote H_P . From H_P emanates an unstable periodic orbit Γ_P , which has one unstable Floquet multiplier. In the literature Γ_P is often referred to as the Pyragas periodic orbit, and it is the control target [13, 24, 38].

In this chapter we take a global view of the controlled system (2.0.1) and perform a detailed bifurcation analysis in the (λ, b_0) -plane. We analyze how the targeted unstable periodic orbit Γ_P is stabilized and also show its domain of stability locally as well as globally. Moreover, we show that the system (2.0.1) has infinitely many Hopf bifurcations in addition to H_P , which are induced by the delay term. We analyze bifurcations of the target periodic orbit and those periodic orbits that emanate from delay-induced Hopf bifurcations. In particular, we find that there are other stable periodic orbits in addition to the target periodic orbit Γ_P . To present the global dynamics of the system we show bifurcation sets in a compactified (λ, b_0) -plane, thus allowing us to present the limiting behavior at infinity. Using this compactification we are able to see how the structure and geometry of system (2.0.1) changes globally as the feedback phase β is varied through a period of 2π . In particular, we find a cyclic-type transition of the infinitely many delay-induced Hopf bifurcation curves. We also show how the domain of stability of Γ_P in the (λ, b_0) -plane changes as β is varied. Finally, we also consider the effect that changing the normal form parameter γ has on the dynamics of system (2.0.1); specifically, we determine for which values of γ the Pyragas control scheme fails.

This chapter is organized as follows. Section 2.1 gives some background on (2.0.1) and a synopsis of the literature on its study. Section 2.2 presents the dynamics of system (2.0.1) close to the Hopf bifurcation H_P in the (λ, b_0) -plane. Section 2.3 considers a more global view of the (λ, b_0) -plane and shows further dynamics induced by the feedback. Section 2.4 studies the effect that changing the parameter β has on the domain of stability of

the target periodic orbit Γ_P and the delay-induced Hopf bifurcation curves. Section 2.5 considers the effect of the parameter γ on the stabilization of Γ_P . Conclusions and a discussion can be found in section 2.6.

2.1 Notation & Background

In system (2.0.1) Pyragas control is applied to the subcritical Hopf normal form. A normal form is a reduced analytic expression of a general problem on the centre manifold, achieved through successive coordinate transformations. Analysis of the normal form is often easier than that of the unsimplified system, yet it yields a precise qualitative overview of the dynamics of the system. Brown et al. [13] showed that near a Hopf bifurcation, the same dynamics are induced, whether Pyragas control is added to the normal form or to the original equations.

System (2.0.2) displays the symmetry associated with the Hopf normal form, namely it is invariant with respect to any rotation in the complex plane about the origin (the S_1 group operation). In fact, the normal form highlights this symmetry property near the Hopf bifurcation, which would otherwise not be discernible in the full system [31]; this symmetry can aid in the analysis of the dynamics. When reducing a system near a Hopf bifurcation to its normal form all quadratic terms can be removed under a non-linear change of coordinates [31]. However, cubic terms of the form $|z(t)|^2 z(t)$ cannot be removed as they are resonant, that is, invariant under the aforementioned symmetry. Therefore, Hopf bifurcations of the zero equilibrium solution of (2.0.2) with a pair of purely imaginary eigenvalues $\eta = \pm i$ produce rotating wave solutions of the form

$$z(t) = r_P e^{i \frac{2\pi}{T(\lambda)} t}, \quad (2.1.1)$$

where $T(\lambda)$ denotes the period of the bifurcating periodic orbit Γ_P . System (2.0.2) is transformed to polar coordinates by the ansatz (2.1.1), yielding,

$$\begin{cases} 0 & = (\lambda + r_P^2) r_P \\ \frac{2\pi}{T(\lambda)} & = (1 + \gamma r_P^2). \end{cases} \quad (2.1.2)$$

From the equations (2.1.2) we find that Γ_P has amplitude $r_P = \sqrt{-\lambda}$, exists for $\lambda < 0$ and has period $T(\lambda) = \frac{2\pi}{1-\gamma\lambda}$. System (2.0.1) maintains the symmetry properties of the Hopf normal form as it is a DDE with a fixed delay, where the delay term enters linearly;

that is, the delay term is also invariant under any complex rotation about the origin. The basic periodic orbits of (2.0.1) are circular and, hence, can be represented by their radius. Since the unstable periodic orbit Γ_P is the target state of the Pyragas control, in (2.0.1) we set

$$\tau = T(\lambda) = \frac{2\pi}{1 - \gamma\lambda}. \quad (2.1.3)$$

Throughout our analysis of (2.0.1) in this chapter we fix τ to the expression (2.1.3). The Hopf bifurcation H_P is also always at $\lambda = 0$ in the DDE (2.0.1), but its criticality may differ from that of H_P in the normal form (2.0.2), where it is always subcritical.

Fiedler et al. [24] first introduced and analyzed system (2.0.1). The main motivation of these authors was to use (2.0.1) as a counterexample to the ‘odd number limitation’, which states that only unstable periodic orbits with an even number of real unstable Floquet multipliers can be stabilized with Pyragas control [57]. The principal focus of [24] is the successful local stabilization of the target unstable periodic orbit Γ_P , which emanates from the subcritical Hopf bifurcation H_P . The periodic orbit Γ_P has one real Floquet multiplier greater than unity, hence, its stabilization provided a counterexample to the odd-number limitation. Fundamentally, this successful stabilization is possible due to the choice of the feedback gain as $b_0 e^{i\beta}$ in (2.0.1). The authors of [24] do not fix the delay τ ; they discuss the mechanism for local stabilization and present the results in the two-parameter (λ, τ) -plane. Fiedler et al. show that the addition of feedback induces a secondary Hopf bifurcation. From this Hopf bifurcation emanates a stable periodic orbit. This stable periodic orbit then undergoes a transcritical bifurcation with the target state Γ_P . In this transcritical bifurcation the two periodic orbits exchange stability, resulting in Γ_P becoming stable. Beyond discussing how stabilization works, Fiedler et al, [24] establish a domain within the (λ, τ) -plane in which the target orbit Γ_P is stable. In particular, they develop analytical expressions for the upper and lower limits of the control amplitude b_0 for this domain when λ is small. This analysis also yields the result that stabilization fails when the feedback gain $b_0 e^{i\beta}$ is real, that is to say, when $\beta = 0$ or $\beta = \pi$.

Just et al. [38] conducted a detailed local bifurcation analysis of system (2.0.1), presented in the (λ, τ) -plane and in the (b_0, τ) -plane. These authors derive the critical level of feedback amplitude given by the b_0 value

$$b_0^c = \left\{ (\lambda, b_0) = \left(0, \frac{-1}{2\pi(\cos \beta + \gamma \sin \beta)} \right) \right\}, \quad (2.1.4)$$

immediately above which the target state Γ_P bifurcates stably from H_P at $\lambda = 0$ (for larger

values of b_0 other instabilities may occur; these are discussed in section 2.3). Moreover, [38] also gives the condition

$$b_0\tau = \frac{-1}{(\cos \beta + \gamma \sin \beta)}, \quad (2.1.5)$$

at which a transcritical bifurcation occurs.

Brown et al. [13] analyze how Pyragas control stabilizes an unstable periodic orbit that emanates from a generic subcritical Hopf bifurcation in an n -dimensional dynamical system. Critical to this successful stabilization is the correct choice of feedback gain $b_0e^{i\beta}$, and [13] presents explicit formulae for choosing both b_0 and β . Furthermore, these authors perform a linear stability analysis and a center manifold reduction to show that there exists a degenerate Hopf bifurcation at the point b_0^c . In fact, [13] shows that the point b_0^c in the (λ, b_0) -plane is a Hopf bifurcation point with a further degeneracy; namely for a solution η of the characteristic equation of the linearized system, one has that $\text{Re}[\frac{d\eta}{d\lambda}(0)] = 0$ when b_0 has the value in (2.1.4). Moreover, at b_0^c , the cubic coefficient of the normal form is purely imaginary. Brown et al. [13] also present a schematic of the local bifurcation set in the (λ, b_0) -plane near the point b_0^c . In particular, they detail where the target unstable periodic orbit Γ_P is stabilized. The authors of [13] also show that stabilization of Γ_P is impossible when the real part of the imaginary cubic coefficient of system (2.0.1) is zero, that is, when $\gamma = 0$.

Erzgräber et al. [23] discuss the effect of the feedback phase β on the dynamics of system (2.0.1). In particular, they focus on the changes to the domain of the stabilized periodic orbit, as β is varied over a period of 2π . These authors present a detailed bifurcation analysis of the equilibrium solution and the target unstable periodic orbit. Furthermore, they also conducted a bifurcation analysis of the stable periodic orbits induced by the addition of the feedback term [24, 38]. These results are presented in the (b_0, β) -plane. The analysis of [23] reveals that the target unstable periodic orbit Γ_P and the delay-induced periodic orbits undergo not only the transcritical bifurcation discussed in [24] and [38], but also torus bifurcations.

2.2 The (λ, b_0) -plane near the point b_0^c

In this section we discuss the dynamics of system (2.0.1) near the Hopf bifurcation H_P that occurs for $\lambda = 0$. Throughout this analysis near b_0^c we fix $\gamma = -10$ and $\beta = \frac{\pi}{4}$ as was

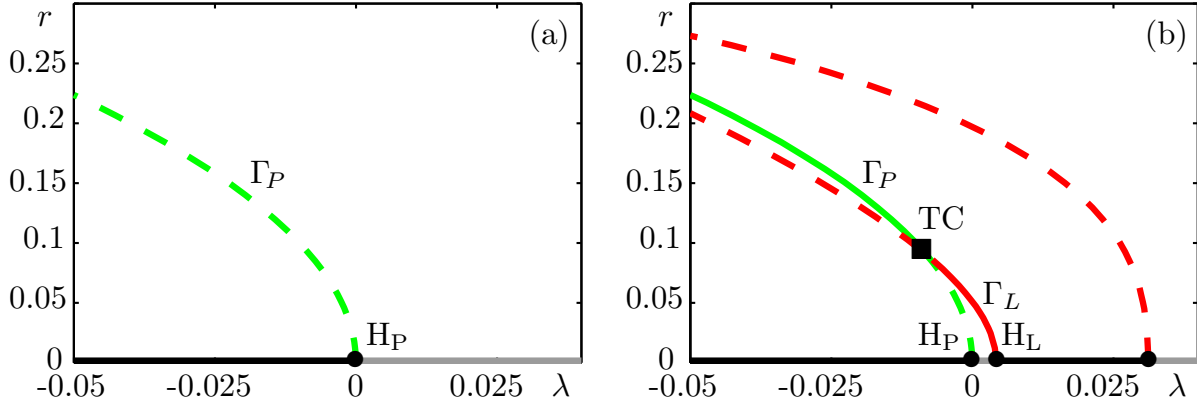


Figure 2.1: One-parameter bifurcation diagrams in λ of (2.0.1). Panel (a) is for $b_0 = 0$ and shows the Hopf bifurcation point H_P (black dot) of the equilibrium and the bifurcating unstable periodic orbit Γ_P (green dashed). Panel (b) is for $b_0 = 0.022$ and shows further delay-induced Hopf bifurcations (black dots). From the Hopf bifurcation H_L emanates a stable periodic orbit Γ_L (red), which exchanges stability with Γ_P at a transcritical bifurcation TC (black square). Solid (dashed) curves indicate stable (unstable) periodic orbits, the solid black (grey) lines indicate where the equilibrium is stable (unstable).

done in [24,38]. In particular, we show the mechanism by which Pyragas control stabilizes the target unstable periodic orbit Γ_P . The analysis is presented by both one-parameter bifurcation diagrams and two-parameter bifurcation sets.

Figure 2.1(a) shows the one-parameter bifurcation diagram in λ of (2.0.1) for $b_0 = 0$, that is, for system (2.0.2) which has no control term; the unstable periodic orbit Γ_P is represented by the (green) dashed curve. The equilibrium solution is stable (black) before it undergoes a Hopf bifurcation at the point H_P , from which Γ_P bifurcates. Figure 2.1(b) is the one-parameter bifurcation diagram of (2.0.1) for $b_0 = 0.022 < b_0^c$. The point H_P is unaffected by the presence of delayed feedback and remains at $\lambda = 0$. However, further Hopf bifurcations are now present and they are shown as the additional black dots on the bottom axis of Fig. 2.1(b). From one of these delay-induced Hopf bifurcations, which we label H_L , emanates a branch of stable periodic orbits. The target periodic orbit Γ_P and the delay-induced stable periodic orbit Γ_L exchange stability at the transcritical bifurcation TC. The target unstable periodic orbit Γ_P is thereby stabilized.

Figure 2.2 shows the two-parameter bifurcation set in the (λ, b_0) -plane of (2.0.1), near the critical level of feedback amplitude b_0 given by the point b_0^c from (2.1.4). This figure is a computed version of the schematic presented in [13]. The curve H_P is the vertical (green) curve at $\lambda = 0$. The curve of delay-induced Hopf bifurcations H_L is represented by the (red) curve that intersects H_P at the point b_0^c . From the point $(0, b_0^c)$ emerges the transcritical bifurcation curve TC (purple), the curve extends into the region where

$\lambda < 0$. An analytical expression for the curve TC can be found, by combining equations (2.1.3) and (2.1.5), as

$$b_0 = TC(\lambda) = \frac{-1 + \gamma\lambda}{2\pi(\cos \beta + \gamma \sin \beta)}. \quad (2.2.1)$$

The (blue) curve labeled S_L is a saddle-node of limit cycles (SNLC) bifurcation (or fold bifurcation); where a stable delay-induced periodic orbit bifurcates. The curve S_L emanates from the degenerate Hopf bifurcation point DH_L on H_L and extends left in the (λ, b_0) -plane for decreasing values of λ and b_0 . The shaded region in Fig. 2.2 is the domain of stability of the target unstable periodic orbit Γ_P near the point b_0^c . The curve TC forms its lower boundary [13] and the domain is bounded on the right by the Hopf bifurcation curve H_P .

Below b_0^c , the Hopf bifurcation H_P is subcritical and the equilibrium is stable for $\lambda < 0$. In the region to the left of the curve H_P and to the right of the curve H_L the equilibrium is unstable. At b_0^c the Hopf bifurcation H_P changes criticality, hence, immediately above b_0^c , H_P is supercritical. Also, immediately above b_0^c , the target periodic orbit Γ_P bifurcates stably from H_P .

The curve H_L also has sections of differing criticality. Between the point b_0^c and the degenerate Hopf bifurcation point DH_L , the curve H_L is supercritical; from this section bifurcates a stable periodic orbit; see Fig. 2.1(b). If b_0 is decreased this periodic orbit then undergoes a saddle-node of limit cycles bifurcation along the curve S_L . If b_0 is increased it exchanges stability with Γ_P at the transcritical bifurcation TC; see Fig. 2.2. At the point DH_L the Lyapunov coefficient (coefficient of the cubic term in the Hopf normal form) becomes zero and the Hopf bifurcation changes criticality [46].

To the left of b_0^c the curve H_L is subcritical; from this section bifurcates an unstable periodic orbit, which exists for decreasing λ (to the left of H_L). To the right of DH_L the curve H_L is also subcritical; from this section of the curve bifurcates an unstable periodic orbit, which also exists for decreasing λ (to the left of H_L).

2.3 A more global view of the (λ, b_0) -plane

We now consider the (λ, b_0) -plane more globally, again for $\gamma = -10$ and $\beta = \frac{\pi}{4}$. By exploring more of the (λ, b_0) -plane we are able to show that the addition of feedback induces further Hopf bifurcations. From these bifurcations emanate delay-induced periodic orbits;

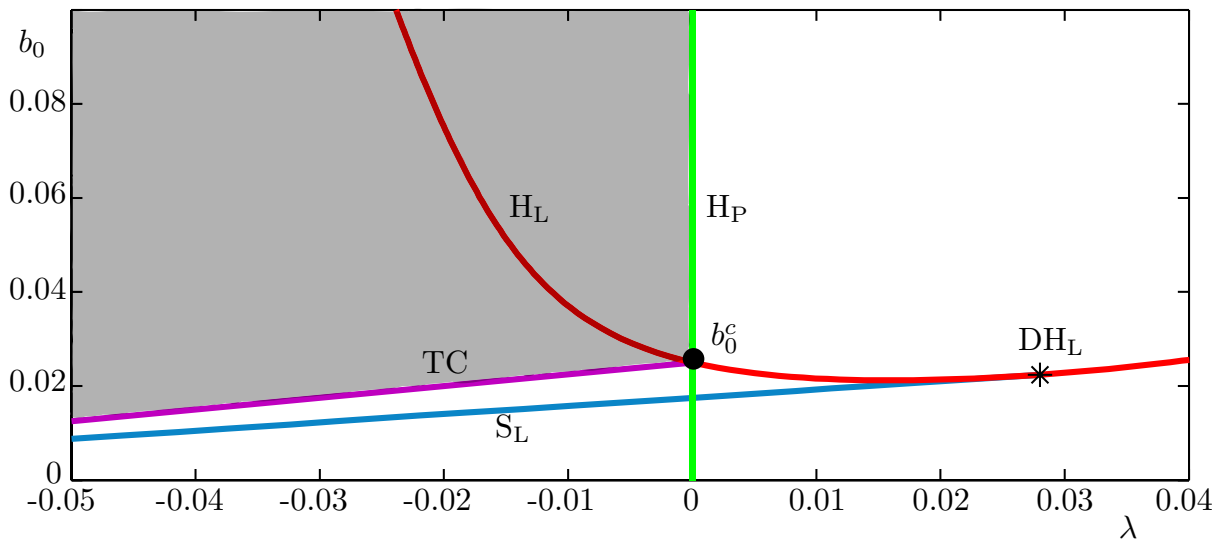


Figure 2.2: Bifurcation set in the (λ, b_0) -plane of (2.0.1) near the point b_0^c , where the curves H_P (green) and H_L (red) intersect. The transcritical bifurcation curve TC (purple) begins at the point b_0^c . The SNLC bifurcation curve S_L (blue) emerges from the degenerate Hopf bifurcation point DH_L (*). The domain of stability of Γ_P is shaded.

we analyze the stability and bifurcations of these periodic orbits and show that there are, in fact, infinitely many stable delay-induced periodic orbits of (2.0.1). We present the overall domain of stability of the target periodic orbit Γ_P and also present a selection of the domains of stability for the stable delay-induced periodic orbits.

2.3.1 Families of Hopf bifurcations and bifurcating periodic orbits

Figure 2.3 shows Hopf bifurcation curves of system (2.0.1) in the (λ, b_0) -plane; for reference, note that Fig. 2.2 is an enlargement of Fig. 2.3 near the point b_0^c . The (λ, b_0) -plane shown in Fig. 2.3 is bounded below at $b_0 = 0$ as is the convention [13, 24, 38]. It also has a left-hand boundary at $\lambda = \frac{1}{\gamma}$ (in this parameter regime where $\gamma = -10$ this is at $\lambda = -0.1$); at this boundary the delay τ becomes undefined. For $\lambda < \frac{1}{\gamma}$ the delay τ defined in (2.1.3) is negative and (2.0.1) is an advanced equation rather than a delay equation, analysis of which is beyond the scope of this thesis. In particular, for $\lambda < \frac{1}{\gamma}$ system (2.0.1) no longer describes Pyragas control.

The curve H_P is again the vertical (green) curve at $\lambda = 0$. By considering a larger view of the (λ, b_0) -plane, the Hopf bifurcation curve H_L can now be seen to form a closed loop. Namely, both of its end points meet at the point b_0^* on the left-hand boundary ($\lambda = \frac{1}{\gamma}$)

of Fig. 2.3. In addition to crossing H_P at the point b_0^c , the curve has a second crossing of H_P at the point HH_0 . The point HH_0 is a non-degenerate double Hopf bifurcation point, at which two pairs of purely imaginary eigenvalues exist; it is given by

$$HH_0 = \left\{ (\lambda, b_0) = \left(0, \frac{\pi - \beta}{2\pi(\sin \beta)} \right) \right\}. \quad (2.3.1)$$

At HH_0 the criticality of H_P changes, it is again subcritical and remains subcritical above HH_0 . Above HH_0 a periodic orbit bifurcates unstably from H_P with a complex conjugate pair of unstable Floquet multipliers. Thus, the target orbit Γ_P is only stable when it bifurcates from H_P between the points b_0^c and HH_0 .

In addition to the curve H_L , two further delay-induced Hopf bifurcation curves H_J^1 and H_R^1 are shown in Fig. 2.3. Both of these curves also emerge from the point b_0^* .

The curve H_J^1 stretches downwards in the plane from b_0^* before turning upwards and extending to infinity in the direction of b_0 . The curve H_J^1 can be split into sections of differing criticality. Figure 2.3 shows a degenerate Hopf bifurcation point DH_1 near the minimum of the curve H_J^1 . At this point the curve H_J^1 changes criticality; to the left of DH_1 , the curve H_J^1 is subcritical. From this section bifurcates an unstable periodic orbit, which exists for decreasing values of b_0 . Between the point DH_1 and the point HH_D^1 the curve H_J^1 is supercritical and from this section emanates a stable periodic orbit that exists for decreasing values of λ and, which we call Γ_J^1 . Above HH_D^1 , a periodic orbit that emanates from H_J^1 is unstable and exists for decreasing λ .

The curve H_R^1 starts at the point b_0^* before crossing the curve H_P at the double Hopf bifurcation point HH_1 and then extending to infinity in both λ and b_0 . All periodic orbits that emanate from H_R^1 are unstable and bifurcate from H_R^1 for decreasing values of b_0 . Those periodic orbits that bifurcate from H_R^1 to the right of the point HH_1 have three unstable Floquet multipliers. The unstable periodic orbits that emanate immediately to the left of HH_1 have five unstable Floquet multipliers.

An equation for these delay-induced Hopf bifurcation curves can be found by using the ansatz $z(t) = re^{i\omega t}$ in system (2.0.1); setting $r = 0$ yields the relationship

$$b_0 = H(\lambda) \equiv \frac{-\lambda^2 - (\omega - 1)^2}{2((\omega - 1) \sin \beta - \lambda \cos \beta)}, \quad (2.3.2)$$

where ω denotes the frequency of the Hopf bifurcation (which is derived in Appendix A). At the point b_0^* , numerical calculations show that the delay-induced Hopf bifurcations

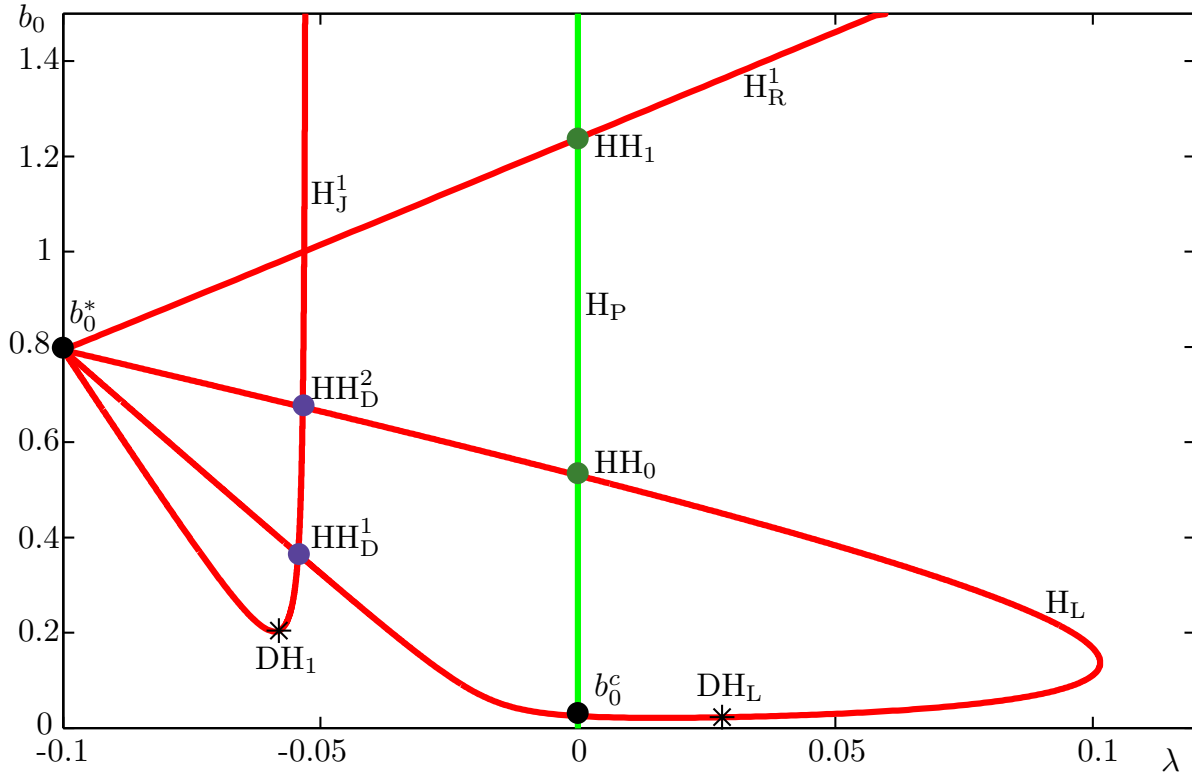


Figure 2.3: Bifurcation set in the (λ, b_0) -plane of (2.0.1), showing the Hopf bifurcation curve H_P (green) and the delay-induced Hopf curves H_L , H_J^1 and H_R^1 (red). Also shown are the double Hopf bifurcation points HH_0 (green), HH_1 (green), HH_D^1 (violet) and HH_D^2 (violet), as well as the points b_0^c and b_0^* (black). Degenerate Hopf bifurcation points on H_L and H_J^1 are marked with an asterisk.

have frequency $\omega = 0$. Substituting $\omega = 0$ and $\lambda = \frac{1}{\gamma}$ into equation (2.3.2) gives the expression

$$b_0^* = \left\{ (\lambda, b_0) = \left(\frac{1}{\gamma}, \frac{\frac{1}{\gamma^2} + 1}{2(\frac{1}{\gamma} \cos \beta + \sin \beta)} \right) \right\}. \quad (2.3.3)$$

Note that $b_0^* \approx (-0.1, 0.7935)$ for $\gamma = -10$ and $\beta = \frac{\pi}{4}$ as shown in Fig. 2.3.

Figure 2.4(a) shows the same part of the (λ, b_0) -plane as Fig. 2.3, but with additional Hopf bifurcation curves. More specifically, the curves H_J^1 and H_R^1 are, in fact, part of the respective families of curves H_J^K and H_R^K , with elements H_J^k and H_R^k respectively ($k = 1, 2, 3, \dots$). A selection of curves for each of these families is shown in Fig. 2.4(a). In addition, two of the double Hopf bifurcation points, where delay-induced Hopf bifurcation curves cross each other, are marked by violet dots and labelled HH_D^1 and HH_D^2 . These two points form part of a set of double Hopf bifurcation points HH_D , where delay-induced Hopf bifurcation curves cross each other.

The curves in the family H_J^K slope downwards in the plane, before reaching a minimum and then extending to infinity in the b_0 -direction. For increasing k , each curve in the family has a minimum with a higher value of b_0 and lower value of λ than the preceding curve. Each curve in the family has a degenerate Hopf bifurcation point DH_k to the right of the minimum of the curve. The curves H_J^k converge in this fashion on the left-hand boundary of the plane at $\lambda = \frac{1}{\gamma}$ as $k \rightarrow \infty$.

The curve H_J^1 intersects other delay-induced Hopf bifurcation curves at double Hopf bifurcation points of the set HH_D . Every time a point in this set is crossed in the direction of increasing b_0 , the periodic orbit bifurcates from H_J^1 with an additional complex pair of unstable Floquet multipliers.

The criticality of the subsequent curves of the family H_J^K is similar to that of H_J^1 . More specifically, the section of H_J^k between the degenerate Hopf bifurcation point DH_k and the first crossing with another delay-induced Hopf bifurcation curve is supercritical. From this section of H_J^k , bifurcates a stable periodic orbit Γ_J^k . These stable delay-induced periodic orbits are discussed in more detail later in this section.

Each curve of the family H_R^K emanates from the point b_0^* and extends to the right of the plane with positive gradient, crossing the curves H_J^k and H_P at double Hopf bifurcation points before extending to infinity in both λ and b_0 . At the left-hand boundary where $\lambda = \frac{1}{\gamma}$, as $k \rightarrow \infty$, each curve H_R^k has a steeper gradient than the preceding curve in the family and the curves are closer together.

As λ is decreased the curve H_R^1 intersects other delay-induced Hopf bifurcation curves at double Hopf bifurcation points that are part of the set HH_D . The unstable periodic orbit that bifurcates from H_R^1 to the left of one of these points has an additional complex pair of unstable Floquet multipliers. The criticality of the subsequent curves in the family are as that of the curve H_R^1 .

Figure 2.4(b) is an enlargement of the lower left part of Fig. 2.4(a). It also shows the transcritical bifurcation curve TC (2.2.1) (purple) from Fig. 2.2 over a much larger range of λ . Figure 2.4(b) shows that TC ends at the left-hand boundary of the plane at the point $(\lambda, b_0) = (\frac{1}{\gamma}, 0)$. Figure 2.4(b) also shows a selection of SNLC bifurcation curves S_J^k and S_R^k of the delay-induced periodic orbits that bifurcate from the H_J^K and H_R^K families of Hopf bifurcation curves respectively.

The curves labelled S_J^k start at degenerate Hopf bifurcation points (DH_k) on H_J^k and end at the point $(\lambda, b_0) = (\frac{1}{\gamma}, 0)$ (on the left-hand boundary). These are SNLC bifurcation

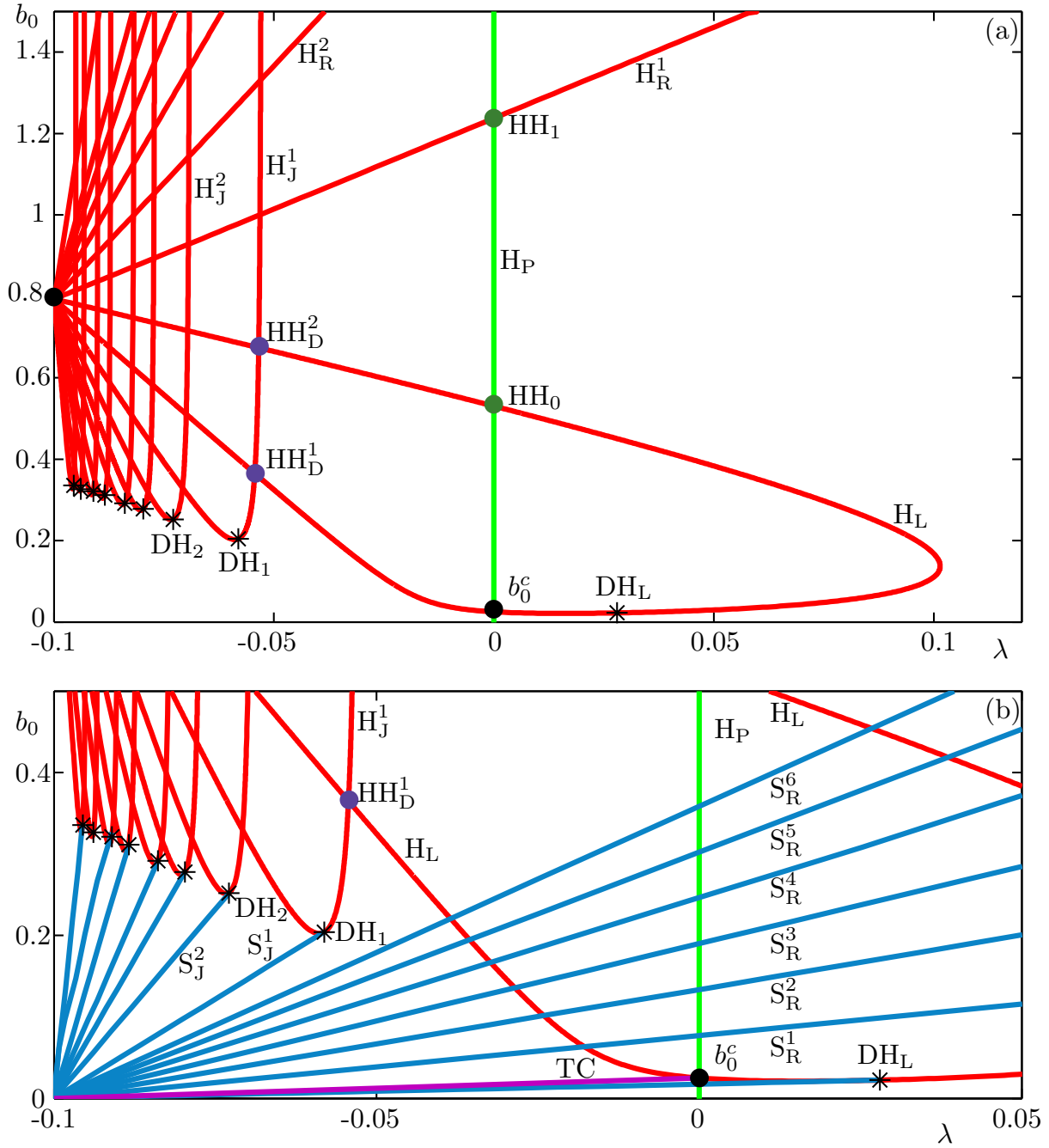


Figure 2.4: Panel (a) shows Hopf bifurcation curves of (2.0.1) in the (λ, b_0) -plane; shown are the curves H_P (green), H_L (red) and a selection of curves from the families H_J^K (red) and H_R^K (red). The enlargement in panel (b) also shows the transcritical bifurcation curve TC (purple) and a selection of curves from the two families of SNLC bifurcations S_J^K (blue) and S_R^K (blue).

curves of periodic orbits that bifurcate from the respective curves in the family H_J^K . For a curve H_J^k the unstable periodic orbit that bifurcates from the section between b_0^c and DH_k undergoes a SNLC bifurcation along the curve S_J^k .

The curves labelled S_R^k are SNLC bifurcation curves of periodic orbits that emanate from

the respective curves of the family H_R^K . The curves start at the point $(\lambda, b_0) = (\frac{1}{\gamma}, 0)$ (on the left-hand boundary) and extend to infinity in both λ and b_0 . The unstable periodic orbit that bifurcates from a curve H_R^k undergoes a SNLC bifurcation along the curve S_R^k , at which it is further destabilized.

2.3.2 Torus bifurcations and the domain of stability of Γ_P

The double Hopf bifurcation points, where the curve H_R^k crosses H_P at the point HH_k form a set HH_K . The points in the set HH_K are given by the expression (derived in Appendix B)

$$HH_k = \left\{ (\lambda, b_0) = \left(0, \frac{\pi(1+k) - \beta}{2\pi(\sin \beta)} \right) \right\}. \quad (2.3.4)$$

At each point in the set HH_K , the frequency ω of the delay-induced Hopf bifurcation is either $\omega = 1$ or $\omega = k + \frac{\beta}{\pi}$. Therefore, when $\beta = \frac{\pi}{4}$ the double Hopf bifurcation points in the set HH_k are resonant. In this parameter regime HH_0 is a double Hopf bifurcation point of 1:4 resonance; see also [16, 50].

As we have already discussed, above HH_0 , all periodic orbits that bifurcate from H_P are unstable. In fact, above each double Hopf bifurcation point of the set HH_K there are further instabilities in the form of an additional complex conjugate pair of unstable Floquet multipliers. That is to say, those periodic orbits bifurcating from H_P between b_0^c and HH_0 have no unstable Floquet multipliers, those that emanate between HH_0 and HH_1 have two unstable Floquet multipliers, those that bifurcate from between HH_1 and HH_2 have four unstable Floquet multipliers and so on. In other words, the point b_0^c forms the lower right corner of the overall domain of stability of Γ_P and HH_0 forms its upper right corner.

Figure 2.5 is an enlargement of the lower left part of Fig. 2.4(a). It shows the overall domain of stability (shaded) of the target periodic orbit Γ_P and a selection of torus bifurcation curves (grey and black). It is common for double Hopf bifurcation points to be the starting point of torus bifurcation curves, and here we show a single torus bifurcation curve emerging from a few of the double Hopf bifurcation points [31, 46].

The curves T_P^0 , T_P^1 and T_P^2 are torus bifurcations of the target periodic orbit Γ_P that emanates from the curve H_P . They start at the points HH_0 , HH_1 and HH_2 respectively and the curves T_P^1 and T_P^2 end at the point $(\lambda, b_0) = (\frac{1}{\gamma}, 0)$ on the left-hand boundary of

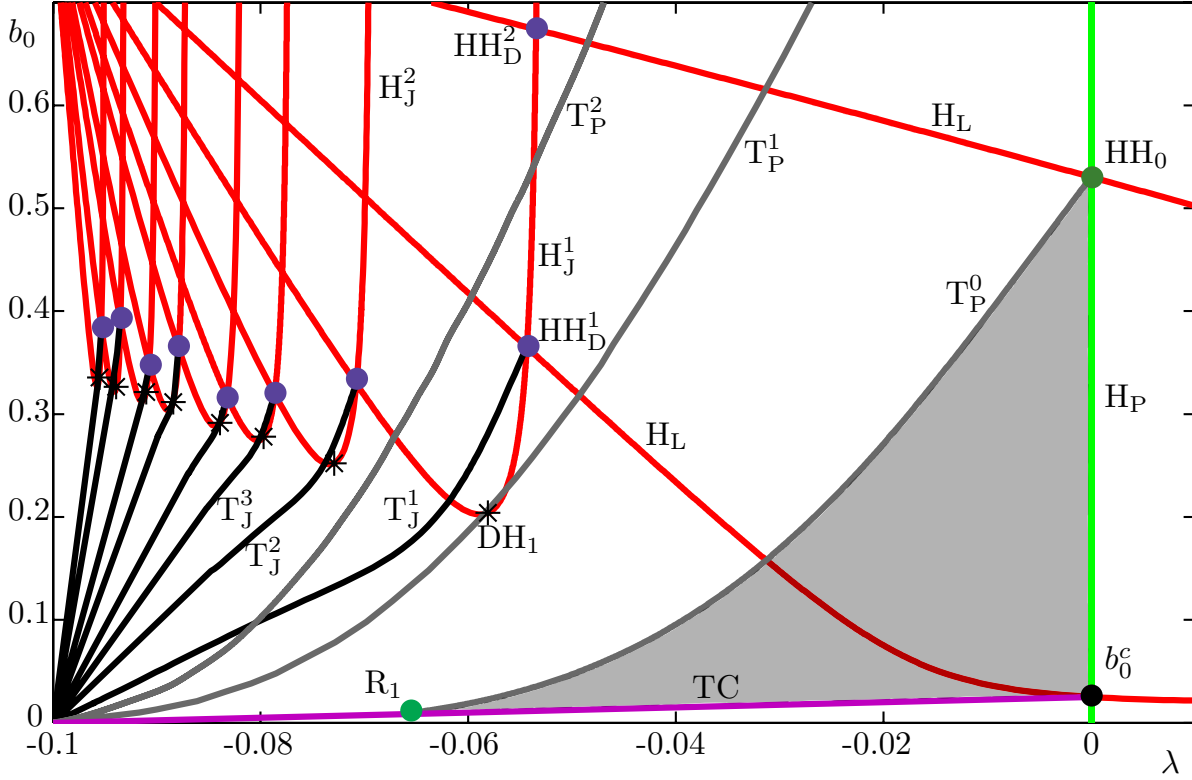


Figure 2.5: The first three torus bifurcation curves of the periodic orbit that bifurcates from the curve H_P (green), labelled T_P^0 , T_P^1 and T_P^2 (grey), and the torus bifurcation curves T_J^k (black) of delay-induced periodic orbits bifurcating from H_J^k . The domain of stability of the target periodic orbit Γ_P is shaded. Also shown are the curve TC (purple), a selection of degenerate Hopf bifurcation points DH (*), the point b_0^ϵ (black dot), the point HH_0 (dark green dot) and the point R_1 (light green dot) where the curve TC meets the curve T_P^0 .

the (λ, b_0) -plane. The curve T_P^0 ends on the transcritical bifurcation curve TC at the 1:1 resonance point R_1 , where the periodic orbits have a double Floquet multiplier at 1.

The overall domain of stability of Γ_P is, therefore, bounded below by the curve TC between the points b_0^ϵ and R_1 , to the left by the curve T_P^0 and to the right by the curve H_P . This shows that the stabilized periodic orbit Γ_P does not remain stable throughout the plane as suggested by the local unbounded domain that was developed by [13] and shown in Fig. 2.2.

Each subsequent torus bifurcation (T_P^1 , T_P^2 , ...) results in an additional unstable complex pair of Floquet multipliers. Thus, as λ is decreased, a periodic orbit Γ_P bifurcating from H_P (below HH_0) is first stabilized by Pyragas control before becoming unstable in the torus bifurcation T_P^0 . It then becomes increasingly unstable as it undergoes further torus bifurcations (in the set T_P^K) as it approaches the left-hand boundary of dynamics in the plane at $\lambda = \frac{1}{\gamma}$. At this boundary, the period of Γ_P (given by $T(\lambda) = \frac{2\pi}{1-\gamma\lambda}$) goes to

infinity.

The periodic orbits that bifurcate from the curve H_L are also destabilized in torus bifurcations. These torus bifurcation curves emerge from the double Hopf bifurcation points of the set HH_D where the curve H_L intersects curves in the family H_J^K .

The curves labelled T_J^1 , T_J^2 and T_J^3 are torus bifurcations of the delay-induced periodic orbits that emanate from the family of curves H_J^K . The curves start at the double Hopf bifurcation points in the set HH_D marked in Fig. 2.5 by violet dots. These torus bifurcation curves also terminate at the point $(\lambda, b_0) = (\frac{1}{\gamma}, 0)$ (on the left-hand boundary). The previously mentioned stable periodic orbits that bifurcate from the family of curves H_J^K are destabilized in these torus bifurcations. As they approach the left-hand boundary of the plane the periodic orbits are further destabilized in additional torus bifurcations that emerge from other points in the set HH_D .

The unstable periodic orbits that bifurcate from the family of SNLC bifurcation curves S_R^K almost immediately undergo a torus bifurcation, in which they are further destabilized. Further to the left of the (λ, b_0) -plane, these unstable periodic orbits undergo further torus bifurcations that emerge from double Hopf bifurcation points in the set HH_D in which they are further destabilized.

We notice two things from numerical evidence. Firstly, at the left-hand boundary of the (λ, b_0) -plane the frequency ω of all the delay-induced Hopf bifurcations is zero. Secondly, at the left-hand boundary, the period of all delay-induced periodic orbits goes to infinity.

2.3.3 Other regions of stable periodic orbits

We now consider in more detail the stable periodic orbits Γ_J^K that bifurcate from the family of Hopf bifurcation curves H_J^K . First, we take a slice at $b_0 = 0.295$ of the (λ, b_0) -plane shown in Fig. 2.5. Figure 2.6(a) shows the resulting one-parameter bifurcation diagram of (2.0.1) in λ , where the bottom axis shows the stability of the equilibrium solution. The green curve is the stable periodic orbit Γ_P , which bifurcates from the Hopf bifurcation H_P . Figure 2.6(a) also shows the stable delay-induced periodic orbits Γ_J^1 , Γ_J^2 and Γ_J^3 (solid red) that bifurcate supercritically from the Hopf bifurcations H_J^1 , H_J^2 and H_J^3 . At each of these Hopf bifurcations the equilibrium changes from being stable (black) to unstable (grey) as λ is reduced. The stable periodic orbits Γ_J^1 , Γ_J^2 and Γ_J^3 become unstable in the torus bifurcations T_J^1 , T_J^2 and T_J^3 , respectively. The grey curves represent already unstable delay-induced periodic orbits that bifurcate from H_L , H_J^1 , H_J^2 and H_J^3 .

Figure 2.6(b) shows the corresponding domains of stability (shaded grey) in the (λ, b_0) -plane, namely those of Γ_P and of the stable delay-induced periodic orbits Γ_J^1 , Γ_J^2 and Γ_J^3 . The regions where the equilibrium is stable are shaded blue. Darker blue shading indicates regions of bistability, where the equilibrium and a periodic orbit are both stable.

As previously discussed, the overall domain of stability of Γ_P is bounded by the curves H_P , TC and T_P^0 . In the part of the domain of stability enclosed by the curves H_L , T_P^0 and TC the equilibrium is also stable. This bistability adds to the complexity of implementing the Pyragas control scheme, because the system may not reach the target periodic orbit even though it is stable.

Similarly to Γ_P , the domain of the stable delay-induced periodic orbit Γ_J^k is bounded on the right by the Hopf bifurcation curve H_J^k between the degenerate Hopf bifurcation point DH_k and the double-Hopf bifurcation point HH_D^k . Its left-hand boundary is the torus bifurcation curve T_J^k and its lower boundary the SNLC bifurcation curve S_J^k . There are also regions where the equilibrium and the delay-induced periodic orbit Γ_J^k are both stable. This region is below the curve H_J^k and between the curves T_J^k and S_J^k .

Our calculations clearly indicate that there are infinitely many curves in the family H_J^K , which accumulate on the left-hand boundary $\lambda = \frac{1}{\gamma}$ of the (λ, b_0) -plane. Indeed when considering the control problem (2.0.1) it is common to take λ as the main bifurcation parameter. However, to make the connection to the stability problem of a general DDE, we now take the delay τ as the main bifurcation parameter. Hence, we consider the bifurcation set of (2.0.1) in the (τ, b_0) -plane as shown in Fig. 2.7(a). The bifurcation curves in Fig. 2.6(b) translate directly to those shown in Fig. 2.7(a) via the parameter transformation $\tau = \frac{2\pi}{1-\gamma\lambda}$ from (2.1.3). The delay τ goes to infinity as λ approaches the left-hand boundary $\lambda = \frac{1}{\gamma}$ of the (λ, b_0) -plane. Fig. 2.7(a) shows the Hopf bifurcation curve H_P (green) at $\tau = 2\pi$ and the delay-induced Hopf bifurcation curves H_L , H_J^1 , H_J^2 , H_J^3 and H_J^4 (red). The domains of stability of the target periodic orbit Γ_P and the stable delay-induced periodic orbits Γ_J^1 , Γ_J^2 , Γ_J^3 and Γ_J^4 are shaded in grey. The equilibrium solution is stable in the regions shaded blue and the darker blue areas are the regions of bistability discussed earlier in this section. These domains are bounded by the same bifurcation curves as those in the (λ, b_0) -plane discussed previously.

Figure 2.7(a) shows that the curves of the family H_J^K form a lobe structure that is common in systems with delay [17, 35, 41, 94–96]. The right end of the curve H_J^k has a horizontal asymptote at $b_0 \approx 0.7935$ (the b_0 value of the point b_0^*) as $\tau \rightarrow \infty$, but its left end has a vertical asymptote at a finite value of τ as $b_0 \rightarrow \infty$. In fact, for $b_0 \rightarrow \infty$ the curves H_J^k are spaced at 2π intervals from each other. This can be shown analytically by considering

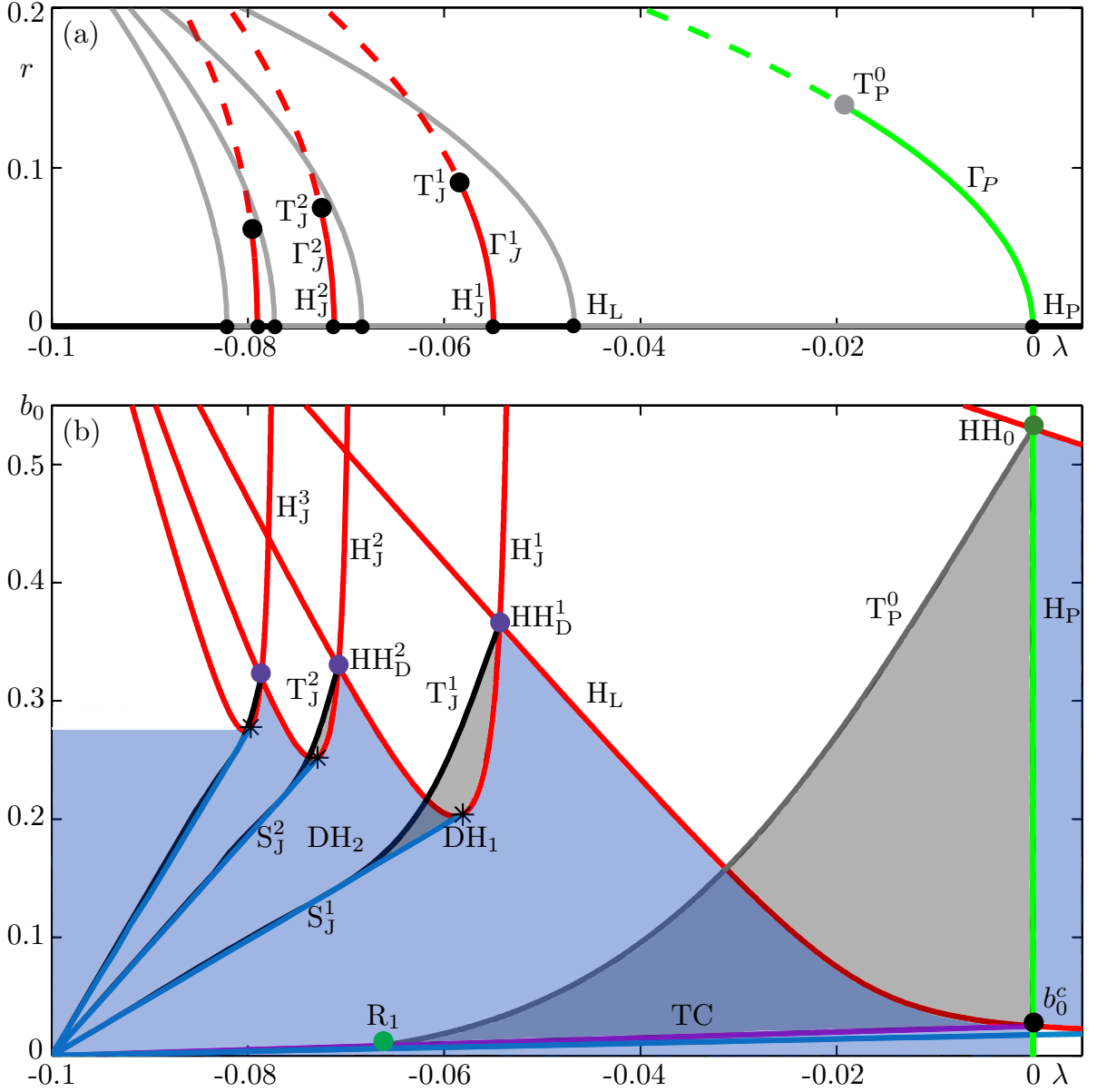


Figure 2.6: Panel (a) is the one-parameter bifurcation diagram of (2.0.1) in λ for $b_0 = 0.295$. Shown are the stable periodic orbit Γ_P bifurcating from H_P and further delay-induced stable periodic orbits Γ_J^1 , Γ_J^2 and Γ_J^3 bifurcating from H_J^1 , H_J^2 and H_J^3 . These stable periodic orbits become unstable at the torus bifurcations T_J^1 , T_J^2 and T_J^3 (black dots). Solid (dashed and grey) curves indicate stable (unstable) periodic orbits, the solid black (grey) lines indicate where the equilibrium is stable (unstable). Panel (b) shows the domains of stability (shaded grey) of the target periodic orbit Γ_P and the stable delay-induced periodic orbits Γ_J^1 , Γ_J^2 and Γ_J^3 . The regions where the equilibrium solution is stable are shaded blue; above the horizontal boundary at $b_0 = 0.28$, the stability region is not well defined, as further curves of the family H_J^K are not shown.

purely imaginary eigenvalues $\eta = i\omega$ of the characteristic equation of (2.0.1). Solving this equation for the frequency ω (simplifying equations (A.0.2) in Appendix A) yields ω as a

When $b_0 \rightarrow \infty$ the part of equations (2.3.5) and (2.3.6) inside the square root becomes $1 - \cos^2(\beta) = \sin^2(\beta)$. Thus, the expressions in the square brackets become 0 and, therefore, the frequency ω tends to 1. Hence, the period $T(\lambda) = \frac{2\pi}{\omega}$ tends to 2π as $b_0 \rightarrow \infty$. In [99], Yanchuk and Perlikowski derive the relationship $\tau_k = \tau_0 + kT(0)$ (for $k = 0, 1, 2, 3, \dots$) between delay and periodicity, which states that periodic orbits reappear infinitely many times for specific values of τ . Here, $\tau_0 = T(0) = 2\pi$, which implies that $\tau_k = 2k\pi$ is the vertical asymptote of the curve H_J^k . In particular, it follows that there are infinitely many Hopf bifurcation curves in the family H_J^K .

Owing to the different slopes of the curves in the family H_J^K , the spacing of associated points on the curves is no longer 2π for finite b_0 . Then the spacing of the curves in the family H_J^K can still be described by the expression linking delay and periodicity given in [99] but with a b_0 -dependent stretching factor. When considering the bifurcation set of (2.0.1) in the (λ, b_0) -plane, this means that there are infinitely many Hopf bifurcation curves that accumulate on the left-hand boundary; see Fig. 2.4(a).

The theory of [99] also suggests that there may be infinitely many stable delay-induced periodic orbits. Figures 2.6(b) and 2.7(a) show that, for large k the domain of stability of the stable delay-induced periodic orbit Γ_J^k becomes impractically small. On the other hand these two figures also show that the domains of stability of Γ_J^1 and Γ_J^2 , are large enough to cause concern when implementing Pyragas control. As we have already discussed, if an initial condition is not carefully chosen, the system could reach one of these stable periodic orbits rather than Γ_P .

Figure 2.7(b) is the one-parameter bifurcation diagram in the delay τ of (2.0.1) for $b_0 = 0.295$; compare with Fig. 2.6(a). It shows the periodic orbit Γ_P (green) and the stable delay-induced periodic orbits $\Gamma_J^1, \Gamma_J^2, \Gamma_J^3$ and Γ_J^4 (red); the already unstable periodic orbits that bifurcate from delay-induced Hopf bifurcation curves are again shown in grey. The stable periodic orbits bifurcate from the Hopf bifurcation points H_J^k , which are equally spaced in τ ; we calculate the spacing for $b_0 = 0.295$ to be approximately $1.1 \times 2k\pi$. Notice from Fig. 2.7(b) that for larger values of k the periodic orbit Γ_J^k is stable for a smaller range of τ , which corresponds to the shrinking domains of stability shown in Fig. 2.7(a).

2.4 The effect of the 2π -periodic feedback phase β

Most previous work on (2.0.1) fixes the 2π -periodic feedback phase at $\beta = \frac{\pi}{4}$. We now vary β , firstly increasing it and then decreasing it from $\frac{\pi}{4}$. In particular, we evaluate the

Panel of Fig. 2.8	Description of curves
(a): $\beta = \frac{\pi}{4}$	The domain of stability of Γ_P in the (λ, b_0) -plane as in Fig. 2.5. Its right-hand boundary is the curve H_P (green) between the points b_0^c (black) and HH_0 (green) and its left-hand boundary is the curve T_P^0 (grey). The lower boundary of the stability domain is the curve TC (purple) between the points b_0^c and R_1 (green).
(b): $\beta = \frac{3\pi}{4}$	The two points HH_0 and b_0^c have moved closer together in the (λ, b_0) -plane. The point R_1 has moved right along the curve TC. The area of the stability domain is reduced.
(c): $\beta = 3.00$	The point b_0^c has moved quickly up in the (λ, b_0) -plane. The point R_1 has moved further right in the (λ, b_0) -plane along the curve TC. The stability domain is still bounded by the same bifurcation curves.
(d): $\beta = 3.12$	Here, the domain of stabilization has become very small. The points b_0^c and HH_0 are very close together and the point R_1 is close to the curve H_P .
(e): $\beta = \pi$	The points b_0^c and HH_0 are equal. The domain of stabilization has disappeared, and thus, control is no longer successful.
(f): $\beta = 3.20$	The point b_0^c is above the point HH_0 in the (λ, b_0) -plane. As β is further increased the point b_0^c moves to infinity before becoming negative. Stabilization for $b_0 > 0$ is no longer possible.

Table 2.1: Description of the effect of an increase in the parameter β on the domain of stability of Γ_P . To accompany Fig. 2.8

effect that β has on the domain of stability of Γ_P , the geometry of delay-induced Hopf bifurcation curves and the positions of the points b_0^c , HH_0 and b_0^* .

2.4.1 The effect on the domain of stability

Figure 2.8 shows how the domain of stability of Γ_P (shaded area) in the (λ, b_0) -plane changes as the parameter β is increased. An overview of these changes to the stability domain is presented in Table 2.1. Figure 2.8(a) shows the stability domain for $\beta = \frac{\pi}{4}$ as in Fig. 2.5. Recall that for $\beta = \frac{\pi}{4}$ the lower boundary of the stability region in the (λ, b_0) -plane is the transcritical bifurcation curve TC between the points b_0^c and R_1 , the upper boundary is the torus bifurcation curve T_P^0 and the right-hand boundary is the Hopf bifurcation curve H_P between the points b_0^c and HH_0 .

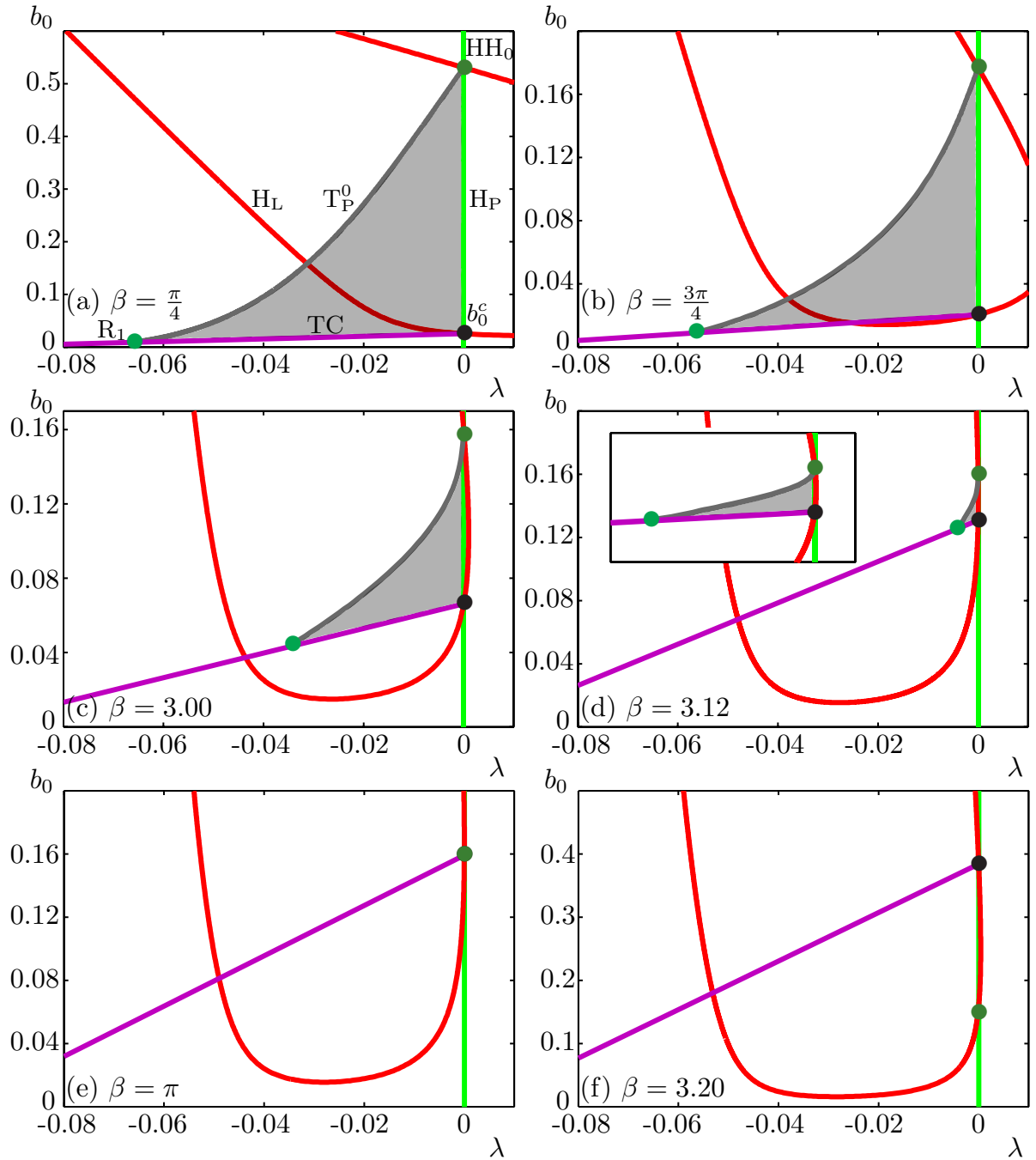


Figure 2.8: The overall domain of stability (shaded) in the (λ, b_0) -plane for different values of increasing β . Panel (a) is for $\beta = \frac{\pi}{4}$ as it is in Fig. 2.5, and panels (b)–(f) are for the stated values of β . Each panel shows the curves H_P (green) and H_L (red) as well as the points b_0^c (black dot) and HH_0 (green dot). The transcritical bifurcation curve TC (purple) and the torus bifurcation curve T_P^0 (grey) meet at the point R_1 (light green dot).

As β is increased, as in Fig. 2.8(b) and (c) for $\beta = \frac{3\pi}{4}$ and $\beta = 3$, respectively, the domain of stability of Γ_P becomes smaller in area, but is still bounded by the same curves. Also, the range of b_0 (the difference in b_0 between the points HH_0 and b_0^c) for which Γ_P bifurcates stably from H_P , decreases. More specifically, the curve H_L shifts left in the plane, the

two points b_0^c and HH_0 move closer together, and the end of the curve T_P^0 at the point R_1 moves right along the curve TC . As β approaches π , the area of the domain of stability shrinks to zero; see panels (d) and (e) for $\beta = 3.12$ and $\beta = \pi$ respectively.

Figure 2.8(e) shows that at $\beta = \pi$, the domain of stabilization has disappeared. Here, the curve H_L is tangent to the curve H_P at $(\lambda, b_0) = (0, \frac{1}{2\pi})$. The points b_0^c and HH_0 are both at the point $(\lambda, b_0) = (0, \frac{1}{2\pi})$. When $\beta = \pi$, the periodic orbits bifurcating from H_L are no longer stable. The targeted unstable periodic orbit that emanates from H_P cannot be stabilized through a transcritical bifurcation (see section 2.2). A periodic orbit that bifurcates from H_P below the point $(\lambda, b_0) = (0, \frac{1}{2\pi})$ has one unstable Floquet multiplier, above $(\lambda, b_0) = (0, \frac{1}{2\pi})$ a periodic orbit that bifurcates from H_P has a complex conjugate pair of unstable Floquet multipliers.

As β is further increased the curve H_L has shifted right in the plane. Furthermore, the points b_0^c and HH_0 have moved through each other; this is shown in panel (f) of Fig. 2.8. Below the point HH_0 , an unstable periodic orbit that bifurcates from the curve H_P has one unstable Floquet multiplier. An unstable periodic orbit that bifurcates from H_P between HH_0 and b_0^c has three unstable Floquet multipliers. Above the point b_0^c , an unstable periodic orbit that bifurcates from H_P has two unstable Floquet multipliers. There exist double Hopf bifurcation points of the set HH_K further up the curve H_P . Every time a point in this set is crossed in the direction of increasing b_0 , the periodic orbit bifurcates from H_P with an additional complex pair of unstable Floquet multipliers. As β is further increased, the point $b_0^c \rightarrow \infty$ as $\beta \rightarrow [\arctan(-\frac{1}{\gamma}) + \pi]$, then for $\beta > [\arctan(-\frac{1}{\gamma}) + \pi]$ the point b_0^c is negative.

The effect on the domain of stability of Γ_P when the feedback phase β is decreased is considered in Fig. 2.9. An overview of the changes to the stability domain shown in Fig. 2.9 is presented in Table 2.2. Figure 2.9(a) again shows the stability domain (shaded) for $\beta = \frac{\pi}{4}$ as in Fig. 2.5. As β is decreased both the points b_0^c and HH_0 move upwards and the point R_1 moves left along the curve TC ; this is shown in panels (b) and (c) for $\beta = 0.5$ and $\beta = 0.2$, respectively. In both of these panels the area of the domain of stability and the range of stability in b_0 increase. As β is decreased below 0.2, the point b_0^c moves upwards at a much faster rate than the point HH_0 and the point R_1 moves right along the curve TC . Thus, the area of the domain of stability of Γ_P becomes smaller; an example of this is shown in Fig. 2.9(d) for $\beta = 0.11$. At approximately $\beta = 0.103$, as shown in panel (e), the points b_0^c and HH_0 are equal where the curve H_L has a point of self-intersection on the curve H_P and the domain of stability of Γ_P has disappeared. Below this point on H_P , a periodic orbit bifurcates unstably from H_P with one unstable Floquet multiplier and above it a periodic orbit bifurcates unstably with a complex conjugate pair of unstable

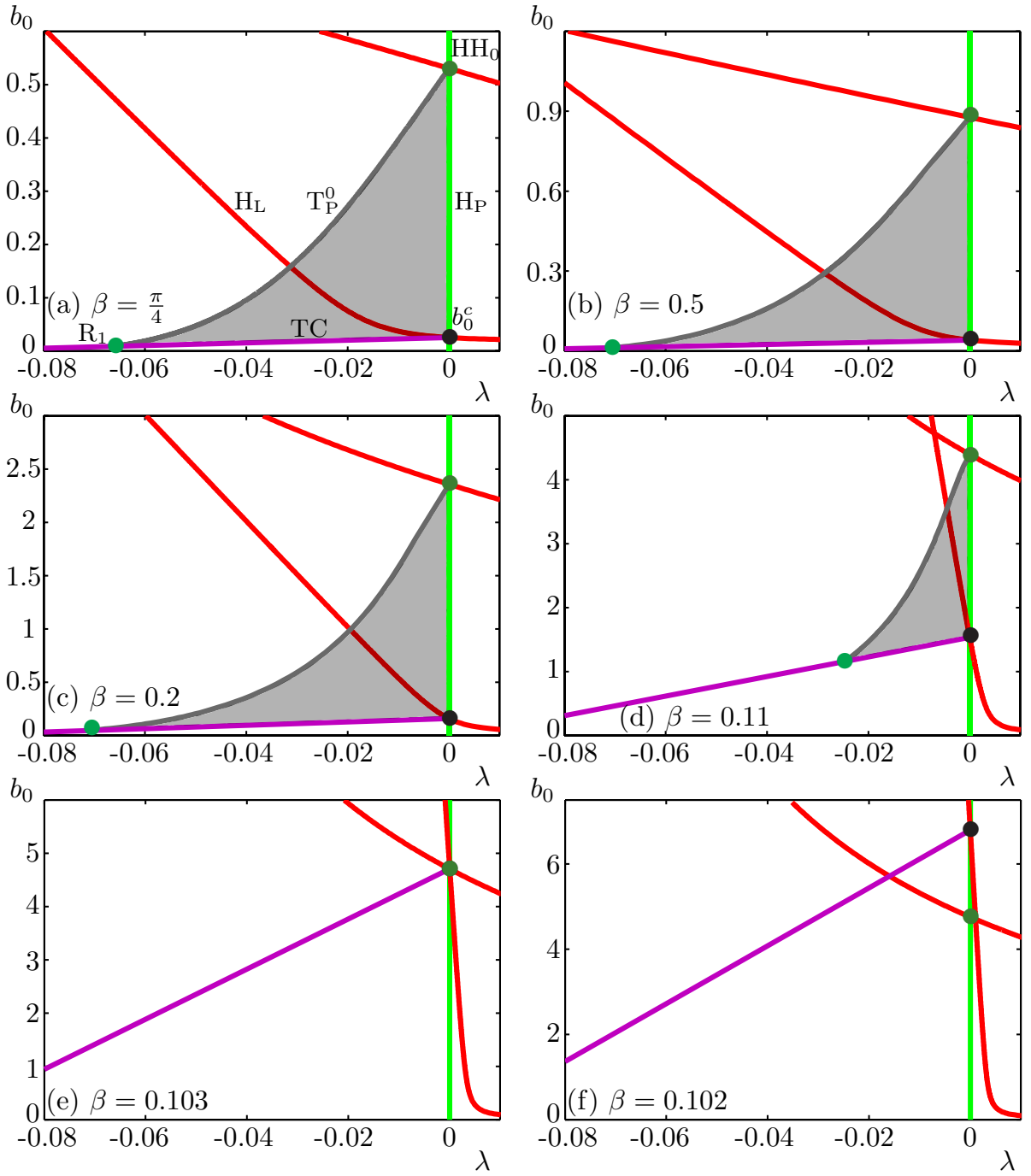


Figure 2.9: The overall domain of stability (shaded) in the (λ, b_0) -plane for different values of decreasing β . Panel (a) is for $\beta = \frac{\pi}{4}$ as it is in Fig. 2.5, and panels (b)–(f) are for the stated values of β . Each panel shows the curves H_P (green) and H_L (red) as well as the points b_0^c (black dot) and HH_0 (green dot). The transcritical bifurcation curve TC (purple) and the torus bifurcation curve T_P^0 (grey) meet at the point R_1 (light green dot).

Floquet multipliers. The maximum range of stability in b_0 is reached at $\beta \approx 0.12$. As β is further decreased, the point b_0^c rises rapidly, going to infinity as $\beta \rightarrow \arctan(-\frac{1}{\gamma})$. Below this value of β the point b_0^c is negative.

Panel of Fig. 2.9	Description of curves
(a): $\beta = \frac{\pi}{4}$	The domain of stability of Γ_P in the (λ, b_0) -plane as in Fig. 2.5. Its right-hand boundary is the curve H_P (green) between the points b_0^c (black) and HH_0 (green) and its left-hand boundary is the curve T_P^0 (grey). The lower boundary of the stability domain is the curve TC (purple) between the points b_0^c and R_1 (green).
(b): $\beta = 0.5$	The two points HH_0 and b_0^c have moved upwards in the (λ, b_0) -plane and the point R_1 has moved left in the (λ, b_0) -plane along the curve TC . Thus, the domain of stability increases in area.
(c): $\beta = 0.2$	The two points HH_0 and b_0^c have moved further upwards in the (λ, b_0) -plane. The point R_1 has also moved further left in the (λ, b_0) -plane along the curve TC . The stability domain is maximized in area.
(d): $\beta = 0.11$	The points b_0^c and HH_0 have moved further up in the (λ, b_0) -plane but the point b_0^c now moves up in the plane at a faster rate than the point HH_0 . The point R_1 has moved right in the (λ, b_0) -plane along the curve TC . Thus, the area of the stability domain is reduced.
(e): $\beta = 0.103$	The points b_0^c and HH_0 are equal. The domain of stabilization has disappeared, and thus, control is no longer successful.
(f): $\beta = 0.102$	The point b_0^c is above the point HH_0 in the (λ, b_0) -plane. As β is further decreased the point b_0^c moves to infinity before becoming negative.

Table 2.2: Description of the effect of a decrease in the parameter β on the domain of stability of Γ_P . To accompany Fig. 2.9

Overall, Fig. 2.8 and Fig. 2.9 show that stabilization of Γ_P is possible only when the point b_0^c is below the point HH_0 in the (λ, b_0) -plane. For a positive value of b_0 , this only occurs when $\beta_c < \beta < \pi$, where $\beta_c \approx 0.103$ is a value of β at which (2.1.4) and (2.3.1) are equal.

Outside of the stability region of Γ_P there are several other attractors in the plane. For example, in panel (c) of Fig. 2.8, to the left of the curve H_L both the equilibrium solution and periodic solutions bifurcating from the curves H_L and H_J^k may be stable depending on exact parameter values; see sections 2.2 and 2.3. To the right of the curve H_L the tori bifurcating from the set of curves T_P^K are initially attracting.

2.4.2 The effect of β on the delay-induced Hopf bifurcation curves

Figures 2.8 and 2.9 show that a change in β causes the Hopf bifurcation curve H_L to deform and move in the plane. This movement of H_L plays a crucial part in changes to the domain of stability of Γ_P . Therefore, we now consider in more detail the effect that changing the parameter β has on the three families of Hopf bifurcation curves (shown in Fig. 2.4(a)).

To gain a truly global overview of how the delay-induced Hopf bifurcation curves move in the (λ, b_0) -plane we must consider the curves beyond the region shown in Fig. 2.3. Hence, we now compactify the (λ, b_0) -plane so that we can also consider how the bifurcation curves behave near infinity. There are several ways to compactify a plane. One common approach is to transform the plane to the Poincaré disk. Here, we choose alternatively to compactify the parameter space as the unit square via individual stereographic transformations for λ and b_0 given by,

$$\hat{b}_0 = \frac{b_0}{1 + b_0}, \quad (2.4.1a)$$

$$\hat{\lambda} = \frac{(\lambda - \frac{1}{\gamma})}{0.25 + (\lambda - \frac{1}{\gamma})}. \quad (2.4.1b)$$

Recall that we do not consider the parameter regions $b_0 < 0$ or $\lambda < \frac{1}{\gamma}$. The coordinate transformation (2.4.1a) for b_0 fixes $\hat{b}_0 = b_0 = 0$ and transforms $b_0 = \infty$ to $\hat{b}_0 = 1$. The coordinate transformation (2.4.1b) for λ works in a similar fashion, but with a shift of $-\frac{1}{\gamma}$

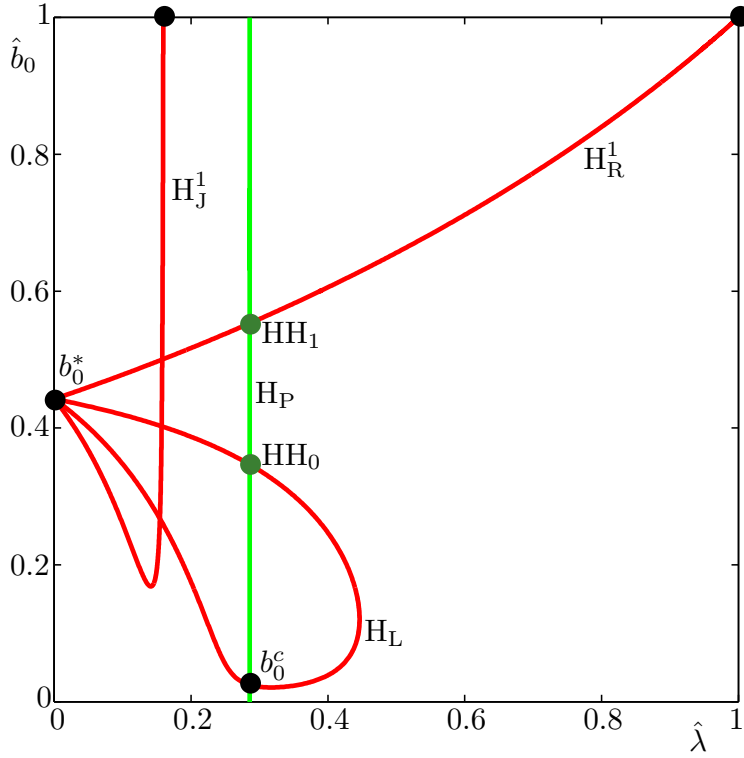


Figure 2.10: The first curves of Hopf bifurcations from each family in the compactified $(\hat{\lambda}, \hat{b}_0)$ -plane. Shown are the curve H_P (green), the delay-induced curves H_L, H_J^1 and H_R^1 (red), the points b_0^c and b_0^* (black dots) and the double Hopf bifurcation points HH_0 and HH_1 (green dots).

so that $\lambda = \frac{1}{\gamma}$ maps to $\hat{\lambda} = 0$ and $\lambda = \infty$ maps to $\hat{\lambda} = 1$. Overall, we obtain a transformed bifurcation set in the unit square $(\hat{\lambda}, \hat{b}_0) \in [0, 1] \times [0, 1]$.

Figure 2.10 shows the Hopf bifurcation curves H_L, H_J^1 and H_R^1 in the $(\hat{\lambda}, \hat{b}_0)$ -plane. The top boundary of the compactified plane represents infinity in b_0 with vertical asymptotes for fixed values of λ . The right boundary of the $(\hat{\lambda}, \hat{b}_0)$ -plane represents infinity in λ with horizontal asymptotes for fixed values of b_0 . The corner point $(1,1)$ corresponds to infinity in both λ and b_0 and the corner point $(0,1)$ corresponds to infinity in b_0 where there is a vertical asymptote at $\lambda = \frac{1}{\gamma}$.

The shapes of the curves H_L, H_J^1 and H_R^1 in the $(\hat{\lambda}, \hat{b}_0)$ -plane in Fig. 2.10 are similar to the equivalent curves before the compactification. Moreover, we can now see that the curve H_J^1 goes to infinity in b_0 at a finite value of λ , whilst the curve H_R^1 goes to infinity in both λ and b_0 , ending at the top right corner $(1,1)$.

We now show how the three families of delay-induced Hopf bifurcation curves change in the $(\hat{\lambda}, \hat{b}_0)$ -plane as the feedback phase β is increased through a period of 2π . An increase or decrease of 2π in β will result in an identical bifurcation set to that shown in Fig. 2.10.

Panel of Fig. 2.11	Description of curve
(a): $\beta = \frac{\pi}{4}$	The curve H_L (red) is connected to the left axis of the $(\hat{\lambda}, \hat{b}_0)$ -plane at the point b_0^* .
(b): $\beta = 3.24$	The two end points of the curve at the point b_0^* have moved up the left side of the $(\hat{\lambda}, \hat{b}_0)$ -plane to $(0,1)$.
(c): $\beta = 3.2420$	The curve H_L has opened up, its right end point has moved along the top boundary of the $(\hat{\lambda}, \hat{b}_0)$ -plane to $(1,1)$. The left end point of the curve is at $(0,1)$.
(d): $\beta = 3.26$	The left end point of the curve has moved right along the top boundary of the $(\hat{\lambda}, \hat{b}_0)$ -plane. Its right end point is still connected to $(1,1)$.
(e): $\beta = 6.2829$	The left end point of the curve has stopped sliding right along the top boundary of the $(\hat{\lambda}, \hat{b}_0)$ -plane.
(f): $\beta = 6.3513$	The left end point of the curve has moved back along top boundary of the $(\hat{\lambda}, \hat{b}_0)$ -plane to $(0,1)$.
(g): $\beta = 6.3628$	The right end point of the curve has disconnected from $(1,1)$ and has moved left along the top of the $(\hat{\lambda}, \hat{b}_0)$ -plane. The left end point of the curve is still at $(0,1)$.
(h): $\beta = 6.6032$	The right end point of the curve is connected to the top of the $(\hat{\lambda}, \hat{b}_0)$ -plane and the left end point has moved down the left side of the plane.
(i): $\beta = \frac{9\pi}{4}$	At $\beta = \frac{9\pi}{4}$ the curve H_J^1 (red) is formed.

Table 2.3: Description of the transformation of the curve H_L into the curve H_J^1 as the parameter β is increased by 2π . To accompany Fig. 2.11.

However, we find that, as β is changed, the Hopf bifurcation curves transition through the plane and transform into other Hopf bifurcation curves in a quite complicated manner.

We start by showing the transitions of the curves H_L , H_J^1 and H_J^2 in the $(\hat{\lambda}, \hat{b}_0)$ -plane. We show how the curves H_R^1 and H_R^2 are formed and move in the plane and, finally, we show how the curve H_L is formed. The transition of each curve is shown in a multi-panel diagram, where each panel shows the $(\hat{\lambda}, \hat{b}_0)$ -plane at a different value of β . For reference, each panel shows the curve H_P in green.

Figure 2.11 shows how the curve H_L transforms into the curve H_J^1 as β is increased from $\beta = \frac{\pi}{4}$ to $\beta = \frac{9\pi}{4}$. An overview of this transformation is given in Table 2.3. Figure 2.11(a) shows the curve H_L , from Fig. 2.10, that emerges from the point b_0^* on the left boundary of the $(\hat{\lambda}, \hat{b}_0)$ -plane. As β is increased from $\frac{\pi}{4}$, the point b_0^* moves up and down the left boundary of the $(\hat{\lambda}, \hat{b}_0)$ -plane. At $\beta = [\arctan(-\frac{1}{\gamma}) + \pi] \approx 3.24$, the point b_0^* has moved to the top left corner $(0,1)$; see panel (b). Panel (c) for $\beta = 3.242$ shows that the two end points of the curve are no longer the same; one end point, the right one, has moved along the top boundary of the $(\hat{\lambda}, \hat{b}_0)$ -plane to the top right corner $(1,1)$. Thus, the Hopf

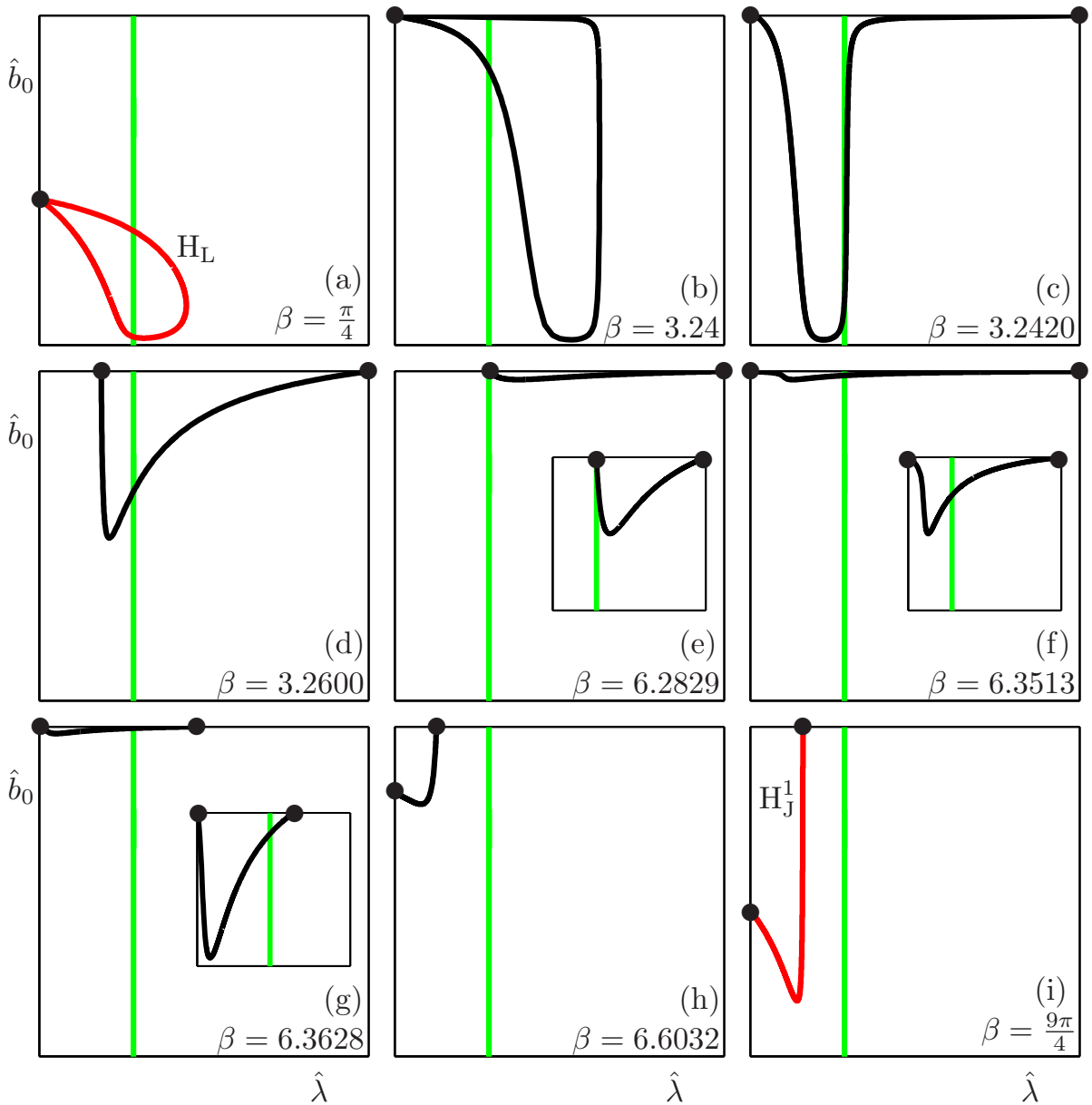


Figure 2.11: Transition of Hopf bifurcation curves in the $(\hat{\lambda}, \hat{b}_0)$ -plane for values of β as stated. The curve H_P is shown in green. The curve H_L (red) for $\beta = \frac{\pi}{4}$ in panel (a) transforms into the curve H_J^1 (red) for $\beta = \frac{9\pi}{4}$ in panel (i). Inserts in (e), (f) and (g) show respective enlargements.

bifurcation curve no longer forms a loop. Panel (d) for $\beta = 3.26$ shows that the left end point of the curve has detached from the corner $(0,1)$, and also moved along the top boundary of the $(\hat{\lambda}, \hat{b}_0)$ -plane. When β is approximately 2π the left end point of the curve has stopped moving right; panel (e) shows the left end point of the curve near its largest value of λ . The left end point of the curve then moves left along the top boundary of the $(\hat{\lambda}, \hat{b}_0)$ -plane, at $\beta = 6.3513$ it reaches the point $(0,1)$; this is shown in the enlargement of panel (f). The enlargement in panel (g) shows that at $\beta = 6.3628$, the right end point of

the curve has detached from the corner point (1,1). The right end point of the curve then moves left along the top boundary of the plane. At $\beta = [\arctan(-\frac{1}{\gamma}) + 2\pi]$ the left end point of the curve starts to move down the left boundary of the $(\hat{\lambda}, \hat{b}_0)$ -plane; an example of this is shown in panel (h). At $\beta = \frac{9\pi}{4}$, the curve H_J^1 is formed, this is shown in panel (i). The left end point of the curve is at b_0^* on the left boundary of the plane and the right end point is connected to the top boundary of the plane. Thus, through a change of 2π in β , the curve H_L transforms into H_J^1 .

Figure 2.12 shows how the curve H_J^1 transforms into the curve H_J^2 as the feedback phase β is increased through a period of 2π . An overview of this transformation is given in Table 2.4. Figure 2.12(a) shows the curve H_J^1 as it appears in the $(\hat{\lambda}, \hat{b}_0)$ -plane in Fig. 2.10 for $\beta = \frac{\pi}{4}$. Its left end point is at the point b_0^* on the left boundary of the $(\hat{\lambda}, \hat{b}_0)$ -plane and the right end point is connected to the top boundary of the plane at infinity in b_0 .

Figure 2.12(b) for $\beta = 3.1416$ shows that the right end point of the curve has moved right along the top boundary of the plane and that there is a slight bend near the right end of the curve. Panel (c) shows that when $\beta = [\arctan(-\frac{1}{\gamma}) + \pi] \approx 3.2328$ the right end point of the curve is attached at the corner (1,1) and the left end point of the curve is attached to the corner (0,1). Panel (d) shows that the left end point of the curve has detached from the corner (0,1) and has moved right along the top boundary of the $(\hat{\lambda}, \hat{b}_0)$ -plane. At the same time the entire Hopf bifurcation curve has shifted upwards in the plane. At $\beta \approx 2\pi$ as in panel (e), the left end point of the curve has stopped moving right along the top boundary of the plane. The left end point of the curve then starts to move left along the top boundary of the $(\hat{\lambda}, \hat{b}_0)$ -plane. Panel (f) for $\beta = 6.3548$ shows that the left end point of the curve connects to the corner (0,1). At $\beta = [\arctan(-\frac{1}{\gamma}) + 2\pi] \approx 6.3701$, the right end point of the curve has detached from the corner (1,1) and has moved left along the top boundary of the $(\hat{\lambda}, \hat{b}_0)$ -plane; this is shown in the enlargement of panel (g). The left end point of the curve then moves down the left boundary of the plane forming the point b_0^* and, thus, the curve H_J^2 is formed. This formation is shown in panels (h) and (i), with the Hopf bifurcation curve H_J^2 shown in red for $\beta = \frac{9\pi}{4}$. Thus, a change of 2π in the phase of the feedback β , transforms the curve H_J^1 into the curve H_J^2 . Although not shown here, we have found that an increase of 2π in β transforms the curve H_J^2 into the curve H_J^3 and the curve H_J^3 into the curve H_J^4 . This is strong evidence for the natural conjecture that a increase of 2π in the feedback phase β transforms the curve H_J^k into the curve H_J^{k+1} .

Figure 2.13 shows how the curves H_R^1 and H_R^2 transition through the $(\hat{\lambda}, \hat{b}_0)$ -plane as β is changed. An overview of the transition of the curves H_R^1 and H_R^2 shown in Fig. 2.13 is presented in Table 2.5. We start with the curve H_R^2 from Fig. 2.4(a) but for $\beta = -\frac{7\pi}{4} = \frac{\pi}{4} - 2\pi$. Although in the (λ, b_0) -plane the curves H_R^1 and H_R^2 are both straight

Panel of Fig. 2.12	Description of curve
(a): $\beta = \frac{\pi}{4}$	The curve H_J^1 (red); the left end point of the curve is connected to the left side of the $(\hat{\lambda}, \hat{b}_0)$ -plane at b_0^* . The right end point of the curve is connected to the top boundary of the $(\hat{\lambda}, \hat{b}_0)$ -plane.
(b): $\beta = 3.1416$	The point b_0^* has moved up the left side of the $(\hat{\lambda}, \hat{b}_0)$ -plane. The right end point of H_J^1 has moved right along the top boundary of the plane.
(c): $\beta = 3.2328$	The left end point of the curve at the point b_0^* has moved to the top left corner of the $(\hat{\lambda}, \hat{b}_0)$ -plane at $(0,1)$. The right end point of the curve has moved right along the top boundary of the plane to $(1,1)$.
(d): $\beta = 6.00$	The left end point of the curve has disconnected from $(0,1)$ and has moved right along the top boundary of the $(\hat{\lambda}, \hat{b}_0)$ -plane.
(e): $\beta = 6.2831$	The left end point of the curve has stopped moving right along the top boundary of the $(\hat{\lambda}, \hat{b}_0)$ -plane. The right end point of the curve is still connected to $(1,1)$.
(f): $\beta = 6.3548$	The left end point of the curve has moved left along the top boundary of the $(\hat{\lambda}, \hat{b}_0)$ -plane to $(0,1)$.
(g): $\beta = 6.3701$	The right end point of the curve has disconnected from $(1,1)$ and has moved left along the top boundary of the $(\hat{\lambda}, \hat{b}_0)$ -plane.
(h): $\beta = 6.5832$	The left end point of the curve has moved down the left side of the $(\hat{\lambda}, \hat{b}_0)$ -plane as the point b_0^* . The right end point of the curve stops is still connected to the top boundary of the plane.
(i): $\beta = \frac{9\pi}{4}$	The curve H_J^2 (red) formed. Its right end point is connected to the top boundary of the $(\hat{\lambda}, \hat{b}_0)$ -plane and its left end point is connected to the left side of the plane at b_0^* .

Table 2.4: Description of the curve H_J^1 transforming into the curve H_J^2 as the parameter β is increased by 2π . To accompany Fig. 2.12.

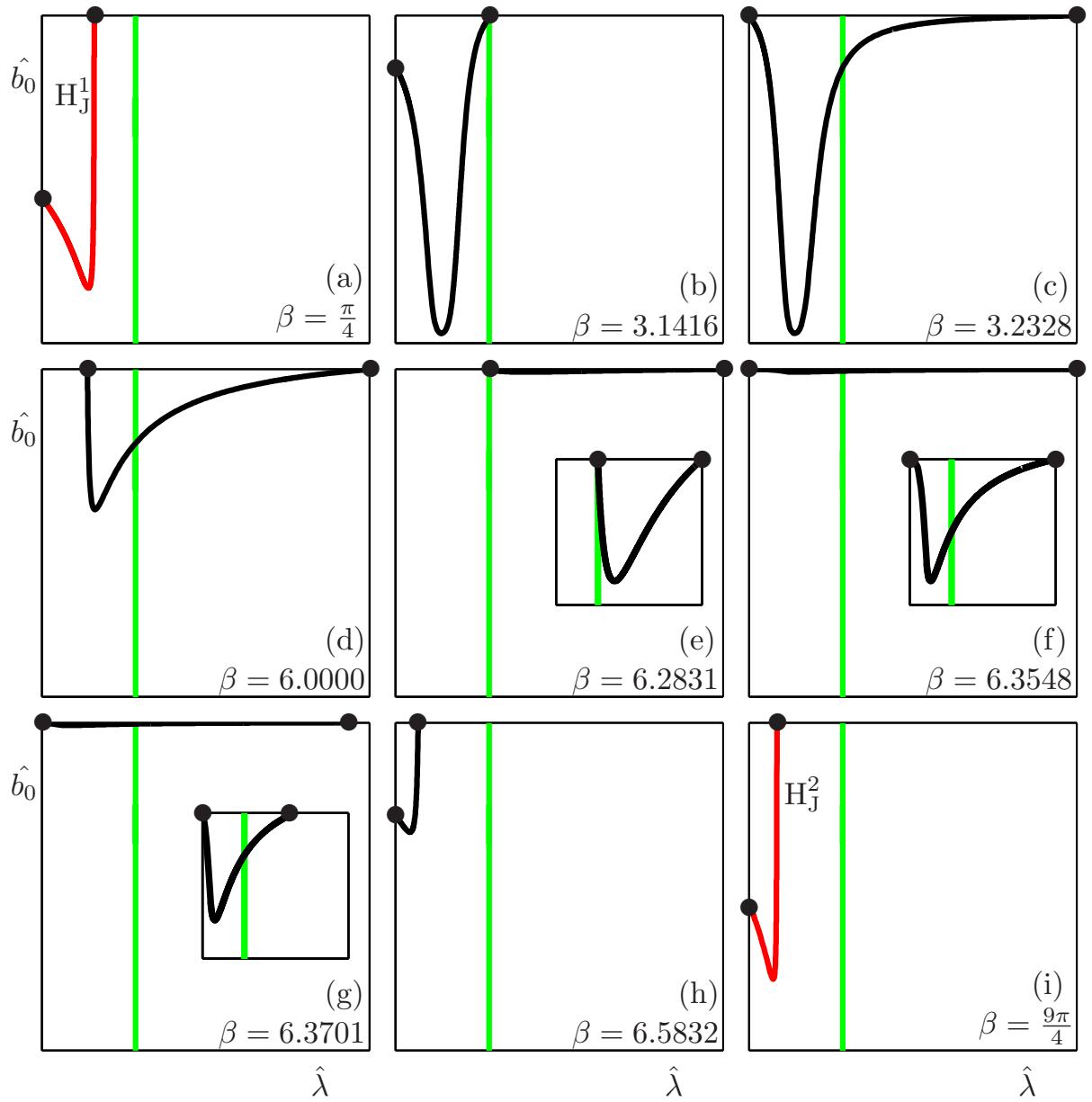


Figure 2.12: Transition of Hopf bifurcation curves in the $(\hat{\lambda}, \hat{b}_0)$ -plane for values of β as stated. The curve H_P is shown in green. The curve H_J^1 (red) for $\beta = \frac{\pi}{4}$ in panel (a) transforms into the curve H_J^2 (red) for $\beta = \frac{9\pi}{4}$ in panel (i). Inserts in (e), (f) and (g) show respective enlargements.

lines, in the $(\hat{\lambda}, \hat{b}_0)$ -plane, H_R^1 and H_R^2 have differing shapes. This is because the curve H_R^2 has a greater gradient than H_R^1 , which results in differently shaped curves when the plane is compactified by (2.4.1).

Figure 2.13(a) shows the Hopf bifurcation curve H_R^2 for $\beta = -\frac{7\pi}{4}$ with its right end point at the corner $(1,1)$ and its left end point connected to the left boundary of the $(\hat{\lambda}, \hat{b}_0)$ -plane at the point b_0^* . As β is increased the right end point of the curve moves left along the

Panel of Fig. 2.13	Description of curve
(a): $\beta = -\frac{7\pi}{4}$	The curve H_R^2 (red); its left end point is connected to the left side of the $(\hat{\lambda}, \hat{b}_0)$ -plane at the point b_0^* . Its right end point is connected to the top boundary of the $(\hat{\lambda}, \hat{b}_0)$ -plane at (1,1).
(b): $\beta = -3.2332$ and (c): $\beta = -3.1318$	The right end point of the curve moves left along the top boundary of the $(\hat{\lambda}, \hat{b}_0)$ -plane. The left end point of the curve moves up the left side of the $(\hat{\lambda}, \hat{b}_0)$ -plane. At $\beta = [\arctan(-\frac{1}{\gamma}) - \pi]$ the curve disappears into the top left-hand corner of the $(\hat{\lambda}, \hat{b}_0)$ -plane at (0,1).
(d): $\beta = 0$	A new curve emerges from the top right-hand corner of the $(\hat{\lambda}, \hat{b}_0)$ -plane. Its left end point immediately starts to move left along the top boundary of the $(\hat{\lambda}, \hat{b}_0)$ -plane. Its right end point is at (1,1).
(e): $\beta = 0.1$	The left end point has moved left along the top boundary of the $(\hat{\lambda}, \hat{b}_0)$ -plane until it reaches the point (0,1). The right end point of the curve is still connected to (1,1).
(f): $\beta = \frac{\pi}{4}$	The left end point of the curve has moved down the left side of the $(\hat{\lambda}, \hat{b}_0)$ -plane as the point b_0^* and the curve H_R^1 (red) is formed.
(g): $\beta = 1.8151$	A secondary curve (blue) emerges from the top right-hand corner of the $(\hat{\lambda}, \hat{b}_0)$ -plane at (1,1). The right end point of this curve is at (1,1) and its left end point is on the top boundary of the $(\hat{\lambda}, \hat{b}_0)$ -plane.
(h): $\beta = 2.0833$	The curve H_R^1 and the secondary curve become tangent at (1,1) and join to form one curve.
(i): $\beta = 2.15$	The curve has disconnected from (1,1). The right end point of the curve is connected to the top boundary of the $(\hat{\lambda}, \hat{b}_0)$ -plane. The left end point of the curve is connected to the left side of the plane.
(j): $\beta = 2.35$	The right end point of the curve has moved left along the top boundary of the $(\hat{\lambda}, \hat{b}_0)$ -plane and the left end point has moved up the left side of the plane.
(k): $\beta = 2.85$ and (l): $\beta = 3.1416$	The curve has moved towards the top left corner of the $(\hat{\lambda}, \hat{b}_0)$ -plane at (0,1). Its right end point has moved left along the top boundary of the plane and its left end point has moved up the left side of the plane. At $\beta = [\arctan(-\frac{1}{\gamma}) + \pi]$ the curve disappears into the top left-hand corner of the $(\hat{\lambda}, \hat{b}_0)$ -plane at the point (0,1).

Table 2.5: Description of the formation and transition of the curves H_R^1 and H_R^2 in the $(\hat{\lambda}, \hat{b}_0)$ -plane, as the parameter β is increased. To accompany Fig. 2.13.

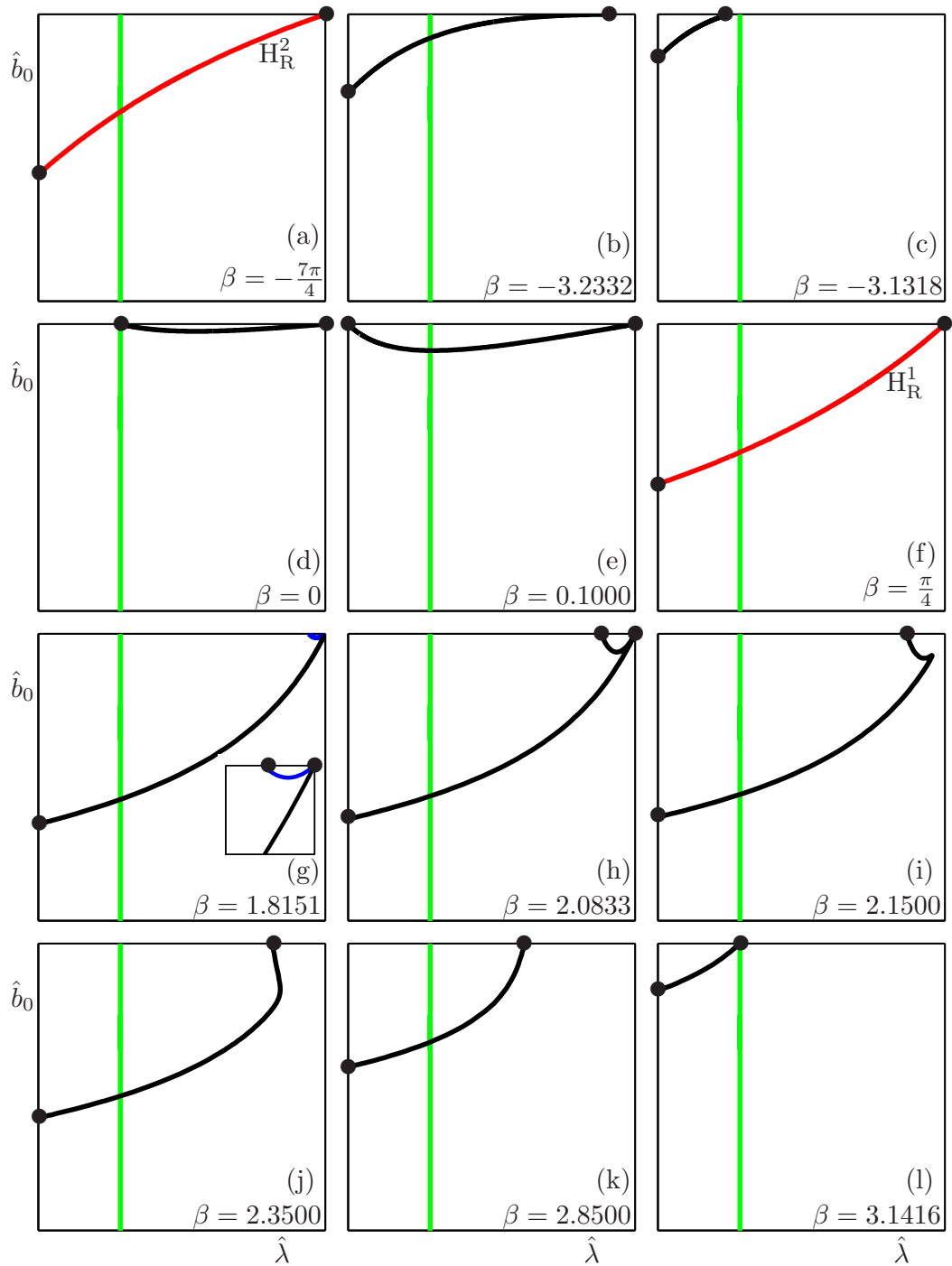


Figure 2.13: Transition of Hopf bifurcation curves in the $(\hat{\lambda}, \hat{b}_0)$ -plane for values of β as stated. The curve H_P is shown in green. The curve H_R^2 (red) for $\beta = -\frac{7\pi}{4}$ is shown in panel (a) and the curve H_R^1 (red) for $\beta = \frac{\pi}{4}$ is shown in panel (f).

top boundary of the $(\hat{\lambda}, \hat{b}_0)$ -plane and the left end point of the curve moves up the left boundary of the plane; this is shown in panels (b) and (c). The curve disappears into the top left corner $(0,1)$ of the $(\hat{\lambda}, \hat{b}_0)$ -plane at $\beta = [\arctan(-\frac{1}{\gamma}) - \pi]$. At $\beta \approx -0.06$ another Hopf bifurcation curve emerges from the top right corner $(1,1)$ of the $(\hat{\lambda}, \hat{b}_0)$ -plane. It

starts to extend downwards in the plane, with its right endpoint at (1,1). The left end point of the curve starts to move left along the top boundary of the plane. Figure 2.13(d) shows the curve at $\beta = 0$; the right end point of the curve is at the corner (1,1) and the left end point of the curve is connected to the top boundary of the plane. Panel (e) shows that the left end point of the curve has connected to the point (0,1) at $\beta = \arctan(-\frac{1}{\gamma}) \approx 0.1$. The left end point of the curve then starts to move down the left boundary of the $(\hat{\lambda}, \hat{b}_0)$ -plane as the point b_0^* . Panel (f) shows the Hopf bifurcation curve H_R^1 as it appears in Fig. 2.10 at $\beta = \frac{\pi}{4}$. The curve has its right end point at the corner (1,1) and its left end point at the point b_0^* on the left boundary of the $(\hat{\lambda}, \hat{b}_0)$ -plane. It should be noted that the curve H_R^2 is formed in a similar way to the curve H_R^1 . A curve appears from the corner (1,1), the left end point of this curve firstly moves left along the top boundary of the curve and then after reaching the corner (0,1) it moves down the left boundary of the $(\hat{\lambda}, \hat{b}_0)$ -plane. The right end point of the curve remains at the corner (1,1).

Figure 2.13(g) shows that at $\beta = 1.8151$ a second Hopf bifurcation curve has appeared from the top right corner (1,1) of the $(\hat{\lambda}, \hat{b}_0)$ -plane. The right end point of this secondary curve is at the corner (1,1) and the left end point immediately starts to move left along the top boundary of the $(\hat{\lambda}, \hat{b}_0)$ -plane. This secondary curve is shown in blue in the enlargement in Fig. 2.13(g). The right end points of both curves become tangent at the corner (1,1) when $\beta = 2.0833$. At this point the two Hopf bifurcation curves join; this is shown in panel (h). As shown in panel (i) for $\beta = 2.15$, the curve has moved away from the point (1,1), its right end point is connected to the top boundary of the plane and its left end point is connected to the left boundary of the plane. Panel (j) for $\beta = 2.35$ shows that the curve then straightens out near where it was connected to the corner (1,1). The right end point of the curve then starts to move left along the top boundary of the plane. Panel (k) shows the curve with its left end point connected to the left boundary of the $(\hat{\lambda}, \hat{b}_0)$ -plane and its right end point connected approximately midway across the top boundary of the $(\hat{\lambda}, \hat{b}_0)$ -plane. The left end point of the curve starts to move up the left boundary of the $(\hat{\lambda}, \hat{b}_0)$ -plane and the right end point moves further left along the top boundary of the plane. Thus, the Hopf bifurcation curve moves into the top left corner (0,1) of the $(\hat{\lambda}, \hat{b}_0)$ -plane; this is shown in Fig. 2.13(l) where the curve has both its right and left end points near the corner (0,1). When $\beta = [\arctan(-\frac{1}{\gamma}) + \pi]$, the curve disappears into the top left corner (0,1) of the plane. At approximately $\beta = 4.2009$ another Hopf bifurcation curve emerges from infinity in both λ and b_0 at the corner (1,1); this is shown in Fig. 2.14. The transition of this Hopf bifurcation curve in the $(\hat{\lambda}, \hat{b}_0)$ -plane shown in Fig. 2.14 is described in Table 2.6.

Panels (a) and (b) of Fig. 2.14 show this curve at $\beta = 4.5182$ and $\beta = 4.7143$ respectively, it has formed into a figure of eight shape that starts and ends at the corner (1,1) of the

Panel of Fig. 2.14	Description of curve
(a): $\beta = 4.5182$ and (b): $\beta = 4.7143$	A curve emerges from the top left-hand corner of the $(\hat{\lambda}, \hat{b}_0)$ -plane. It forms a figure of eight shape with both of its end points connected to the top right-hand corner of the plane at (1,1). The curve extends down into the $(\hat{\lambda}, \hat{b}_0)$ -plane.
(c): $\beta = 5.6096$	The left end point of the curve has moved left along the top boundary of the $(\hat{\lambda}, \hat{b}_0)$ -plane. The curve has extended further downwards in the plane and a loop shape has become more evident.
(d): $\beta = 6.3797$	The left end point of the curve has connected to the top left hand corner of the $(\hat{\lambda}, \hat{b}_0)$ -plane at (0,1). The right end point of the curve is still connected to (1,1).
(e): $\beta = 6.3829$	The right end point of the curve has disconnected from (1,1) and moved left along the top boundary of the $(\hat{\lambda}, \hat{b}_0)$ -plane.
(f): $\beta = 6.3863$	The right end point of the curve has connected to (0,1).
(g): $\beta = 6.4143$	The two end points of the curve have joined and moved down the left side of the $(\hat{\lambda}, \hat{b}_0)$ -plane as the point b_0^* .
(h): $\beta = 6.4578$	The left end of the curve moves below the right end of the curve. The curve is now a closed loop.
(i): $\beta = \frac{9\pi}{4}$	The curve H_L (red) is formed.

Table 2.6: Description of the formation of the curve H_L , as the parameter β is increased. To accompany Fig. 2.14.

$(\hat{\lambda}, \hat{b}_0)$ -plane. This curve stretches downwards into the plane. Panel (c) shows the curve at $\beta = 5.6096$, where the left end point of the curve has detached from the corner (1,1). This end point of the curve moves left along the top boundary of the plane until it reaches the corner (0,1), forming the point b_0^* ; see panel (d). Panel (e) shows the curve at $\beta = 6.3829$, the right end point of the curve has detached from the corner (1,1) and has moved left along the top boundary of the plane. In panel (f) for $\beta = 6.3863$ the right end point of the curve joins the left end point at the the corner (0,1) of the $(\hat{\lambda}, \hat{b}_0)$ -plane. Both ends of the curve remain joined and move down the left boundary of the plane, the curve starts as a figure of eight shape before deforming into an closed loop; see panels (g) and (h). Panel (i) shows the red curve H_L as it appears in Fig. 2.10, here for $\beta = \frac{9\pi}{4}$.

Overall, Figures 2.11–2.14 show that the movement of delay-induced Hopf bifurcation curves through the $(\hat{\lambda}, \hat{b}_0)$ -plane, as β is changed through a period of 2π , is highly non-trivial. As β is increased by 2π , the curve H_L transforms into the curve H_J^1 , the curve H_J^1 transforms into the curve H_J^2 and so on. This means that although a shift of 2π in the phase β obviously results in an identical bifurcation set, the Hopf bifurcation curves transform into different Hopf bifurcation curves rather than settling back into their original positions.

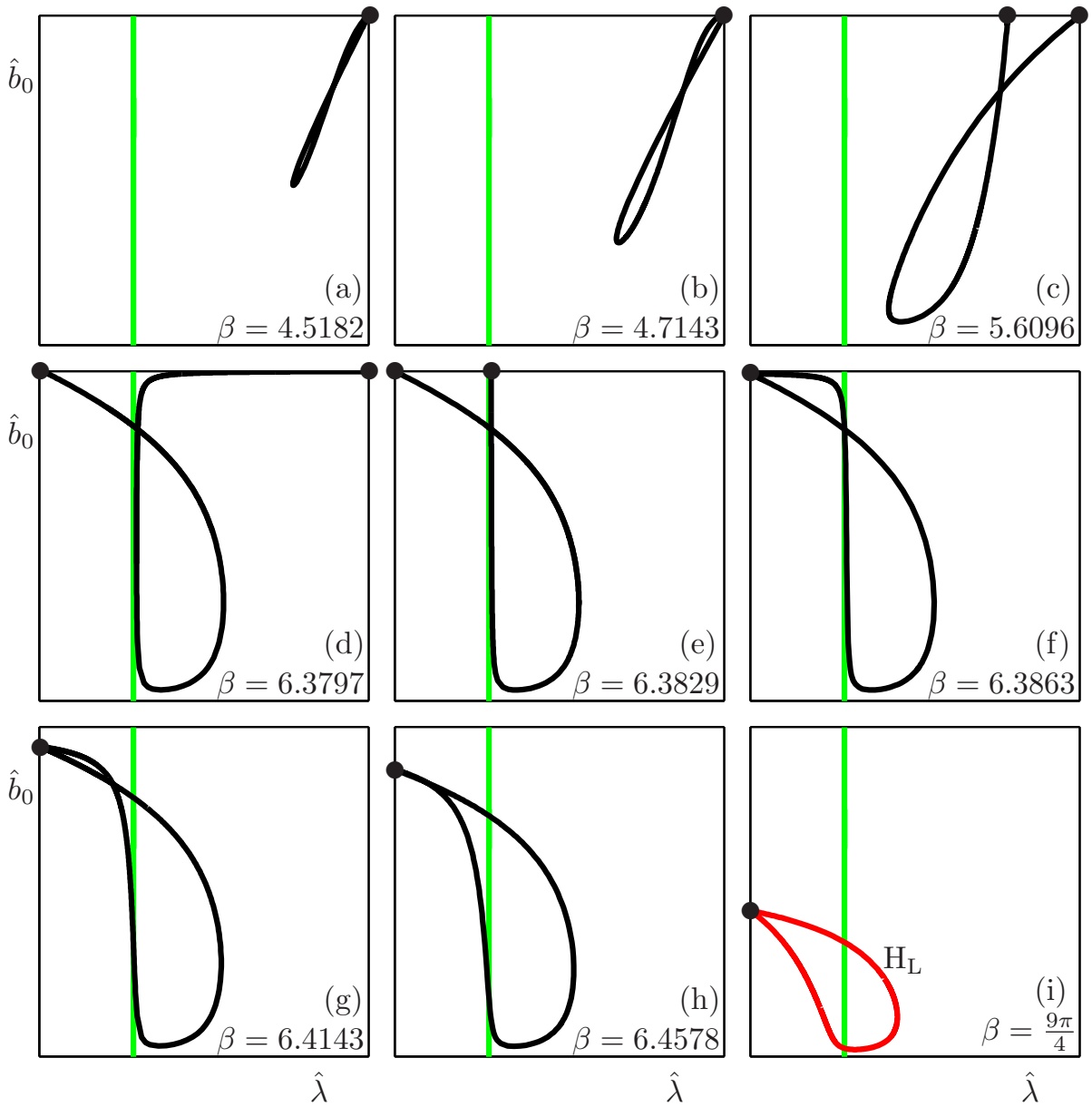


Figure 2.14: Transition of Hopf bifurcation curves in the $(\hat{\lambda}, \hat{b}_0)$ -plane for values of β as stated. Shown are the curves H_P (green) and H_L (red) for $\beta = \frac{9\pi}{4}$ in panel (i).

We also note that the delay-induced Hopf bifurcation curves all have movements to and from infinity at the values $\beta = [\arctan(-\frac{1}{\gamma}) + m\pi]$ (where $m \in \mathbb{Z}$). This is where the b_0 -coordinates of the points b_0^c (equation (2.1.4)) and b_0^* (equation (2.3.3)) go to infinity. Moreover, for this value of β the curve H_L no longer forms a closed loop. As we found earlier in this section, this fact plays an important role in whether or not a domain of stability of Γ_P exists; see Figs. 2.8 and 2.9.

The effect of a change in β has on the entire bifurcation set (including SNLC/torus bifurcations of periodic orbits shown in Fig. 2.14 and Fig. 2.15) is an even more complex

transition than the above analysis revealed for only the delay-induced Hopf bifurcation curves. A complete analysis of how every bifurcation curve of periodic orbits transitions through the plane as β changes is beyond the scope of this analysis. However, we have shown how the bifurcation curves of periodic orbits and the double Hopf bifurcation points b_0^c and HH_0 , that bound the domain of stability of Γ_P , move as β is changed; see Fig. 2.8 and Fig. 2.9. We conjecture that the other bifurcation curves of periodic orbits that emerge from the Hopf bifurcation curves move in accordance with how the Hopf bifurcation curves move in the (λ, b_0) -plane.

2.5 The effect of the parameter γ

Previous work has shown that stabilization of Γ_P is impossible when $\gamma = 0$ [13]. However, why stabilization fails at $\gamma = 0$ has not been fully explained geometrically. Here we show how the domain of stability of Γ_P disappears as γ is increased to 0. We also consider the effect of γ on the curve H_L and the two points b_0^c and HH_0 . We observe that the transition of H_L in the compactified $(\hat{\lambda}, \hat{b}_0)$ -plane, when γ is increased, causes the points b_0^c and HH_0 to cross and then stabilization of Γ_P fails. Finally, we present the region in the (β, γ) -plane where a successful stabilization of the target periodic orbit Γ_P is possible.

Figure 2.15 shows how the overall domain of stability (shaded) of Γ_P for $\beta = \frac{\pi}{4}$ changes as γ is increased. An overview of these changes to the stability domain is presented in Table 2.7.

Panel (a) shows the domain of stability as in Fig. 2.5, bounded by the curves H_P , T_P^0 and TC . As γ is increased the point b_0^c moves upwards, while the point HH_0 is independent of γ and so does not move. Panels (b) and (c), for $\gamma = -8$ and $\gamma = -5$, respectively, show that the point R_1 has moved left along the curve TC . It should be noted that an increase in γ shifts the left-hand boundary at $\lambda = \frac{1}{\gamma}$ further left in the (λ, b_0) -plane. Since the curve TC starts at b_0^c and ends at this boundary, along with its starting point changing, the gradient of the curve TC is also changing; see equation (2.2.1). As the point R_1 shifts left in the (λ, b_0) -plane the area of the domain of stability of Γ_P increases; however, the range of stability in b_0 (the difference in b_0 between the points HH_0 and b_0^c) for Γ_P decreases. At approximately $\gamma = -1.63$ the point R_1 stops moving left in the (λ, b_0) -plane; for this value of γ the area of the domain of stability of Γ_P is maximal. As γ is increased further the point R_1 starts to move right along the curve TC , reducing the area of the domain of stability of Γ_P . Figure 2.15(d) for $\gamma = -1.5$ shows that the point R_1 has moved right in the (λ, b_0) -plane and is now close to the starting point b_0^c of the curve TC ; hence, the

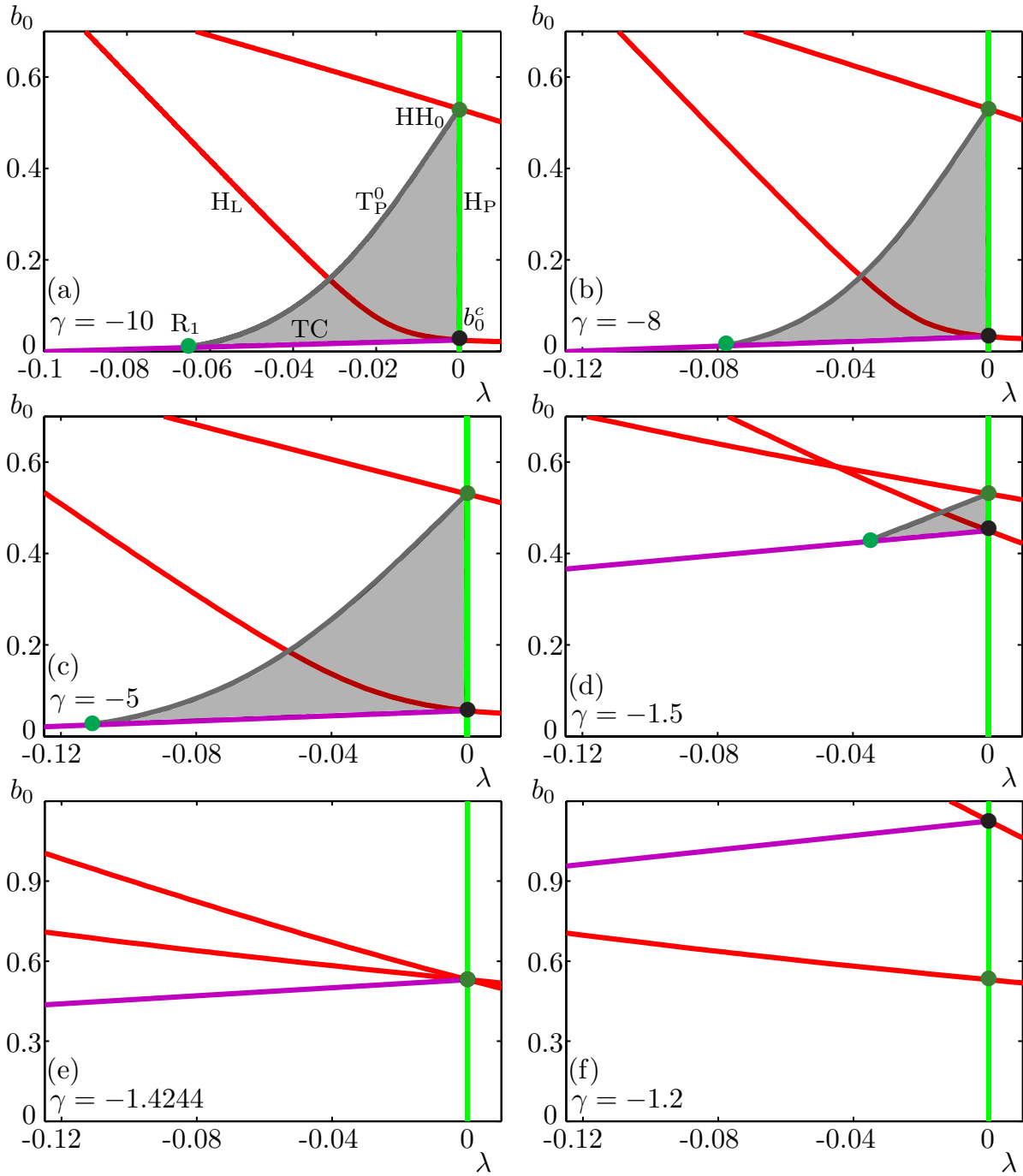


Figure 2.15: The overall domain of stability (shaded) in the (λ, b_0) -plane for different values of increasing γ . Panel (a) is for $\gamma = -10$ as it is in Fig. 2.5, and panels (b)-(f) are for the stated values of γ . Each panel shows the curves H_P (green) and H_L (red) as well as the points b_0^c (black dot) and HH_0 (green dot). The transcritical bifurcation curve TC (purple) and the torus bifurcation curve T_P^0 (grey) meet at the point R_1 (light green dot).

range of stability of Γ_P in b_0 is much smaller than for lower values of γ . The point b_0^c has moved up in the (λ, b_0) -plane and is just below the point HH_0 . Thus, the upper and lower boundary curves of the stability domain, T_P^0 and TC , are close to each other resulting in

Panel of Fig. 2.15	Description of curves
(a): $\gamma = -10$	The domain of stability of Γ_P in the (λ, b_0) -plane as in Fig. 2.5. Its right-hand boundary is the curve H_P (green) between the points b_0^c (black) and HH_0 (green) and its left-hand boundary is the curve T_P^0 (grey). The lower boundary of the stability domain is the curve TC (purple) between the points b_0^c and R_1 (green).
(b): $\gamma = -8$ and (c): $\gamma = -5$	The point R_1 has moved left in the (λ, b_0) -plane along the curve TC increasing the area of the stability domain. The point b_0^c remains at approximately the same level and the point HH_0 is not affected by a change in γ .
(d): $\gamma = -1.5$	The point b_0^c has moved up in the (λ, b_0) -plane and the point R_1 has moved right in the plane along the curve TC. Thus, the domain of stability has decreased in area.
(e): $\gamma = -1.4244$	The points b_0^c and HH_0 are equal and the domain of stability has disappeared.
(f): $\gamma = -1.2$	The point b_0^c has moved above the point HH_0 in the (λ, b_0) -plane. Stabilization is no longer possible.

Table 2.7: Description of the effect of an increase in the parameter γ on the domain of stability of Γ_P . To accompany Fig. 2.15

a small domain of stability.

Figure 2.15(e) shows that at $\gamma = -1.4244$, the points b_0^c and HH_0 are equal, and the domain of stability of Γ_P has disappeared. A periodic orbit bifurcating from H_P below this point is unstable with one unstable Floquet multiplier. A periodic orbit that bifurcates from H_P above this point is also unstable but has a complex conjugate pair of unstable Floquet multipliers. As γ is increased further the point b_0^c moves above the point HH_0 ; an example of this is shown in panel (f) for $\gamma = -1.2$. When $\gamma = -1$ the point b_0^c goes to infinity, and for $\gamma > -1$ the point b_0^c is negative.

Figure 2.16 shows the transition of the curve H_L in the $(\hat{\lambda}, \hat{b}_0)$ -plane as the parameter γ is changed. Note that, due to the γ -dependent compactification of the λ coordinate by (2.4.1b), the curves H_L and H_P are shifted right as γ is increased from its starting value of -10 . Thus, the last couple of panels of Fig. 2.16 show the Hopf bifurcation curves on the far right of the $(\hat{\lambda}, \hat{b}_0)$ -plane. An overview of the transition of the curve H_L is presented in Table 2.8.

Figure 2.16(a) shows the curve H_L (red) and the curve H_P (green) for $\gamma = -10$. The Hopf bifurcation curve H_L forms a closed loop shape with both end points connected at the point b_0^* on the left boundary of the $(\hat{\lambda}, \hat{b}_0)$ -plane. As γ is increased, the lower portion of

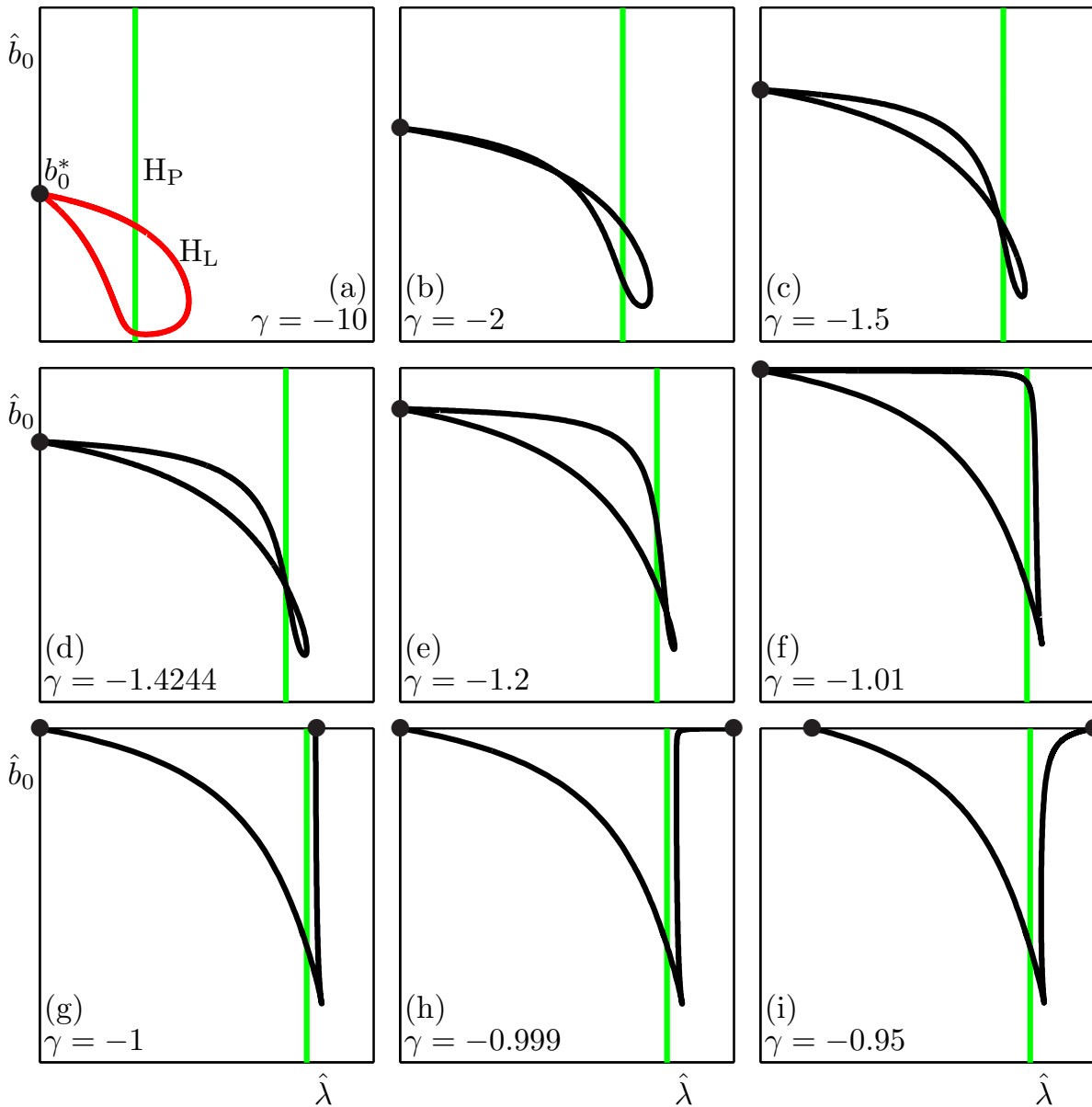


Figure 2.16: Transition of Hopf bifurcation curves in the $(\hat{\lambda}, \hat{b}_0)$ -plane for values of γ as stated. Shown are the curves H_P (green) and H_L (red) for $\gamma = -10$ in panel (a).

the curve shifts upwards in the plane, deforming the loop structure and the curve develops a point of self-intersection; an example of this is shown in shown in panel (b) for $\gamma = -2$. When $\gamma = -1.5$ as in panel (c), the point of self intersection of the Hopf bifurcation curve has moved right in the $(\hat{\lambda}, \hat{b}_0)$ -plane and the curve forms a more distinct figure of eight shape. The point b_0^* has shifted up the left boundary of the $(\hat{\lambda}, \hat{b}_0)$ -plane. Panel (d) for $\gamma = -1.4244$ shows that the Hopf bifurcation curve has its point of self-intersection on the curve H_P . As was shown in Fig. 2.15 at this value of γ stabilization of Γ_P is no longer possible.

Panel of Fig. 2.16	Description of curves
(a): $\gamma = -10$	The curves H_L (red) and H_P (green) as they appear in Fig. 2.10 in the $(\hat{\lambda}, \hat{b}_0)$ -plane. The curve H_L is connected to the left side of the plane at the point b_0^* .
(b): $\gamma = -2$ and (c): $\gamma = -1.5$	The bottom section of the curve H_L has moved upwards and the curve has formed a point of self intersection. The curve extends to the right of the $(\hat{\lambda}, \hat{b}_0)$ -plane.
(d): $\gamma = -1.4244$	The point of self intersection of the curve is on the curve H_P . The two end points of the curve are still at b_0^* on the left side of the $(\hat{\lambda}, \hat{b}_0)$ -plane.
(e): $\gamma = -1.2$	The point of self intersection of the curve is now to the right of H_P .
(f): $\gamma = -1.01$	The point b_0^* has moved to the top left-hand corner of the $(\hat{\lambda}, \hat{b}_0)$ -plane at $(0,1)$.
(g): $\gamma = -1$	The right end point of the curve has disconnected from $(0,1)$ and moved right along the top boundary of the $(\hat{\lambda}, \hat{b}_0)$ -plane. The curve H_L is no longer a closed loop and only crosses the curve H_P once.
(h): $\gamma = -0.999$	The right end point of the curve has connected to $(1,1)$.
(i): $\gamma = -0.95$	The left end point of the curve moves left along the top boundary of the $(\hat{\lambda}, \hat{b}_0)$ -plane.

Table 2.8: Description of the curve H_L as the parameter γ is increased. To accompany Fig. 2.16.

As γ is increased further, the self-intersection point of the curve moves to the right of H_P ; an example of this is shown in Fig. 2.16(e) for $\gamma = -1.2$. Panel (f) shows the Hopf bifurcation curve at $\gamma = -1.01$, where the point b_0^* has moved up the left boundary of the $(\hat{\lambda}, \hat{b}_0)$ -plane to the corner $(0,1)$, and the curve has opened up from its figure of eight shape. When $\gamma = -1$ as in panel (g), the right end point of the curve has detached from the corner $(0,1)$ and has shifted along the top boundary of the $(\hat{\lambda}, \hat{b}_0)$ -plane to the right of the curve H_P . Thus, the curve only crosses H_P once. As described earlier in this section, the point b_0^c is negative for this value of γ and remains negative as γ is increased further; see equation (2.1.4).

Figure 2.16(h) shows that at $\gamma = -0.999$ the right end point of the curve has moved to the top right corner $(1,1)$ of the $(\hat{\lambda}, \hat{b}_0)$ -plane. The left end point of the curve is still connected to the corner $(0,1)$. The left end point of the curve then detaches from $(0,1)$ for $\gamma \approx -0.995$ and starts to move right along the top boundary of the $(\hat{\lambda}, \hat{b}_0)$ -plane. Panel (i) for $\gamma = -0.95$ shows the curve with its left end point connected to the top boundary, whilst its right end point is still connected to the top right corner $(1,1)$. The left end point of the curve continues to move right along the top boundary of the $(\hat{\lambda}, \hat{b}_0)$ -plane as the value of γ is increased.

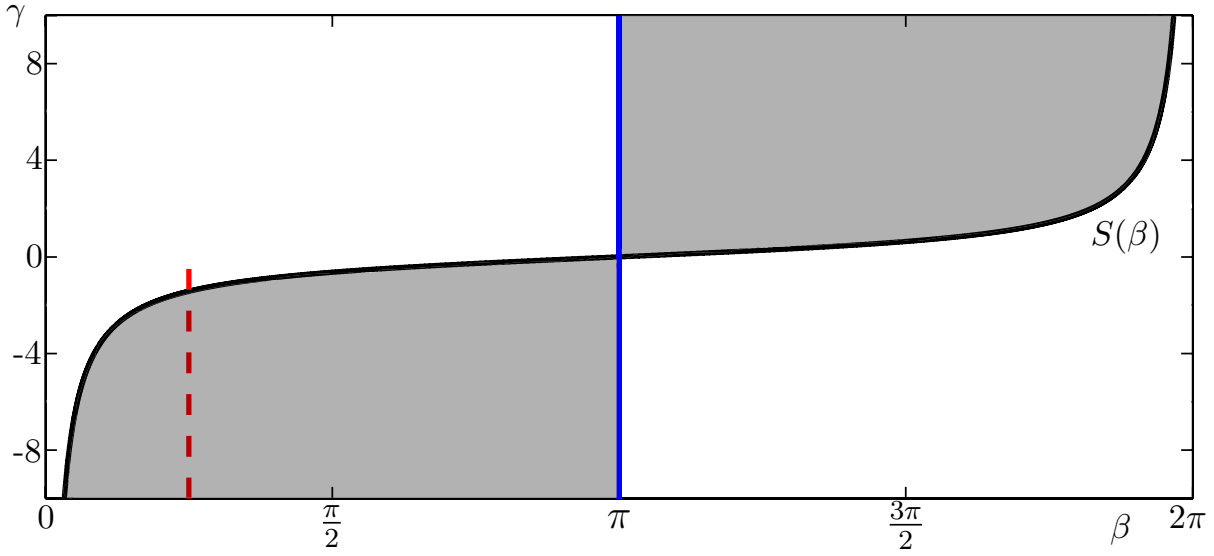


Figure 2.17: A section of the two-parameter (β, γ) -plane of system (2.0.1). The black curve represents the stability boundary $S(\beta)$ from equation (2.5.1). The vertical blue line is where $\beta = \pi$. In the shaded regions stabilization is possible. The red dashed line is the path with $\beta = \frac{\pi}{4}$ taken in Fig. 2.16.

As previously discussed, stabilization is only possible when the b_0 -coordinate of the point HH_0 is greater than that of the point b_0^c ; see also [13, 63]. From this relationship and the points b_0^c and HH_0 given by equations (2.1.4) and (2.3.1), we can find an overall stability boundary as the union of the curve $\gamma = S(\beta)$ and the line $\beta = \pi$, where $S(\beta)$ is given by

$$S(\beta) \equiv -\frac{1}{\pi - \beta} - \frac{1}{\tan \beta}. \quad (2.5.1)$$

Equation (2.5.1) defines the stability boundary $\gamma = S(\beta)$ (black) shown in Fig. 2.17 in the (β, γ) -plane. When $0 < \beta < \pi$ stabilization fails on and above this curve, for $\pi < \beta < 2\pi$ stabilization fails on and below this curve. The vertical dashed red line in Fig. 2.17 is at $\beta = \frac{\pi}{4}$, and the panels in Fig. 2.16 have values of γ on this line. In the shaded regions in the (β, γ) -plane the targeted periodic orbit Γ_P can be stabilized by Pyragas control with an appropriate choice of λ and b_0 . The stability boundary $S(\beta)$ defines the upper and left boundaries of the lower shaded region. It also forms the lower and right boundaries for the upper shaded region. The vertical (blue) curve at $\beta = \pi$ marks the right boundary of the lower shaded region and the left boundary of the upper shaded region. As explained in section 2.4, stabilization is impossible when $\beta = \pi$. For $\pi < \beta < 2\pi$ the dynamics presented in this chapter are replicated for negative b_0 through the symmetry relation $(\pi - \beta, \gamma) \rightarrow (2\pi - \beta, -\gamma)$. Therefore, the shaded region on the right of Fig. 2.17 is a rotation of the shaded region on the left. The shaded regions extend in γ to negative and positive infinity, respectively.

2.6 Conclusion

In this chapter we have considered the global effects of the addition of Pyragas control to the subcritical Hopf normal form. The addition of feedback induces infinitely many Hopf bifurcation curves, which can be classified as belonging to three families H_L , H_J^K and H_R^K . In particular, we have shown that, in addition to the target periodic orbit, system (2.0.1) has (a possibly infinite number of) other stable periodic orbits. Thus, system (2.0.1) may converge to a periodic orbit that is not the one targeted by Pyragas control. Furthermore, we have identified a region of bistability, where both the equilibrium solution and the target periodic orbit Γ_P are stable. This means that the system may not actually reach this periodic orbit if the initial condition is chosen incorrectly. We characterized the bifurcation curves that form the boundaries of the overall domains of stability of the target periodic orbit Γ_P and of the stable delay-induced periodic orbits. Moreover, we have shown how the domain of stability of Γ_P changes as the phase of the feedback β is increased. From this it was shown that, as β is increased or decreased from its original value of $\frac{\pi}{4}$, the degenerate Hopf bifurcation point b_0^c and the double Hopf bifurcation point HH_0 move closer together in the (λ, b_0) -plane. As this happens both the area of the domain and the range in b_0 for which Γ_P is stable are reduced. When the points b_0^c and HH_0 are equal, the domain of stability disappears. There appear to be no remaining pockets of stability of Γ_P in the (λ, b_0) -plane and thus, the Pyragas control scheme fails.

In addition to showing the geometry of the delay-induced Hopf bifurcations in the conventional parameter regime (where $\beta = \frac{\pi}{4}$ and $\gamma = -10$) we have shown how these curves change in the (λ, b_0) -plane when the feedback phase β is varied. To fully understand the highly non-trivial changes in these Hopf bifurcation curves, the (λ, b_0) -plane was compactified to the $(\hat{\lambda}, \hat{b}_0)$ -plane. We found that, as β is increased by 2π , the curve H_L transforms into the curve H_J^1 , the curve H_J^1 into the curve H_J^2 , the curve H_J^2 into the curve H_J^3 and so on. We also found that the Hopf bifurcation curves of the family H_R^K emerge from the top right corner $(1,1)$ of the $(\hat{\lambda}, \hat{b}_0)$ -plane at infinity in λ and b_0 and, as β is increased, they disappear into the top left corner $(0,1)$ of the $(\hat{\lambda}, \hat{b}_0)$ -plane.

We also considered the effect of a change in the parameter γ . We showed that as γ is increased the point b_0^c moves up in the (λ, b_0) -plane. Furthermore, the γ -dependent left-hand boundary of this plane and the gradient of the transcritical bifurcation curve TC also changes as γ is increased. Thus, the range in b_0 for which Γ_P is stable starts to decrease as soon as γ is increased. However, the area of the domain of stability of Γ_P initially increases as γ is increased. As γ is increased further the area of this domain then starts to reduce. When the points b_0^c and HH_0 are equal the domain of stability of Γ_P

disappears. Again, there are no remaining pockets of stability for Γ_P , and thus, at this point the Pyragas control scheme fails. Brown et al. [13] have shown that stabilization fails for $\gamma = 0$; here we have shown that stabilization of the target periodic orbit actually fails on a stability boundary $S(\beta)$ in the (β, γ) -plane [63]. This stability boundary defines regions in the (β, γ) -plane for which stabilization is possible.

Overall, this chapter shows that it is very useful to take a global point of view of a Pyragas controlled system to ascertain if, how and where the target periodic orbit is stabilized. It also highlights that care must be taken when implementing Pyragas control. Even when the delay is set as the exact parameter-dependent period, if parameters are not set carefully the system may converge to a stable delay-induced periodic orbit rather than the target periodic orbit. Moreover, the existence of bistability in part of the domain of stability of Γ_P means that there is no guarantee that the system reaches the target state in the respective parameter regime.

We have considered the application of Pyragas control to the subcritical Hopf normal form. Therefore, it is a natural conjecture that the dynamics found here will also be relevant for any systems with delay near a subcritical Hopf bifurcation, which is supported by the local results of Brown et al. [13]. In chapter 4 we consider the Lorenz system subject to Pyragas control, which was studied locally near the subcritical Hopf bifurcation by Postlethwaite and Silber [65]. We find that the global dynamics induced when Pyragas control is applied to the Lorenz system closely match those described in this chapter.

3

Effect of delay mismatch in Pyragas feedback control

The results in this chapter have been published in [66]. In this chapter we consider the general question: with which kind of precision must the delay τ be set to the target period $T(\mu)$? Specifically, the aim is to understand whether the Pyragas control scheme (1.2.1) is an effective form of control of the target periodic orbit if the delay τ is not set exactly as the parameter dependent target period $T(\mu)$, but is approximated by a simpler functional form. In other words, when does the control scheme yield a stable periodic orbit that is sufficiently close in period, amplitude and parameter space to the target periodic orbit?

To answer this question, we again consider the subcritical Hopf normal form subject to Pyragas control given by equation (2.0.1) in chapter 2. For convenience we restate it here

$$\dot{z} = (\lambda + i)z(t) + (1 + i\gamma)|z(t)|^2z(t) + b_0e^{i\beta}[z(t - \tau) - z(t)]. \quad (3.0.1)$$

Recall that, $z \in \mathbb{C}$ and $\lambda, \gamma \in \mathbb{R}$, and the complex number $b_0e^{i\beta}$ is the feedback gain, where $b_0 \in \mathbb{R}$ is the control amplitude and β is the 2π -periodic phase of the feedback. System (3.0.1) without control, i.e. with $b_0 = 0$, has a Hopf bifurcation H_P at $\lambda = 0$.

From H_P bifurcates an unstable branch of periodic orbits Γ_P , which exists for $\lambda < 0$, with amplitude $\sqrt{-\lambda}$ and has the parameter-dependent period given by the function

$$T(\lambda) = \frac{2\pi}{1 - \gamma\lambda}. \quad (3.0.2)$$

From (3.0.2) we see that, at the Hopf bifurcation H_P , where $\lambda = 0$, the period of Γ_P is 2π . Throughout our analysis of (3.0.1) in this chapter we use the parameter values $\gamma = -10$ and $\beta = \frac{\pi}{4}$ and vary the parameter λ , as is the convention [13, 24, 67]. We consider the following three cases, where the unstable branch of periodic orbits Γ_P is the target state of the Pyragas control scheme.

The exact-period case.

This is the standard setup of Pyragas control [24, 69], where the delay in (3.0.1) is set to $\tau = T(\lambda)$. We present the overall domain of stability of Γ_P in the two-parameter (λ, b_0) -plane, where the target periodic orbit Γ_P is successfully stabilized. This choice of parameter plane is natural as λ is conventionally taken as the primary bifurcation parameter and b_0 is the strength of the feedback. It should be noted that all previous work on (3.0.1) has assumed that $\tau = T(\lambda)$ and has been primarily focused on the mechanism of stabilization close to the Hopf bifurcation H_P [13, 24, 38]. Furthermore, as Pyragas control is non-invasive in the exact-period case, the symmetry properties of the normal form are preserved (details of these symmetry properties can be found in [31]). We use the exact-period case here as a benchmark for comparison with the cases where $\tau \neq T(\lambda)$.

To study the effect of setting the delay not equal to the target period, we consider the following two cases:

The constant-period case.

Here we assume that the period of Γ_P is known at the Hopf bifurcation H_P at $\lambda = 0$ and the delay in (3.0.1) is set to

$$\tau = T_C = T(0) = 2\pi. \quad (3.0.3)$$

Hence, the period T_C and, thus, the delay τ are no longer parameter dependent.

The linear-period case.

Here we set the delay to the linear approximation

$$\tau = T_L(\lambda) = 2\pi(1 + \gamma\lambda), \quad (3.0.4)$$

of the target period $T(\lambda)$ in (3.0.2). Hence, we again assume that the period of Γ_P is known at H_P and, in addition, we assume that the slope at H_P , $\frac{dT(\lambda)}{d\lambda}|_{\lambda=0} = 2\pi\gamma$ is also known.

We say that the Pyragas control scheme has been successful if three criteria are satisfied:

- (A) A periodic orbit with amplitude and period close to Γ_P is a stable solution.
- (B) Any residual control force is sufficiently small.
- (C) The stabilized periodic orbit exists in a similar neighborhood around the curve H_P in the (λ, b_0) -plane as the stabilized periodic orbit Γ_P in the benchmark exact-period case.

The first two criteria are natural assumptions about the stabilization of a periodic orbit and the third criterion stems from the parameter dependence of the target period $T(\lambda)$ given by (3.0.2). In the exact-period case, the system is driven to Γ_P and there is no residual control force, that is, the control is truly non-invasive. For the constant and linear-period cases where $\tau \neq T(\lambda)$, on the other hand, the feedback is no longer non-invasive due to the period mismatch, meaning that there will always be some residual control force. Moreover, the periodic orbit emanating from H_P will not be exactly the same as the target periodic orbit Γ_P . Therefore, in the constant and linear-period cases we do not expect to stabilize the exact periodic orbit Γ_P . Instead our aim is to find a periodic orbit that is as close as possible in amplitude, period and parameter space to Γ_P , and to achieve this with as small a residual control force as possible.

By design, the delay at the Hopf bifurcation H_P for $\lambda = 0$ is the same in all period cases, that is,

$$\tau = T(0) = T_C = T_L(0) = 2\pi. \quad (3.0.5)$$

To consider stabilization successful, we require that the stabilized periodic orbit remains close in parameter space to the target periodic orbit Γ_P away from H_P as the parameter λ is varied. For the exact-period case Pyragas control stabilizes the branch of periodic orbits Γ_P and its overall domain of stability exists to the left of the Hopf bifurcation curve H_P in the (λ, b_0) -plane; see section 3.1. In other words, we only consider the Pyragas control scheme successful if the periodic orbit stabilized in the constant-period and linear-period cases exists for similar values of λ and b_0 as where Γ_P exists in the benchmark exact-period case, i.e. for $\lambda < 0$.

Our results in the following sections show that for the constant-period case Pyragas control stabilizes a branch of periodic orbits bifurcating from H_P , which we call Γ_C . This branch exists for $\lambda > 0$, whereas the target periodic orbit Γ_P exists for $\lambda < 0$. Furthermore, the overall domain of stability of Γ_C exists to the right of H_P in the (λ, b_0) -plane and there is a large residual control force. Therefore, we say that the Pyragas control scheme is not successful in the constant-period case. For the linear-period case Pyragas control stabilizes a branch of periodic orbits bifurcating from H_P , which we call Γ_L . The stable branch Γ_L has a period and amplitude close to that of Γ_P and exists for a similar range of λ . Moreover, the overall domain of stability of Γ_L in the (λ, b_0) -plane is very similar to that of Γ_P in the benchmark exact-period case, that is, it exists to the left of H_P and is bounded by similar bifurcation curves. In addition, the residual control force in the linear-period case is small. Thus, we say that the Pyragas control scheme is successful in the linear-period case.

To understand the connection between the successful linear-period case and the unsuccessful constant-period case, we consider a third case of setting the period:

The variable-slope case.

Introducing a homotopy parameter h into the linear-period approximation (3.0.4) gives

$$\tau = T_h(\lambda) = 2\pi(1 + h\gamma\lambda). \quad (3.0.6)$$

Hence, for $h = 1$ one has the linear-period case with $T_1(\lambda) = T_L(\lambda)$ and for $h = 0$ one has the constant-period case with $T_0(\lambda) = T_C$.

In other words, changing h from 1 to 0 allows us to consider the influence of the slope of the

linear approximation on the Pyragas control scheme. We find that a linear approximation with a shallower slope can still result in successful stabilization.

This chapter is organized as follows. In section 3.1 we present bifurcation diagrams and the domain of stability of the exact-period case. We perform a bifurcation analysis of the constant-period case in section 3.2 and of the linear-period case in section 3.3. In section 3.4 we consider the homotopy from the linear-period to the constant-period case. Conclusions can be found in section 3.5.

3.1 The exact-period case

We start by presenting the bifurcation analysis of system (3.0.1) for the exact-period case, where $\tau = T(\lambda)$ as in (3.0.2). Specifically, the overall domain of stability of $\Gamma_{\mathcal{P}}$ in the (λ, b_0) -plane will serve as a benchmark with which to compare the constant-period and linear-period cases, which are analyzed in the next two sections. Previous work has primarily focused on the mechanism of stabilization near the Hopf bifurcation point $H_{\mathcal{P}}$; details of this analysis can be found in [13, 24, 38]. Here we show the overall domain of stability of $\Gamma_{\mathcal{P}}$ in the (λ, b_0) -plane, which has not been presented previously. A global bifurcation analysis of (3.0.1) with $\tau = T(\lambda)$ in dependence on the parameters λ, b_0, β and γ is the subject of [67].

Figure 3.1 shows the one-parameter bifurcation diagram in λ for $b_0 = 0.3$, shown in panel (a) in terms of the radius $r = |z|$ and in panel (b) in terms of the observed period T . This representation is chosen throughout this chapter because all periodic orbits of the subcritical Hopf normal form are sinusoidal and uniquely characterized by their amplitude and period. Shown along the bottom axis of panel (a) is the equilibrium solution ($r = 0$); it is stable when black and unstable when grey. Also shown is the Hopf bifurcation $H_{\mathcal{P}}$, denoted by a green dot, and two further delay-induced Hopf bifurcations of the equilibrium (red dots), in-between which the equilibrium is stable. Figure 3.1(a) shows that the target branch of periodic orbits $\Gamma_{\mathcal{P}}$ (green) bifurcates stably (solid curve) from the Hopf bifurcation $H_{\mathcal{P}}$ before becoming unstable (dashed curve) at the torus bifurcation $T_{\mathcal{P}}^0$ (black dot). Also shown is a further torus bifurcation of the unstable periodic orbit; there are, in fact, infinitely many torus bifurcations along $\Gamma_{\mathcal{P}}$, see [67] for details. Thus, $\Gamma_{\mathcal{P}}$ is stable only for a small range of λ .

Figure 3.1(b) shows that the period of $\Gamma_{\mathcal{P}}$ increases quickly as λ is reduced. In fact, as $\lambda \rightarrow -0.1$ the period $T(\lambda)$ in (3.0.2) goes to infinity (recall that $\gamma = -10$).

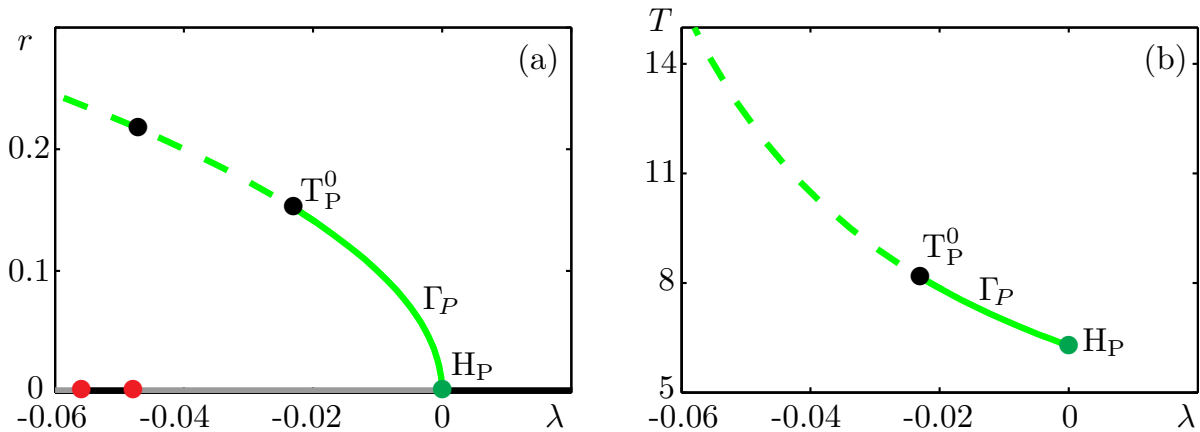


Figure 3.1: One-parameter bifurcation diagram in λ for $b_0 = 0.3$ of (3.0.1) for the exact-period case, shown in terms of the radius r in (a) and the period T in (b). The equilibrium solution is stable (unstable) when black (grey), it becomes stable at the Hopf bifurcation H_P from which bifurcates the branch of periodic orbits Γ_P . Also shown are the torus bifurcation T_P^0 , a further torus bifurcation and two further delay-induced Hopf bifurcations. Solid (dashed) curves indicate stable (unstable) periodic orbits. Other parameter values are $\beta = \frac{\pi}{4}$ and $\gamma = -10$.

Figure 3.2 shows the bifurcation set in the (λ, b_0) -parameter plane of (3.0.1) for the exact-period case. Panel (a) shows the curve of Hopf bifurcations H_P (green) at $\lambda = 0$ and a selection of further delay-induced Hopf bifurcation curves H_L , H_R^1 and H_R^2 (red). It also shows the overall domain of stability of Γ_P (shaded), which is bounded by H_P , the torus bifurcation curve T_P^0 (grey) and the transcritical bifurcation curve TC (purple). The parameter plane has a left-hand boundary at $\lambda = \frac{1}{\gamma} = -0.1$, where the delay $\tau = T(\lambda)$ given by (3.0.2) is undefined.

Figure 3.2(a) shows that the curve H_P is intersected twice by the loop-shaped curve H_L . The lower crossing b_0^c is a Hopf bifurcation point with a further degeneracy [13]. Below b_0^c the Hopf bifurcation H_P is subcritical and above b_0^c it is supercritical. Immediately above the point b_0^c , the branch of periodic orbits Γ_P bifurcates stably from H_P .

The second intersection of H_P and H_L is the double-Hopf bifurcation point HH_0 , where the equilibrium solution has two pairs of purely imaginary eigenvalues [31]. The point HH_0 introduces further instabilities in the form of an additional complex conjugate pair of unstable Floquet multipliers. The curves H_R^1 and H_R^2 are part of an infinite family of Hopf bifurcation curves, each of which intersects H_P at a double-Hopf bifurcation point. Above each of these double-Hopf bifurcation points Γ_P bifurcates with an additional complex pair of unstable Floquet multipliers and, as such, Γ_P only bifurcates stably from H_P between the points b_0^c and HH_0 [67].

Another family of delay-induced Hopf bifurcation curves that are not shown here exist

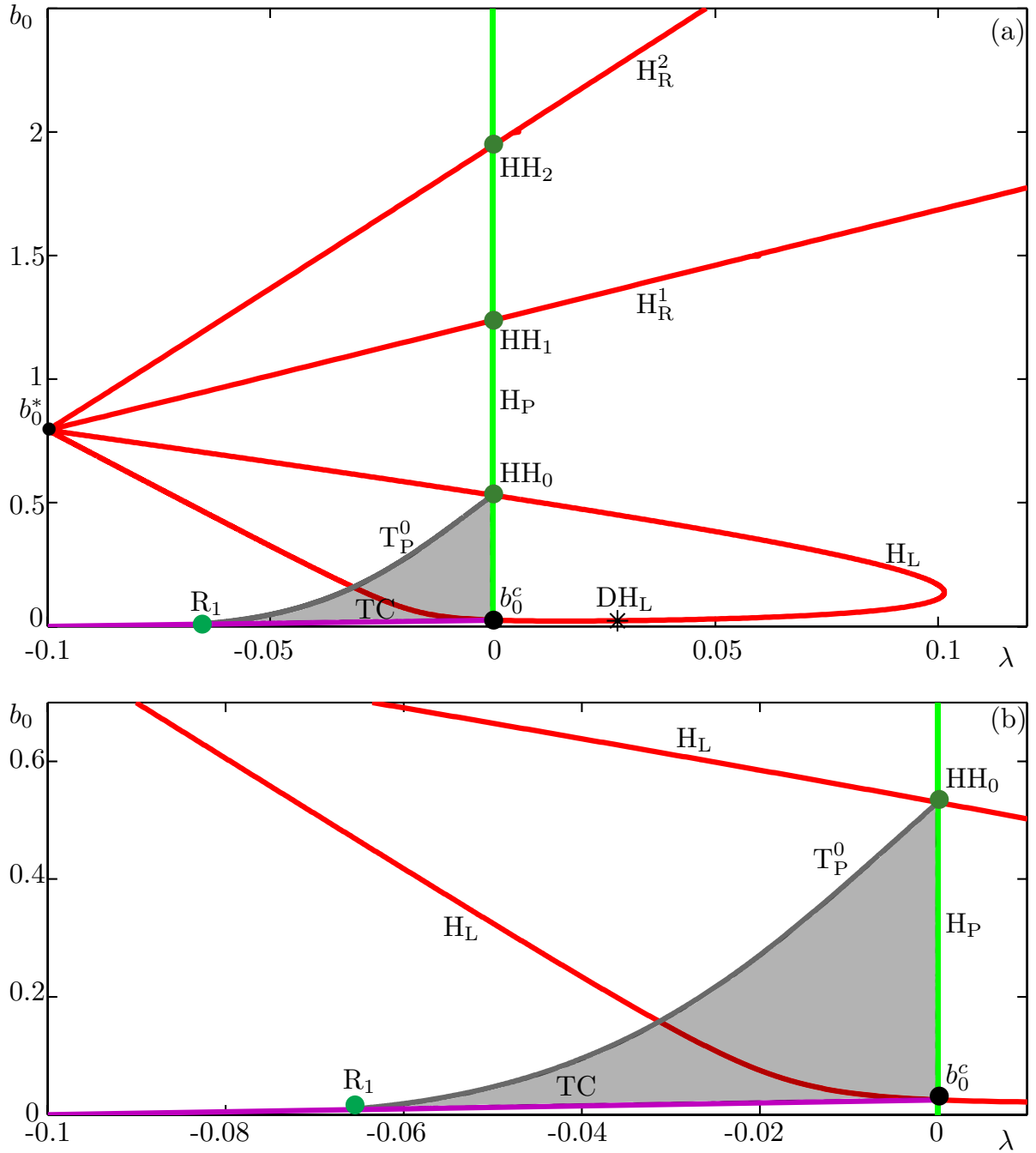


Figure 3.2: Bifurcation set in the (λ, b_0) -plane of (3.0.1) for the exact-period case. Shown in (a) are the Hopf bifurcation curve H_P and the delay-induced Hopf bifurcation curves H_L , H_J^1 , H_J^2 , H_R^1 and H_R^2 . Also, shown are the double-Hopf bifurcation points HH_0 , HH_1 , HH_2 , HH_D^1 , HH_D^2 and degenerate Hopf bifurcation point DH_L (*). The torus bifurcation curve T_P^0 meets the transcritical bifurcation curve TC at the point R_1 . An enlargement of the overall domain of stability of Γ_P (shaded) is shown in (b). Other parameter values are $\beta = \frac{\pi}{4}$ and $\gamma = -10$.

to the left of the (λ, b_0) -plane. From these curves bifurcate stable delay-induced periodic orbits, which in turn have further bifurcations. Further details on the global structure, criticality and stability of all the bifurcation curves of (3.0.1) for the exact-period case

can be found in [67].

Figure 3.2(b) is an enlargement that shows the overall domain of stability of Γ_P (shaded) in more detail. The right-hand boundary of the stability domain is the curve H_P between the points b_0^c and HH_0 . The left-hand boundary of the domain is given by the torus bifurcation curve T_P^0 , which starts at the point HH_0 and ends on the transcritical bifurcation curve TC at a 1:1 resonance point R_1 , where the periodic orbits undergoing the transcritical bifurcation have the same frequency as the torus bifurcation. The lower boundary of the domain of stability is the part of the curve TC between its starting point b_0^c and the point R_1 . The curve TC ends on the left-hand boundary of the (λ, b_0) -plane at the point $(\lambda, b_0) = (-0.1, 0)$.

Thus, condition (C) for successful stabilization in the constant and linear-period cases translates to the questions: is there a domain of stability in the (λ, b_0) -plane that exists predominately to the left of the curve H_P ? Is this domain bounded by bifurcation curves similar to the transcritical and torus bifurcation curves in the exact-period case?

3.2 The constant-period case

Figure 3.3 shows the one-parameter bifurcation diagram in λ for $b_0 = 0.3$ for the constant-period case; it is shown in panel (a) in terms of the radius $r = |z|$ and in panel (b) in terms of the observed period T . Shown along the bottom axis of panel (a) is the equilibrium solution ($r = 0$), which is stable when black and unstable when grey. It becomes unstable at the Hopf bifurcation H_P (green dot) at $\lambda = 0$ and is then further destabilized at the delay-induced Hopf bifurcation H_D^1 (red dot). Figure 3.3(a) shows the branch of periodic orbits Γ_C (green) bifurcating stably (solid curve) from H_P . In contrast to the target branch of periodic orbits Γ_P in the previous section, Γ_C exists for $\lambda > 0$. The branch Γ_C is only stable between H_P and the torus bifurcation T_P^0 (black dot), where a complex conjugate pair of Floquet multipliers leave the unit circle. There is also a saddle-node of limit cycles (SNLC) bifurcation S_P^1 (blue dot) on the unstable part of Γ_C , where a further Floquet multiplier leaves the unit circle. The branch ends at the delay induced Hopf bifurcation H_D^1 .

Figure 3.3(b) shows how the observed period T of Γ_C changes as λ is varied. Recall that the periods of Γ_C and Γ_P are both equal to 2π at the Hopf bifurcation point H_P . The period of Γ_C increases gradually as λ is increased and reaches its maximum when the branch ends at the Hopf bifurcation H_D^1 . We cannot directly compare the periods of Γ_P

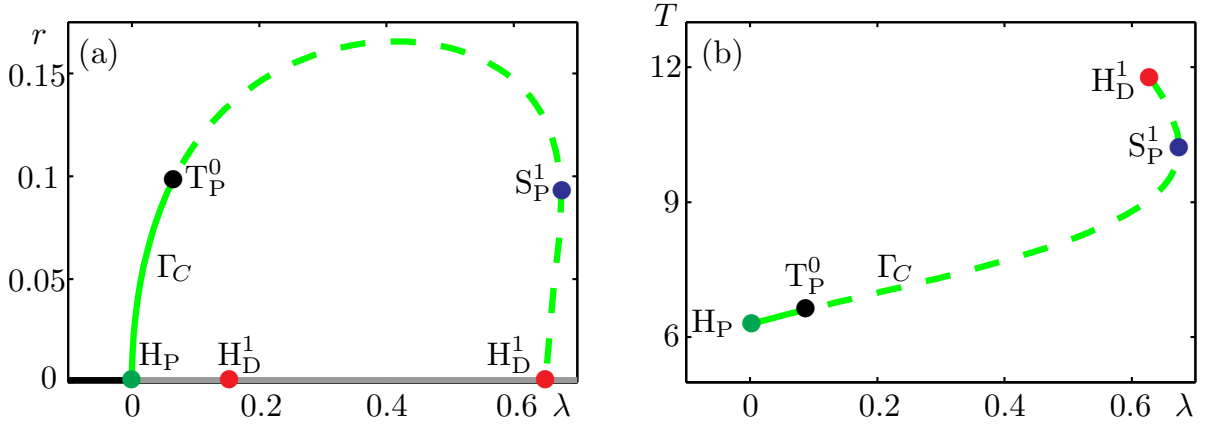


Figure 3.3: One-parameter bifurcation diagram in λ of (3.0.1) in the constant-period case for $b_0 = 0.4$, shown in terms of the radius r in (a) and the period T in (b). The equilibrium solution is stable (unstable) when black (grey), it becomes unstable at the Hopf bifurcation H_P from which bifurcates the branch of periodic orbits Γ_C . On the branch Γ_C are the torus bifurcation T_P^0 and the SNLC bifurcation S_P^1 . The branch ends at the delay-induced Hopf bifurcation H_D^1 . Solid (dashed) curves indicate stable (unstable) periodic orbits. Other parameter values are $\beta = \frac{\pi}{4}$ and $\gamma = -10$.

and Γ_C as they exist for different ranges of λ .

Figure 3.4 shows the bifurcation set in the (λ, b_0) -plane of (3.0.1) for the constant-period case. Note that the b_0 -ranges of Fig. 3.4(a) and (b) are the same as in Fig. 3.2(a) and (b) but the λ -ranges are different. The Hopf bifurcation H_P (green) is the vertical curve at $\lambda = 0$. As all three period cases are the same at $\lambda = 0$, the curve H_P is intersected by delay-induced Hopf bifurcation curves at the same double-Hopf bifurcation points HH_0, HH_1, HH_2 as for the exact-period case. In contrast to the exact-period case, the delay-induced Hopf bifurcation curves H_D^1, H_D^2 and H_D^3 (red) do not form a closed loop. Also, shown in Fig. 3.4(a) is the domain of stability of Γ_C (shaded).

The enlargement in Fig. 3.4(b) shows that the overall domain of stability of Γ_C exists almost entirely to the right of H_P . Its left-hand boundary is the curve H_P between the points b_0^c and HH_0 and its lower boundary is given by the part of the SNLC bifurcation curve S_P^1 (blue) between the degenerate Hopf bifurcation point DH and the curve H_P . The right-hand boundary of the domain is the torus bifurcation curve T_P^0 (grey), that starts at the double-Hopf bifurcation point HH_0 and ends on the curve S_P^1 at the 1:1 resonance point R_P (green dot). The inset in Fig. 3.4(b) shows that the curve S_P^1 crosses H_P at the point b_0^s before turning and ending at the point b_0^c . This results in a very small portion of the domain of stability existing to the left of H_P .

Figure 3.5 is a one-parameter bifurcation diagram in λ for $b_0 = 0.02$, which is a b_0 value between the points b_0^s and b_0^c . It shows the branch of periodic orbits Γ_C bifurcates

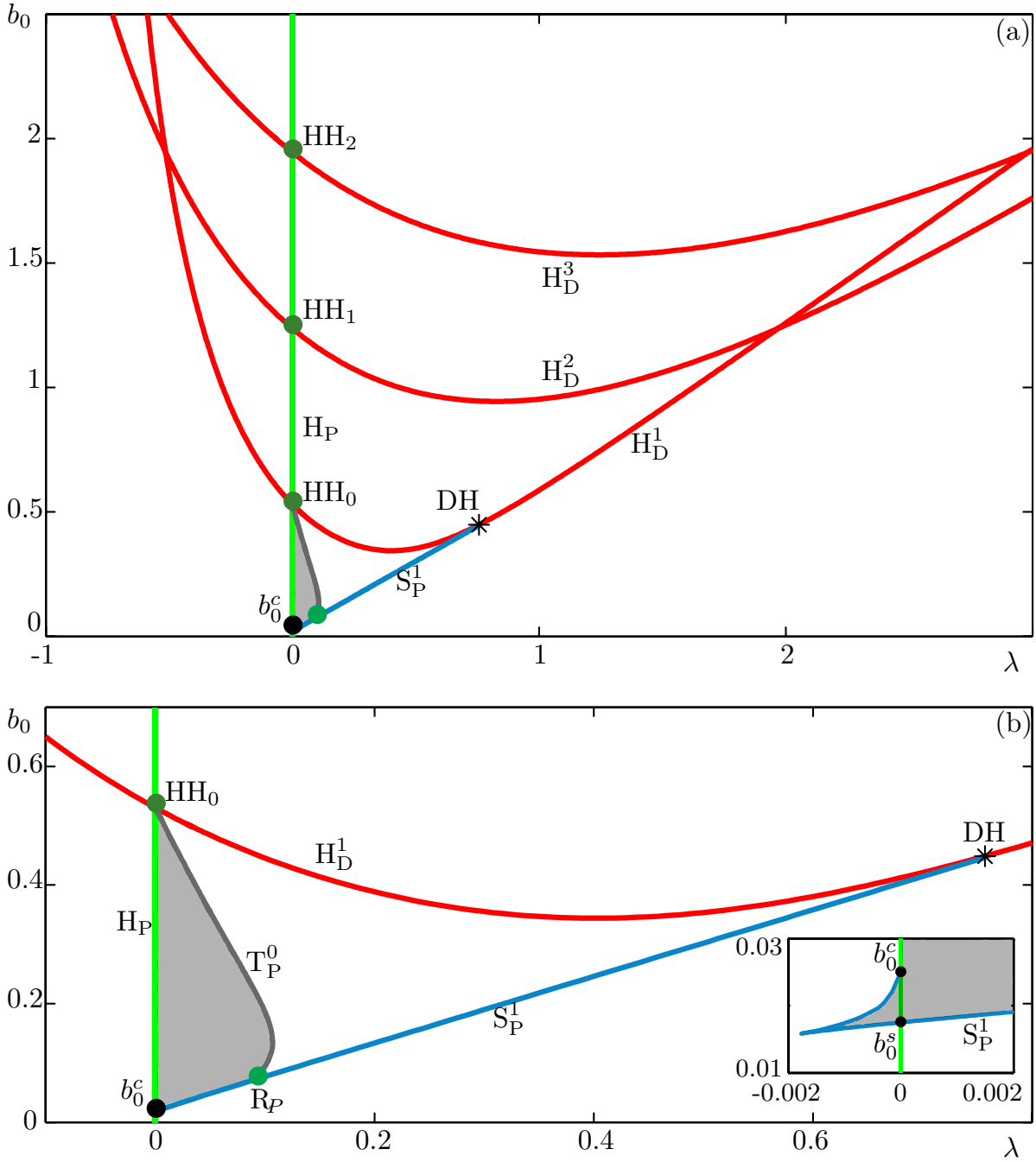


Figure 3.4: Bifurcation set in the (λ, b_0) -plane of (3.0.1) for the constant-period case. Shown are the Hopf bifurcation curve H_P and the delay-induced Hopf bifurcation curves H_D^1 , H_D^2 and H_D^3 . Also, shown are the double-Hopf bifurcation points HH_0 , HH_1 , HH_2 and the degenerate Hopf bifurcation point DH (*). An enlargement of the overall domain of stability of Γ_C (shaded) is shown in (b). The torus bifurcation curve T_P^0 and the SNLC bifurcation curve S_P^1 meet at the point R_P . Also shown are the points b_0^c and b_0^s . Other parameter values are $\beta = \frac{\pi}{4}$ and $\gamma = -10$.

unstably from H_P , is subcritical, and exists for $\lambda < 0$. The branch is stabilized in a SNLC bifurcation along the curve S_P^1 . Between b_0^c and HH_0 , the periodic orbit Γ_C bifurcates stably from H_P and exists for $\lambda > 0$.

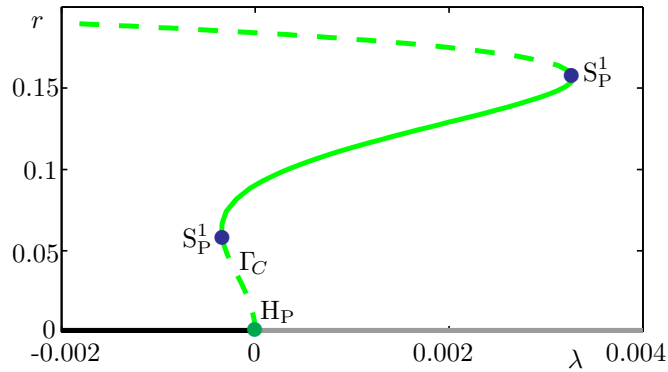


Figure 3.5: One-parameter bifurcation diagram in λ of (3.0.1) in the constant-period case for $b_0 = 0.02$. Shown is the Hopf bifurcation H_P from which bifurcates the branch of periodic orbits Γ_C . The branch undergoes the SNLC bifurcation S_P^1 twice. Solid (dashed) lines indicate stable (unstable) periodic orbits, the solid black (grey) lines indicate where the equilibrium solution is stable (unstable)

As Γ_C is not stable in the same neighbourhood of H_P as Γ_P , the constant-period case does not satisfy criterion (C). Moreover, we have found that the residual control force is large so that criterion (B) is also not satisfied; close to the torus bifurcation T_P^0 the amplitude of the residual feedback force is approximately 30% of the amplitude of Γ_C . Thus, we conclude that keeping the period constant does not result in a successful form of control.

3.3 The linear-period case

Figure 3.6 shows the one-parameter bifurcation diagram in λ for $b_0 = 0.3$ for the linear-period case; it is shown in panel (a) in terms of the radius $r = |z|$ and in panel (b) in terms of the observed period T . Again, shown along the bottom axis of panel (a) is the equilibrium solution ($r = 0$), it is stable when black and unstable when grey. It changes stability twice, once at the Hopf bifurcation H_P (green dot) and also at a delay-induced Hopf bifurcation H_D^1 (red dot). Figure 3.6(a) shows that the branch of periodic orbits Γ_L (green) bifurcates stably (solid curve) from the Hopf bifurcation H_P and exists for $\lambda < 0$. The branch Γ_L is only stable between H_P and the torus bifurcation point T_P^0 (black dot). There is a SNLC bifurcation on the branch at the point S_P^2 (blue dot), where again a further Floquet multiplier leaves the unit circle. The branch ends at the delay-induced Hopf bifurcation H_D^1 . Whilst Γ_L is stable it has an amplitude very close to that of Γ_P (black); see Fig. 3.6(a).

At the Hopf bifurcation point H_P , the residual feedback force is zero. The amplitude of the feedback grows much more slowly than the amplitude of Γ_L . In particular, whilst

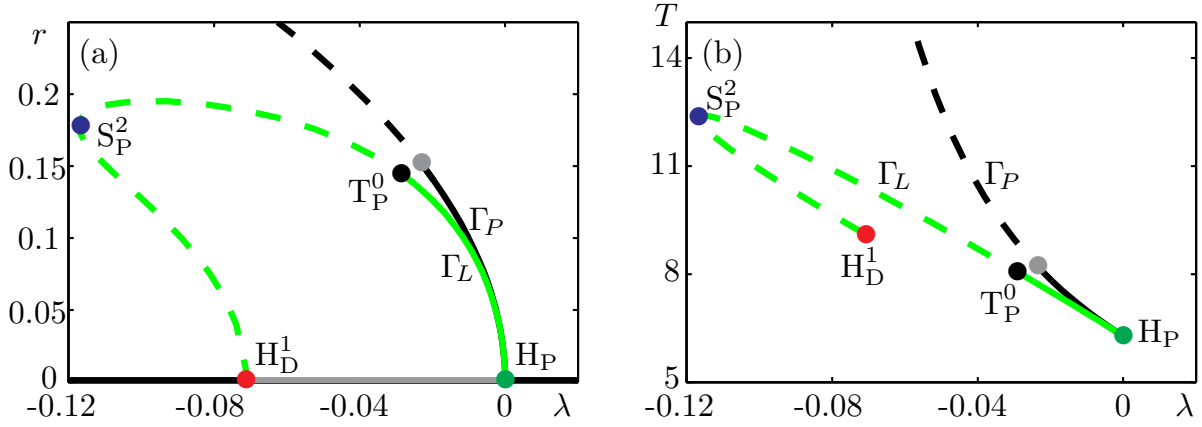


Figure 3.6: One-parameter bifurcation diagram in λ for $b_0 = 0.3$ of (3.0.1) for the linear-period case, shown in terms of the radius r in (a) and the period T in (b); also shown is the branch of periodic orbits Γ_P . The equilibrium solution is stable (unstable) when black (grey), it becomes stable at the Hopf bifurcation H_P from which bifurcates the branch of periodic orbits Γ_L . On the branch are the torus bifurcation T_P^0 and the SNLC bifurcation S_P^2 . The branch ends at the delay-induced Hopf bifurcation H_D^1 . Solid (dashed) curves indicate stable (unstable) periodic orbits. Other parameter values are $\beta = \frac{\pi}{4}$ and $\gamma = -10$.

the branch is stable the residual feedback force is very small. More specifically, along the stable section of the branch close to the torus bifurcation T_P^0 , the amplitude of the residual control force is approximately 6% of the amplitude of Γ_L .

Figure 3.6(b) shows how the period of Γ_L changes as λ is varied. For reference the period of the target periodic orbit Γ_P (black) from Fig. 3.1(b) is also shown. The periods of Γ_P and Γ_L are both equal to 2π at $\lambda = 0$, and Fig. 3.6(b) shows that they remain very close for $-0.03 \lesssim \lambda \leq 0$. For $\lambda \lesssim -0.03$ they diverge, with the period of Γ_P increasing quickly and going to infinity at $\lambda = -0.1$. The period of Γ_L increases more gradually. We conclude that the linear-period case fulfills criteria (A) and (B) for successful stabilization.

Figure 3.7 is the bifurcation set in the (λ, b_0) -plane of (3.0.1) for the linear-period case. Again note that the ranges of b_0 shown in Fig. 3.7 are the same as in Figs. 3.2 and 3.4, but the λ -ranges are different. Figure 3.7(a) shows the Hopf bifurcation curve H_P (green), which is intersected by the delay induced Hopf bifurcation curves H_D^1 , H_D^2 and H_D^3 (red) at the points b_0^c , HH_0 , HH_1 and HH_2 . The curve H_D^1 forms a loop that resembles the curve H_L for the exact-period case in Fig. 3.2(a). It has a point of self intersection labelled HH_c . Figure 3.7(a) also shows the overall domain of stability of Γ_L (shaded).

The enlargement in Fig. 3.7(b) shows that the overall domain of stability (shaded) of Γ_L exists predominately to the left of H_P . Its right-hand boundary is the curve H_P between the points b_0^c and HH_0 and its lower boundary is given by the SNLC bifurcation curve S_P^2 (blue) between the points b_0^c and the 1:1 resonance point R_P (green dot). The left-hand

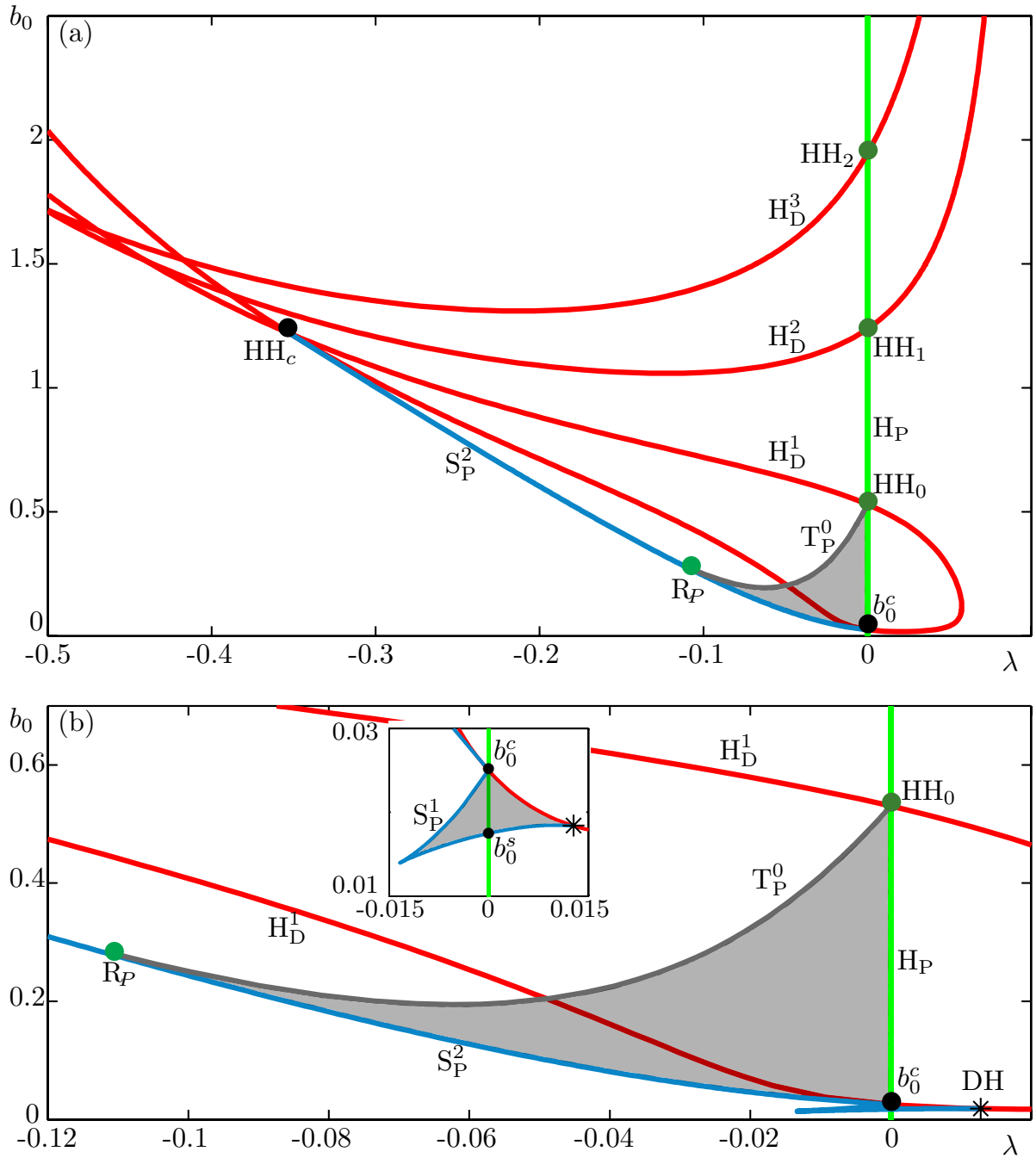


Figure 3.7: Bifurcation set in the (λ, b_0) -plane of (3.0.1) for the linear-period case. Shown are the Hopf bifurcation curve H_P and the delay-induced Hopf bifurcation curves H_D^1 , H_D^2 and H_D^3 . From the point b_0^c emerges the SNLC bifurcation curve S_P^2 , this curve ends at the point HH_c , where H_D^1 intersects itself. Also, shown are the double-Hopf bifurcation points HH_0 , HH_1 and HH_2 . The torus bifurcation curve T_P^0 meets the SNLC bifurcation curve S_P^2 at the point R_P . An enlargement of the overall domain of stability of Γ_L (shaded) is shown in (b); the inset shows the point b_0^s and the SNLC bifurcation curve S_P^1 , which starts at the degenerate Hopf bifurcation point DH (*). Other parameter values are $\beta = \frac{\pi}{4}$ and $\gamma = -10$.

boundary of the domain is the torus bifurcation curve T_P^0 (grey), which starts at the double-Hopf bifurcation point HH_0 and ends on the curve S_P^2 at the point R_P . The inset

in Fig. 3.7(b) shows another very small domain of stability (shaded) of Γ_L lower in the (λ, b_0) -plane. The left and lower boundaries of this lower domain of stability are given by the SNLC bifurcation curve S_P^1 , which starts at the degenerate Hopf bifurcation point DH on H_D^1 , crosses the curve H_P at the point b_0^s before turning and ending at the point b_0^c .

The periodic orbit Γ_L only bifurcates stably from H_P between the points b_0^c and HH_0 . At b_0^c the criticality of H_P changes from subcritical below to supercritical above.

If Γ_L bifurcates from H_P between b_0^s and b_0^c , it is initially unstable and exists for $\lambda < 0$. The branch becomes stable at the SNLC bifurcation S_P^1 and ends at the delay-induced Hopf bifurcation H_D^1 .

Comparing Figs. 3.2 and 3.7, we see that for $-0.05 \lesssim \lambda \lesssim 0.02$, the bifurcation set in the (λ, b_0) -plane for the linear-period case resembles that for the exact-period case. In both cases the domain of stability exists to the left of the curve H_P , and its left-hand boundary is the torus bifurcation curve T_P^0 . Note that the symmetry properties of the exact-period case are lost in the linear-period case. Therefore, the lower boundary of the domain of stability in the linear-period case is a SNLC bifurcation curve rather than a transcritical bifurcation curve as in the exact-period case. There is also the slight difference that the curve S_P^2 slopes upwards in the plane whereas the curve TC slopes downwards. In addition, in the linear-period case there exists a very small domain of stability to the right of H_P (see the inset of Fig. 3.7(b)), which because of its size, we consider negligible. This domain of stability does not exist in the exact-period case. Nonetheless we conclude that for the linear-period case criterion (C) for successful stabilization is satisfied.

Therefore, the linear-period case fulfills all three stabilization criteria, and we conclude that it constitutes a successful form of control.

3.4 The variable-slope case

We now consider the variable-slope case, where the delay in (3.0.1) is set as in (3.0.6). Recall that when $h = 1$ the delay is as that of the linear-period case and when $h = 0$ the delay is as that of the constant-period case.

Figure 3.8 shows qualitative changes of the bifurcation set in the (λ, b_0) -plane, illustrated by representative panels for chosen values of h . We focus on how the bifurcation curves

that define the domain of stability move as h is varied. Hence, the curves H_D^2 and H_D^3 are not shown in Fig. 3.8; see [67] for how all of the delay-induced Hopf bifurcation curves for the exact-period case move in the (λ, b_0) -plane as the parameters β and γ are changed. Overall, Fig. 3.8 shows that the upper domain of stability to the left of H_P increases in area as h is reduced to 0.5, that is, when the slope is reduced by half. As h is reduced further, the area of this domain decreases, but it remains of a substantial size until approximately $h = 0.16$. When h is reduced below this value the point b_0^{HH} where H_P and H_D^1 intersect moves quickly upwards in the (λ, b_0) -plane and the domain rapidly reduces in area. At $h \approx 0.1424$ the upper domain to the left of H_P vanishes. This means that a linear approximation with a slope that is approximately 50% shallower than that used in (3.0.4) can still result in successful stabilization.

More specifically, Fig. 3.8(a) is the bifurcation set of (3.0.1) for the linear-period case ($h = 1$) as in Fig. 3.7(a). We define the range of stability of Γ_L as the values of b_0 for which the branch of periodic orbits bifurcates stably from H_P . Thus, for Γ_L the range of stability is $b_0^c < b_0 < HH_0$.

Figure 3.8(b) and (c) show that, as h is reduced, the upper left domain of stability increases in area. The right end point of the curve S_P^2 has moved left along H_D^1 away from the point b_0^c and the point R_P has moved up the curve S_P^2 to the point HH_c . Also, the bottom of the curve H_D^1 has shifted upwards in the (λ, b_0) -plane such that the lower intersection of H_P by H_D^1 is above the point b_0^c . We call this intersection point b_0^{HH} , and it is given by

$$b_0^{HH} = \left\{ (\lambda, b_0) = \left(0, \frac{1}{2\pi(\cos \beta + h\gamma \sin \beta)} \right) \right\}. \quad (3.4.1)$$

The shift upwards of H_D^1 results in the domain of stability on the right-hand side of H_P growing in area.

Panel (d) for $h = 0.16$ shows that the lower intersection of the curves H_D^1 and H_P at the point b_0^{HH} has moved well above the point b_0^c in the (λ, b_0) -plane. Hence, the domain of stability on the right of H_P has increased in area and range and the upper domain of stability to the left of H_P has decreased in area and range. The curve H_D^1 has shifted right in the (λ, b_0) -plane and its point of self-intersection HH_c is close to the curve H_P . The SNLC bifurcation curve S_P^2 has disappeared into the point HH_c .

Panel (e) for $h = 0.1424$ shows that the point HH_c coincides with the points HH_0 and b_0^{HH} on the curve H_P , resulting in the disappearance of the upper domain of stability to the left of H_P . The torus bifurcation curve T_P^0 has disappeared into the point HH_0 . The

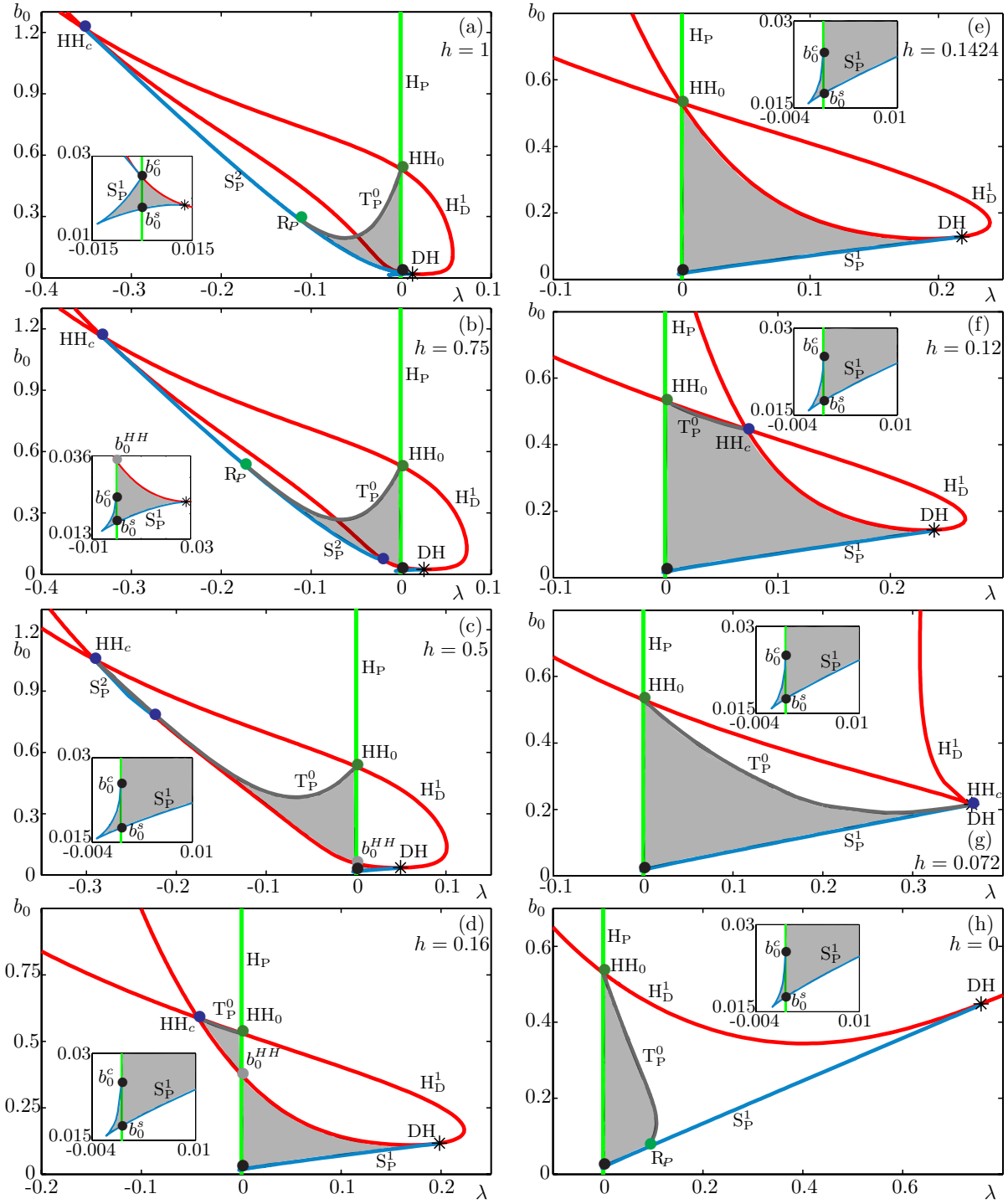


Figure 3.8: The overall domain of stability in the (λ, b_0) -plane of the stabilized branch of periodic orbits (shaded) as the homotopy parameter h is reduced from 1 to 0. Panel (a) is for $h = 1$ as in Fig. 7(b), panels (b)-(g) are for the given value of h and panel (h) is for $h = 0$ as in Fig. 4(b). Each panel shows the Hopf bifurcation curves H_P and H_D^1 , the SNLC bifurcation curve S_P^1 and the points b_0^c , b_0^s , HH_0 and HH_c . The torus bifurcation curve T_P^0 meets the SNLC bifurcation curve S_P^2 at the point R_P . Other parameter values are $\beta = \frac{\pi}{4}$ and $\gamma = -10$.

curve H_D^1 has moved right in the (λ, b_0) -plane and thus, the domain of stability to the right of H_P has increased in area.

Figure 3.8(f) for $h = 0.12$ shows that the curve H_D^1 and the point HH_c have moved right in the (λ, b_0) -plane. The torus bifurcation curve T_P^0 connects the points HH_0 and HH_c and now forms the upper boundary of the domain of stability to the right of H_P .

Panel (g) for $h = 0.072$ shows that, when the curve H_D^1 no longer self-intersects (i.e. there is no loop), the point HH_c is at the degenerate Hopf bifurcation point DH . The curve T_P^0 now ends at this point where $HH_c = DH$. As h is further reduced, the right end point of the curve T_P^0 moves left along the curve S_P^1 as the point R_P , reducing the area of the domain of stability.

Figure 3.8(h) for $h = 0$ shows the bifurcation set in Fig. 3.4(b) for the constant-period case.

3.5 Conclusions

We considered the generic subcritical Hopf normal form subject to Pyragas control. Specifically, we analyzed the effect of setting the delay in the Pyragas control term to a simpler functional form of the period of the targeted periodic orbit. We have shown that at least a linear approximation of the target period $T(\lambda)$ is required for Pyragas control to yield a stable periodic orbit that is sufficiently close to the stable periodic orbit found in the benchmark exact-period case. In fact, investigation of the variable-slope case showed that the Pyragas control scheme is still successful if a linear approximation is used that is up to 50% shallower.

Brown et al. [13] showed that locally near any subcritical Hopf bifurcation, a Pyragas controlled system exhibits the same dynamics as the subcritical Hopf normal form subject to Pyragas control (3.0.1) for the exact-period case. We therefore expect that our results for the exact-period, constant-period and linear-period cases will be observed more generally in systems with Pyragas control near a subcritical Hopf bifurcation. In fact, in chapter 4 we find that the results of this chapter are indeed relevant for the Lorenz system subject to Pyragas control.

In this chapter, we only consider the standard parameter values for the control phase β and the imaginary part of the cubic coefficient γ , which is also referred to as the frequency detuning or chirp; that is, we set $\beta = \frac{\pi}{4}$ and $\gamma = -10$ [13, 24, 38]. In [67] we show that stabilization is possible for other values of β and γ (but not for all), and that the feedback induces infinitely many stable periodic orbits other than the target periodic orbit. The

existence of these stable regions means that, if the location/period of the target periodic orbit with respect to system parameters is unknown, the system may converge to a delay-induced stable periodic orbit rather than the targeted one. Thus, an experiment may seem successful when the system is at a stable periodic orbit but this periodic orbit may be different from the one that was originally targeted.

Experimental verification of this work remains an intriguing challenge. Indeed, in an actual experiment it is not known how the target period changes with parameters. We have shown that finding an approximation of the slope of the target period is necessary for the Pyragas scheme to be successful. Obtaining such an approximation appears feasible from a limited number of measurements, especially for experiments that are close to a subcritical Hopf bifurcation. For example, the semiconductor laser studied by Schikora et al. [79, 80] may well be a good candidate system. Instead of using a constant delay term that is adjusted in interactive steps, a parameter-dependent linear approximation of the target period could be derived from the points where the delay is adjusted and then used as part of the experimental setup. This scheme would be expected to stabilize a periodic orbit that is close in location, amplitude and period to the target periodic orbit. Furthermore, as we have shown, a linear approximation of this type should also maintain a low residual control force. In particular, this approach may make the experiment more automated by removing the need for the operator to manually change the delay, while not requiring inclusion of a continuation of the period of the target periodic orbit itself.

4

The Lorenz system subject to Pyragas time-delayed feedback control

In this chapter our aim is to show that the overall dynamics found in the subcritical Hopf normal form subject to Pyragas control (see chapter 2, [67]) are also relevant for other systems with Pyragas control near a subcritical Hopf bifurcation. To this end, we consider the Lorenz equations subject to Pyragas time-delayed feedback control. Note that the Lorenz system is quite different to the subcritical Hopf normal form analyzed in chapters 2 and 3. First, it is of higher dimension and, second, for the Lorenz system we add feedback to the whole system, whereas in the Hopf normal form analysis we are able to add feedback directly onto the centre manifold. A further explanation of the addition of feedback to the Lorenz system is given in the following paragraphs. The equations were derived by Lorenz [52] as a simplified model of thermal convection in the atmosphere, and take the form

$$\begin{aligned}\dot{x}(t) &= \sigma(y(t) - x(t)), \\ \dot{y}(t) &= \rho x(t) - y(t) - x(t)z(t), \\ \dot{z}(t) &= -\alpha z(t) + x(t)y(t).\end{aligned}\tag{4.0.1}$$

Note that we use α as the parameter name, rather than the standard β , in the third equation of (4.0.1), to avoid confusion with the feedback phase β of the Hopf normal form subject to Pyragas control. Equations (4.0.1) are perhaps the most famous example of a chaotic system. In particular, the butterfly-shaped Lorenz attractor, which can be found for the classical parameter values $\sigma = 10$, $\alpha = \frac{8}{3}$ and $\rho = 28$, has garnered fame even outside of the mathematical community. For further information on the Lorenz system and its dynamics see, for example, [12, 19, 20, 93] and the references therein.

System (4.0.1) is most often studied for the parameter regime $\sigma = 10$, $\alpha = \frac{8}{3}$ and $\rho > 0$, that is, ρ is taken as the primary bifurcation parameter. The origin is always an equilibrium; it is stable for $\rho < 1$ and it loses stability in a supercritical pitchfork bifurcation for $\rho = 1$. For $\rho > 1$, there exist the two further equilibria

$$p^\pm = \left(\pm\sqrt{\alpha(\rho - 1)}, \pm\sqrt{\alpha(\rho - 1)}, \rho - 1 \right), \quad (4.0.2)$$

which are each other's counterparts under the symmetry transformation $(x, y, z) \rightarrow (-x, -y, z)$ of the Lorenz system. The equilibria p^\pm (4.0.2) lose stability in a subcritical Hopf bifurcation at

$$\rho_H = \frac{\sigma(\sigma + \alpha + 3)}{(\sigma - \alpha - 1)} \approx 24.7368, \quad (4.0.3)$$

for $\sigma = 10$ and $\alpha = \frac{8}{3}$. For $\rho > \rho_H$, the equilibria p^\pm are saddle points. From the Hopf bifurcation at ρ_H emanate two unstable periodic orbits. We target the unstable periodic orbit Γ_P near p^+ that bifurcates in the Hopf bifurcation H_P at ρ_H . It has one real unstable Floquet multiplier, one Floquet multiplier equal to one and one real stable Floquet multiplier. The periodic orbit Γ_P exists for $\rho_{\text{hom}} < \rho < \rho_H$; at $\rho_{\text{hom}} \approx 13.926$ the periodic orbit ends in a homoclinic bifurcation of the origin. This homoclinic bifurcation is also referred to as a homoclinic explosion point [93] and is the source of the complicated dynamics exhibited in the Lorenz system. For $\rho > \rho_{\text{hom}}$ there are, in addition to Γ_P , infinitely many periodic orbits of saddle type. The homoclinic explosion point at ρ_{hom} does not produce a chaotic attractor; instead one finds transient chaos until the system reaches one of the attracting equilibria p^\pm [42, 93]. At $\rho = \rho_{\text{het}} \approx 24.0579$ there is a heteroclinic bifurcation, where there is a connecting orbit between the origin and each of the unstable periodic orbits that bifurcate from p^\pm . This heteroclinic bifurcation at ρ_{het} creates a chaotic attractor. Therefore, for $\rho_{\text{het}} < \rho < \rho_H$ there exist two stable equilibria p^\pm and a chaotic attractor. For $\rho > \rho_H$, the equilibria p^\pm become saddles, and the only attractor is the chaotic attractor. For $\rho = 28$, the system has the famous Lorenz strange attractor, which is a global attractor.

We apply Pyragas control to the Lorenz equations in the manner first suggested by Postlethwaite and Silber [65]. We start by shifting and rescaling coordinates so that the equilibrium point p^+ is at the origin. This is done via the transformation

$$\begin{pmatrix} u \\ v \\ w \end{pmatrix} = \begin{pmatrix} \sqrt{\alpha(\rho-1)}(x - \sqrt{\alpha(\rho-1)}) \\ \sqrt{\alpha(\rho-1)}(y - \sqrt{\alpha(\rho-1)}) \\ (\rho-1)(z - (\rho-1)) \end{pmatrix},$$

which yields the system

$$\begin{aligned} \dot{u}(t) &= \sigma(v(t) - u(t)), \\ \dot{v}(t) &= u(t) - v(t) - (\rho-1)w(t) - (\rho-1)u(t)w(t), \\ \dot{w}(t) &= \alpha(u(t) + v(t) - w(t) + u(t)v(t)). \end{aligned} \tag{4.0.4}$$

When the control term is added to (4.0.4) the full controlled system is

$$\begin{pmatrix} \dot{u}(t) \\ \dot{v}(t) \\ \dot{w}(t) \end{pmatrix} = J(\rho) \begin{pmatrix} u(t) \\ v(t) \\ w(t) \end{pmatrix} + \begin{pmatrix} 0 \\ -(\rho-1)u(t)w(t) \\ \alpha u(t)v(t) \end{pmatrix} + \Pi \begin{pmatrix} u(t-\tau) - u(t) \\ v(t-\tau) - v(t) \\ w(t-\tau) - w(t) \end{pmatrix}, \tag{4.0.5}$$

where

$$J(\rho) = \begin{pmatrix} -\sigma & \sigma & 0 \\ 1 & -1 & -(\rho-1) \\ \alpha & \alpha & -\alpha \end{pmatrix}. \tag{4.0.6}$$

Close to the Hopf bifurcation point H_P , the target unstable periodic orbit Γ_P will lie on the two-dimensional centre manifold with an extra stable direction. One approach to applying Pyragas feedback would be to reduce the uncontrolled three-dimensional Lorenz system (4.0.4) to a two-dimensional system that governs the dynamics on the centre manifold. A normal form transformation (up to the cubic term) would then remove all nonlinear terms except the one that is proportional to $|z|^2z$, which is the cubic term of the Hopf normal form. Thereby, the reduced system would be in Hopf normal form as in equation (2.0.1) from chapters 2 and 3. Pyragas feedback control could then be applied to this system in exactly the same way as shown in chapter 2. However, it is unpractical from an application point of view to perform this reduction to normal form for every system to which one would like to apply Pyragas control – especially in an experimental setting,

where the governing equations may be unknown.

Here we consider the alternative approach, of applying the Pyragas scheme, where control is added to the original system but only applied in the respective unstable directions. This is achieved by defining the feedback gain matrix Π in (4.0.5) as $\Pi = EGE^{-1}$, where

$$G = \begin{pmatrix} 0 & 0 & 0 \\ 0 & b_0 \cos(\eta) & -b_0 \sin(\eta) \\ 0 & b_0 \sin(\eta) & b_0 \cos(\eta) \end{pmatrix}. \quad (4.0.7)$$

and E is given below. The matrix G corresponds to the feedback gain of the Hopf normal form (applied to the last two coordinates). Here, $b_0 \in \mathbb{R}$ is the control amplitude and we use the convention that $b_0 \geq 0$. The parameter η is the 2π -periodic feedback phase. Note we use the notation η instead of the standard β as in chapters 2 and 3. Due to the coordinate transformation $\Pi = EGE^{-1}$, choosing a value of η here is not directly equivalent to choosing the same value of β in the Hopf normal form analysis. The same is of course true for the parameter b_0 , however, since b_0 just undergoes a linear scaling, for simplicity we use the same notation. The matrix G is related to Π via the coordinate transformation E , which is the matrix of eigenvectors that puts $J(\rho_H)$ in Jordan normal form, that is,

$$E^{-1}J(\rho_H)E = \begin{pmatrix} \mu_H^S & 0 & 0 \\ 0 & 0 & -\omega_H \\ 0 & \omega_H & 0 \end{pmatrix}. \quad (4.0.8)$$

By selecting the feedback gain in this way, we ensure that there is no feedback in the stable direction, which has eigenvalue $\mu_H^S < 0$ but that there is feedback in the unstable directions, which have eigenvalues $\pm\omega_H$ tangent to the center manifold. Further explanation for this choice of feedback gain can be found in [65].

In [14] Brown showed that, close to the Hopf bifurcation point H_P , applying feedback to the original Lorenz equations (4.0.4) is equivalent to applying feedback to the system after it has been reduced to the Hopf normal form. In other words, the dynamics locally near H_P are the same both when feedback is added to the original Lorenz equations and when feedback is added to the already reduced system. Here, we consider whether the same is true of the dynamics more globally, that is, further away from the Hopf bifurcation H_P . The question is, are the overall dynamics of the Lorenz system subject to Pyragas control (presented in the rest of this chapter) described by those of the Hopf normal form subject to Pyragas control (shown in chapters 2 and 3)?

To answer this question, we take a global view of system (4.0.5) and perform a detailed bifurcation analysis in the (ρ, b_0) -plane. We show the overall domain of stability of the target periodic orbit Γ_P and also domains of stability of further delay-induced periodic orbits. We find that these domains are qualitatively the same as those found in the analysis of the Hopf normal form subject to Pyragas control; see chapter 2. Furthermore, we consider the effect of the feedback phase η on the domain of stability of Γ_P and find where control fails for system (4.0.5). Moreover, we show that η can be chosen suitably to ensure excellent agreement with the Hopf normal form subject to Pyragas control. Lastly, we consider a delay mismatch in (4.0.5), where the delay τ is set close to but not exactly as the period of the target periodic orbit Γ_P . We find that also for the Lorenz system at least a linear approximation of the period of Γ_P is required for the control scheme to be successful. For convenience throughout the rest of this chapter, we refer to the analysis of the subcritical Hopf normal form subject to Pyragas control presented in chapters 2 and 3 as the normal form case, and the analysis of the Lorenz system subject to Pyragas control as the Lorenz case.

This chapter is organized as follows. Section 4.1 gives some background on (4.0.5) and an outline of the results presented in [65], including a local bifurcation analysis. Section 4.2 considers a more global view of the (ρ, b_0) -plane and shows the wider delay-induced dynamics. In section 4.3 we consider the effect of the 2π -periodic feedback phase η on the domain of stability of Γ_P . Section 4.4 presents the results of a delay mismatch in system (4.0.5). Conclusions and discussions can be found in section 4.5.

4.1 Background and local bifurcation analysis

4.1.1 The period as a function of ρ

A key ingredient for the standard setup of Pyragas control is setting the delay τ to the period of the target periodic orbit. For the Lorenz system (4.0.1) there is no analytic function for the period $T(\rho)$ of Γ_P . Instead, we use the same method as presented in [65]. That is, for $\rho < \rho_H$ we represent the period $T(\rho)$ as a data set obtained from a numerical continuation in ρ of the period of Γ_P . Close to the homoclinic bifurcation at $\rho_{\text{hom}} \approx 13.926$, we approximate the period as a set of data points obtained from $T(\rho_{\text{hom}}) = -0.974 \log(\rho - \rho_{\text{hom}})$, which represents the period $T(\rho)$ of Γ_P going to infinity at the homoclinic bifurcation. We take a spline through the data points from the numerical continuation and the data points from the logarithmic function to ensure that $T(\rho)$ is

continuous and has continuous first derivative. For $\rho > \rho_H$ we extrapolate the data set for the period of Γ_P with the function

$$\tau = \frac{\tau_H}{1 + 0.0528(\rho - \rho_H)}, \quad (4.1.1)$$

where $\tau_H \approx 0.6528$ is the period of Γ_P at the Hopf bifurcation H_P . Again, this ensures that at the Hopf bifurcation H_P at $\rho = \rho_H$ the period $T(\rho)$ is continuous and has continuous first derivative. Throughout our analysis of (4.0.5) we fix the delay to $\tau = T(\rho)$ obtained as explained above.

4.1.2 Stabilization of Γ_P near the point b_0^c

Postlethwaite and Silber [65] performed a bifurcation analysis of (4.0.5) close to the Hopf bifurcation H_P . In their analysis they fix the parameter values $\sigma = 10$, $\alpha = \frac{8}{3}$ and the feedback phase $\eta = \frac{\pi}{4}$. They found that the mechanism of stabilization in (4.0.5) is the same as the normal form case; see chapter 2. That is, the target unstable periodic orbit Γ_P exchanges stability with a stable delay-induced periodic orbit in a transcritical bifurcation. In the rest of this section we review the results of [65] and compare them with our analysis of the normal form case in chapter 2. Throughout this analysis, we also fix the parameter values $\sigma = 10$, $\alpha = \frac{8}{3}$ and $\eta = \frac{\pi}{4}$.

Figure 4.1(a) shows the one-parameter bifurcation diagram in ρ of (4.0.5) for $b_0 = 0$, i.e. without feedback. The stability of the equilibrium p^+ is shown along the bottom axis; it is stable when black and unstable when grey. It loses stability at the Hopf bifurcation point H_P , from which the unstable periodic orbit Γ_P (green dashed curve) bifurcates. Figure 4.1(b) shows the one-parameter bifurcation diagram in ρ of (4.0.5) for $b_0 = 0.19$. The point H_P remains at $\rho = \rho_H$ but there are now further delay-induced Hopf bifurcations. These are indicated by additional dots on the bottom axis of Fig. 4.1(b). From the Hopf bifurcation point H_L bifurcates a stable periodic orbit Γ_L . The periodic orbits Γ_P and Γ_L exchange stability at the transcritical bifurcation TC (black square).

Figure 4.1(c) is a phase portrait of 4.0.5 in projection onto the (u, v) -plane; the equilibrium p^+ is at $(u, v) = 0$. It shows a selection of periodic orbits from the family Γ_P for $16 < \rho < 24$, that is, for various values of ρ along the branch Γ_P shown in Fig. 4.1(b). The periodic orbit Γ_P is unstable when colored grey and stable when colored green, the thicker black periodic orbit is at the transcritical bifurcation TC. Figure 4.1(d) is again a phase portrait of 4.0.5 in projection onto the (u, v) -plane but it shows the family of periodic orbits Γ_L

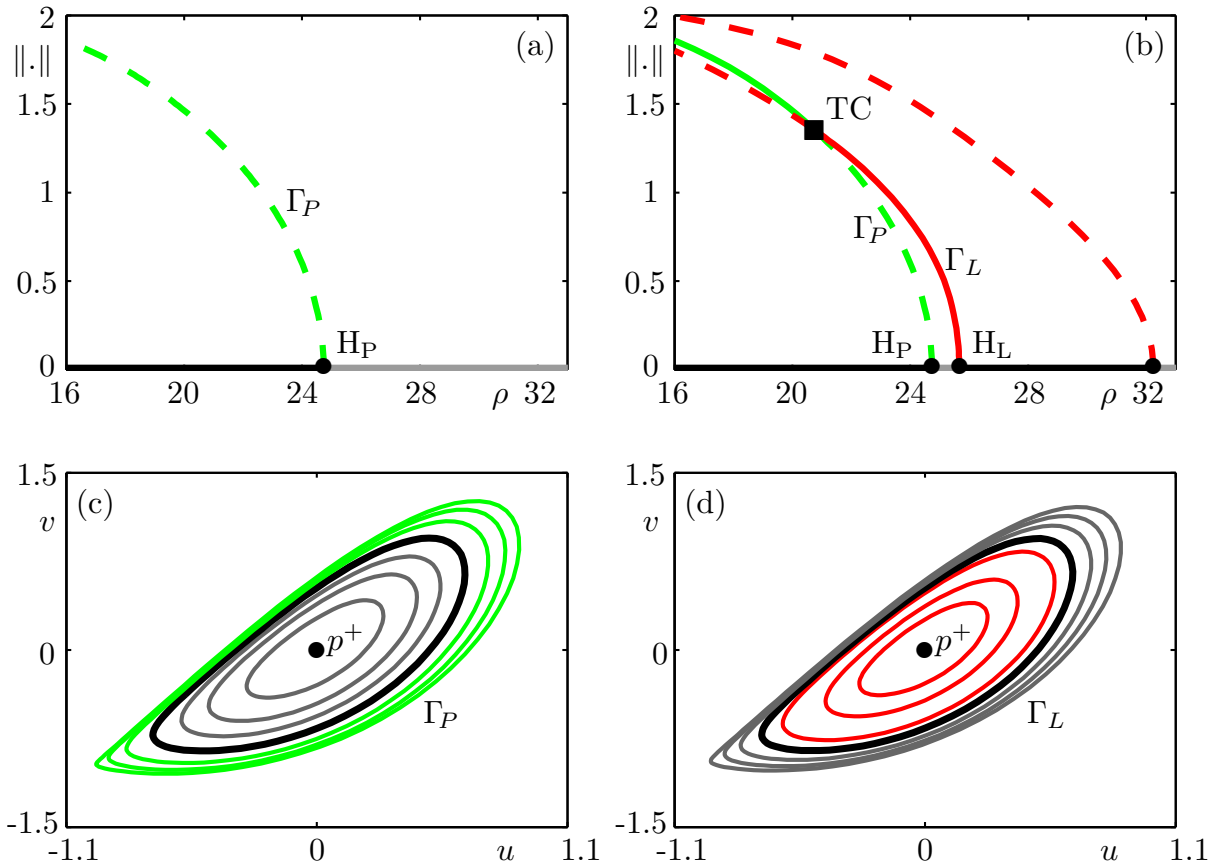


Figure 4.1: One-parameter bifurcation diagrams in ρ of (4.0.5). Panel (a) is for $b_0 = 0$ and shows the Hopf bifurcation point H_P (black dot) of the equilibrium and the bifurcating unstable periodic orbit Γ_P (green dashed). Panel (b) is for $b_0 = 0.19$ and shows further delay-induced Hopf bifurcations (black dots). From the bifurcation H_L emanates a stable periodic orbit Γ_L (red), which exchanges stability with Γ_P at a transcritical bifurcation TC (black square). Solid (dashed) curves indicate stable (unstable) periodic orbits, the solid black (grey) lines indicate where the equilibrium is stable (unstable). Panels (c) and (d) are phase portraits of (4.0.5) for various values of ρ (more details are given in the text) in projection onto the (u, v) -plane, showing the families of periodic orbits Γ_P and Γ_L respectively. Stable (unstable) periodic orbits are colored (grey) and the black periodic orbits in each panel are at the transcritical bifurcation TC. Other parameter values: $\sigma = 10$, $\alpha = \frac{8}{3}$ and $\eta = \frac{\pi}{4}$.

for $16 < \rho < 25$. The periodic orbit is stable when colored red and unstable when colored grey. Again the thicker black periodic orbit is at the transcritical bifurcation TC. From panels (c) and (d) we see that the outer most periodic orbits shown are already starting to deform as they approach the homoclinic bifurcation at $\rho = \rho_{\text{hom}}$.

In [65] the authors find that there exists a critical level of feedback amplitude b_0^c , immediately above which Γ_P bifurcates stably from H_P . In [14] Brown performed a centre manifold reduction of (4.0.5) and derived the analytical expression

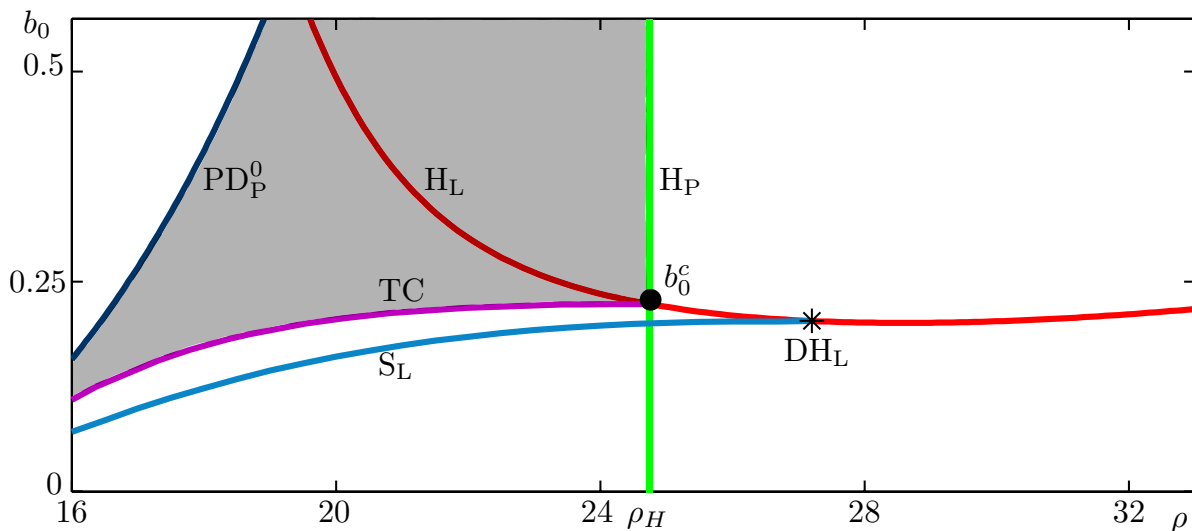


Figure 4.2: Bifurcation set in the (ρ, b_0) -plane of (4.0.5) near the point b_0^c , where the curves H_P (green) and H_L (red) intersect. The transcritical bifurcation curve TC (purple) begins at the point b_0^c . The SNLC bifurcation curve S_L (blue) emerges from the degenerate Hopf bifurcation point DH_L (*). The domain of stability of Γ_P is shaded. Other parameter values: $\sigma = 10$, $\alpha = \frac{8}{3}$ and $\eta = \frac{\pi}{4}$.

$$b_0^c = \left\{ (\rho, b_0) = \left(\rho_H, \frac{-\omega_0}{2\pi(\cos(\eta) + \hat{\gamma} \sin(\eta))} \right) \right\} \quad (4.1.2)$$

for the point b_0^c in the (ρ, b_0) -plane, where ω_0 is the linear frequency and $\hat{\gamma} \approx -10.82$ is a parameter obtained from the centre manifold reduction.

Figure 4.2 shows the two-parameter bifurcation set in the (ρ, b_0) -plane of (4.0.5) near the point b_0^c . This bifurcation set is also shown in [65]. The Hopf bifurcation curve H_L (red) intersects the Hopf bifurcation curve H_P (green) at the point b_0^c . From the point b_0^c emerges the transcritical bifurcation curve TC (purple). The curve TC extends into the left of the (ρ, b_0) -plane. The (blue) curve S_L , which is not shown in [65], is a saddle-node of limit cycles (SNLC) bifurcation (or fold bifurcation), where a stable delay-induced periodic orbit bifurcates. The curve S_L starts at the degenerate Hopf bifurcation point DH_L on the curve H_L and extends to the left of the (ρ, b_0) -plane. The curve PD_P^0 (dark blue) is a period-doubling bifurcation curve, where the stabilized periodic orbit Γ_P loses stability [65]. This was also found by Postlethwaite and Silber in [65]. Figure 4.2 also shows the local domain of stability of Γ_P (shaded). Its right-hand boundary is the curve H_P above the point b_0^c , the curve TC is its lower boundary and the curve PD_P^0 forms its left boundary.

Below b_0^c the Hopf bifurcation H_P is subcritical and the equilibrium p^+ is stable for $\rho < \rho_H$. Above b_0^c , H_P is supercritical and Γ_P bifurcates stably from H_P . The equilibrium is unstable

in the region to the left of the curve H_P and to the right of the curve H_L . Between the point b_0^c and the degenerate Hopf bifurcation point DH_L , the curve H_L is supercritical and from this segment of the curve bifurcates the stable periodic orbit Γ_L . At the point DH_L , the criticality of the curve H_L changes. The segments of the curve H_L to the right of DH_L and to the left of b_0^c are subcritical; from these parts of the curve bifurcate unstable periodic orbits.

Comparing Fig. 4.1 and Fig. 2.1 (a similar comparison was made in [65]), we see that the local mechanism of stabilization is exactly the same for the Lorenz case and the normal form case. That is, the target periodic orbit Γ_P is stabilized in a transcritical bifurcation with a delay-induced periodic orbit. Moreover, comparing Fig. 4.2 and 2.2, we see that the local domain of stability of Γ_P is very much the same in both cases. That is, in both cases the stability domain is bounded by the same bifurcation curves. The right-hand boundary of the domain of stability both here and for the normal form case is the Hopf bifurcation curve H_P and its lower boundary is the transcritical bifurcation curve TC. Also in both systems, we find the SNLC bifurcation curve S_L , which emerges from the degenerate Hopf bifurcation point DH_L . We find that the criticality of the Hopf bifurcation curves H_P and H_L is the same in both the Lorenz and normal form cases. In particular, the curve H_P is subcritical below the point b_0^c and supercritical above. Also in both cases, the curve H_L has a supercritical segment between the points b_0^c and DH_L , and all other parts of the curve are subcritical. There is the difference that in Fig. 4.2 the period-doubling bifurcation curve PD_P^0 forms the left-hand boundary of the stability domain, whereas this curve is not present in Fig. 2.2 for the normal form case. This issue is discussed in more detail in section 4.3.

4.2 A more global view of the (ρ, b_0) -plane

We now consider the (ρ, b_0) -plane more globally to show that the addition of feedback induces further Hopf bifurcations. We also present the overall domain of stability for the target periodic orbit Γ_P and present the domain of stability of a delay-induced periodic orbit. We compare these stability domains with those found for the normal form case.

4.2.1 Families of Hopf bifurcations

Figure 4.3 shows Hopf bifurcation curves of (4.0.5) in the (ρ, b_0) -plane. The (ρ, b_0) -plane is bounded below by $b_0 = 0$. It also has a left-hand boundary at $\rho = \rho_{\text{hom}} \approx 13.926$. Here system (4.0.5) has a homoclinic bifurcation, where Γ_P disappears and, hence, $\tau = T(\rho)$ goes to infinity. This is very similar to the normal form case, in which the (λ, b_0) -plane has a left-hand boundary at $\lambda = \frac{1}{\gamma}$ where the period of the target periodic orbit and hence the delay τ , goes to infinity; see chapter 2.

The curve H_P is again the vertical green curve at $\rho = \rho_H$. The Hopf bifurcation curve H_L (red) forms a loop, where the two end points of the curve end on the left-hand boundary of the (ρ, b_0) -plane at different values of b_0 . In addition to crossing H_P at b_0^0 , the curve H_L also intersects H_P at the non-degenerate double Hopf bifurcation point HH_0 . At this point there exist two pairs of purely imaginary eigenvalues. Above HH_0 the periodic orbit Γ_P bifurcates unstably from H_P with a complex conjugate pair of unstable Floquet multipliers.

In addition to the curve H_L , further delay-induced Hopf bifurcation curves are also shown in Fig. 4.3. The curve H_J^1 starts at the left-hand boundary of the (ρ, b_0) -plane, stretches downwards in the plane before turning and extending to infinity in b_0 . The curve H_I^1 in Fig. 4.3 has a supercritical segment between the degenerate Hopf bifurcation point DH_1 and the double Hopf bifurcation point HH_D^1 . From this part of the curve bifurcates a stable periodic orbit Γ_J , which exists for decreasing ρ . The segments of the curve H_I^1 above HH_D^1 and to the left of DH_1 are subcritical; from these segments bifurcates an unstable periodic orbit.

The curve H_R^1 starts on the left-hand boundary of the (ρ, b_0) -plane, crosses the curve H_P at the double Hopf bifurcation point HH_1 and then extends to infinity in both ρ and b_0 . The curve H_R^1 is part of a family of Hopf bifurcation curves H_R^K . The first six curves of the family are shown in Fig. 4.3, and we conjecture that there are in fact infinitely many curves in the family.

All periodic orbits that bifurcate from H_R^1 are unstable. The criticality of each curve in the family H_R^K is as that of H_R^1 . Each curve of the family H_R^K starts at a higher point on the left-hand boundary of the (ρ, b_0) -plane than the preceding curve. It then extends to infinity in both ρ and b_0 with a steeper gradient than the preceding curve in the family. Each curve H_R^k of the family H_R^K crosses the curve H_P at the double Hopf bifurcation point HH_k ; for example the curve H_R^2 crosses H_P at the point HH_2 . Above each of these double Hopf bifurcation points the target periodic orbit Γ_P bifurcates with a further complex

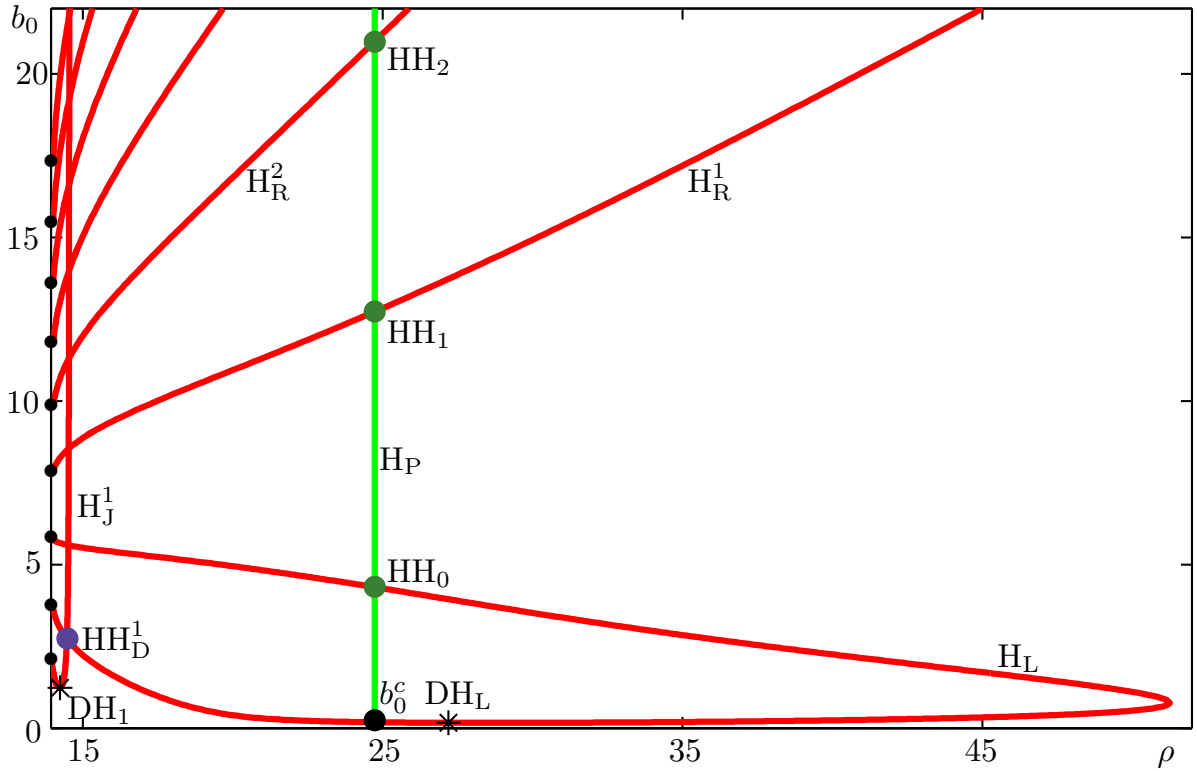


Figure 4.3: Bifurcation set in the (ρ, b_0) -plane of (4.0.5) showing the Hopf bifurcation curve H_P (green) and the delay-induced Hopf curves H_L and H_J^1 . Also shown are the first six curves of the family of delay-induced Hopf bifurcations H_R^K (red), the point b_0^c (black) and the double Hopf bifurcation points HH_0 (green), HH_1 (green), HH_2 (green) and HH_D^1 (violet). Degenerate Hopf bifurcation points DH_L and DH_1 are marked by asterisks. Other parameter values: $\sigma = 10$, $\alpha = \frac{8}{3}$ and $\eta = \frac{\pi}{4}$.

conjugate pair of unstable Floquet multipliers. Thus, Γ_P only bifurcates stably from H_P between the points b_0^c and HH_0 .

We now compare the Hopf bifurcation curves shown in Fig. 4.3 for the Lorenz case with those shown in Fig. 2.4 for the normal form case. We find that the curve H_L has the shape of a loop in both figures. There is the slight difference that in Fig. 4.3 for the Lorenz case the two end points of the curve H_L are at the left-hand boundary of the (ρ, b_0) -plane for different values of b_0 , whereas in Fig. 2.4, for the normal form case, the two end points of the curve H_L are at the same point. Moreover, all delay-induced Hopf bifurcation curves emerge from the same point on the left-hand boundary of the respective parameter planes but in Fig. 4.3 they emerge from points with different values of b_0 . Colloquially speaking, Fig. 4.3 is as Fig. 2.4 but “chopped off” or truncated at about $\lambda = -0.065$. We conjecture that this truncation is due to the presence of the homoclinic bifurcation at ρ_{hom} , where all periodic orbits disappear. It may well be that the delay-induced Hopf bifurcation curves do indeed start from the same point and that there are more ‘J’-shaped curves, but that

close to the left-hand boundary of the plane, the very steep increase in delay (due to the homoclinic bifurcation) makes these curves difficult to find numerically.

Again, comparing Fig. 4.3 and Fig. 2.4, we see that the respective curves H_J^1 are practically identical in both figures. There is a slight difference that in Fig. 4.3 we only find one ‘J’-shaped curve, whereas in Fig. 2.4, for the normal form case, we find a family of curves. The respective curves H_R^1 are also practically identical in Figs. 4.3 and 2.4. Furthermore, we find the family of Hopf bifurcation curves H_R^K in both cases. Again, there is the slight difference that in Fig. 4.3 for the Lorenz case the curves in the family H_R^K start at different values of b_0 , whereas in Fig. 2.4 for the normal form case, all curves in the family start at a single point.

We now compare the criticality of the Hopf bifurcation curves present in the Lorenz and normal form cases. In both the Lorenz case and the normal form case, the Hopf bifurcation curve H_P is supercritical between the points b_0^c and HH_0 and subcritical elsewhere. Thus, in both cases, the target periodic orbit Γ_P only bifurcates stably from H_P between the points b_0^c and HH_0 . Also, in both cases we find an identical supercritical segment of the curve H_J^1 , from which bifurcates the stable periodic orbit Γ_J . The existence of this stable periodic orbit in both cases shows that the addition of feedback induces not only the same local dynamics, but that the dynamics also closely agree more globally. The criticality of the curve H_R^1 is also the same in both the Lorenz and normal form cases. In particular, no stable periodic orbits bifurcate from the family of curves H_R^K in either case.

Comparing Figs. 4.3 and 2.4 and taking into account the criticality of the Hopf bifurcation curves shown in these figures, we have found that the addition of feedback induces practically identical global dynamics in both the Lorenz and normal form cases. In particular, we find the same delay-induced Hopf bifurcation curves and also the same delay-induced stable periodic orbit Γ_J . The difference is that the bifurcation set in the (ρ, b_0) -plane is truncated at the homoclinic bifurcation point ρ_{hom} when compared to the (λ, b_0) -plane in the normal form case. Hence, in the Lorenz case we find a subset of the Hopf bifurcation curves of the normal form case.

4.2.2 Overall domain of stability of Γ_P

Figure 4.4 shows the overall domain of stability (shaded grey) of the target periodic orbit Γ_P in the (ρ, b_0) -plane. The regions in which the equilibrium p^+ is stable are shaded blue; darker blue regions are areas of bistability, where both the equilibrium and a periodic orbit are stable.

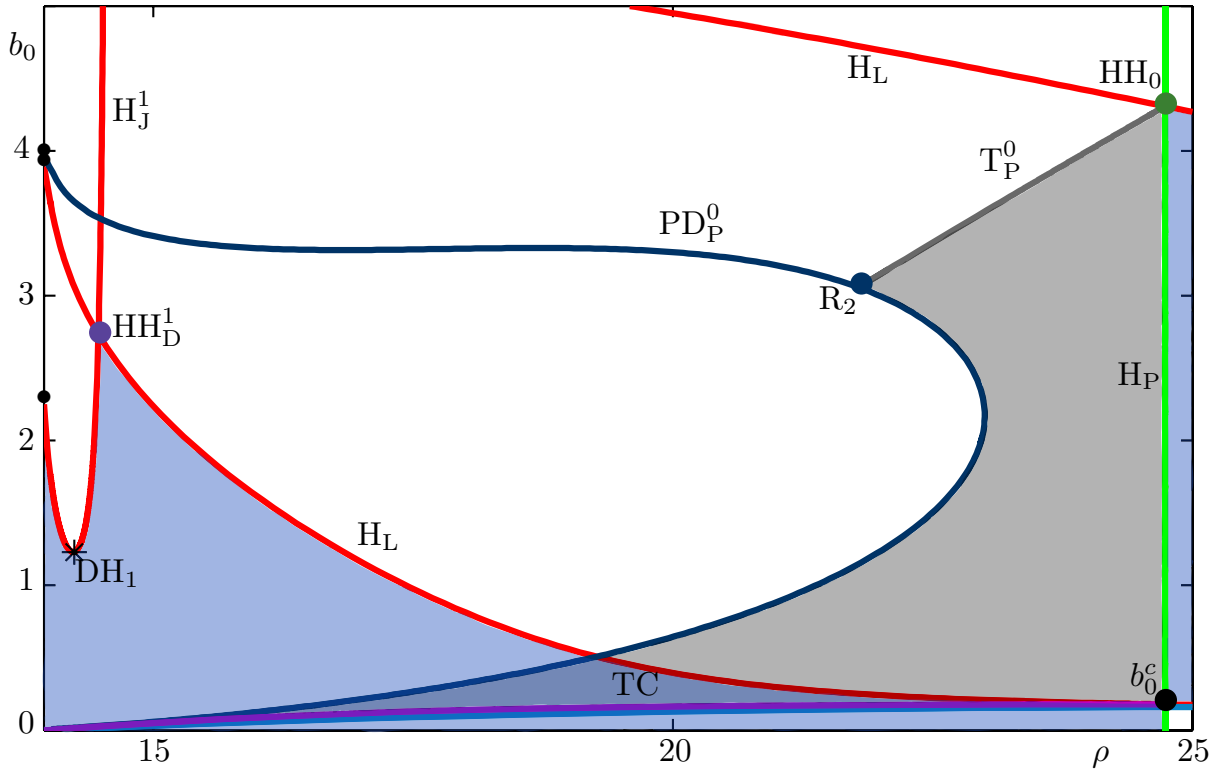


Figure 4.4: The overall domain of stability (shaded grey) of the target periodic orbit Γ_P ; it is bounded by the Hopf bifurcation curve H_P (green), the torus bifurcation curve T_P^0 (grey), the period-doubling bifurcation curve PD_P^0 (dark blue) and the transcritical bifurcation curve TC (purple). The regions where the equilibrium solution is stable is shaded blue. Other parameter values: $\sigma = 10$, $\alpha = \frac{8}{3}$ and $\eta = \frac{\pi}{4}$.

The right-hand boundary of the overall domain of stability of Γ_P is the Hopf bifurcation curve H_P between the points b_0^c and HH_0 . Its lower boundary is the transcritical bifurcation curve TC , which starts at the point b_0^c and ends on the left-hand boundary of the (ρ, b_0) -plane at $b_0 = 0$. The left boundary of the stability domain of Γ_P is the period-doubling bifurcation curve PD_P^0 (dark blue). The curve PD_P^0 starts on the left-hand boundary of the (ρ, b_0) -plane at approximately $b_0 = 4$; it extends to the right of the plane for increasing values of ρ . At approximately $\rho = 22.5$ the curve PD_P^0 turns and extends back to the left of the plane. It ends on the left-hand boundary of the (ρ, b_0) -plane at $b_0 = 0$. The upper boundary of the domain of stability of Γ_P is the torus bifurcation curve T_P^0 (grey), which starts at the double Hopf bifurcation point HH_0 and ends on the curve PD_P^0 at the 1:2 resonance point R_2 (dark blue). Therefore, depending on the value of b_0 , the stabilized periodic orbit Γ_P loses stability either in the period-doubling bifurcation PD_P^0 , where a Floquet multiplier leaves the unit circle along the negative real axis, or in the torus bifurcation T_P^0 , where a complex conjugate pair of Floquet multipliers leave the unit circle. There is a small region of bistability, where the equilibrium p^+ and the target periodic orbit Γ_P are both stable. This region is enclosed by the curves H_L , TC

and PD_P^0 . The periodic orbit Γ_P can be followed all the way to the left-hand boundary of the (ρ, b_0) -plane. Here its period goes to infinity as it undergoes a homoclinic bifurcation.

We now compare the overall domain of stability of Γ_P in the Lorenz case, shown in Fig. 4.4, with that in the normal form case shown in Fig. 2.6. We find that in both cases the right-hand boundary of the stability domain is H_P between the points b_0^c and HH_0 . Its lower boundary is the transcritical bifurcation curve TC and its upper boundary is the torus bifurcation curve T_P^0 . There is also a small region of bistability in each case, where the equilibrium and Γ_P are both stable. There is the difference that in Fig. 4.4 for the Lorenz case a part of the left-hand boundary of the stability domain is the period-doubling bifurcation curve PD_P^0 , whereas this curve is not present in Fig. 2.6 for the normal form case. Nonetheless, the domain of stability of Γ_P closely agrees in both the Lorenz and the normal form cases; in particular, close to the curve H_P it is identical.

4.2.3 Other regions of stability in the (ρ, b_0) -plane

We now consider the stability of the equilibrium p^+ in the (ρ, b_0) -plane. Figure 4.5(a) is an enlargement of Fig. 4.3 that shows the stability regions of p^+ (shaded blue). The equilibrium p^+ is stable in the region to the left of the Hopf bifurcation curve H_P and below the Hopf bifurcation curves H_L and H_J^1 . It is also stable in the region enclosed by the curve H_L to the right of the curve H_P . This latter region of stability is due to the addition of feedback. In the uncontrolled Lorenz system (4.0.1) the equilibrium p^+ is never stable for $\rho > \rho_H \approx 24.7368$.

Comparing Fig. 4.5(a) with Figs. 2.6 and 2.7 for the normal form case, we find that the equilibrium p^+ is stable in the same regions of the plane as the origin in the normal form case. When there is no control, in both cases the equilibrium solution, that is p^+ in the Lorenz case and the origin in the normal form case, is never stable to the right of the Hopf bifurcation H_P . However, the addition of feedback results in both equilibrium solutions being stable in a region of parameter space to the right of H_P , which is bounded by H_L .

Figure 4.5(b) shows a phase portrait of (4.0.5) in projection onto the (u, w) -plane for $\rho = 31$ and $b_0 = 0.4$, that is, for parameter values where p^+ is stable to the right of H_P . It shows the stable equilibrium p^+ and a saddle periodic orbit (red) that bifurcates from H_L . The inset in Fig. 4.5(b) is an enlargement near the equilibrium p^+ . The boundary of the basin of attraction of p^+ is the stable manifold of the saddle periodic orbit (red). Trajectories outside the basin of attraction of p^+ converge to a chaotic attractor that resembles the Lorenz attractor. The existence of this chaotic attractor is evidence that

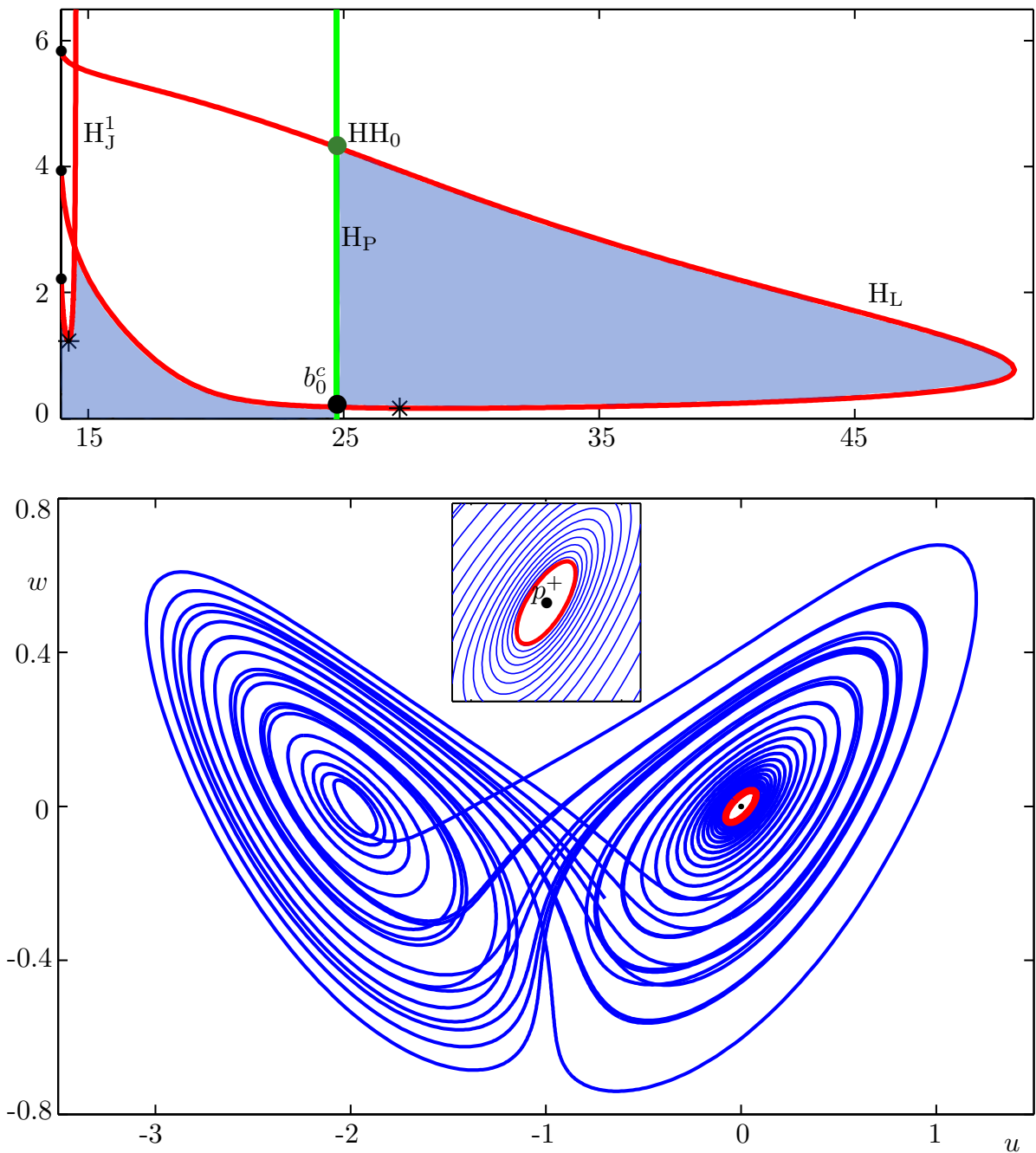


Figure 4.5: Panel (a) is an enlargement of Fig. 4.3, that shows in addition the stability of the equilibrium p^+ (shaded blue). Panel (b) shows a chaotic attractor of (4.0.5) for $\rho = 31$ and $b_0 = 0.4$ in projection onto the (u, w) -plane. It co-exists with the stable equilibrium p^+ (black dot), and the boundary of stability is formed by the stable manifold of the saddle periodic orbit (red).

the addition of feedback only effects the dynamics of (4.0.5) close to p^+ . In particular, the equilibrium p^- is still a saddle in the presence of feedback, as the control is not symmetric.

Figure 4.6(a) is as Fig. 4.4 but in addition shows further period-doubling bifurcation

curves PD_P^1 and PD_P^2 . It also shows the domain of stability of the delay-induced periodic orbit Γ_J (shaded grey). The regions where the equilibrium p^+ is stable are shaded blue.

Similarly to the curve PD_P^0 , Fig. 4.6(a) shows that the curves PD_P^1 and PD_P^2 (light blue) start at the left-hand boundary of the (ρ, b_0) -plane, extend to the right of the plane for increasing ρ , and then turn and end at the left-hand boundary of the plane at $b_0 = 0$. There are further period-doubling bifurcation curves to the left of the curve PD_P^0 , which are not shown as they are very close to PD_P^2 . We suspect that there might be a region of chaos to the left of the curve PD_P^2 ; but it proved to be too small to find by numerical simulations.

Figure 4.6(b) is the one-parameter bifurcation diagram in ρ of (4.0.5) for $b_0 = 1.5$, shown in terms of the observed period T . There is indeed a period-doubling cascade as ρ is reduced from the Hopf bifurcation H_P at $\rho = \rho_H$. The periodic orbit Γ_P (green) bifurcates stably from H_P and becomes unstable (grey) at the period-doubling bifurcation PD_P^0 (dark blue). From PD_P^0 bifurcates a stable periodic orbit with double the period of Γ_P . This periodic orbit loses stability at PD_P^1 , from which bifurcates another period-doubled stable periodic orbit. This process continues in this fashion through PD_P^2 and further period-doubling bifurcations. Figure 4.6(c) is the phase portrait of (4.0.5) projected onto the (u, v) -plane for $\rho = 22$ and $b_0 = 1.5$. It shows the unstable periodic orbit Γ_P (grey) and the stable period-doubled periodic orbit (dark green) immediately after the bifurcation PD_P^0 . The equilibrium p^+ at $(u, v) = (0, 0)$ is unstable.

Figure 4.7 is an enlargement of Fig. 4.6(a) that shows the domain of stability (shaded grey) of the delay-induced periodic orbit Γ_J in more detail. Again, the equilibrium p^+ is stable in the region shaded blue and the darker blue shading indicates regions of bistability, where both p^+ and Γ_J are stable. Similarly to Γ_P , the domain of stability of Γ_J is bounded on the right by the Hopf bifurcation H_J^1 between the degenerate Hopf bifurcation point DH_1 and the double Hopf bifurcation point HH_D^1 (violet). The lower boundary of the domain of stability is the SNLC bifurcation curve S_J^1 (blue), which starts at DH_1 and ends on the left-hand boundary of the (ρ, b_0) -plane. The upper boundary of the domain of stability is the torus bifurcation curve T_J^1 (black), which starts at HH_D^1 and ends on the left-hand boundary of the plane at the same point as the curve S_J^1 .

Comparison of Fig. 4.7 with Fig. 2.6 shows that the stability domain of Γ_J is topologically the same in both the Lorenz and the normal form cases. By this we mean that in both cases the stability domain is bounded by the same bifurcation curves and that these curves have the same starting and ending points. For the normal form case, there are further curves of the family H_J^K , which each have a stability domain associated with a

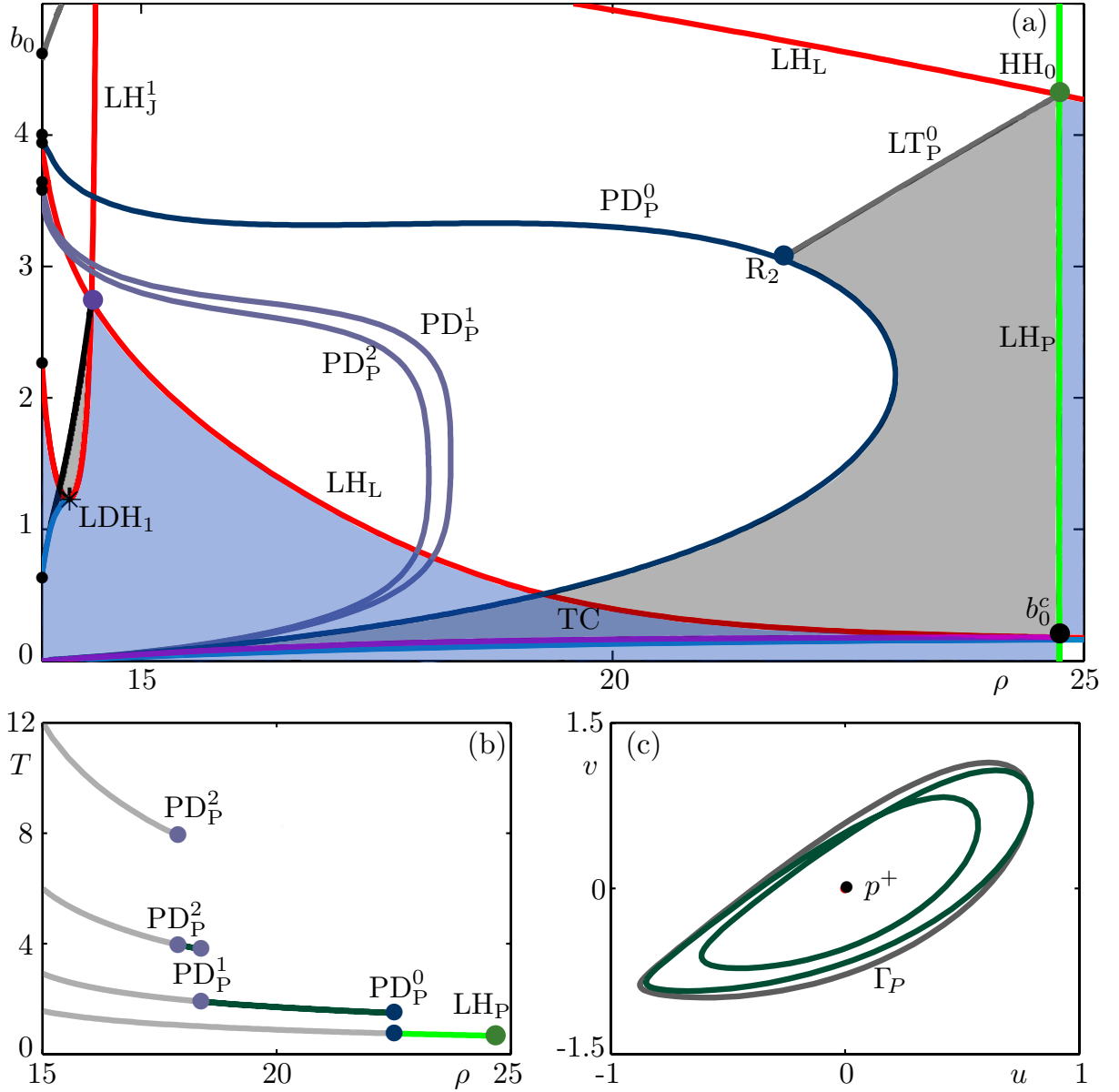


Figure 4.6: Panel (a) is the bifurcation set from Fig. 4.4, with the additional period-doubling bifurcation curves PD_P^1 and PD_P^2 (light blue). Panel (b) is the one-parameter bifurcation diagram in ρ of (4.0.5) for $b_0 = 1.5$, showing the periodic orbit Γ_P bifurcating from the Hopf bifurcation H_P and the periodic orbits that bifurcate from the period-doubling bifurcations PD_P^0 , PD_P^1 and PD_P^2 ; stable (unstable) periodic orbits are shown in color (grey). Panel (c) is a phase portrait of (4.0.5) shown in the (u, v) -space for $\rho = 22$ and $b_0 = 1.5$, showing the unstable periodic orbit Γ_P (grey) and the stable period-doubled orbit (dark green) immediately after the period-doubling bifurcation PD_P^0 . Other parameter values: $\sigma = 10$, $\alpha = \frac{8}{3}$ and $\eta = \frac{\pi}{4}$.

bifurcating stable periodic orbit. We did not find such further stability regions for the Lorenz case, owing to the fact that its bifurcation set is truncated at ρ_{hom} with respect to the bifurcation set of the normal form case. Nevertheless, the fact that a region of stability of a delay-induced periodic orbit exists, shows that the normal form case is relevant for

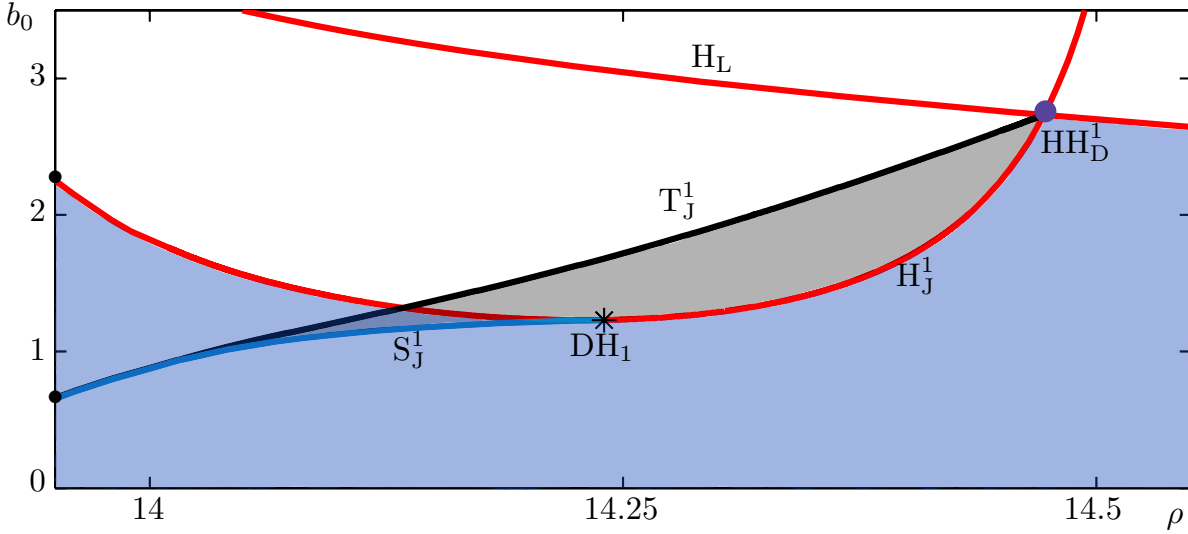


Figure 4.7: The overall domain of stability (shaded grey) of the delay-induced periodic orbit Γ_J , which is bounded by the Hopf bifurcation curve H_J^1 , the torus bifurcation curve T_J^1 (black) and the SNLC bifurcation curve S_J^1 (blue). Also shown is the Hopf bifurcation curve H_L (red), the degenerate Hopf bifurcation point DH_1 (*) and the double Hopf bifurcation point HH_D^1 (violet). The equilibrium is stable in the regions shaded blue.

the Lorenz system quite far from the curve H_P .

4.3 The effect of the 2π -periodic feedback phase η

So far we have kept the 2π -periodic phase η fixed at $\frac{\pi}{4}$ as is the convention [13, 24, 65]. It should be noted that setting $\eta = \frac{\pi}{4}$ in (4.0.5) is not the same as setting $\beta = \frac{\pi}{4}$ in the normal form case and this is why we use the different notation. In (4.0.5) the feedback matrix G , which contains the parameter η undergoes the coordinate transformation E . Therefore, the actual phase β of the feedback (as defined for the normal form case) will be a transformation of η and, thus, there may be a better choice of η for which the Lorenz case agrees even more closely with the normal form case. As such, we now vary the parameter η and show the effect that it has on the domain of stability of Γ_P .

We firstly consider the effect of a decrease in η . We find that even a small decrease in η results in the points b_0^c and HH_0 moving up to large values of b_0 in the (ρ, b_0) -plane. Therefore, we compactify the (ρ, b_0) -plane in the b_0 -coordinate via a stereographic transformation for b_0 , given by

Panel of Fig. 4.8	Description of curves
(a): $\eta = \frac{\pi}{4}$	The domain of stability of Γ_P in the (ρ, \hat{b}_0) -plane as in Fig. 4.4 but shown in terms of the compactified parameter \hat{b}_0 . Its right-hand boundary is the curve H_P (green) between the points b_0^c and HH_0 and its left-hand boundary is the period-doubling bifurcation curve PD_P^0 (dark blue). The lower boundary of the stability domain is the curve TC (purple) and its upper boundary is the curve T_P^0 (grey), which ends on the curve PD_P^0 at the 1 : 2 resonance point R_2 .
(b): $\eta = 0.2$	Both the points b_0^c and HH_0 have moved up in the (ρ, \hat{b}_0) -plane. The curve PD_P^0 has moved left in the plane. The boundaries of the stability domain are as before.
(c): $\eta = 0.15$	The curve PD_P^0 has developed a hook shape. The curve T_P^0 still ends on the curve PD_P^0 at the point R_2 .
(d): $\eta = 0.0926$	The point HH_0 is at the top boundary of the (ρ, \hat{b}_0) -plane, i.e. at infinity in b_0 . The curves PD_P^0 , T_P^0 and TC meet at the tip of the hook of PD_P^0 .
(e): $\eta = 0.0923$	The point b_0^c is close to the top boundary of the (ρ, \hat{b}_0) -plane. The end point of the curve T_P^0 has moved right along the curve TC as the 1 : 1 resonance point R_1 reducing the area of the domain of stability.
(f): $\eta = 0.0921$	The point b_0^c has reached the top boundary of the (ρ, \hat{b}_0) -plane. The point R_1 has moved right along the curve TC into the point b_0^c , and thus, the domain of stability has disappeared. Stabilization for $b_0 > 0$ is no longer possible.

Table 4.1: Description of the effect of a decrease in the parameter η on the domain of stability of Γ_P . To accompany Fig. 4.8

$$\hat{b}_0 = \frac{b_0}{1 + b_0}. \quad (4.3.1)$$

Recall that we do not consider $b_0 < 0$. The coordinate transformation (4.3.1) keeps $\hat{b}_0 = b_0 = 0$ but transforms $b_0 = \infty$ to $\hat{b}_0 = 1$. We now consider the (ρ, \hat{b}_0) -plane, where the left-hand boundary of the plane is the homoclinic bifurcation at $\rho = \rho_{\text{hom}} \approx 13.926$ as before and its top boundary is at $\hat{b}_0 = 1$, which represents infinity in b_0 .

Figure 4.8 shows how the domain of stability of Γ_P (shaded) changes in the (ρ, \hat{b}_0) -plane as the feedback phase η is reduced from $\frac{\pi}{4}$. An overview of the changes depicted in each panel of Fig. 4.8 is given in Table 4.1.

Figure 4.8(a) is the domain of stability for $\eta = \frac{\pi}{4}$ as in Fig. 4.4 but shown in terms of

the compactified parameter \hat{b}_0 . Panel (b) for $\eta = 0.2$ shows that the period-doubling bifurcation curve PD_P^0 has shifted left in the (ρ, \hat{b}_0) -plane. The points b_0^c and HH_0 have moved up in the plane, with HH_0 now very close to infinity in b_0 , this results in a large range of stability. The curve H_L has shifted up and to the right in the (ρ, \hat{b}_0) -plane, with its two end points on the left-hand boundary of the plane close to $\hat{b}_0 = 1$. For $\eta = 0.15$, as in panel (c), the two end points of the curve H_L are now at $\hat{b}_0 = 1$. The curve PD_P^0 has shifted further left in the plane and has developed a hook shape. The torus bifurcation curve T_P^0 is still connected to PD_P^0 at the point R_2 .

Figure 4.8(d) for $\eta = 0.0926$ shows that the two end points of the curve H_L are no longer connected to the left-hand boundary of the (ρ, \hat{b}_0) -plane; they have moved right in the (ρ, \hat{b}_0) -plane along its top boundary. The point HH_0 is also at the top boundary of the plane, that is, at infinity in b_0 . The torus bifurcation curve T_P^0 , the period-doubling bifurcation curve PD_P^0 and the transcritical bifurcation curve TC all meet at the tip of the hook of PD_P^0 . As η is further reduced the curve T_P^0 connects to the curve TC at the 1 : 1 resonance point R_1 (green dot). Panel (e) for $\eta = 0.0923$ shows that the point R_1 has moved right along the curve TC , reducing the area of the domain of stability. The point b_0^c is now close to the point HH_0 . As η is further reduced the point R_1 continues to slide right along the curve TC and the point b_0^c moves further up in the (ρ, \hat{b}_0) -plane, shrinking the area of the domain of stability. For $\eta = 0.0921$ as in panel (f), the point b_0^c has reached the top boundary of the (ρ, \hat{b}_0) -plane and the domain of stabilization has disappeared. For $\eta < 0.0921 = [\arctan(-\frac{1}{\gamma})]$, the point b_0^c becomes negative; see equation (4.1.2).

Comparing Fig. 4.8 with Fig. 2.9 for the normal form case, we observe that the domain of stabilization also disappeared as β was reduced in the normal form case. However, the mechanism for the loss of stabilization in the normal form case is quite different to that shown here for the Lorenz case. In the normal form case the two points b_0^c and HH_0 move through each other for relatively low values of b_0 , whereas for the Lorenz case the entire domain of stabilization moves up in the plane and only completely disappears when the point b_0^c is at infinity.

For completeness we must confirm that no Hopf bifurcation curves cross the curve H_P between the points b_0^c and HH_0 when η is reduced. If there are such curves, then the resulting double Hopf bifurcation points would introduce instabilities and the areas shaded in Fig. 4.8 would not actually be the domain of stability of Γ_P . To check this we show how the family of Hopf bifurcation curves H_R^K move in the (ρ, \hat{b}_0) -plane as η is reduced from $\frac{\pi}{4}$.

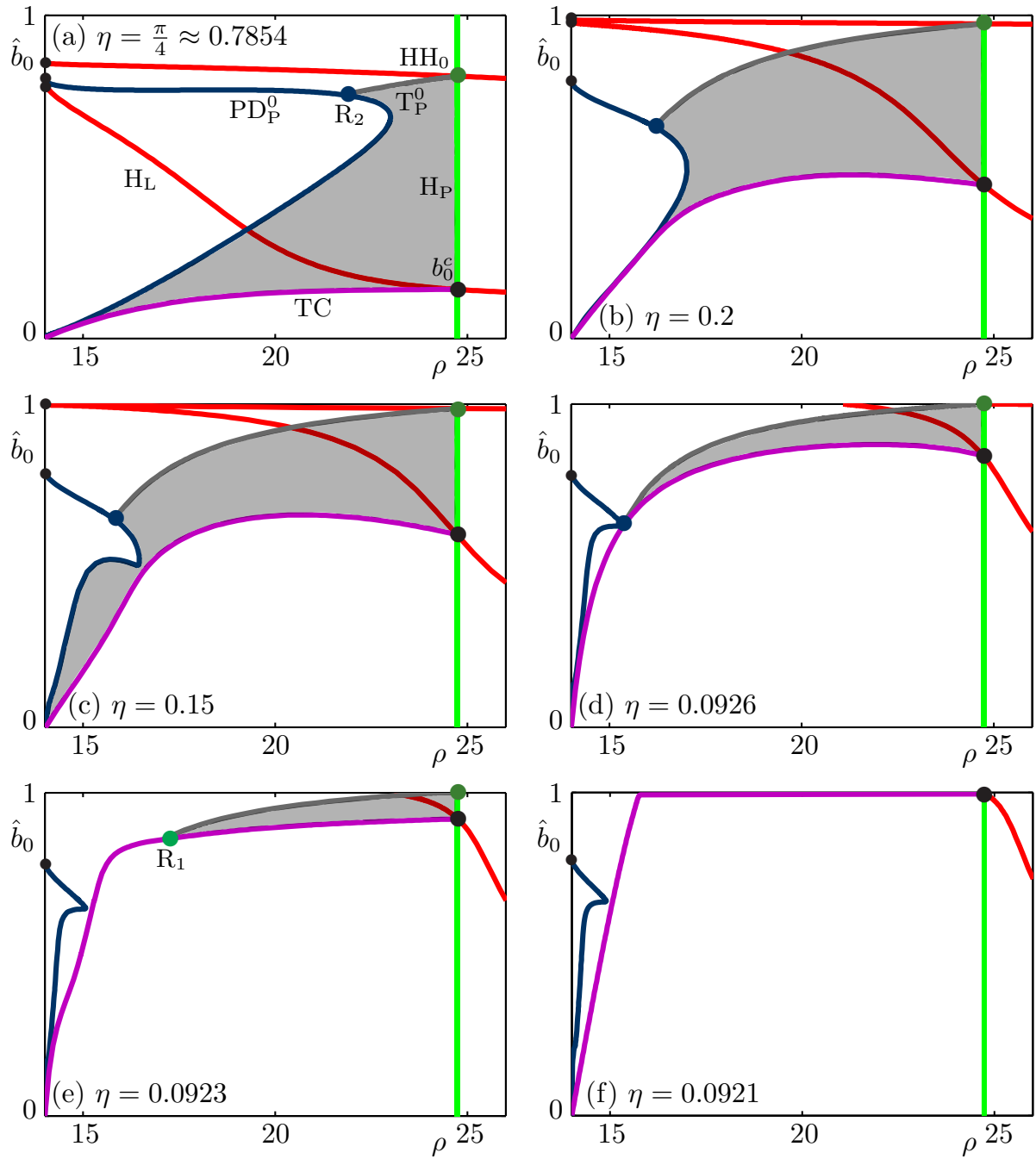


Figure 4.8: The overall domain of stability of Γ_P (shaded) in the (ρ, \hat{b}_0) -plane for different values of decreasing η . Panel (a) is for $\eta = \frac{\pi}{4}$ and panels (b)–(f) are for the stated values of η . Each panel shows the curves H_P (green) and H_L (red) as well as the points b_0^c (black dot) and HH_0 (green dot). Also shown are the period-doubling bifurcation curve PD_P^0 (dark blue), the transcritical bifurcation curve TC (purple) and the torus bifurcation curve T_P^0 (grey). Other parameter values: $\sigma = 10$, $\alpha = \frac{8}{3}$.

Figure. 4.9 shows how the curve H_R^1 moves in the (ρ, \hat{b}_0) -plane as η is reduced from $\frac{\pi}{4}$ to 0.0921. Panel (a) for $\eta = \frac{\pi}{4}$ shows the left end point of the curve H_R^1 is attached to the left-hand boundary of the plane. The curve H_R^1 crosses the curve H_P once at the point

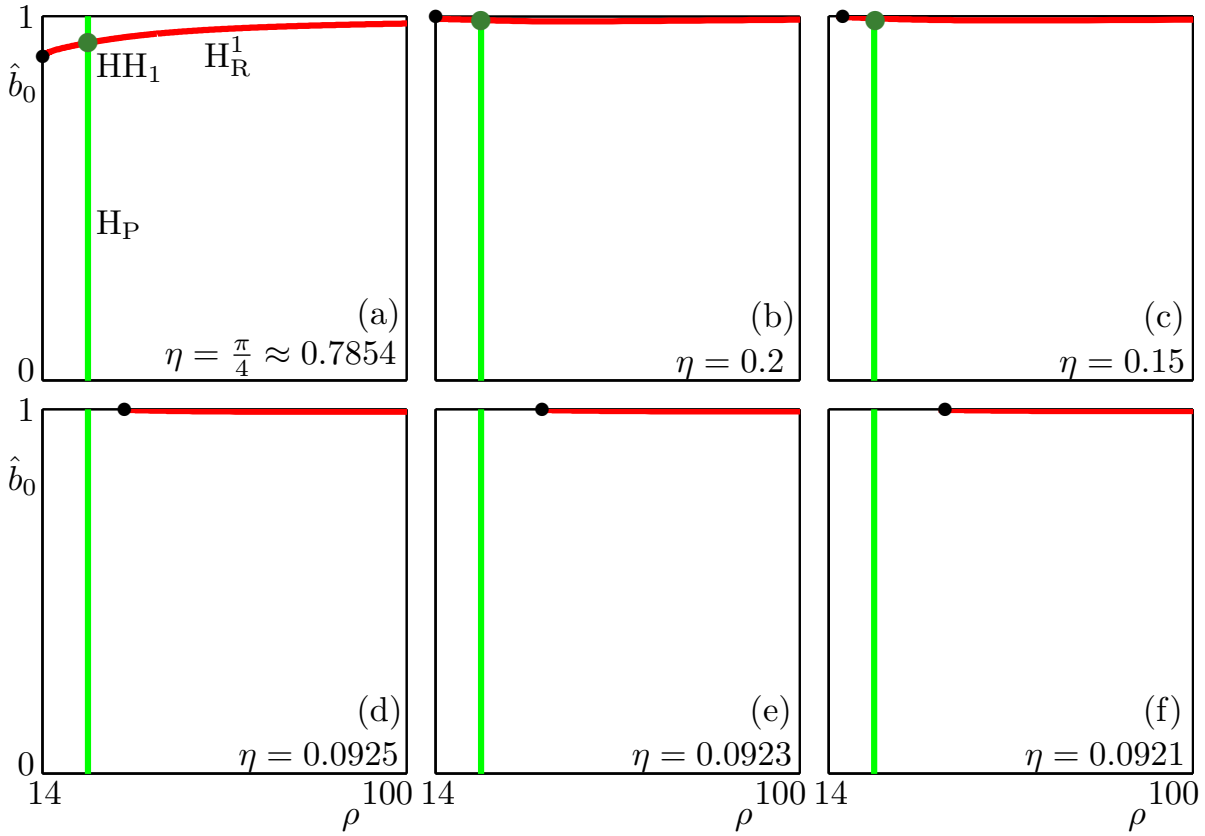


Figure 4.9: Transition of the Hopf bifurcation curve H_R^1 (red) in the (ρ, \hat{b}_0) -plane for values of η as stated. The curve H_P is shown in green and the point HH_0 is marked with a green dot.

HH_1 . Panel (b) for $\eta = 0.2$ shows that the left end point of the curve has moved up the left-hand boundary of the (ρ, \hat{b}_0) -plane and has reached its top boundary at $\hat{b}_0 = 1$. Panel (c) for $\eta = 0.15$ shows the curve has detached from the left-hand boundary and moved right along the top boundary of the (ρ, \hat{b}_0) -plane. Figure 4.9(d) for $\eta = 0.0926$ shows that curve H_R^1 no longer crosses H_P . Its left end point is now on the top boundary of the plane but to the right of the curve H_P . For this value of η the domain of stability has an upper boundary at $\hat{b}_0 = 1$ but exists to the left of the curve H_P ; see Fig. 4.8(d). As η is further increased, as in Fig. 4.9(e) and (f), the left end point of H_R^1 continues to move right along the top boundary of the (ρ, \hat{b}_0) -plane.

The other curves of the family H_R^K also move to the right of the curve H_P in the (ρ, \hat{b}_0) -plane as η is reduced from $\frac{\pi}{4}$. Hence, there are no double Hopf bifurcation points on the curve H_P between b_0^c and HH_0 and, therefore, the domain of stability shown in Fig. 4.8 is indeed as shown.

We now consider the effect of an increase in η on the domain of stability of the target periodic orbit Γ_P . Figure 4.10 shows how the domain of stability of Γ_P (shaded) changes

Panel of Fig. 4.10	Description of curves
(a): $\eta = \frac{\pi}{4}$	The domain of stability of Γ_P in the (ρ, b_0) -plane as in Fig. 4.4. Its right-hand boundary is the curve H_P (green) between the points b_0^c and HH_0 and its left-hand boundary is the period-doubling bifurcation curve PD_P^0 (dark blue). The lower boundary of the stability domain is the curve TC (purple) and its upper boundary is the curve T_P^0 (grey), which ends on the curve PD_P^0 at the 1:2 resonance point R_2 .
(b): $\eta = 2.50$	The point HH_0 has moved down in the (ρ, b_0) -plane (note the b_0 -axis scales in panels (a) and (b)). The curve PD_P^0 has moved left in the plane. The curve T_P^0 extends further to the left of the (ρ, b_0) -plane but still ends on the curve PD_P^0 at the point R_2 .
(c): $\eta = 2.71$	The point R_2 has moved left in the (ρ, b_0) -plane along the curve PD_P^0 . The curves PD_P^0 , T_P^0 and TC meet at the lower left-hand corner of the plane at $(\rho_{\text{hom}}, 0)$.
(d): $\eta = 3$	The point b_0^c has moved up in the (ρ, b_0) -plane. The end point of the curve T_P^0 has moved right along the curve TC as the 1:1 resonance point R_1 reducing the area of the domain of stability.
(e): $\eta = \pi$	The points b_0^c and HH_0 are equal, where the curve H_L is tangent to the curve H_P . The point R_1 has moved right along the curve TC into the point b_0^c , and thus, the domain of stability has disappeared.
(f): $\eta = 3.22$	The point b_0^c has moved above the point HH_0 and stabilization is no longer possible.

Table 4.2: Description of the effect of an increase in the parameter η on the domain of stability of Γ_P . To accompany Fig. 4.10

in the (ρ, b_0) -plane as the feedback phase η is increased. An overview of the changes depicted in each panel of Fig. 4.10 is given in Table 4.2.

Figure 4.10(a) shows the domain of stability for $\eta = \frac{\pi}{4}$ as in Fig. 4.4. Recall, that its right-hand boundary is the Hopf bifurcation curve H_P between the points b_0^c and HH_0 , its lower boundary is the transcritical bifurcation curve TC, its upper boundary is the torus bifurcation curve T_P^0 and its left-hand boundary is the period-doubling bifurcation curve PD_P^0 . We define the range of stability in b_0 of Γ_P to be the difference in b_0 between the points HH_0 and b_0^c .

As η is increased, as in Fig. 4.10(b) for $\eta = 2.50$, the curve PD_P^0 has moved left in the (ρ, b_0) -plane. The point R_2 , where T_P^0 and PD_P^0 meet, has moved down the curve PD_P^0 . The torus bifurcation curve T_P^0 thereby extends further to the left of the (ρ, b_0) -plane.

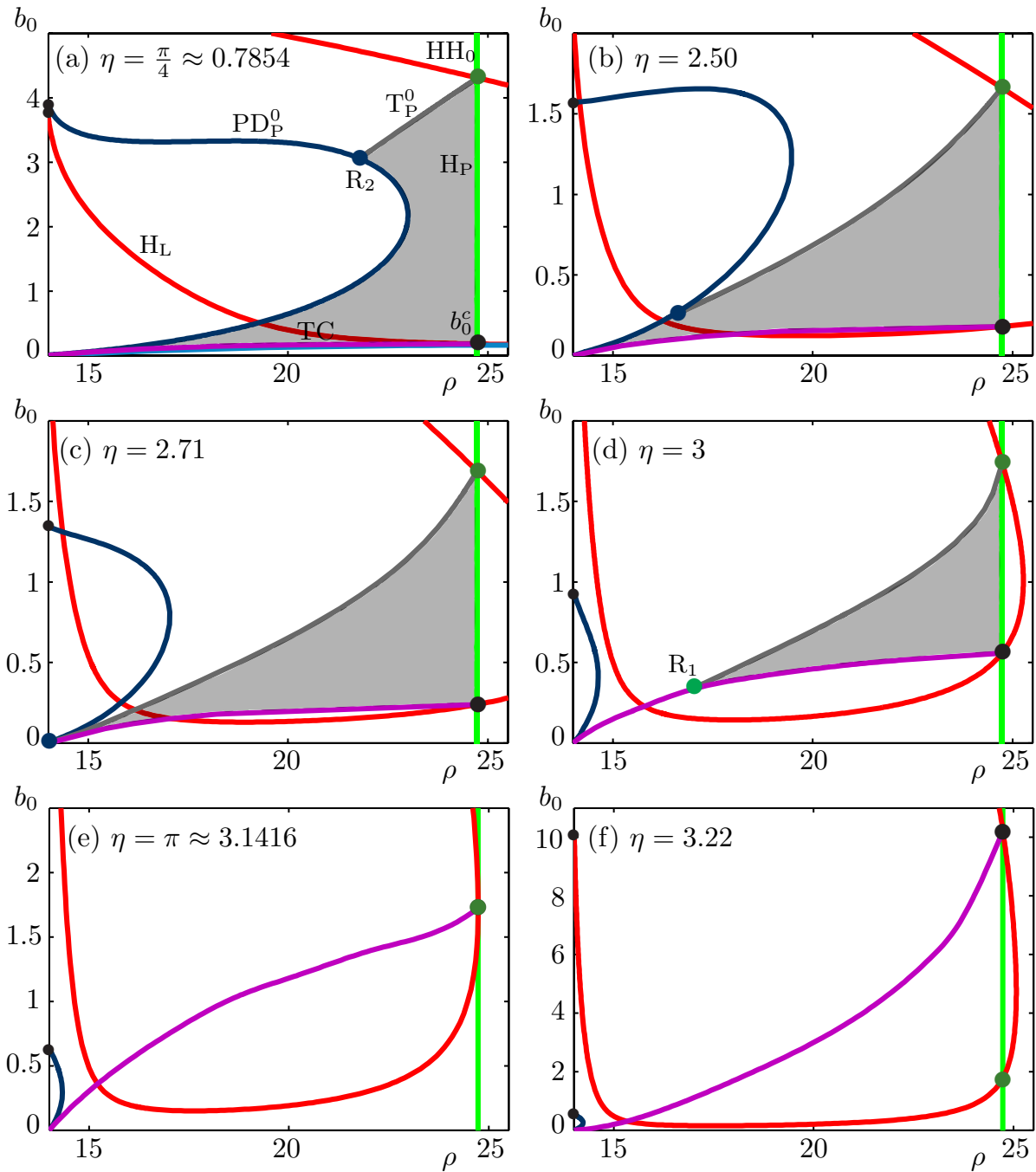


Figure 4.10: The overall domain of stability of Γ_P (shaded) in the (ρ, b_0) -plane for different values of increasing η . Panel (a) is for $\eta = \frac{\pi}{4}$ as it is in Fig. 4.4, and panels (b)–(f) are for the stated values of η . Each panel shows the curves H_P (green) and H_L (red) as well as the points b_0^c (black dot) and HH_0 (green dot). Also shown are the period-doubling bifurcation curve PD_P^0 (dark blue), the transcritical bifurcation curve TC (purple) and the torus bifurcation curve T_P^0 (grey). Other parameter values: $\sigma = 10$, $\alpha = \frac{8}{3}$.

The range of stability decreases as the point b_0^c moves up in the plane and the point HH_0 moves down in the plane.

For $\eta = 2.71$, as in Fig. 4.10(c), the point R_2 has moved to the end point of the curve PD_P^0 at the left-hand boundary of the (ρ, b_0) -plane for $b_0 = 0$. At this point the torus bifurcation curve T_P^0 connects to the transcritical bifurcation curve TC at the 1:1 resonance point R_1 . As η is further increased the end of the curve T_P^0 , that is, the point R_1 , moves right along the curve TC. At the same time the Hopf bifurcation curve H_L shifts left in the (ρ, b_0) -plane, which results in the points b_0^c and HH_0 moving closer together. Thus, the range of stability decreases as does the area of the domain of stability of Γ_P ; see panel (d) for $\eta = 3$.

Figure 4.10(e) shows that at $\eta = \pi$ the domain of stability of Γ_P has disappeared. The curve H_L has shifted further to the left of the plane and is tangent with the curve H_P . Here, the points b_0^c and HH_0 are equal. For $\eta = \pi$, the periodic orbit Γ_L bifurcating from H_L is no longer stable and, therefore, the target periodic orbit Γ_P cannot be stabilized in the transcritical bifurcation TC. In panel (f) for $\eta = 3.22$, the curve H_L has shifted right in the plane. The points b_0^c and HH_0 have moved through each other, so that b_0^c is now above HH_0 . Below HH_0 , Γ_P bifurcates from H_P with one unstable Floquet multiplier, between HH_0 and b_0^c it bifurcates with three unstable Floquet multipliers and immediately above b_0^c it bifurcates with two unstable Floquet multipliers. As η is further increased the point $b_0^c \rightarrow \infty$ as $\eta \rightarrow [\arctan(-\frac{1}{\gamma}) + \pi]$. For $\eta > [\arctan(-\frac{1}{\gamma}) + \pi]$ the point b_0^c is negative; see equation (4.1.2).

Comparing Fig. 4.10 with Fig. 2.8 for the normal form case, we see that in both cases there is a loss of stabilization at $\eta = \pi$ and $\beta = \pi$. Moreover, the mechanism for this loss of stabilization is the same for both cases. That is, the points b_0^c and HH_0 move closer together in the (ρ, b_0) -plane and at $\eta = \pi$ they become equal. In Fig. 4.10 for the Lorenz case, we see that for $\eta > 2.71$ the domain of stability of Γ_P is bounded by the same bifurcation curves as in Fig. 2.8 for the normal form case. Namely, the upper boundary of the stability domain is the torus bifurcation curve T_P^0 between the points HH_0 and R_1 and its lower boundary is the transcritical bifurcation curve TC between the points b_0^c and R_1 .

4.3.1 Best match for η

So far in this chapter we have shown that the global dynamics of (4.0.5) closely agree with those of the normal form case. The main difference we have found is the existence of the period-doubling bifurcation curve PD_P^0 (and further period-doubling bifurcation curves) in the Lorenz case, which forms the left-hand boundary of the stability domain of Γ_P .

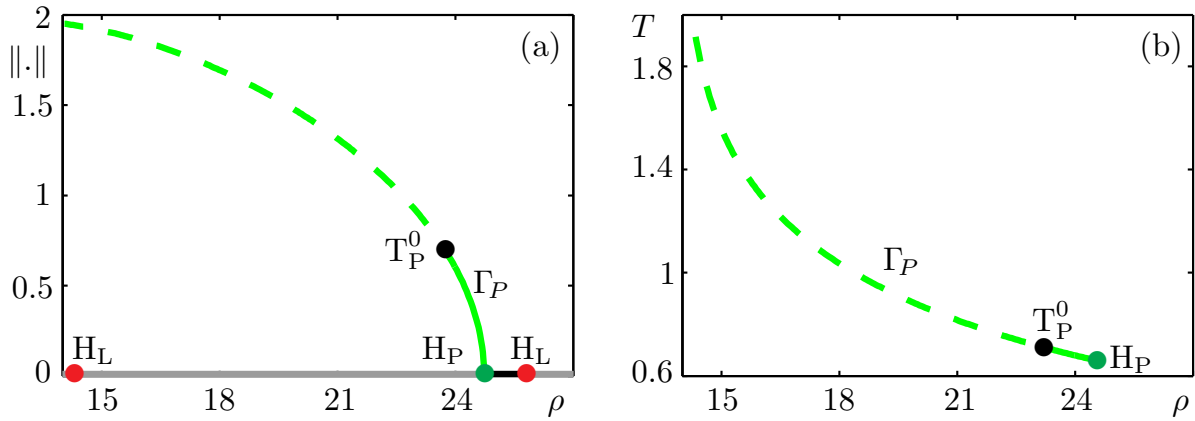


Figure 4.11: One-parameter bifurcation diagram in ρ for $b_0 = 1.4$ of (4.0.5), shown in terms of the amplitude in (a) and the period T in (b). The equilibrium p^+ is stable (unstable) when black (grey), it becomes stable at the Hopf bifurcation point H_P (green) from which bifurcates the branch of periodic orbits Γ_P (green). Also shown are the delay-induced Hopf bifurcation points H_L (red) and the torus bifurcation point T_P^0 (black). Solid (dashed) curves indicate stable (unstable) periodic orbits. Other parameter values: $\sigma = 10$, $\alpha = \frac{8}{3}$ and $\eta = 2.8$.

As we have already discussed setting $\eta = \frac{\pi}{4}$ in (4.0.5) is not equivalent to setting $\beta = \frac{\pi}{4}$ in the normal form case. From Fig. 4.10 we found that the domain of stability of Γ_P is topologically the same (i.e. bounded by the same bifurcation curves) as in the normal form case when $2.71 < \eta < \pi$. We now consider this range of η and, more specifically, show that (4.0.5) with $\eta = 2.8$ provides a near perfect match with the normal form case for $\beta = \frac{\pi}{4}$.

Figure 4.11 shows the one-parameter bifurcation diagram in ρ of (4.0.5) for $b_0 = 1.4$ and $\eta = 2.8$. It is shown in panel (a) in terms of its amplitude and in panel (b) in terms of the observed period T . Shown along the bottom axis of panel (a) is the equilibrium p^+ , which is stable when black and unstable when grey. The Hopf bifurcation H_P is denoted by a green dot and two further delay-induced Hopf bifurcations H_L are denoted by red dots. Figure 4.11(a) shows that the periodic orbit Γ_P bifurcates stably (solid curve) from H_P . It becomes unstable (dashed curve) at the torus bifurcation point T_P^0 (black dot), where a complex conjugate pair of Floquet multipliers leaves the unit circle. Panel (b) shows that the period of Γ_P increases quickly as ρ is reduced. At $\rho = \rho_{\text{hom}} \approx 13.926$ the period of Γ_P goes to infinity as it undergoes a homoclinic bifurcation with a fixed point.

We now compare Fig. 4.11 for the Lorenz case with Fig. 3.1 for the normal form case. Both figures are topologically equivalent, that is, in both cases the stable periodic orbit Γ_P bifurcates supercritically from the Hopf bifurcation H_P before losing stability in the torus bifurcation T_P^0 . Also, in both cases the period of Γ_P goes to infinity at the left-hand

boundaries of the respective planes.

Figure 4.12 shows the bifurcation set of (4.0.5) in the (ρ, b_0) -plane. As before, the (ρ, b_0) -plane has a left-hand boundary at $\rho = \rho_{\text{hom}} \approx 13.926$, where there is the homoclinic bifurcation. Figure 4.12(a) shows the Hopf bifurcation H_P (green) at $\rho = \rho_H$ and the delay-induced Hopf bifurcation curves H_J^1 , H_R^1 , H_R^2 and H_R^3 (red). It also shows the domain of stability of Γ_P (shaded). In addition, it shows the curve H_J^2 , which was not present in the bifurcation set of (4.0.5) for $\eta = \frac{\pi}{4}$ in Fig. 4.3. The curve H_J^2 emerges out of the left-hand boundary of the (ρ, b_0) -plane at $\eta \approx 2.63$.

Figure 4.12(b) is an enlargement of Fig. 4.12(a) that shows the overall domain of stability of Γ_P (shaded grey) in more detail. The equilibrium is stable in the regions shaded blue and darker blue areas are regions of bistability. The right-hand boundary of the domain of stability is the curve H_P between the points b_0^c and HH_0 . The upper boundary is the torus bifurcation curve T_P^0 , which starts at the double Hopf bifurcation point HH_0 and ends on the transcritical bifurcation curve TC at the 1:1 resonance point R_1 . The lower boundary of the stability domain is the curve TC between its starting point b_0^c and the point R_1 . There is a small region of bistability between the curves TC and T_P^0 and to the left of the curve H_L , where both the equilibrium p^+ and Γ_P are stable. The SNLC bifurcation curve S_L emerges from the degenerate Hopf bifurcation point DH_L and ends on the left-hand boundary of the plane for $b_0 = 0$.

Figure 4.12(c) shows the domain of stability of the delay-induced periodic orbit Γ_J (shaded grey), which bifurcates from the Hopf bifurcation curve H_J^1 . The equilibrium p^+ is stable in the regions shaded blue and darker blue areas are regions of bistability. The left boundary of the stability domain is the curve H_J^1 between the degenerate Hopf bifurcation point DH_1 and the double Hopf bifurcation point HH_D^1 . Its upper boundary is the torus bifurcation curve T_J^1 , which starts at the point HH_D^1 and ends on the left-hand boundary of the (ρ, b_0) -plane. The lower boundary of the stability domain is the SNLC bifurcation curve S_J^1 , which starts at the point DH_1 and ends on the left-hand boundary of the plane.

Comparing Fig. 4.12 for the Lorenz case with Figs. 2.4 and 2.6 for the normal form case, we find that the bifurcation set of the Lorenz case with $\eta = 2.8$ very closely matches the bifurcation set of the normal form case with $\beta = \frac{\pi}{4}$. In particular, we find that the overall domain of stability of Γ_P is topologically the same in both cases. Furthermore, the domain of stability of the delay-induced periodic orbit Γ_J that bifurcates from H_J^1 is also topologically the same in both cases.

Moreover, in Fig. 4.12 we now find an additional ‘J’-shaped curve H_J^2 that was not present

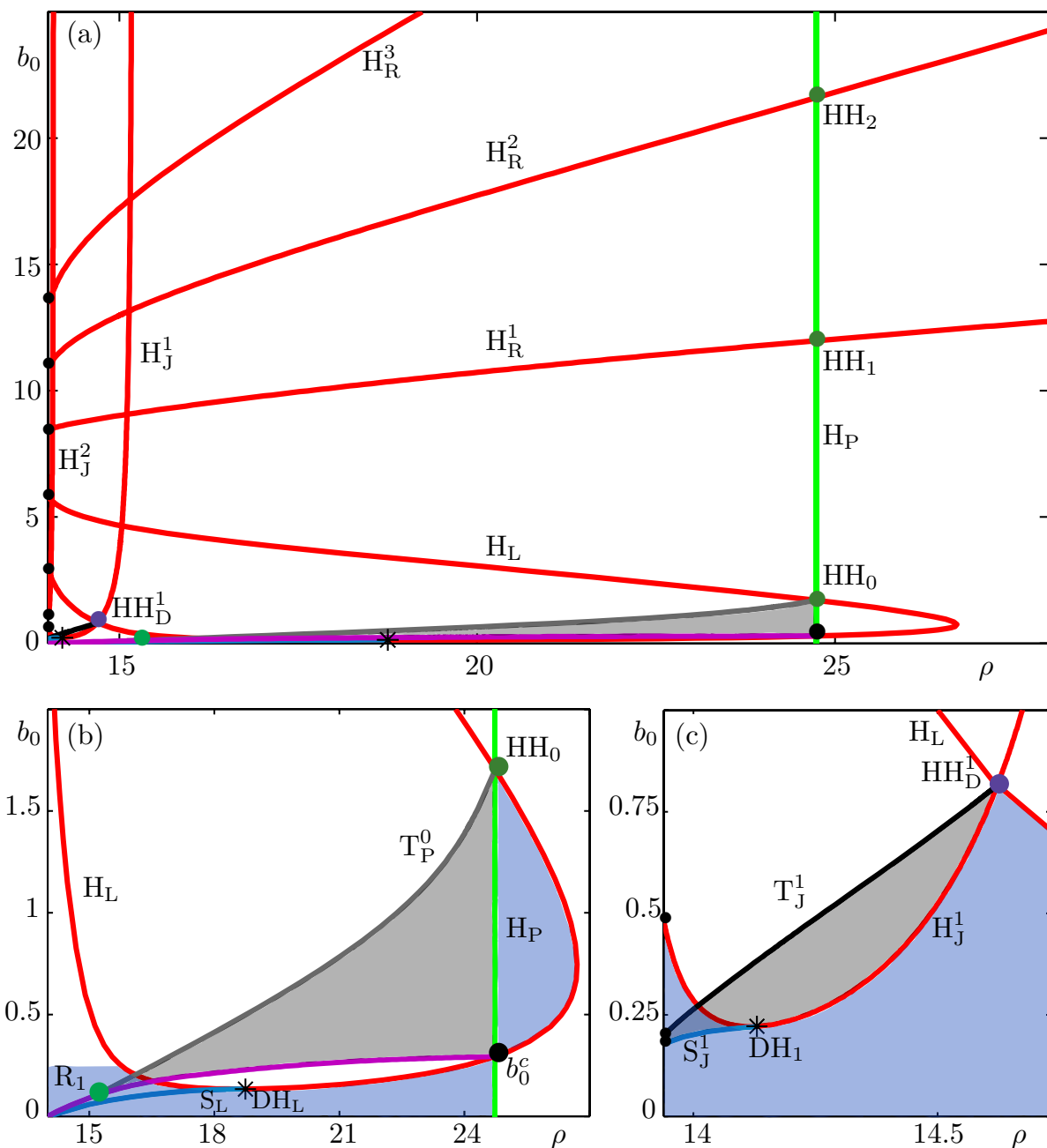


Figure 4.12: Bifurcation set in the (ρ, b_0) -plane of (4.0.5). Shown in (a) are the Hopf bifurcation curve H_P (green) and the delay-induced Hopf bifurcation curves H_L , H_J^1 , H_J^2 , H_R^1 , H_R^2 and H_R^3 (red). Also shown are the overall domains of stability of Γ_P and Γ_J (shaded) and the double Hopf bifurcation points HH_0 , HH_1 , HH_2 (green) and HH_D^1 (violet). An enlargement of the stability domain of Γ_P is shown in (b). The torus bifurcation curve T_P^0 (grey) meets the transcritical bifurcation curve TC (purple) at the point R_1 . Panel (c) is an enlargement of the stability domain of Γ_J , which in addition shows the SNLC bifurcation curve S_J^1 (blue) bifurcating from the degenerate Hopf bifurcation point DH_1 and the torus bifurcation curve T_J^1 (black). The equilibrium p^+ is stable in the regions shaded blue. Above the horizontal boundary at $b_0 \approx 0.2$ in panel (b), the stability region is not defined, as further delay-induced Hopf bifurcation curves are not shown. Other parameter values: $\sigma = 10$, $\alpha = \frac{8}{3}$ and $\eta = 2.8$.

in Fig. 4.3. It resembles the curve H_J^2 in Fig. 2.4. There is the difference that in the Lorenz case H_J^2 is nested inside H_J^1 , whereas in the normal form case it is not. Thus, we find that for $\eta = 2.8$ the bifurcation set of the Lorenz case is a slightly less truncated version of the bifurcation set of the normal form case for $\beta = \frac{\pi}{4}$. That is, Fig. 4.12 is Fig. 2.4 “chopped off” a bit further to the left of the plane than Fig. 4.3. There is also the slight difference that in Fig. 4.12(b) the SNLC bifurcation curve S_L exists entirely to the left of H_P , whereas in the normal form case it starts on H_L to the right of H_P . Nonetheless, we conclude that the normal form case provides an excellent description of the Lorenz case over a very wide region of the (ρ, b_0) -plane.

4.4 Investigation of delay mismatch

We now consider a delay mismatch in system (4.0.5). That is, we analyze the effect of setting the delay in (4.0.5) not exactly as the period $T(\rho)$ of the target periodic orbit Γ_P . As opposed to the normal form case (see chapter 3), however, we do not have an analytic form for $T(\rho)$. Instead, we consider two approximations of $T(\rho)$ derived from the numerical data set and the extrapolation function (4.1.1), which we used in section 4.1. Unlike the normal form case, this setup is, therefore, more closely related to an actual experiment, where in general the user will not have an analytic parameter dependent function for the target period.

We consider the following two cases of delay mismatch, where we fix $\sigma = 10$, $\alpha = \frac{8}{3}$ and also set $\eta = 2.8$; that is, we consider the best match between the Lorenz case and the normal form case.

The constant-period case

Here we set the delay in (4.0.5) as the period of Γ_P at the Hopf bifurcation H_P , that is, we set

$$\tau = T_C = T(\rho_H) = 0.6528 \quad (4.4.1)$$

Thus, the period T_C and therefore the delay τ are no longer parameter dependent.

The linear-period case

Here we set the delay in (4.0.5) to the linear approximation

$$\tau = T_L(\rho) = -0.0345\rho + 1.5062 \quad (4.4.2)$$

of the target period $T(\rho)$. The linear approximation (4.4.2) is derived from the period of Γ_P at H_P and its slope is derived from the data set which describes $T(\rho)$ at $\rho = \rho_H$.

We compare these two cases to the analysis of (4.0.5) presented in Figs. 4.11 and 4.12, which we refer to as the benchmark exact-period case. Note that the delay at the Hopf bifurcation H_P for $\rho = \rho_H$ is again the same in all three period cases, that is,

$$\tau = T(\rho_H) = T_C = T_L(\rho) = 0.6528 \quad (4.4.3)$$

As before, we say that the Pyragas control scheme has been successful if the three criteria (A), (B) and (C), from chapter 3 are satisfied. We only consider the Pyragas control scheme successful if the periodic orbit stabilized in the constant-period and linear-period cases exists for $\rho < \rho_H$ and for similar values of b_0 as Γ_P in the benchmark exact-period case; see Figs. 4.11 and 4.12. More specifically, the domain of stability in the constant-period and linear-period cases should exist to the left of the Hopf bifurcation curve H_P and be bounded by bifurcation curves similar to T_P^0 and TC in the exact-period case.

4.4.1 The constant-period case

Figure 4.13 shows the one-parameter bifurcation diagram in ρ for $b_0 = 1.4$ for the constant-period case. It is shown in panel (a) in terms of its amplitude and in panel (b) in terms of the observed period T . Shown along the bottom axis of panel (a) is the equilibrium solution p^+ , which is stable when black and unstable when grey. It is stable between the Hopf bifurcation points H_D^1 (red) and H_P (green). From H_P bifurcates the stable branch of periodic orbits Γ_C (green). In contrast to the target branch Γ_P , the branch Γ_C exists for $\rho > \rho_H$. The branch Γ_C loses stability at the torus bifurcation T_P^0 (black dot), where a complex conjugate pair of Floquet multipliers leave the unit circle. There is a SNLC bifurcation S_P^1 (blue dot) on the unstable part of Γ_C , where a further Floquet multiplier leaves the unit circle. The branch ends at the delay-induced Hopf bifurcation H_D^1 .

Figure 4.13(b) shows how the observed period T of Γ_C changes as ρ is varied. Recall that both Γ_P and Γ_C have period equal to 0.6528 at the Hopf bifurcation point H_P . As ρ is varied the period increases gradually and reaches its maximum at H_D^1 . We cannot directly

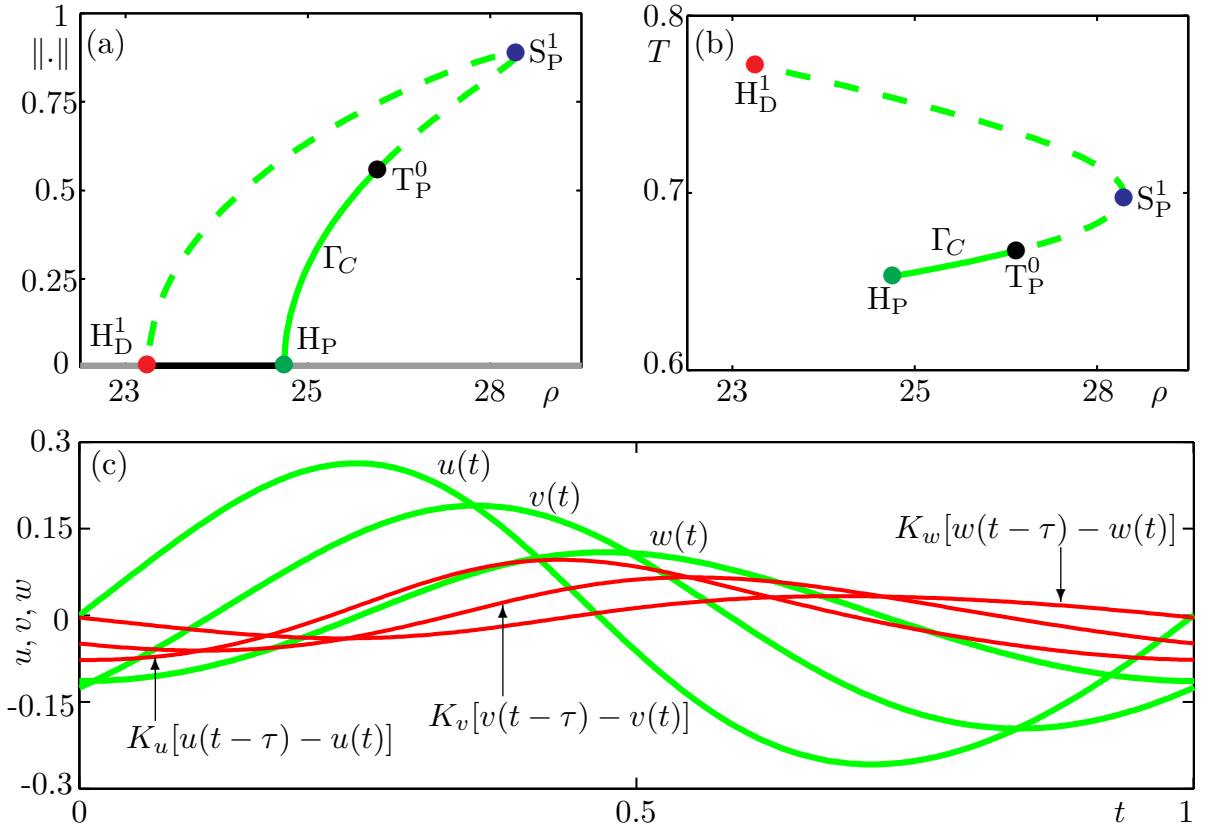


Figure 4.13: One-parameter bifurcation diagram in ρ for $b_0 = 1.4$ of (4.0.5) for the constant-period case, shown in terms of the amplitude in (a) and the period T in (b). The equilibrium p^+ is stable (unstable) when black (grey), it becomes unstable at the Hopf bifurcation point H_P (green) from which bifurcates the branch of periodic orbits Γ_C (green). Also shown is the delay-induced Hopf bifurcation point H_D^1 (red), the torus bifurcation point T_P^0 (black) and the SNLC bifurcation point S_P^1 (blue). Solid (dashed) curves indicate stable (unstable) periodic orbits. Panel (c) shows the u, v and w components of the solution profile (green) of the stable periodic orbit Γ_C at $\rho = 25.5$ and $b_0 = 1.4$; the red curves are the solution profiles of the residual feedback components $K_u[u(t-\tau) - u(t)]$, $K_v[v(t-\tau) - v(t)]$ and $K_w[w(t-\tau) - w(t)]$ (defined in the text). Other parameter values: $\sigma = 10$, $\alpha = \frac{8}{3}$ and $\eta = 2.8$.

compare the observed periods of Γ_P and Γ_C , because whilst stable, both branches exist for different ranges of ρ . Figure 4.13(c) shows the solution profile (green) of the stable periodic orbit Γ_C at $\rho = 25.5$ and $b_0 = 1.4$, which is close to the torus bifurcation T_P^0 . Also shown are the residual control force components $K_u[u(t-\tau) - u(t)]$, $K_v[v(t-\tau) - v(t)]$, $K_w[w(t-\tau) - w(t)]$ (red). Here we define K_u as the sum of the terms in the first column of the matrix Π from (4.0.5), that is, the summation of the feedback gain with respect to the variable u . The terms K_v and K_w are defined in a similar fashion for the variables v and w using the second and third columns of Π respectively. Figure 4.13(c) shows that the residual control force is large; the maximum amplitude of $K_u[u(t-\tau) - u(t)]$ is approximately 35% of the amplitude of the maximum solution $u(t)$. Therefore, criterion (B) for successful stabilization is not satisfied.

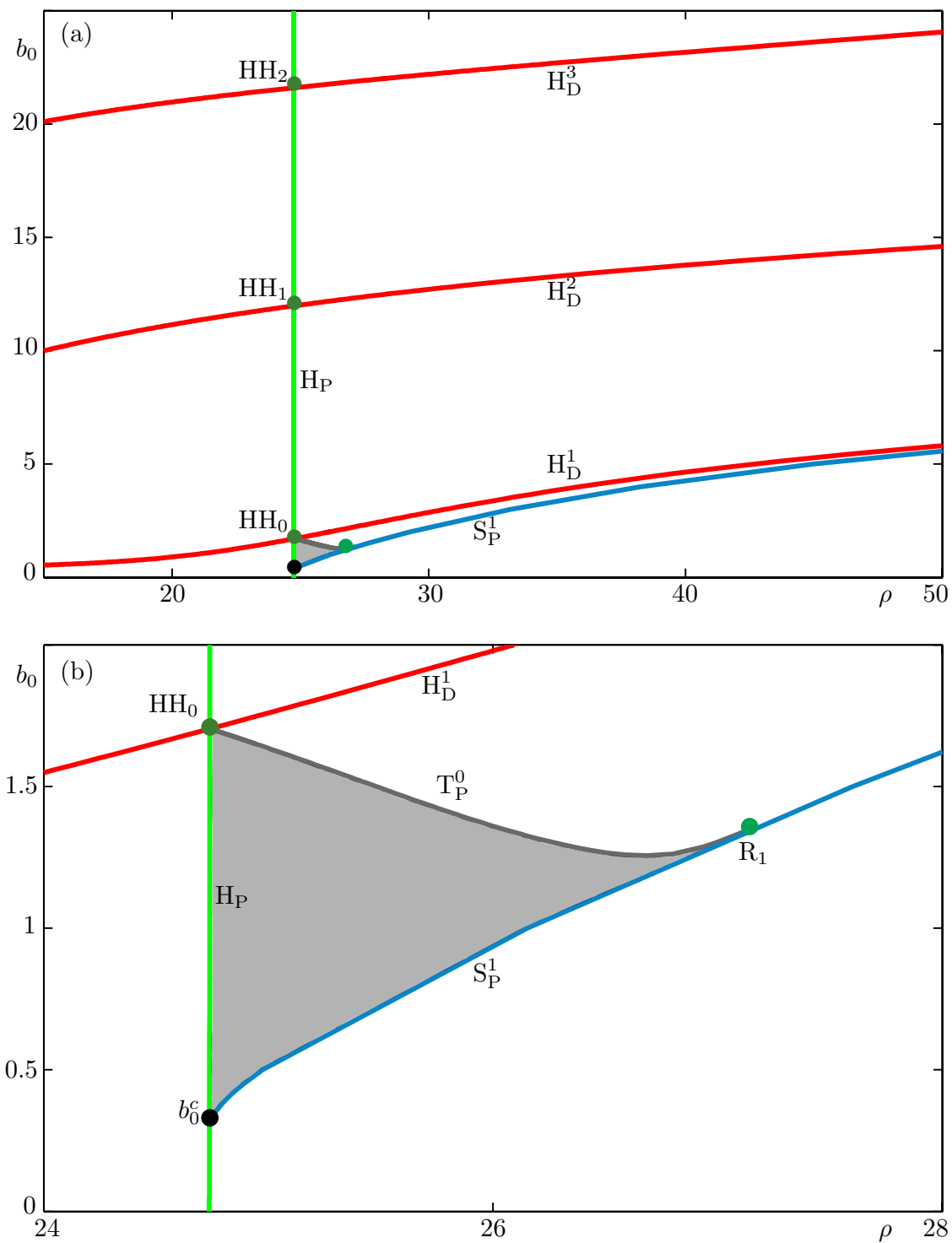


Figure 4.14: Bifurcation set in the (ρ, b_0) -plane of (4.0.5) for the constant-period case. Shown are the Hopf bifurcation curve H_P (green) and the delay-induced Hopf bifurcation curves H_D^1 , H_D^2 and H_D^3 (red). Also shown are the double Hopf bifurcation points HH_0 , HH_1 and HH_2 (green). An enlargement of the overall domain of stability of Γ_C (shaded) is shown in (b). The torus bifurcation curve T_P^0 (grey) meets the SNLC bifurcation curve S_P^1 (blue) at the point R_1 . Other parameter values: $\sigma = 10$, $\alpha = \frac{8}{3}$ and $\eta = 2.8$.

Figure 4.14 shows the bifurcation set in the (ρ, b_0) -plane of (4.0.5) for the constant-period case. Note that the b_0 -ranges of Fig. 4.14 are the same as in Fig 4.12 but the ρ ranges are different. The Hopf bifurcation curve H_P (green) is the vertical curve at $\rho_H \approx 24.7368$. As all three cases are the same at ρ_H , the curve H_P is intersected by delay-induced Hopf bifurcation curves (red) at the same double Hopf bifurcation points HH_0 , HH_1 and HH_2 (green) as in the exact-period case. However, unlike in the exact-period case, the delay-induced Hopf bifurcations H_D^1 , H_D^2 and H_D^3 do not form distinct families. Figure 4.14(a) also shows the domain of stability of Γ_C (shaded).

The enlargement in Fig. 4.14(b) shows that the overall domain of stability of Γ_C exists to the right of the curve H_P in the (ρ, b_0) -plane. The left-hand boundary of the stability domain is the curve H_P between the points b_0^c and HH_0 . Its upper boundary is the torus bifurcation curve T_P^0 (black), which starts at the point HH_0 and ends on the SNLC bifurcation curve S_P^1 (blue) at the 1:1 resonance point R_1 . The lower boundary of the stability domain is the curve S_P^1 between the points b_0^c and R_1 .

As Γ_C is not stable in the same neighborhood of H_P as the target periodic orbit Γ_P , the constant-period case does not satisfy criterion (C). Thus, we conclude that keeping the period constant does not result in a successful form of control for the Lorenz case; this result agrees with our findings for the normal form case in chapter 2. In both cases control is not successful and the stability domain of Γ_C is topologically the same. In particular, it exists to the right of the curve H_P in the respective parameter planes.

4.4.2 The linear-period case

Figure 4.15 shows the one-parameter bifurcation diagram in ρ for $b_0 = 1.4$ for the linear-period case. It is shown in panel (a) in terms of its amplitude and in panel (b) in terms of the observed period T . Shown along the bottom axis of panel (a) is the equilibrium solution p^+ , which is stable when black and unstable when grey. From the Hopf bifurcation point H_P (green) bifurcates the stable branch of periodic orbits Γ_L , which exists for $\rho < \rho_H$. The branch Γ_L is only stable between H_P and the torus bifurcation point T_P^0 , where a complex conjugate pair of Floquet multipliers leave the unit circle. The branch ends at the delay-induced Hopf bifurcation H_D^1 . Whilst Γ_L is stable it has an amplitude very close to that of Γ_P ; compare with Γ_P (black) in Fig. 4.15(a). Figure 4.15(b) shows how the observed period T of Γ_L changes as ρ is varied. For reference the period of Γ_P (black) from 4.11(b) is also shown. Both Γ_P and Γ_L have period equal to 0.6528 at the Hopf bifurcation point H_P . The periods of Γ_P and Γ_L are almost identical whilst both branches

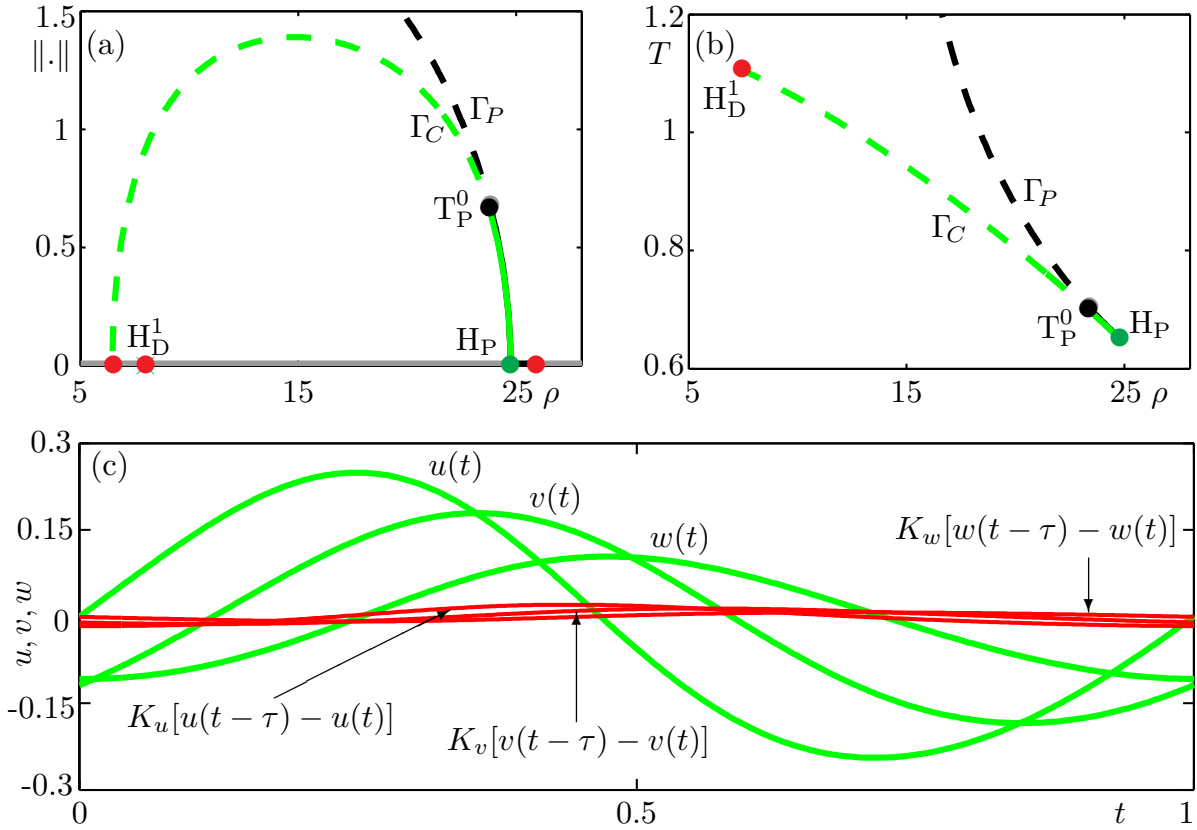


Figure 4.15: One-parameter bifurcation diagram in ρ for $b_0 = 1.4$ of (4.0.5) for the linear-period case, shown in terms of the amplitude in (a) and the period T in (b). The equilibrium p^+ is stable (unstable) when black (grey), it becomes stable at the Hopf bifurcation point H_P (green) from which bifurcates the branch of periodic orbits Γ_L (green). Also shown are the delay-induced Hopf bifurcation points H_D^1 (red) and the torus bifurcation point T_P^0 (black). For reference the branch of periodic orbits Γ_P (black) from Fig. 4.11 is also shown. Solid (dashed) curves indicate stable (unstable) periodic orbits. Panel (c) shows the u, v and w components of the solution profile (green) of the stable periodic orbit Γ_C at $\rho = 25.5$ and $b_0 = 1.4$; the red curves are the solution profiles of the residual feedback components $K_u[u(t-\tau) - u(t)]$, $K_v[v(t-\tau) - v(t)]$ and $K_w[w(t-\tau) - w(t)]$. Other parameter values: $\sigma = 10$, $\alpha = \frac{8}{3}$ and $\eta = 2.8$.

are stable, that is, for $22.5 \lesssim \rho < \rho_H$. For $\rho \lesssim 22.5$, the periods diverge, with the period of Γ_P increasing quickly and going to infinity at $\rho = \rho_{\text{hom}}$. The period of Γ_L increases more gradually, reaching its maximum at the Hopf bifurcation point H_D^1 .

Figure 4.15(c) shows the solution profile (green) of the stable periodic orbit Γ_L at $\rho = 24$ and $b_0 = 1.4$, which is close to the torus bifurcation T_P^0 . Also shown are the residual control force components $K_u[u(t-\tau) - u(t)]$, $K_v[v(t-\tau) - v(t)]$, $K_w[w(t-\tau) - w(t)]$ (red), where $K_{u,v,w}$ is the feedback gain with respect to the variables u, v and w . Figure 4.15(c) shows that the residual control force is small; the maximum amplitude of $K_u[u(t-\tau) - u(t)]$ is approximately 4% of the amplitude of the maximum solution $u(t)$. We conclude that the linear-period case satisfies criteria (A) and (B) for successful stabilization.

Figure 4.16 is the bifurcation set in the (ρ, b_0) -plane of (4.0.5) for the linear-period case. Again, the ranges of b_0 shown in Fig. 4.16 are the same as in Figs. 4.12 and 4.14 but the ρ -ranges are different. Figure 4.16(a) shows that the curve H_P (green) is intersected by the delay-induced Hopf bifurcation curves H_D^1 , H_D^2 and H_D^3 at the points b_0^c , HH_0 , HH_1 and HH_2 . The curve H_D^1 resembles the curve H_L in the exact-period case; see Fig. 4.12. It has a point of self-intersection labelled HH_c . Also shown in Fig. 4.16(a) is the overall domain of stability of Γ_L (shaded).

The enlargement in Fig. 4.16(b) shows the domain of stability of Γ_L (shaded) in more detail. In particular, it shows that the stability domain exists entirely to the left of the curve H_P . The right-hand boundary of this domain is the curve H_P between the points b_0^c and HH_0 . The lower boundary of the stability domain is the curve H_D^1 between the points b_0^c and HH_c . Its upper boundary is the torus bifurcation curve T_P^0 (black), which starts at the point HH_0 and ends at the point HH_c .

The periodic orbit Γ_L only bifurcates stably between the points b_0^c and HH_0 . The criticality of H_P changes at b_0^c from subcritical below to supercritical above. Above HH_0 the criticality of H_P once again changes to being subcritical.

Comparing Figs. 4.12 and 4.16, we see that for $18 \lesssim \rho \lesssim 26$, the bifurcation set in the (ρ, b_0) -plane for the linear-period case resembles that for the exact-period case very closely. In particular, the stability domain in both cases exists entirely to the left of the curve H_P and its upper boundary is given by the torus bifurcation curve T_P^0 . There is the slight difference that in the linear-period case the lower boundary of the domain of stability is the Hopf bifurcation curve H_D^1 rather than a transcritical bifurcation curve as in the exact-period case. Nevertheless, we say that for the linear-period case criterion (C) for successful stabilization is fulfilled.

Therefore, the linear-period case satisfies all three stabilization criteria, and thus, we conclude that it constitutes a successful form of control for the Lorenz case; again this result agrees with that for the normal form case in chapter 2. Comparing the bifurcation sets of the two linear-period cases, shown in Fig. 4.16 and Fig. 3.7, we see that domain of stability of Γ_L in the Lorenz case closely agrees with that in the normal form case. There is the slight difference that in the Lorenz case the lower boundary of the stability domain is the Hopf bifurcation curve H_D^1 rather than the SNLC bifurcation curve S_P^2 in the normal form case. However, if we compare Fig. 4.16 with Fig. 3.8(c), which shows the domain of stability of Γ_L for a linear-period approximation with a shallower slope, we find that the stability domains in both cases are topologically the same.

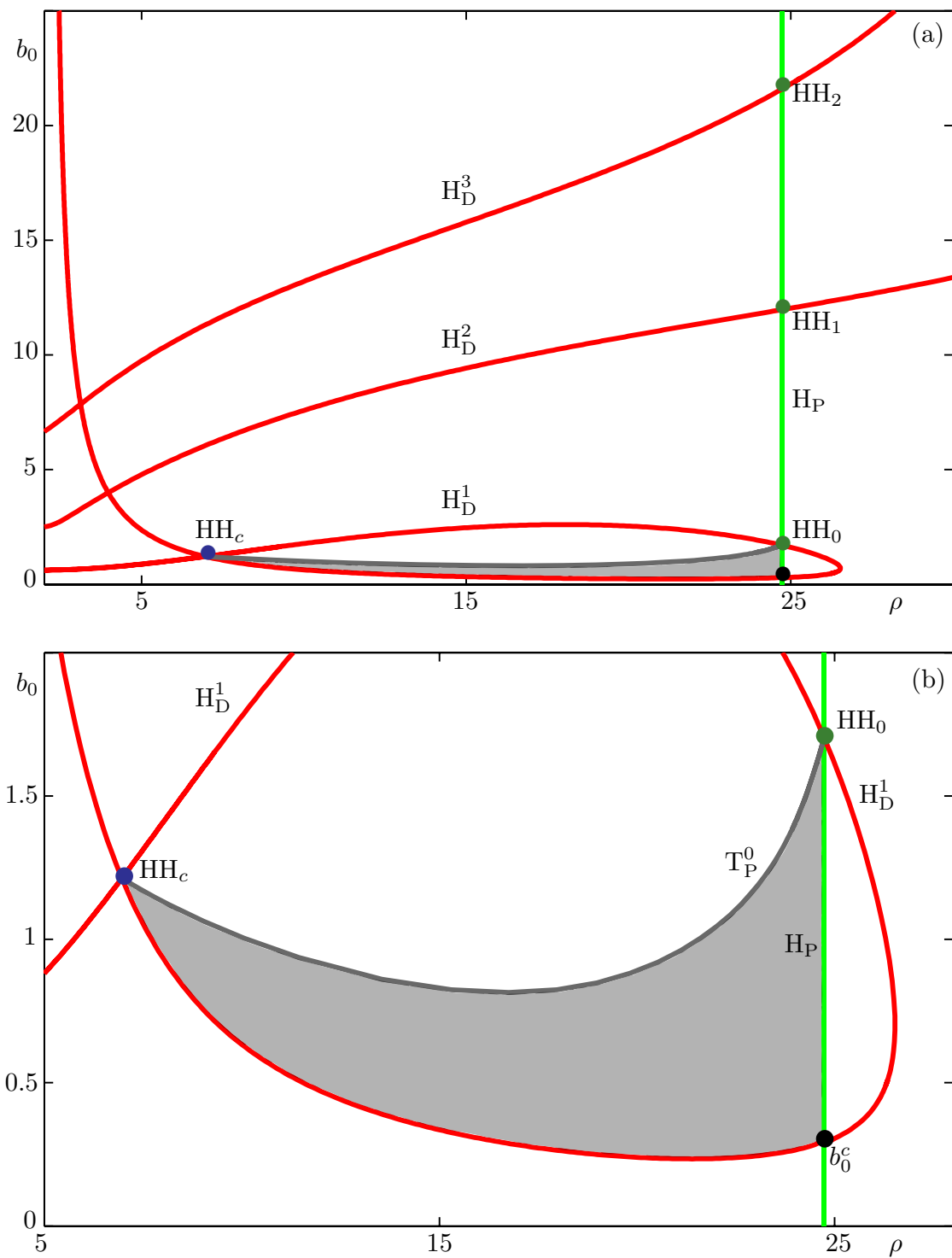


Figure 4.16: Bifurcation set in the (ρ, b_0) -plane of (4.0.5) for the linear-period case. Shown are the Hopf bifurcation curve H_P (green) and the delay-induced Hopf bifurcation curves H_D^1 , H_D^2 and H_D^3 (red). Also shown are the double Hopf bifurcation points HH_0 , HH_1 and HH_2 (green). An enlargement of the overall domain of stability of Γ_L (shaded) is shown in (b). The torus bifurcation curve T_P^0 (grey) meets the Hopf bifurcation curve H_D^1 (blue) at the point HH_c . Other parameter values: $\sigma = 10$, $\alpha = \frac{8}{3}$ and $\eta = 2.8$.

Overall, we have shown that the normal form case is predictive of the dynamics of the Lorenz case not only in the standard setup of Pyragas control (exact-period case) but also when there is a delay mismatch in the control scheme.

4.5 Conclusions

Our aim was to show that the global dynamics found in the normal form case can also be found in any system with Pyragas control near a subcritical Hopf bifurcation. Therefore, we considered as a specific example, the Lorenz equations subject to Pyragas time-delayed feedback control. Overall, we found that the normal form case is predictive, over a very large area of the relevant parameter plane, for global dynamics induced when Pyragas control is applied near a subcritical Hopf bifurcation. We have shown the existence of a further stable delay-induced periodic orbit in both the normal form and Lorenz cases. We have also shown that the normal form case is predictive of the dynamics induced when there is a delay mismatch in the system. This work can be interpreted as a considerable extension of that of Brown [14] who showed that the normal form case is predictive of the dynamics close to the subcritical Hopf bifurcation, where the target periodic orbit is born.

The analysis presented here does suggest that the predictiveness of the normal form depends on the parameter range over which the target periodic orbit exists and how it disappears. For example, in the Lorenz case the target periodic orbit does not exist for all ρ and disappears in a homoclinic bifurcation. As such, we found that the bifurcation set of the Lorenz case is a truncated version of the bifurcation set of the normal form case. In this regard, an important consideration is to make a choice for the feedback phase in the control term before transformation, in such a way that it matches the feedback phase in the normal form case. Future work will be focused on investigating other systems with periodic orbits that disappear in different bifurcations, to examine the predictiveness of the normal form case.

The results presented here are directly relevant for experiments as we have shown that the normal form case has a wider reach than just near the Hopf bifurcation H_P . Therefore, even if equations for the system are unknown, the user should be aware of the global dynamics of the normal form case. We expect differences in different experiments but, in general, all global features of the normal form case must be expected. Whether they all occur or not will depend on the system and, in particular, on the region of existence of the target periodic orbit and the mechanism of its disappearance.

5

The complex Ginzburg–Landau equation subject to Pyragas feedback control

5.1 Introduction

Understanding pattern formation in spatially extended non-equilibrium systems has been a research topic of great interest for a number of years. The existence of simple spatial or spatio-temporal patterns in such systems is well understood on the basis of equivariant bifurcation theory [30]. In certain systems these patterns can be unstable, in which case the system may reach a state of spatio-temporal chaos. Recently, there has been a large amount of research into schemes designed to control this spatio-temporal chaos, with the aim of realizing an otherwise unstable patterned state [2, 47, 75, 90, 98]. In nonlinear optics for example, Fourier filters have been used successfully to control spatio-temporal patterns [8, 54, 97]. Here, we consider time-delayed feedback control of the form suggested by Pyragas [69].

Socolar et al. [92] introduced a generalization of Pyragas time-delayed feedback control referred to as “extended time-delay autosynchronisation” (ETDAS). For a system $V(x, t)$, the ETDAS control scheme has a temporal feedback term of the form

$$\epsilon_V(x, t) = \kappa \sum_{n=0}^{\infty} R^n [V(x, t_n) - V(x, t_{n+1})], \quad (5.1.1)$$

where $t_n = t - n\tau$, $\kappa \in \mathbb{R}$ is the feedback gain and $R \in \mathbb{R}$ is a parameter chosen between 0 and 1. In [10], Bleich and Socolar apply the ETDAS control scheme to the supercritical cubic complex Ginzburg–Landau equation (CGLE) with one spatial variable. The CGLE is a partial differential equation (PDE) originally introduced to describe superconductivity. It also describes nonlinear waves, Rayleigh–Bérnard convection and a number of other phenomena. For more information on the CGLE see, for example [1, 18, 48] and the references therein. In [10] the authors found that the addition of feedback can stabilize unstable traveling wave solutions of the CGLE. In particular, the control scheme is successful even in parameter regimes where spatio-temporal chaos is found in the uncontrolled system.

In [33], Harrington and Socolar found that unstable traveling wave solutions of the two-dimensional (i.e. with two spatial independent variables) supercritical cubic CGLE could not be stabilized using the ETDAS control scheme. This is due to the existence of so-called torsion-free modes, that is, modes which have purely real Floquet multipliers. This result is based on the “odd-number limitation” developed by Nakajima [57], which states that a periodic orbit with an odd number of positive real Floquet multipliers cannot be stabilized by Pyragas control for any feedback gain value. Although the odd-number limitation has been disproved for periodic orbits [24] it is still relevant to hyperbolic equilibrium points. In [33] the analysis of the traveling wave solutions of the CGLE is reduced to an analysis of the stability of an equilibrium point, and therefore, the theory of Nakajima is still applicable.

Lu et al. [53] modified the original Pyragas time-delayed feedback control scheme to include a spatial feedback term, which takes into account the spatial periodicity of the targeted pattern. They applied a linear combination of time-delay and spatial feedback to the two-dimensional Maxwell-Bloch equations, describing the evolution of a complex electric field E of a laser system. The overall spatial feedback term applied in [53] is of the form,

$$F_S = \rho \{ [E(x + x_0, y, t) - E(x, y, t)] + [E(x, y + y_0, t) - E(x, y, t)] \}, \quad (5.1.2)$$

where, $\mathbf{g}_1 = (x_0, 0)$ and $\mathbf{g}_2 = (0, y_0)$ are translation vectors of the feedback. The feedback is non-invasive when the targeted pattern is periodic in both of the \mathbf{g}_j -directions with spatial periods $|\mathbf{g}_j|$ [64]. Using this modified Pyragas method, Lu et al. [53] were able to remove spatio-temporal chaos or optical turbulence from a three level laser system.

Montgomery and Silber [56] applied the modified Pyragas control scheme suggested in [53] to the supercritical cubic CGLE with one complex spatial variable, which is given by

$$\frac{\partial A}{\partial t} = A + (1 + ib_1)\nabla^2 A - (b_3 - i)|A|^2 A, \quad (5.1.3)$$

where $A = A(x, t) \in \mathbb{C}$ and $b_1, b_3 \in \mathbb{R}$; since the Hopf bifurcation is supercritical we require $b_3 > 0$. The aim of [56] was to stabilize traveling wave solutions of the CGLE (5.1.3) in the Benjamin–Feir regime, where all traveling wave solutions are unstable to long-wave perturbations. In [7], Benjamin and Feir analyzed the instability of periodic waves in deep water. This work was subsequently extended by Lange and Newell [49]. Specifically, the authors of [7, 49] found that all uniform oscillations ($k = 0$) of (5.1.3) are unstable if $b_1 > b_3 > 0$. The Benjamin–Feir instability is in fact a generalization of the Eckhaus instability [34].

The authors of [56] considered traveling wave solutions of the form $Re^{ikx+i\omega t}$, where R is the amplitude of the solution, k is the wavenumber and ω is its frequency. They analyzed the linear stability of these traveling wave solutions by considering the effect of small amplitude perturbations for some perturbation wavenumber q . The resulting linearised uncontrolled system has one eigenvalue that is always stable (negative real part) and one eigenvalue which has real part (for small q) given by

$$q^2 \left[\left(\frac{b_1}{b_3} - 1 \right) + \frac{2k^2}{b_3 R^2} \left(1 + \frac{1}{b_3^2} \right) \right] + O(q^3). \quad (5.1.4)$$

In the Benjamin–Feir regime where $b_1 > b_3 > 0$, (5.1.4) is positive for all k , and thus, the eigenvalue is unstable. In other words, long-wave (i.e small q) perturbations will grow.

In [56] the Pyragas feedback term takes the form

$$F = K[A(x, t) - A(x, t - \tau)] + \rho[A(x + \Delta x, t) - A(x, t)], \quad (5.1.5)$$

where the parameter K is the gain of the temporal feedback and ρ is the gain of the spatial feedback term. It should be noted that in [56] both K and ρ are taken as purely real parameters. The delay is set as $\tau = \frac{2\pi}{\omega}$ and the spatial shift is set as $\Delta x = \frac{2\pi}{|k|}$.

Montgomery and Silber found that traveling wave solutions of (5.1.3) can be stabilized using purely temporal feedback, and that there is an optimal level of feedback gain given by $K = -\frac{1}{\tau}$. That is, they found that one only need consider $K = -\frac{1}{\tau}$ to determine if the target traveling wave can be stabilized by temporal feedback.

The analysis presented in [56] was extended to the supercritical CGLE with two spatial independent variables by Postlethwaite and Silber [64]. These authors also extend the result of [33] by showing that the addition of spatial feedback allows for the stabilization of traveling wave solutions for all perturbation wavevectors q . In particular, [64] describes how the spatial feedback terms Δx_j must be chosen in two dimensions to ensure that the control remains non-invasive and to select the direction of the targeted traveling wave solutions. Furthermore, they show that if Δx_j are chosen appropriately, then the optimal level of temporal feedback gain $K = -\frac{1}{\tau}$ derived in [56] for the one-dimensional CGLE, is also the optimal level for the two-dimensional CGLE.

Here we aim to extend the results of [56] to the *subcritical* cubic CGLE with one spatial variable. That is, we perform a linear stability analysis of the traveling wave solutions of the system and attempt to stabilize the equilibrium of the linearized system for all perturbation wavenumbers q . Our aim is to remove the instability associated with the subcriticality of the CGLE. We do not investigate the existence of any Benjamin–Feir-type instability in the system. We find that traveling wave solutions of the subcritical cubic CGLE with one spatial variable cannot be stabilized for all q with the modified Pyragas control scheme. In particular, we show that the linearized system always has an unstable eigenvalue for the perturbation wavenumber $q = 0$. This result is proved analytically for the case of purely real temporal feedback gain. We conjecture that the same is true of the case where temporal feedback gain is complex and we provide numerical evidence to support this theory.

This chapter is organized as follows. Section 5.2 presents a linear stability analysis of the subcritical CGLE, firstly without feedback and then with feedback. In section 5.3 we consider the stability of traveling wave solutions of the subcritical CGLE when purely spatial feedback is applied. In sections 5.4 and 5.5, we consider the effects of temporal feedback, firstly, with a real feedback gain, and secondly, with a complex feedback gain. Section 5.6 contains a discussion and conclusions.

5.2 Linear stability analysis

The subcritical cubic CGLE with one complex spatial variable is an amplitude equation that describes a disturbance $\hat{A}(\hat{x}, \hat{t}) \in \mathbb{C}$ in a spatially extended system close to the onset of a Hopf bifurcation; it is given by

$$\frac{\partial \hat{A}}{\partial \hat{t}} = (c_0 - ic_1)\hat{A} + (c_2 - ic_3)\nabla^2 \hat{A} + (c_4 - ic_5)|\hat{A}|^2 \hat{A}. \quad (5.2.1)$$

As we consider a subcritical Hopf bifurcation we assume $c_4 > 0$, and to avoid backward diffusion $c_2 > 0$. Equation (5.2.1) can be rescaled to a form similar to that of (5.1.3) as follows [34]. We first apply the transformation $\hat{A} \rightarrow \hat{A}e^{-ic_1 t}$ to give

$$\frac{\partial \hat{A}}{\partial \hat{t}} = c_0 \hat{A} + (c_2 - ic_3)\nabla^2 \hat{A} + (c_4 - ic_5)|\hat{A}|^2 \hat{A}. \quad (5.2.2)$$

We then rescale the amplitude $\hat{A} = \sqrt{\left(\frac{c_0}{c_5}\right)}A$ and apply the coordinate transformation $x = \sqrt{\left(\frac{c_0}{c_2}\right)}\hat{x}$ and $t = c_0\hat{t}$, which gives

$$\nabla^2 \hat{A} = \left(\frac{c_0}{c_2}\right) \nabla^2 A \text{ and } \frac{\partial \hat{A}}{\partial \hat{t}} = c_0 \frac{\partial A}{\partial t}.$$

Substituting these terms into (5.2.2) gives

$$\frac{\partial A}{\partial t} = A + \left(1 - i\frac{c_3}{c_2}\right) \nabla^2 A + \left(\frac{c_4}{c_5} - i\right) |A|^2 A. \quad (5.2.3)$$

Let $b_1 = -\frac{c_3}{c_2}$ and $b_3 = \frac{c_4}{c_5}$ to give

$$\frac{\partial A}{\partial t} = A + (1 + ib_1)\nabla^2 A + (b_3 - i)|A|^2 A. \quad (5.2.4)$$

Here, b_1 and b_3 are real parameters and since we consider the case of a subcritical Hopf bifurcation, the parameter b_3 is positive. We again consider traveling wave solutions of the form

$$A = Re^{ikx+i\omega t}, \quad (5.2.5)$$

where R is the amplitude of the solution and ω is its frequency. The amplitude R and frequency ω are linked by the wavenumber k through the following dispersion relations

$$\begin{aligned} R^2 &= \frac{k^2 - 1}{b_3}, \\ \omega &= -b_1 k^2 - R^2. \end{aligned} \quad (5.2.6)$$

As b_3 is positive, the wavenumber satisfies $|k| > 1$. We calculate the linear stability of the traveling wave solution by considering small-amplitude perturbations for a perturbation wavenumber q . We substitute the ansatz

$$A = R e^{ikx + i\omega t} (1 + a_+(t) e^{iqx} + a_-(t) e^{-iqx}) \quad (5.2.7)$$

into (5.2.4) and linearize in a_+ and a_- . This gives the following system of ordinary differential equations (ODEs) in the complex variables a_+ and a_-^* (the complex conjugate of a_-),

$$\frac{d}{dt} \begin{pmatrix} a_+(t) \\ a_-^*(t) \end{pmatrix} = \begin{pmatrix} -2kq d_1 - q^2 d_1 + d_2 R^2 & d_2 R^2 \\ d_2^* R^2 & 2kq d_1^* - q^2 d_1^* + d_2^* R^2 \end{pmatrix} \begin{pmatrix} a_+(t) \\ a_-^*(t) \end{pmatrix}, \quad (5.2.8)$$

such that $d_1 = 1 + ib_1$, $d_2 = b_3 - i$. The characteristic equation of system (5.2.8) is

$$\begin{aligned} &\phi^2 + [-2b_3 R^2 + (4ikb_1)q + 2q^2]\phi \\ &+ [(-i4kR^2(1 + b_1 b_3))q + (-4k^2(1 + b_1^2) - 2R^2(b_3 - b_1))q^2 + (1 + b_1^2)q^4] = 0. \end{aligned} \quad (5.2.9)$$

The eigenvalues of (5.2.8) are thus

$$\phi_{1,2} = \frac{(2b_3 R^2 - (4ikb_1)q - 2q^2) \pm \sqrt{D}}{2}, \quad (5.2.10)$$

where

$$D = [4b_3^2 R^4 + (i16kR^2)q + (16k^2 - 8R^2 b_1)q^2 + (i16kb_1)q^3 - 4b_1^2 q^4]. \quad (5.2.11)$$

Ignoring higher-order terms in q the expansion of the square root of the discriminant D is

$$\sqrt{D} = 2b_3R^2 \left[1 + \frac{2ikq}{b_3^2R^2} - \frac{b_1q^2}{b_3^2R^2} + \frac{2k^2q^2}{b_3^2R^4} + \frac{2k^2q^2}{b_3^4R^4} \cdots \right]. \quad (5.2.12)$$

Thus, for small q system (5.2.8) has one eigenvalue with real part given by

$$\phi_1 = 2(k^2 - 1) + \left[- \left(1 + \frac{b_1}{b_3} \right) + \frac{2k^2}{b_3R^2} \left(1 + \frac{1}{b_3^2} \right) \right] q^2 + O(q^3). \quad (5.2.13)$$

and one eigenvalue with real part given by

$$\phi_2 = \left[- \left(1 - \frac{b_1}{b_3} \right) - \frac{2k^2}{b_3R^2} \left(1 + \frac{1}{b_3^2} \right) \right] q^2 + O(q^3). \quad (5.2.14)$$

Note that for $b_1/b_3 < 1$ the eigenvalue ϕ_2 is always less than or equal to zero for small q . When $q = 0$ the eigenvalue ϕ_1 given by (5.2.13) is equal to $2(k^2 - 1)$, which is always positive as, from the dispersion relation (5.2.6), $|k| > 1$. The eigenvalue ϕ_2 given by (5.2.14) is equal to zero at $q = 0$.

Figure 5.1 shows how the real part of the two eigenvalues of (5.2.8) changes as q is increased for $k = 1.8$, $b_1 = 2.5$ and $b_3 = 2$. When q is large enough, that is, the perturbations are sufficiently short wave, both eigenvalues are stable.

In this chapter we focus primarily on the instability at $q = 0$. Since we consider control successful only if the traveling wave is stabilized for all perturbation wavenumbers q , it is sufficient to show that Pyragas control is not successful overall by showing that it cannot remove the instability at $q = 0$.

We apply the modified Pyragas control scheme of the form suggested in [53, 56] to (5.2.4) to give

$$\frac{\partial A}{\partial t} = A + (1 + ib_1)\nabla^2 A + (b_3 - i)|A|^2 A + F, \quad (5.2.15)$$

where

$$F = K[A(x, t) - A(x, t - \tau)] + \rho[A(x + \Delta x, t) - A(x, t)]. \quad (5.2.16)$$

Again $\rho \in \mathbb{R}$ is the gain of the spatial feedback term and K is the gain of the temporal feedback. In this chapter we consider temporal feedback gain of the form

$$K = b_0 e^{i\beta}. \quad (5.2.17)$$

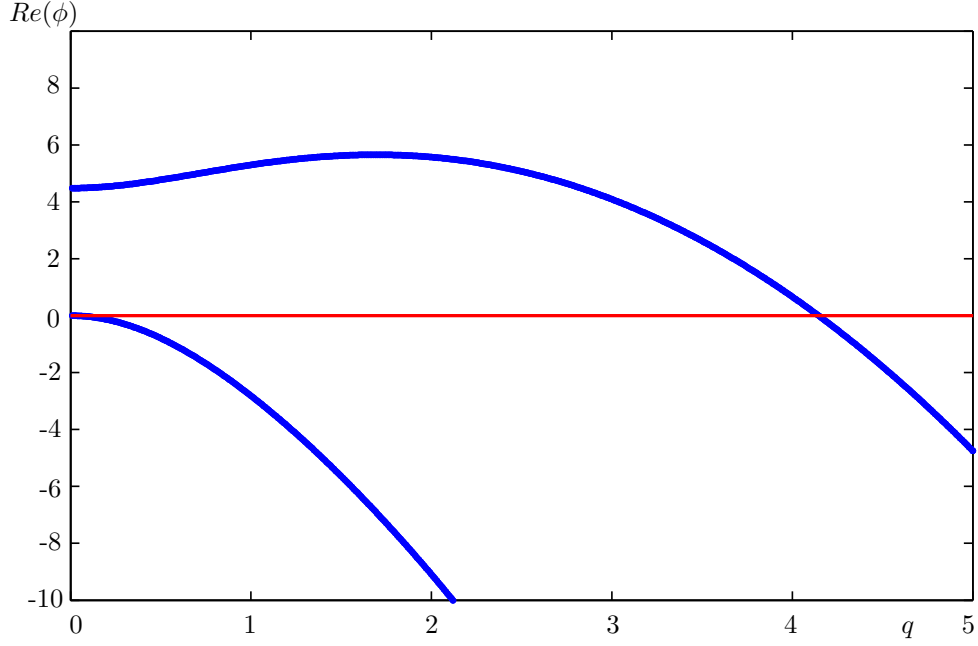


Figure 5.1: The blue curves are the real part of the two eigenvalues of (5.2.18) without feedback as the parameter q is increased. The horizontal red line is where the real part of the eigenvalues is equal to zero. Other parameter values: $k = 1.8, b_1 = 2.5, b_3 = 2$.

where $b_0 \in \mathbb{R}$ is the feedback strength and β is the 2π -periodic feedback phase. We consider both the case when the temporal feedback gain is real, $\beta = 0$, and the case when temporal feedback is complex. It should be noted that if a solution $A(x, t)$ is temporally periodic with period $T = \frac{\tau}{n}$ ($n \in \mathbb{Z}$) and spatially periodic with period $S = \frac{\Delta x}{m}$ ($m \in \mathbb{Z}$), the feedback vanishes on the target, and therefore, the control is non-invasive. Thus, for a targeted traveling wave with wavenumber k and frequency ω the delay τ is set as $\frac{2\pi}{|\omega|}$ (assuming $\omega \neq 0$) and the spatial shift is set as $\Delta x = \frac{2\pi}{k}$. Throughout our analysis we fix the delay and spatial shift as these functions. Note that the delay and spatial shift cannot be set independently as they are related through the dispersion relation (5.2.6).

We substitute the ansatz (5.2.7) into the system with feedback (5.2.15). This now gives the following system of DDEs in a_+ and a_-^* (the complex conjugate of a_-),

$$\frac{d}{dt} \begin{pmatrix} a_+(t) \\ a_-^*(t) \end{pmatrix} = J \begin{pmatrix} a_+(t) \\ a_-^*(t) \end{pmatrix} + K \left[\begin{pmatrix} a_+(t) \\ a_-^*(t) \end{pmatrix} - \begin{pmatrix} a_+(t - \tau) \\ a_-^*(t - \tau) \end{pmatrix} \right], \quad (5.2.18)$$

where

$$J = \begin{pmatrix} -2kqd_1 - q^2d_1 + d_2R^2 + \rho(e^{iq\Delta x} - 1) & d_2R^2 \\ d_2^*R^2 & 2kqd_1^* - q^2d_1^* + d_2^*R^2 + \rho(e^{iq\Delta x} - 1) \end{pmatrix} \quad (5.2.19)$$

and $d_1 = 1 + ib_1, d_2 = b_3 - i$. The matrix J has eigenvalues m_1 and m_2 such that $Re(m_1) > Re(m_2)$. In the rest of this chapter we consider the controlled system (5.2.18) and analyze the effects of spatial and temporal feedback.

5.3 Spatial feedback in one-dimension

In this section we consider (5.2.18) with purely spatial feedback, that is, $\rho \neq 0$ and $K = b_0 = 0$. We start by reviewing a result from [56] for the supercritical CGLE (5.1.3). In [56] Montgomery and Silber showed that the addition of spatial feedback adds the term $\rho(\cos(q\Delta x) - 1)$ to the real part of the two eigenvalues of (5.1.3). Recall that, to ensure that the feedback is non-invasive in the one-dimensional system, the spatial shift term Δx is set to $\frac{2\pi}{k}$. Therefore, when the perturbation wavenumber q is an integer multiple of the wavenumber k , the term $\rho(\cos(q\frac{2\pi}{k}) - 1) = 0$. Moreover, this term is also equal to zero when $q = 0$.

The spatial feedback term applied here for the linearized system (5.2.18) is the same as in the supercritical case. Thus, the real part of the eigenvalues m_1 and m_2 of the matrix J in (5.2.19) are the same as the real part of the eigenvalues ϕ_1 and ϕ_2 in uncontrolled system (5.2.8), but with the added term $\rho(\cos(q\Delta x) - 1)$. Hence, the real part of the eigenvalues of J are

$$\begin{aligned} Re(m_1) &= Re(\phi_1) + \rho(\cos(q\Delta x) - 1) \\ Re(m_2) &= Re(\phi_2) + \rho(\cos(q\Delta x) - 1) \end{aligned} \tag{5.3.1}$$

Therefore, as with the supercritical case in [56], when q is zero or a multiple of k the spatial feedback term is zero and the spatial control switches off. When this happens the real part of the eigenvalues is the same as without feedback, that is $m_1 = \phi_1$ and $m_2 = \phi_2$. In particular, the unstable eigenvalue at $q = 0$ is still given by $m_1 = \phi_1 = 2(k^2 - 1)$.

Figure 5.2 shows the real part of the two eigenvalues of (5.2.18) as q is changed for $\rho = 10, k = 1.8, b_1 = 2.5$ and $b_3 = 2$. The dashed curve shows the leading eigenvalue from Fig. 5.1 for the system (5.2.18) without feedback. Figure 5.2 shows that the unstable eigenvalue is stabilized for some values of q but for $q = 0, q = 1.8$ and $q = 3.6$, that is, where q is an integer multiple of k , the eigenvalue becomes unstable again. At these points the eigenvalues m_1 and m_2 are the same as the eigenvalues ϕ_1 and ϕ_2 of the uncontrolled system (5.2.8). This switching on and off the feedback results in the oscillatory pattern visible in Fig. 5.2. As in the case with no feedback, the unstable eigenvalue does eventually

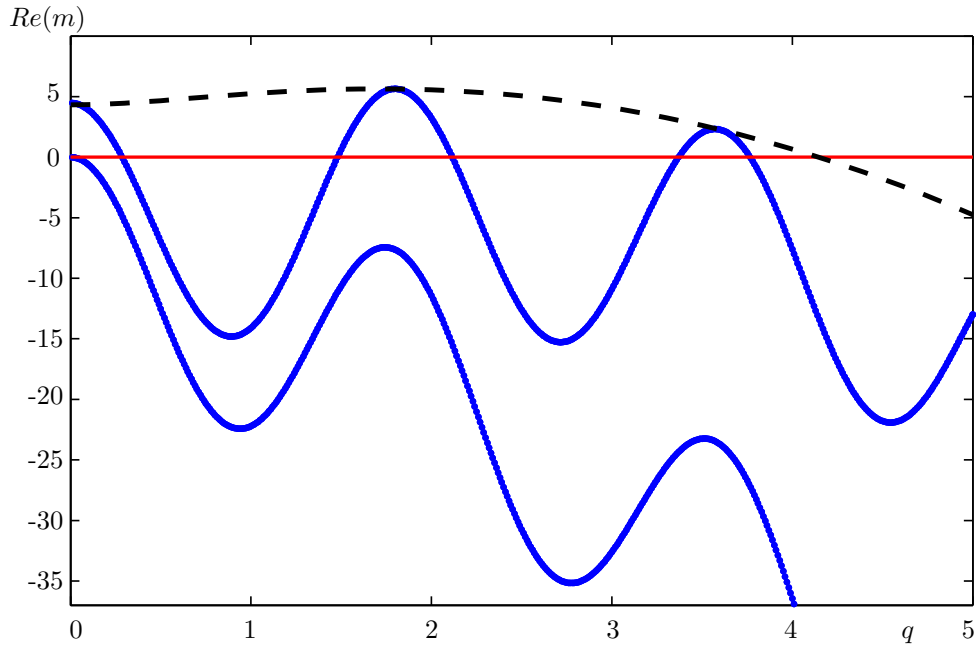


Figure 5.2: The blue curves are the real part of the two eigenvalues of (5.2.18) for $\rho = 10$ as the parameter q is increased. The horizontal red line is where the real part of the eigenvalues is equal to zero. The dashed black curve is the real part of the leading eigenvalue of 5.2.18 without feedback as in Fig. 1. Other parameter values: $k = 1.8, b_1 = 2.5, b_3 = 2, b_0 = 0$.

become stable with sufficiently short-wave perturbation wavenumber q . However, spatial feedback alone is not sufficient to stabilize traveling wave solutions of (5.2.15) for all perturbation wavenumbers q .

5.4 Temporal feedback with real feedback gain

We now consider system (5.2.18) with purely temporal feedback with a real feedback gain, that is, $K = b_0 \neq 0$, and $b_0 \in \mathbb{R}$. Throughout this section we restrict our analysis of (5.2.18) to the case where $q = 0$.

To analyze the effect of the temporal feedback we first diagonalize the matrix J (5.2.19) and change coordinates in the manner suggested in [64]. This gives

$$\begin{aligned}\dot{\alpha}_1(t) &= m_1 \alpha_1(t) + b_0(\alpha_1(t) - \alpha_1(t - \tau)), \\ \dot{\alpha}_2(t) &= m_2 \alpha_2(t) + b_0(\alpha_2(t) - \alpha_2(t - \tau)),\end{aligned}\tag{5.4.1}$$

where $\alpha_{1,2}$ are the transformed variables, that is, they are linear combinations of a_+ and a_-^* . Again the terms m_1 and m_2 are the eigenvalues of the matrix J , such that $Re(m_1) >$

$Re(m_2)$. Note that the change of coordinates associated with the diagonalization of J does not affect the Pyragas feedback terms. This is explained as follows. The system (5.2.18) can be written as

$$\dot{X} = JX + b_0X_\tau, \quad (5.4.2)$$

where

$$X = \begin{pmatrix} a_+(t) \\ a_-^*(t) \end{pmatrix} \text{ and } X_\tau = \left[\begin{pmatrix} a_+(t) \\ a_-^*(t) \end{pmatrix} - \begin{pmatrix} a_+(t-\tau) \\ a_-^*(t-\tau) \end{pmatrix} \right]. \quad (5.4.3)$$

The matrix J is diagonalized by the transformation $J = PDP^{-1}$, where D is the diagonal matrix of eigenvalues m_1 and m_2 . Substituting $J = PDP^{-1}$ into (5.4.2) results in the coordinate transformation $Y = P^{-1}X$. Therefore, the system given in terms of Y is

$$\begin{aligned} \dot{Y} &= P^{-1}\dot{X} = P^{-1}(PDP^{-1}PY + b_0Y_\tau), \\ \dot{Y} &= DY + b_0Y_\tau, \end{aligned} \quad (5.4.4)$$

which is of the same form as (5.4.2).

We now consider the case when $q = 0$. Recall that for $q = 0$ the spatial feedback term vanishes and so the eigenvalue m_1 in (5.4.1) is the same as in the uncontrolled system, that is, $m_1 = \phi_1 = 2(k^2 - 1)$. The characteristic equation associated with the solution $\alpha_1(t) = e^{\psi_1 t}$ of (5.4.1) is

$$\psi_1 = m_1 + b_0(1 - e^{-\psi_1 \tau}), \quad (5.4.5)$$

where $\psi_1 = \mu + i\nu$. Equation (5.4.5) has infinitely many solutions, one of which is purely real, i.e. $\nu = 0$. This eigenvalue is the solution of $f(\mu) = \mu$ where

$$f(\mu) = 2(k^2 - 1) + b_0(1 - e^{-\mu \tau}). \quad (5.4.6)$$

Recall that $2(k^2 - 1) > 0$ and $\tau > 0$. We claim that equation (5.4.6) always has a positive solution regardless of the sign of b_0 . If $b_0 > 0$ and $\mu > 0$, the continuous function $f(\mu)$ is increasing and $f(0) = 2(k^2 - 1) > 0$. It has a horizontal asymptote at $f(\mu) = b_0 > 0$. Thus, for μ large enough, $f(\mu) < \mu$ and, therefore, since $f(\mu)$ is continuous there must be a $\mu > 0$ for which $f(\mu) = \mu$. Hence, there will always be an unstable eigenvalue. If $b_0 < 0$ and $\mu > 0$, the function $f(\mu)$ is decreasing and again $f(0) = 2(k^2 - 1) > 0$. It

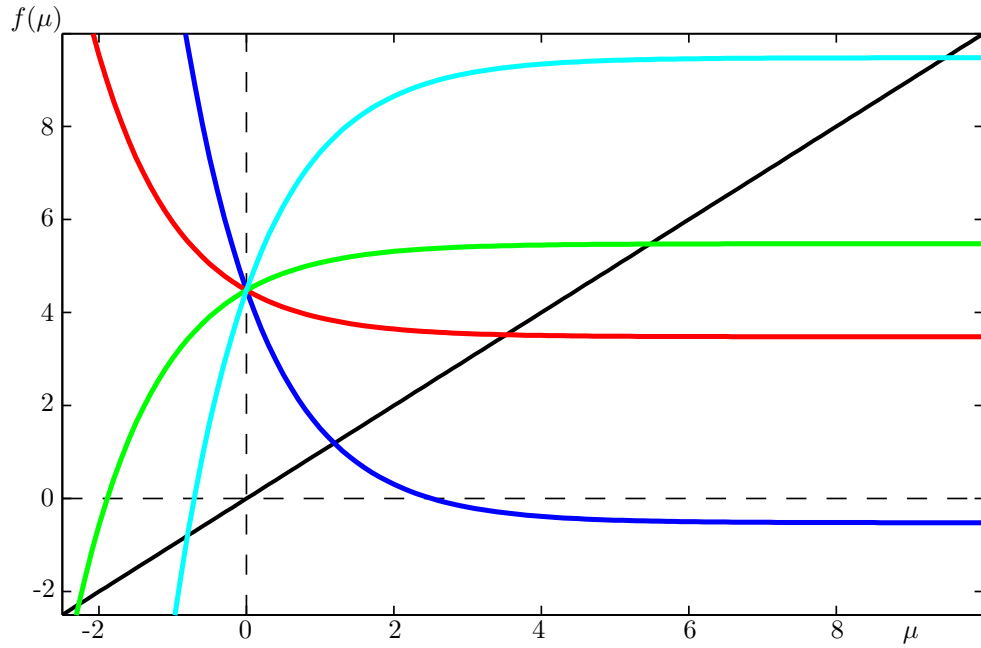


Figure 5.3: The function $f(\mu)$ for $b_0 = 5$ (cyan), $b_0 = \frac{1}{\tau}$ (green), $b_0 = -\frac{1}{\tau}$ (red) and $b_0 = -5$ (blue). The dashed horizontal and vertical black lines are at $f(\mu) = 0$ and $\mu = 0$ respectively, the solid black line is where $f(\mu) = \mu$. Other parameter values: $k = 1.8, b_1 = 2.5, b_3 = 2, q = 0, \rho = 0$.

again has a horizontal asymptote at $f(\mu) = b_0 < 0$. Again, for μ large enough, $f(\mu) < \mu$ and, therefore, since $f(\mu)$ is continuous there must be a $\mu > 0$ for which $f(\mu) = \mu$. The function is, therefore, positive for small positive μ ; specifically, it is positive for

$$0 < \mu < -\frac{\ln(1 + \frac{2(k^2 - 1)}{b_0})}{\tau}.$$

The function $f(\mu)$ will always intersect the line $\mu = f(\mu)$ in this interval and, thus, there is always a positive solution and, therefore, an unstable eigenvalue.

Figure 5.3 shows this result for four different choices of feedback gain: $b_0 = -5$ (blue), $b_0 = 5$ (cyan), $b_0 = 1$ (green) and $b_0 = -1$ (red). For each value of b_0 there is an intersection between the curve $f(\mu)$ and the line $\mu = f(\mu)$ (black) in the first quadrant of the $(\mu, f(\mu))$ -plane, indicating a positive solution.

We have shown that for any real b_0 , system (5.2.18) always has an unstable eigenvalue, specifically when $q = 0$. Thus, temporal feedback with real feedback gain cannot stabilize traveling wave solutions of (5.2.15). Note that we only consider $\tau > 0$; if $\tau < 0$ then (5.2.18) would be an advanced equation rather than a delay equation, analysis of which is beyond the scope of this work.

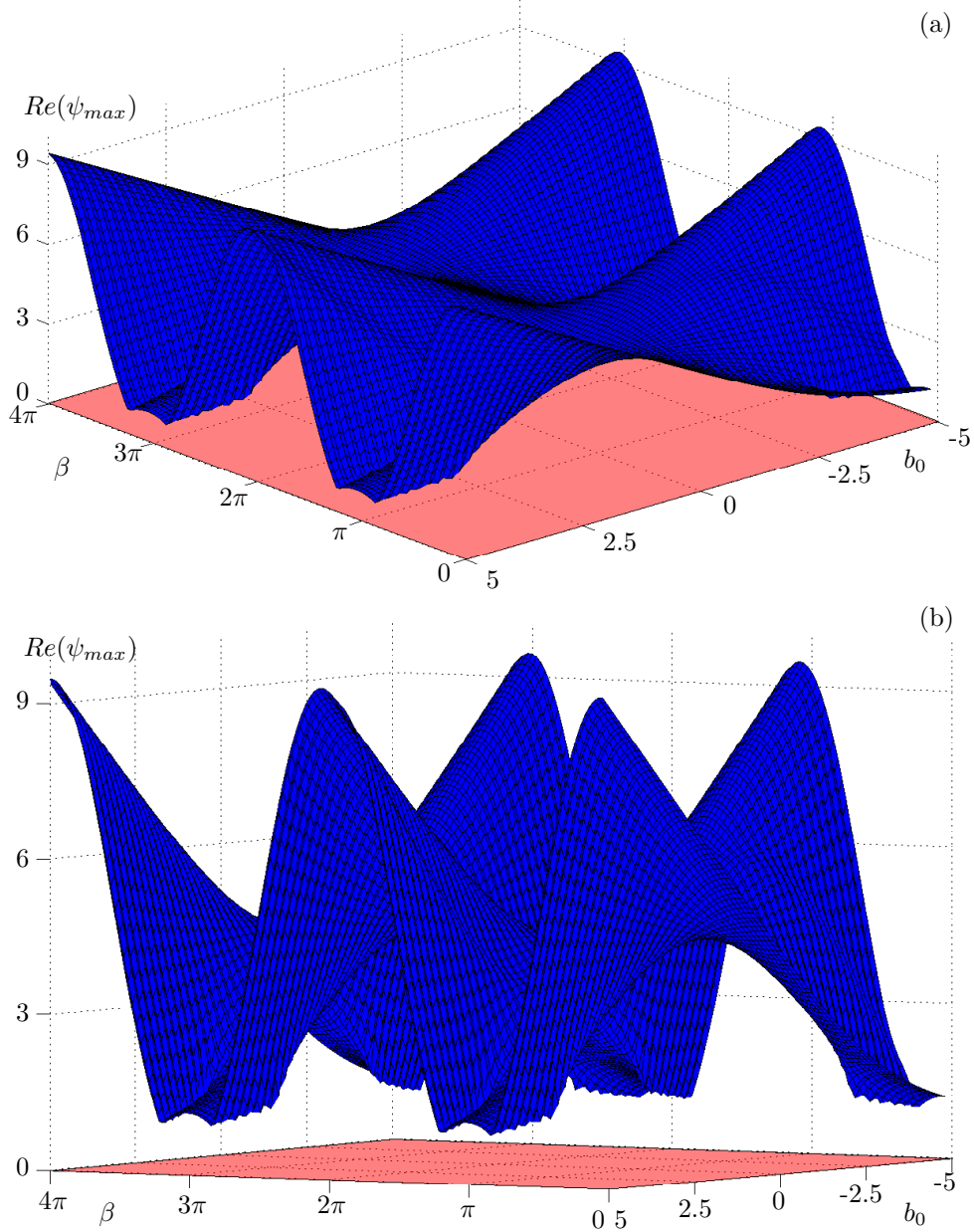


Figure 5.4: The surface of the real part of the leading complex conjugate pair of eigenvalues of (5.2.18) for temporal feedback with complex feedback gain for a range of the parameters b_0 and β ; shown in different perspectives in panels (a) and (b), together with the (red) zero plane. Other parameter values: $k = 1.8, b_1 = 2.5, b_3 = 2, q = 0, \rho = 0$.

5.5 Temporal feedback with complex feedback gain

In this section we consider system (5.2.18) with complex temporal feedback gain $K = b_0 e^{i\beta}$, where b_0 is the strength of the feedback and β is the 2π -periodic feedback phase. This is a more natural choice of feedback gain as all the coefficients and the variable in

the CGLE are complex. Furthermore, it has been shown in other applications of Pyragas control [13, 65] that stabilization of the target solution is not possible with a purely real feedback gain. Similarly to the previous section, we restrict our analysis of (5.2.18) to the case where $q = 0$, for which the spatial feedback term vanishes. In contrast to the case in the previous section, the eigenvalue ψ_1 of (5.2.18) with the largest real part is now complex (one of a complex conjugate pair of eigenvalues). It satisfies

$$\psi_1 = m_1 + b_0 e^{i\beta} (1 - e^{-\psi_1 \tau}), \quad (5.5.1)$$

where $\psi_1 = \mu + i\nu$ and again m_1 is the eigenvalue with the largest positive real part of the matrix J . Setting $q = 0$ and splitting (5.5.1) into real and imaginary parts yields

$$\begin{aligned} \mu &= 2(k^2 - 1) + b_0(\cos(\beta) - e^{-\mu\tau} \cos(\beta) \cos(\nu\tau) - e^{-\mu\tau} \sin(\beta) \sin(\nu\tau)), \\ \nu &= b_0 e^{-\mu\tau} (\cos(\beta) \sin(\nu\tau) - \sin(\beta) \cos(\nu\tau)). \end{aligned} \quad (5.5.2)$$

Proving that there is always an unstable eigenvalue at $q = 0$ from (5.5.2) is difficult. Instead, we use DDE-Biftool to continue the equilibrium solution with its stability information (in the form of the leading 100 eigenvalues) in the parameters b_0, β, b_1, b_3 and k , whilst maintaining the parameter restrictions $k > 1$ and $b_3 > 0$. In this process, we fix $q = 0$ and continue the equilibrium solution of (5.2.18) in a chosen parameter. We stop the continuation when the real part of the leading pair of eigenvalues is closest to zero and then continue from this point in a different parameter. As is presented next, we find that the real part of the leading eigenvalue appears to be always positive. Hence, we conjecture that the control scheme cannot successfully stabilize the targeted traveling wave solution.

We start with continuation in the temporal feedback parameters b_0 and β . The surface in Fig. 5.4(a) shows the real part of the leading complex conjugate pair of eigenvalues $Re(\psi_{max})$ of (5.2.18) against the feedback parameters b_0 and β . The red plane is where $Re(\psi_{max}) = 0$. The blue surface is found from a series of continuations of the equilibrium solution and its eigenvalues in the parameters β and b_0 . The other parameters are fixed as $k = 1.8$, $b_1 = 2.5$ and $b_3 = 2$. From the continuation data we find by a post-processing step the leading complex conjugate pair of eigenvalues of the equilibrium and then plot it for the respective value of β and b_0 . Therefore, the surface shown in Fig. 5.4(a) is not a continuation of a single eigenvalue, but rather, different sections of the surface may correspond to different eigenvalues with switch-over points between them. In other words, where two relevant branches of eigenvalues cross, meaning there are two eigenvalues with

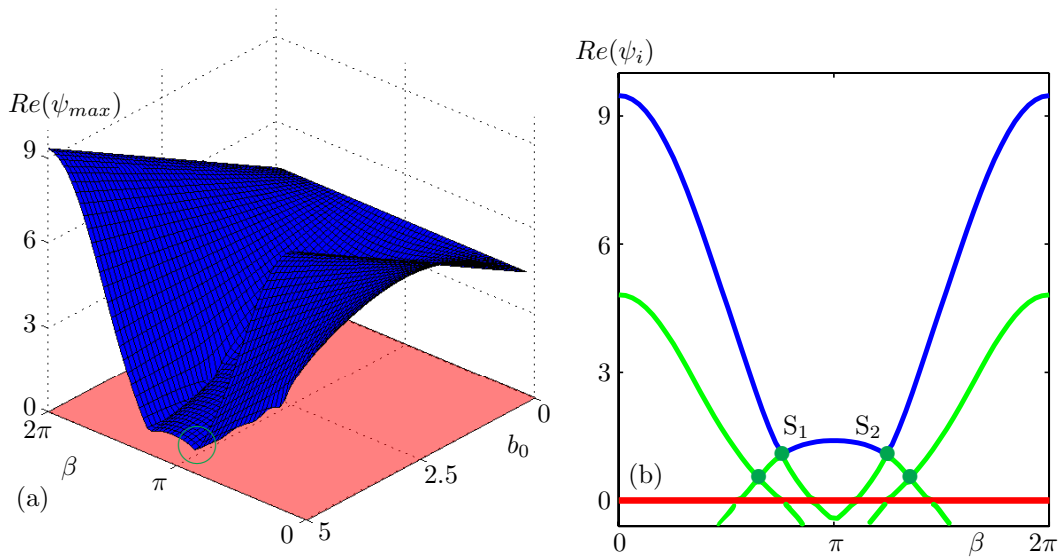


Figure 5.5: Panel (a) shows a part of the surface from Fig. 5.4(a) for $0 < \beta < 2\pi$ and $0 < b_0 < 5$. Panel (b) is the corresponding slice through the surface at $b_0 = 5$, which shows the real part of the leading eigenvalue $Re(\psi_{max})$ (blue) and the real parts of additional eigenvalues (green) of (5.2.18). The green dots indicate switch-over points between different eigenvalues. Other parameter values: $k = 1.8, b_1 = 2.5, b_3 = 2, q = 0, \rho = 0$.

equal largest real part, we switch to plot the increasing branch of eigenvalues. This is why the surface is not smooth everywhere, and points on the surface where there is discontinuous derivative correspond to switch-over points of eigenvalues.

The surface of the eigenvalue with largest real part in Fig. 5.4(a) is 2π -periodic in β . This is most easily seen by following the edge of the surface along the β -axis. Figure 5.4(b) shows the same surface but from a different perspective. Here we clearly see that the surface never intersects the plane at $Re(\psi_{max}) = 0$ and, hence, there is no combination of b_0 and β for which the equilibrium solution is stable.

Figure 5.5(a) shows the surface from Fig. 5.4(a) in the smaller parameter ranges $0 < b_0 < 5$ and $0 < \beta < 2\pi$. For $\beta \approx 2.5$ and $b_0 \approx 5$ the surface starts to dip downwards (outlined by a green circle) and it appears that $Re(\psi_{max})$ will approach zero as b_0 is increased. This dip is more easily seen in Fig. 5.5(b), which is the slice through the surface at $b_0 = 5$. The blue curve represents the surface and the dip in the surface can now be seen to be the switch-over point S_1 (green dot). Here, two branches of eigenvalues cross and a new branch is now the one with the largest real part. Figure 5.5(b) also shows other switch-over points (green dots) between branches of eigenvalues including the symmetric counterpart of S_1 the point S_2 . Here, the branch of eigenvalues with the largest real part once again switches. The points S_1 and S_2 are the global minima of the surface shown in

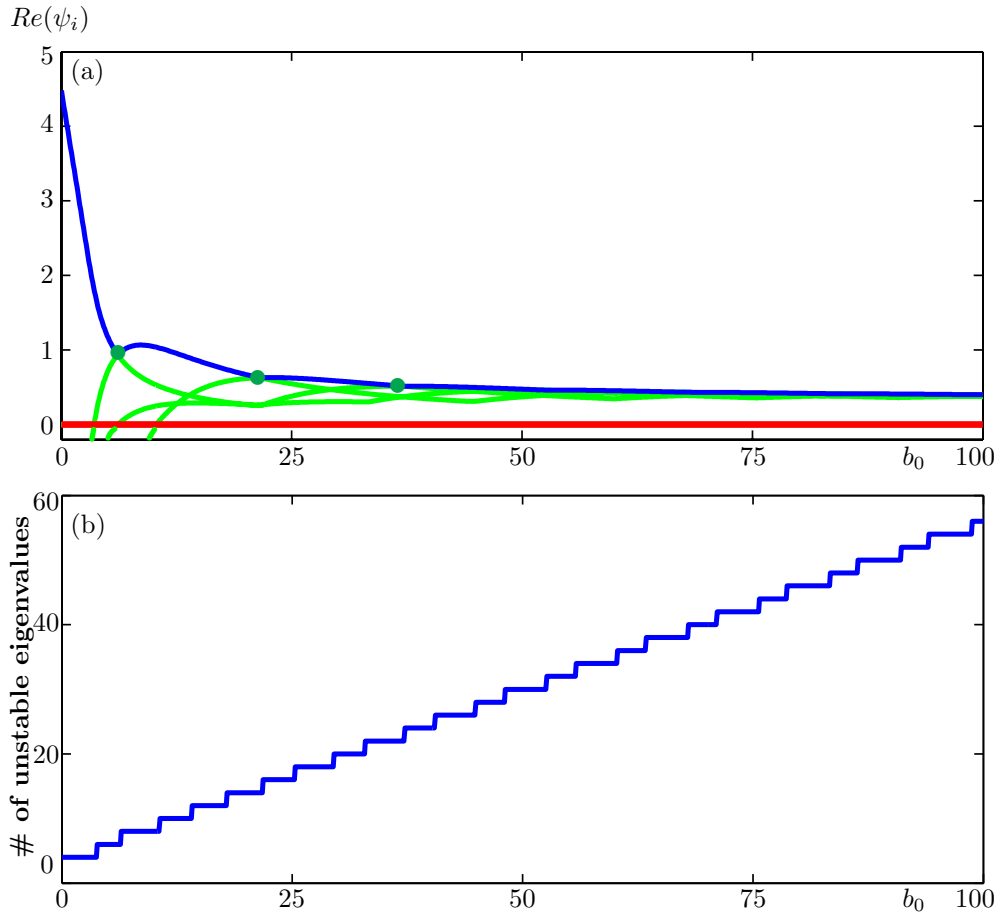


Figure 5.6: Panel (a) shows the real part of the leading eigenvalue $Re(\psi_{max})$ (blue) and the real part of additional eigenvalues (green) of (5.2.18) for complex temporal feedback gain as the parameter b_0 is changed. Panel (b) shows the number of unstable eigenvalues of the (5.2.18) for complex temporal feedback gain as b_0 is changed. Other parameter values: $k = 1.8, b_1 = 2.5, b_3 = 2, q = 0, \rho = 0, \beta = 2.5$.

Fig. 5.5(a) and are therefore the “best choices” of β . Since the feedback phase is periodic, adding or subtracting 2π from these values of β also results in another “best choice”. It should be noted that there are many more branches of eigenvalues with negative real part close to zero. As such there are many more switch-over points and, therefore, plotting these branches accurately becomes quite difficult.

Figure 5.6(a) shows a continuation of the equilibrium solution and its leading eigenvalues in a large range of b_0 from the point S_1 , i.e. the point with $\beta \approx 2.5$ shown in Fig. 5.5(b). We continue the equilibrium and its eigenvalues for both increasing and decreasing values of b_0 . Note that the continuation does not contain the constraint that the two eigenvalues at S_1 remain equal. Such a continuation would require an additional condition that the two eigenvalues at this point are always equal and, as such, would make the continuation far more computationally intensive.

Figure 5.6(a) shows the eigenvalue with the largest real part $Re(\psi_{max})$ (blue) for each value of b_0 and some additional leading eigenvalues (green). It shows that, as b_0 is increased from zero, $Re(\psi_{max})$ does initially decrease. As b_0 is further increased more eigenvalues (green) cross the real axis and become unstable. These additional unstable eigenvalues give rise to a series of switch-over points (green dots) where the eigenvalue with the largest real part changes; the first three switch-over points are shown in Fig. 5.6(a). The more b_0 is increased the more eigenvalues become unstable. These eigenvalues accumulate along a horizontal asymptote at $Re(\psi_{max}) \approx 0.4$.

Figure 5.6(b) shows the number of unstable eigenvalues of (5.2.18) as b_0 is changed, again for $\beta = 2.5$. It shows that, the number of unstable eigenvalues increases effectively linearly with b_0 . As previously discussed, the unstable eigenvalues accumulate along a horizontal asymptote. Thus, due to this increasing number of unstable eigenvalues, we conclude that increasing b_0 does not lead to a better parameter choice. This increasing instability as the value of b_0 becomes larger is common in systems with time-delayed feedback; see, for example, chapter 2, where Pyragas control is applied to the subcritical Hopf normal form.

The analysis presented so far shows that the surface in Fig. 5.4(a) does not cross the zero plane. The task is now to consider the effect that the parameters b_1 , b_3 and k have on the surface. In other words, is the surface above the zero plane for all values of b_1 , b_3 and k ? Since the equilibrium and its eigenvalues are dependent continuously on parameters, this must be the case for b_1 , b_3 and k suitably close to the values $b_1 = 2.5$, $b_3 = 2$ and $k = 1.8$ for which the surface in Fig. 5.4(a) was obtained. However, the real task is to show that the surface is above the zero plane for any choice of b_1 , b_3 and k . Showing this by a three-parameter continuation of the surface itself is not feasible. Hence, as an alternative we continue here the equilibrium solution and its eigenvalues from the point S_1 in each of the three parameters. This is a specific check to see whether the real part of the leading eigenvalue of the equilibrium is ever negative. It should be noted that a change in b_1 , b_3 or k changes the frequency ω in (5.2.6), which in turn changes the delay τ .

We start by continuing the equilibrium solution and its eigenvalues from S_1 in the parameter b_1 ; all other parameters are fixed.

Figure 5.7(a) shows the eigenvalue with the largest real part $Re(\psi_{max})$ (blue) and a further eigenvalue (green) of the equilibrium solution for $-10 < b_1 < 10$. It shows that, as b_1 is increased from its starting value of $b_1 = 2.5$, $Re(\psi_{max})$ does not change significantly. However, as b_1 is decreased from 2.5 the value of $Re(\psi_{max})$ decreases. For $b_1 \approx -0.3$, we find a switch-over point between two branches of eigenvalues. As before, at this

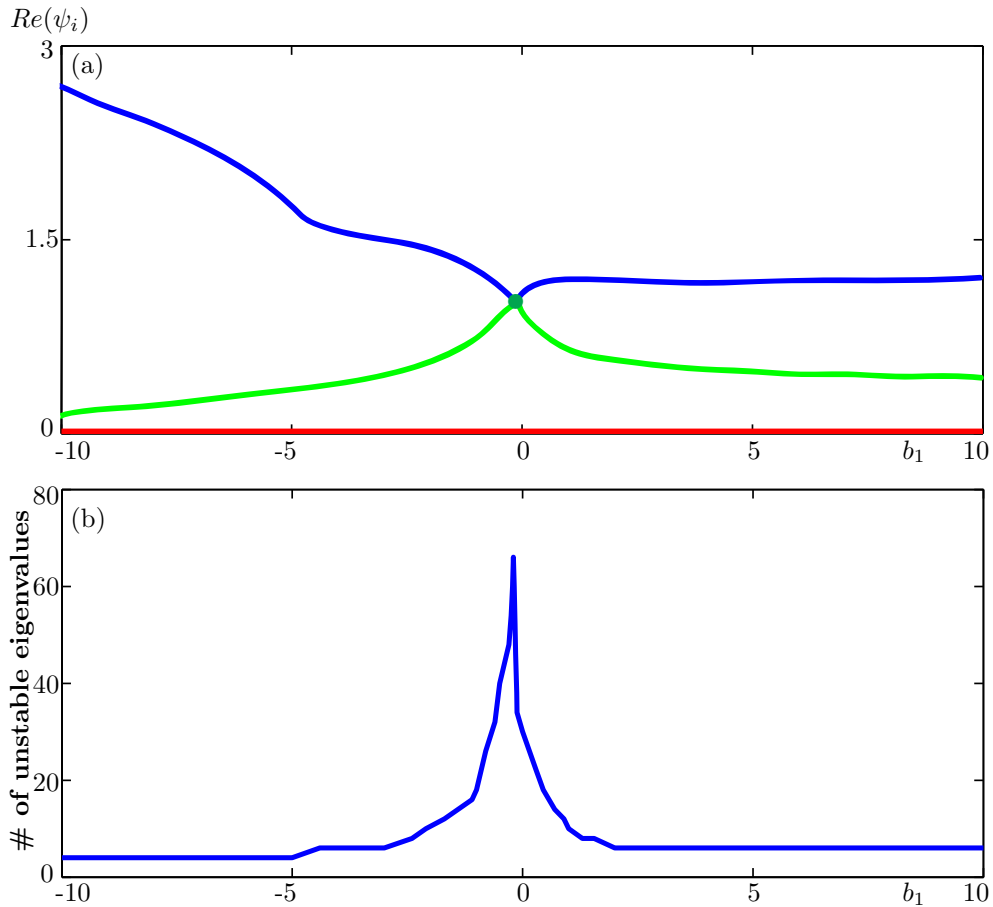


Figure 5.7: Panel (a) shows the real part of the leading eigenvalue $Re(\psi_{max})$ (blue) and the real part of an additional eigenvalue (green) of (5.2.18) for complex temporal feedback gain as the parameter b_1 is changed. Panel (b) shows the number of unstable eigenvalues of (5.2.18) for complex temporal feedback gain as b_1 is changed. Other parameter values: $k = 1.8, b_0 = 5, b_3 = 2, q = 0, \rho = 0, \beta = 2.5$.

point there are two eigenvalues with the largest real part. As b_1 is decreased further, $Re(\psi_{max})$ increases. Thus, it appears as if a small negative value of b_1 is an optimum choice; however, from Fig. 5.7(b) we see that there is a peak in the number of unstable eigenvalues of (5.2.18) at $b_1 \approx -0.3$. When b_1 is small and negative, the number of unstable eigenvalues increases substantially. This is a direct result of a large increase in the delay for this range of b_1 ; see (5.2.6). We do not show these additional unstable eigenvalues in Fig. 5.7(a) due to the difficulty in identifying individual branches. The unstable eigenvalues are very close to each other near zero and, therefore, DDE-Biftool frequently switches between different branches of eigenvalues. This means that extracting accurate branches becomes very difficult. For more negative values of b_1 , the number of unstable eigenvalues levels out at 4 and for positive values of b_1 the number of eigenvalues levels out at 6. We have found no value of b_1 in our numerous continuations for which the number of unstable eigenvalues is zero.

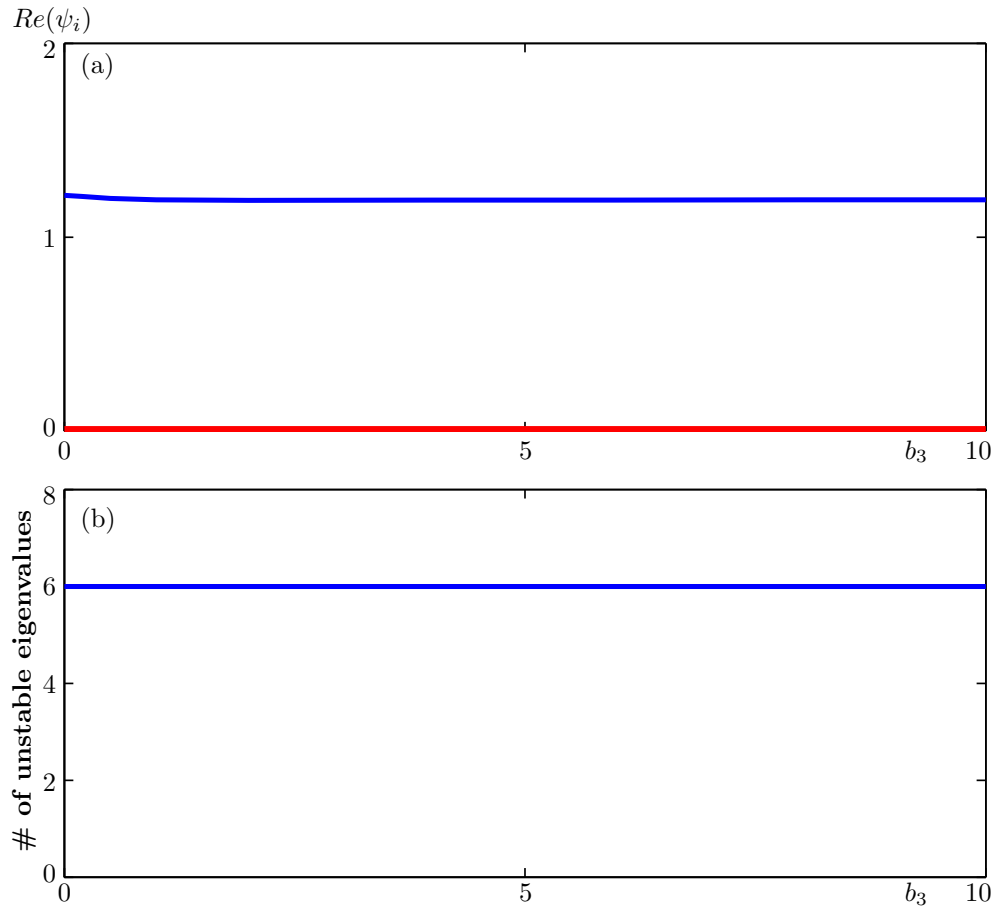


Figure 5.8: Panel (a) shows the real part of the leading eigenvalue $Re(\psi_{max})$ (blue) of (5.2.18) for complex temporal feedback gain as the parameter b_3 is changed. Panel (b) shows the number of unstable eigenvalues of (5.2.18) for complex temporal feedback gain as b_3 is changed. Other parameter values: $k = 1.8, b_0 = 5, b_1 = 2.5, q = 0, \rho = 0, \beta = 2.5$.

We now continue the equilibrium solution and its leading eigenvalues from S_1 in the parameter b_3 , again all other parameters are fixed and again $b_1 = 2.5$. Figure 5.8(a) shows the eigenvalue with the largest real part $Re(\psi_{max})$ (blue) of the equilibrium solution for $0 < b_3 < 10$. As previously discussed, b_3 is always taken to be positive, so in this analysis we do not consider $b_3 < 0$. Figure 5.8(a) shows that an increase in the parameter b_3 has little effect on $Re(\psi_{max})$. We have found that an increase in b_3 does not significantly change the delay τ . As b_3 is reduced, however, the delay also decreases and $Re(\psi_{max})$ increases slightly. When b_3 is very close to zero, the delay is very small. It is well known that the numerical routines of DDE-Biftool lose reliability for very small delay and, as such, we cannot continue all the way to $b_3 = 0$. Moreover, we managed to continue the equilibrium and its leading eigenvalues down to $b_3 = 0.001$. Figure 5.8(b) shows the number of unstable eigenvalues of (5.2.18) as b_3 is changed. For the range shown, a change in b_3 does not effect the number of unstable eigenvalues, which remains at 6 in this case. We found this to be the case in all our continuations in b_3 .

We now continue the equilibrium solution from S_1 in the parameter k , again all other parameters are fixed and again $b_3 = 2$. Figure 5.9(a) shows the eigenvalue with the largest real part $Re(\psi_{max})$ (blue) of the equilibrium solution for $1 < k < 9$. It shows that, as k is increased, $Re(\psi_{max})$ grows quickly. As k is reduced, $Re(\psi_{max})$ decreases and approaches zero. The inset in Figure 5.9(a) is an enlargement near $k = 1$, which shows that $Re(\psi_{max})$ is positive for all $k > 1$. Recall that in this analysis we only consider $|k| > 1$, since for $|k| = 1$ the amplitude R given in (5.2.6) is zero. The inset appears to show that at $k = 1$ the eigenvalue $Re(\psi_{max}) = 0$; however, there are in fact two pairs of unstable complex conjugate eigenvalues with very small real part. Figure 5.9(b) shows the number of unstable eigenvalues of (5.2.18) as k is changed. It shows that, for the range of k shown, there are always at least four unstable eigenvalues. In all of our continuations, we have found no value of k for which the surface crosses the zero plane.

Overall, we have performed a large number of calculations of the leading eigenvalue; the ones presented here in Figs. 5.4–5.9 provide a representative sample. Our numerical investigation leads us to conjecture that the control scheme with complex temporal feedback gain is never successful in stabilizing traveling wave solutions of (5.2.15). Whilst finding a mathematical proof of this conjecture remains a considerable challenge, the analysis presented here gives us confidence that this might be possible.

5.6 Conclusions

In this chapter we implemented the modified version of Pyragas feedback control suggested in [53] in an attempt to stabilize traveling wave solutions of the subcritical cubic CGLE (5.2.4). We considered both spatial and temporal feedback of the form suggested in [53, 56]. In a similar fashion to [56], we performed a linear stability analysis of the full system and studied the stability of the equilibrium solution of the linearized system. We have shown that traveling wave solutions of (5.2.15) cannot be stabilized for all perturbation wavenumbers q with this particular this setup of Pyragas control. Specifically for $q = 0$, we have shown that the spatial feedback term becomes zero and we have shown analytically that (5.2.15) always has an unstable eigenvalue when the temporal feedback gain is real. Furthermore, we have provided strong numerical evidence that suggests that there is always an unstable eigenvalue even if the temporal feedback gain is complex.

Recently, Puzyrev et al. [68] considered the stability of traveling wave solutions of the cubic-quintic CGLE with delayed feedback; this feedback was purely temporal and not of Pyragas type. They found that in the subcritical case, where the real part of the cubic

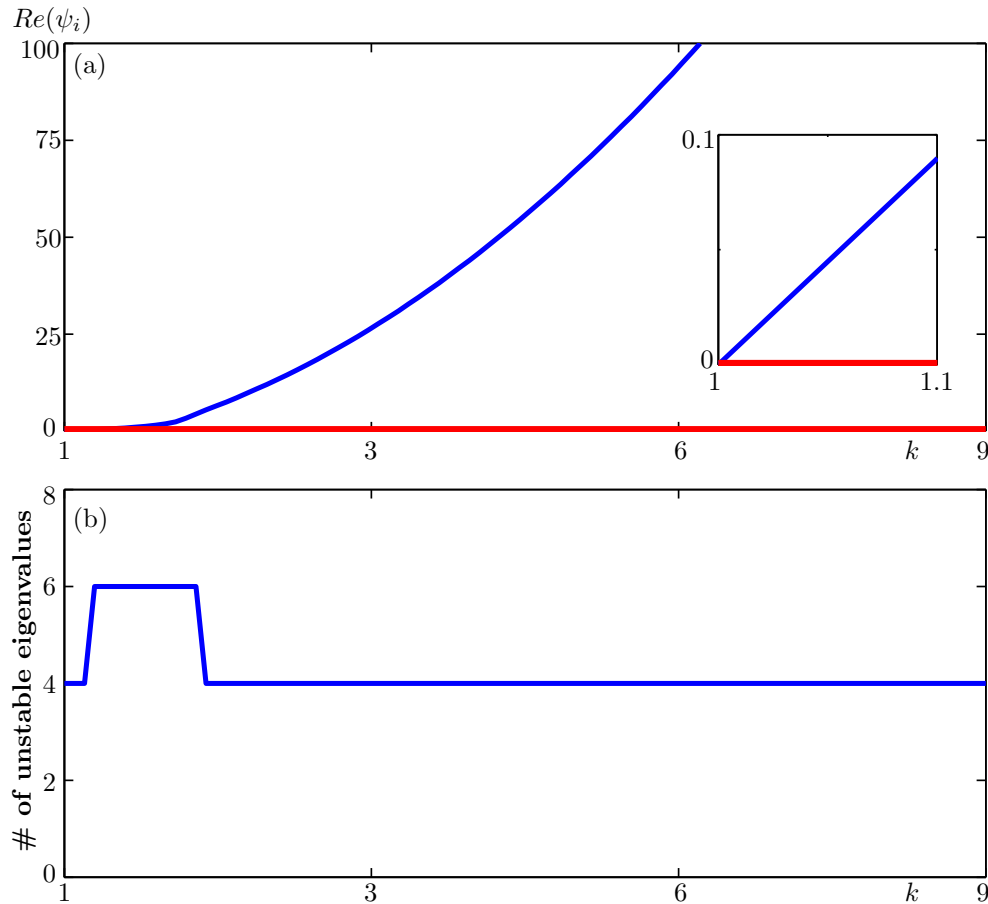


Figure 5.9: Panel (a) shows the real part of the leading eigenvalue $Re(\psi_{max})$ (blue) of (5.2.18) for complex temporal feedback gain as the parameter k is changed. Panel (b) shows the number of unstable eigenvalues of (5.2.18) for complex temporal feedback gain as k is changed. Other parameter values: $b_1 = 2.5, b_0 = 5, b_3 = 2, q = 0, \rho = 0, \beta = 2.5$.

nonlinearity is positive, a quintic term was required for the traveling wave solution to become stable. We refer the reader to [68] for a full explanation of this mechanism of stabilization. The authors of [68] also use the real part of the linear coefficient of the CGLE as the main bifurcation parameter. In our study of the subcritical CGLE, this parameter has been scaled to unity. Therefore, analysis of the subcritical cubic-quintic CGLE subject to the modified Pyragas scheme does seem like a promising avenue of research.

One could also apply Pyragas control of this form to other one-dimensional spatially extended systems near a subcritical Hopf bifurcation and see if the control scheme is successful or not in these systems. In fact, Kraft et al. [45] have already shown that the modified Pyragas scheme does not stabilize traveling wave solutions of the Swift-Hohenberg equation. Thus, it may be that further modifications of the Pyragas scheme suggested by [53] are required for control to be successful in these spatially extended

systems.

6

Discussion and future work

This thesis analyzed the global dynamics that are induced when Pyragas time-delayed feedback control is employed to stabilize an unstable periodic orbit that bifurcates from a subcritical Hopf bifurcation. We also analyzed the effect of a delay mismatch in the Pyragas control scheme. Our analysis of the global dynamics of both the Hopf normal form and the Lorenz system subject to Pyragas control highlighted the care that must be taken when applying the control scheme. In particular, we showed that it is important to consider the global dynamics of a Pyragas controlled system to ensure that the desired target state is indeed achieved. A comparison of the two controlled systems showed that the Hopf normal form subject to Pyragas control is predictive of the global dynamics of other Pyragas controlled systems near a subcritical Hopf bifurcation. The extent of this predictive nature is dependent on the parameter range over which the target periodic orbit exists and also how this periodic orbit disappears. Furthermore, we have shown that the Hopf normal form is also predictive of the success of the control scheme when there is a delay mismatch in the system. We also considered the application of Pyragas control to a spatially extended system, namely, the subcritical cubic CGLE. We showed that the control scheme is not successful in stabilizing traveling wave solutions of the CGLE with either spatial or temporal feedback.

In chapter 2, we presented the global dynamics of the subcritical Hopf normal form subject to Pyragas control. We defined the overall domain of stability of the target periodic orbit and characterized the bifurcation curves that form its boundaries. Furthermore, we showed how this stability domain changes when the feedback phase β and the Hopf normal form parameter γ are varied. In particular, we found the exact values of β and γ for which the control scheme is not successful. We also showed that the addition of feedback induces infinitely many Hopf bifurcation curves and possibly infinitely many stable periodic orbits. Moreover, we found regions of bistability, where both the equilibrium solution and the target periodic orbit are stable. The existence of bistability and further stable periodic orbits means that the user must carefully choose parameter values and the initial condition so that the system reaches the intended target state. It is difficult to choose these suitable parameter values without considering the global dynamics of the controlled system.

Chapter 3 considered the effect of a delay mismatch in the Pyragas control scheme. Specifically, we considered the subcritical Hopf normal form subject to Pyragas control as in chapter 2, but where the delay was now set, firstly, as a constant approximation of the target period and, secondly, as a linear approximation of the target period. We showed that for the control scheme to be considered successful the delay must be set as at least a linear approximation of the target parameter-dependent period. Furthermore, we showed that the control scheme is successful even with a linear approximation with a considerably shallower slope.

In chapter 4 we considered the Lorenz system subject to Pyragas control. We analyzed both the global dynamics that are induced when Pyragas control is applied in its standard form and also the dynamics when there is a delay mismatch. We found that the Hopf normal form with feedback is predictive of the dynamics found in the Lorenz system with feedback. In particular, we found that the region of stability of the target periodic orbit in parameter space is topologically the same for each system provided the feedback phase is chosen to match. That is, it is bounded by the same bifurcation curves that start and finish at the same points. We also showed the existence of further stable delay-induced periodic orbits in the Lorenz system, which again have stability domains that are topologically the same as those in the Hopf normal form. We found that the Hopf normal form is also predictive of the dynamics when there is a delay mismatch. In both the Lorenz system and the Hopf normal form we found that the delay must be set as at least a linear approximation of the target period for the control scheme to be considered successful.

In chapter 5 we applied the spatially extended Pyragas control scheme developed in [53] to the subcritical cubic CGLE. Our aim was to stabilize traveling wave solutions of the CGLE

in a similar fashion to Montgomery and Silber [56] who successfully stabilized traveling wave solutions of the supercritical cubic CGLE. However, we showed that traveling wave solutions of the subcritical cubic CGLE cannot be stabilized using spatial or temporal feedback. This was proved analytically for the case of spatial feedback and temporal feedback with real feedback gain. For the case of temporal feedback with complex feedback gain we provided numerical evidence that supports our conjecture that stabilization of traveling wave solutions is not possible.

The work presented in this thesis suggests a number of different directions for future work. Experimental verification of our findings is an appealing prospect. In particular, the results of chapters 2–4 are relevant for experiments in which Pyragas control is applied near a subcritical Hopf bifurcation, for example, those in [9, 29, 73, 77, 80]. Our results suggest that, even if the equations of the experimental system are unknown, the user should expect all of the global features of the Hopf normal form subject to Pyragas control. As previously discussed, the appearance of all these features is dependent on the region of existence of the target periodic orbit. Furthermore, our analysis of a delay mismatch suggests an approach to setting the delay in the control scheme that is far less computationally intensive than the methods in [74, 88]. In this approach the user could derive a linear approximation of the target period from a limited number of experimental measurements and set this approximation as the delay in the control scheme.

Another direction of future work would be to apply Pyragas control to systems that have an unstable periodic orbit that bifurcates from another type of bifurcation, such as a fold bifurcation or homoclinic bifurcation, rather than the subcritical Hopf bifurcation that has been the focus of this thesis. Fiedler et al. [25] have successfully applied Pyragas control to stabilize rotating waves near a fold bifurcation. Here, it would be interesting to see whether there is a general mechanism of stabilization of a periodic orbit near a fold bifurcation as there seems to be for a periodic orbit near a subcritical Hopf bifurcation, and also whether the global dynamics of two controlled systems near a fold bifurcation are similar. Based on the results presented here for Pyragas controlled systems near a subcritical Hopf bifurcation, it is not unreasonable to expect that two Pyragas controlled systems near a fold bifurcation may well have similar dynamics. Postlethwaite and Watson (personal correspondence, 2012–2014) suggest that Pyragas control cannot stabilize an unstable periodic orbit bifurcating from a homoclinic bifurcation. It would be interesting to determine exactly why this is the case and what alterations if any we can make to the control scheme that result in successful stabilization. This analysis may also give us some insight into why and where the Pyragas scheme fails and, thus, may explain why stabilization of traveling waves of the CGLE in chapter 5 was not successful.

Future work on spatially extended systems will be focused on applying the modified Pyragas control scheme to the subcritical cubic-quintic CGLE. Puzyrev et al. [99] analyze the stability of traveling wave solutions of the cubic-quintic CGLE with delayed feedback, albeit not for a feedback of Pyragas type. They find that a quintic term is required for the traveling wave solution to become stable. Furthermore, they use the real part of the linear coefficient as the primary bifurcation parameter. It may well be that the modified Pyragas scheme is not able to stabilize traveling wave solutions of the cubic CGLE. In this case one could apply another control scheme, such as one of those suggested in [54, 75, 90], or combine Pyragas control with spatio-temporal filtering as in [2].

A

Parametrization of the delay-induced Hopf bifurcation curves

A parametrization for the delay-induced Hopf bifurcations is found by entering the ansatz $z(t) = re^{i\omega t}$ into (2.0.1) and splitting the resulting equation into real and imaginary parts, yielding

$$\begin{aligned} 0 &= \lambda + r^2 + b_0(\cos(\beta - \omega\tau) - \cos \beta), \\ \omega &= 1 + \gamma r^2 + b_0(\sin(\beta - \omega\tau) - \sin \beta). \end{aligned} \tag{A.0.1}$$

At a Hopf bifurcation, $r = 0$; therefore, after re-arranging, equations (A.0.1) can be written as

$$\begin{aligned} \frac{-\lambda}{b_0} + \cos \beta &= \cos(\beta - \omega\tau), \\ \frac{\omega - 1}{b_0} + \sin \beta &= \sin(\beta - \omega\tau). \end{aligned} \tag{A.0.2}$$

Squaring both equations of (A.0.2) and adding them yields the expression (after simplification)

$$-2\lambda b_0 \cos \beta + \lambda^2 + (\omega - 1)^2 + 2(\omega - 1)b_0 \sin \beta = 0. \quad (\text{A.0.3})$$

Solving for b_0 yields the relationship (2.3.2).

B

The double Hopf bifurcation points in the set HH_K

To find an expression for the b_0 coordinate of the set of double Hopf bifurcation points HH_K on H_P , we substitute $\lambda = 0$ (as the points in the set HH_K lie on the curve H_P) and $\tau = 2\pi$ (the delay at $\lambda = 0$) into the equations (A.0.2). This gives

$$\begin{aligned}\cos \beta &= \cos(\beta - 2\pi\omega), \\ \frac{\omega - 1}{b_0} + \sin \beta &= \sin(\beta - 2\pi\omega).\end{aligned}\tag{B.0.1}$$

Therefore, from (B.0.1) either $\beta = \beta - 2\pi\omega + 2\pi k$, which gives $\omega = k$, or $\beta = -(\beta - 2\pi\omega) + 2\pi k$, which gives $\omega = \frac{\beta}{\pi} + k$. Setting $\omega = \frac{\beta}{\pi} + k$ in (B.0.1) and solving for b_0 gives the set of b_0 -coordinates

$$b_0 = \frac{\pi(1 + k) - \beta}{2\pi(\sin \beta)}.\tag{B.0.2}$$

The (λ, b_0) -coordinates of the set of double Hopf bifurcation points HH_K are thus given by

$$\text{HH}_K = \left(0, \frac{\pi(1+k) - \beta}{2\pi(\sin \beta)}\right). \quad (\text{B.0.3})$$

As discussed in this in chapter 2, for stabilization to be possible, given a positive b_0 the point b_0^c (2.1.4) must be below the point HH_0 (2.3.1). If we consider both positive and negative values of b_0 , stabilization is only possible when the following inequality is satisfied

$$\frac{-\beta}{2\pi(\sin \beta)} < \frac{-1}{2\pi(\cos \beta + \gamma \sin \beta)} < \frac{\pi - \beta}{2\pi(\sin \beta)}. \quad (\text{B.0.4})$$

Here $b_0 \neq 0$ and the expression $\frac{-\beta}{2\pi(\sin \beta)}$ is the point HH_{-1} , which is the first negative point of the set HH_K . This inequality cannot be satisfied when $\gamma = 0$, therefore, at this value of the parameter stabilization is impossible [13, 63]. Rearranging the right-hand inequality of (B.0.4) gives the function (2.5.1) along which stabilization fails for a positive b_0 .

Bibliography

- [1] I. S. Aranson and L. Kramer. The world of the complex Ginzburg–Landau equation. *Reviews of Modern Physics*, 74(1):99, 2002.
- [2] N. Baba, A. Amann, E. Schöll, and W. Just. Giant improvement of time-delayed feedback control by spatio-temporal filtering. *Phys. Rev. Lett.*, 89(7):074101, 2002.
- [3] B. Balachandran, T. Kalmár-Nagy, and D. E. Gilsinn. *Delay differential equations: Recent advances and new directions*. Springer, New York, 2009.
- [4] A. G. Balanov, N. B. Janson, and E. Schöll. Delayed feedback control of chaos: Bifurcation analysis. *Phys. Rev. E*, 71(1):016222, 2005.
- [5] D. A. W. Barton and S. G. Burrow. Numerical continuation in a physical experiment: investigation of a nonlinear energy harvester. *Journal of Computational and Nonlinear Dynamics*, 6:011010, 2011.
- [6] D. A. W. Barton, B. P. Mann, and S. G. Burrow. Control-based continuation for investigating nonlinear experiments. *Journal of Vibration and Control*, 18:509–520, 2012.
- [7] T. B. Benjamin and J. E. Feir. The disintegration of wave trains on deep water part 1. theory. *Journal of Fluid Mechanics*, 27(03):417–430, 1967.
- [8] E. Benkler, M. Kreuzer, R. Neubecker, and T. Tschudi. Experimental control of unstable patterns and elimination of spatiotemporal disorder in nonlinear optics. *Phys. Rev. Lett.*, 84(5):879, 2000.
- [9] S. Bielawski, D. Derozier, and P. Glorieux. Controlling unstable periodic orbits by a delayed continuous feedback. *Phys. Rev. E*, 49:971–974, 1994.
- [10] M. E. Bleich and J. E. S. Socolar. Controlling spatiotemporal dynamics with time-delay feedback. *Phys. Rev. E.*, 54(1):R17, 1996.

- [11] S. Boccaletti, C. Grebogi, Y.C. Lai, H. Mancini, and D. Maza. The control of chaos: theory and applications. *Physics Reports*, 329:103 – 197, 2000.
- [12] H. Broer and F. Takens. *Dynamical systems and chaos*, volume 172. Springer, 2011.
- [13] G. Brown, C. M. Postlethwaite, and M. Silber. Time-delayed feedback control of unstable periodic orbits near a subcritical Hopf bifurcation. *Physica D*, 240:859 – 871, 2011.
- [14] G. C. Brown. *An Analysis of Hopf Bifurcation Problems with Time-Delayed Feedback Control*. PhD thesis, Northwestern University, December 2011.
- [15] E. Bureau, F. Schilder, I. Ferreira Santos, J. Juel Thomsen, and J. Starke. Experimental bifurcation analysis of an impact oscillator –tuning a non-invasive control scheme. *Journal of Sound and Vibration*, 332:5883–5897, 2013.
- [16] S. A. Campbell and V. G. LeBlanc. Resonant Hopf-Hopf interactions in delay differential equations. *Journal of Dynamics and Differential Equations*, 10(2):327–346, 1998.
- [17] S. A. Campbell and E. Stone. Analysis of the chatter instability in a nonlinear model for drilling. *Journal of Computational and Nonlinear Dynamics*, 1(4):294–306, 2006.
- [18] P. E. Cladis and P. P. Muhoray. *Spatio-temporal patterns in non-equilibrium complex systems*. Addison-Wesley, 1995.
- [19] E. J. Doedel, B. Krauskopf, and H. M. Osinga. Global bifurcations of the Lorenz manifold. *Nonlinearity*, 19(12):2947, 2006.
- [20] E. J. Doedel, B. Krauskopf, and H. M. Osinga. Global invariant manifolds in the transition to preturbulence in the Lorenz system. *Indagationes Mathematicae*, 22(3):222–240, 2011.
- [21] R. D. Driver. *Ordinary and delay differential equations*, volume 20. Springer, New York, 1977.
- [22] K. Engelborghs, T. Luzyanina, and G. Samaey. DDE-Biftool: a Matlab package for bifurcation analysis of delay differential equations. *TW Report*, 305, 2000.
- [23] H. Erzgräber and W. Just. Global view on a nonlinear oscillator subject to time-delayed feedback control. *Physica D: Nonlinear Phenomena*, 238(16):1680 – 1687, 2009.
- [24] B. Fiedler, V. Flunkert, M. Georgi, P. Hövel, and E. Schöll. Refuting the odd-number limitation of time-delayed feedback control. *Phys. Rev. Lett.*, 98:114101, 2007.

- [25] B. Fiedler, S. Yanchuk, V. Flunkert, P. Hövel, H. J. Wünsche, and E. Schöll. Delay stabilization of rotating waves near fold bifurcation and application to all-optical control of a semiconductor laser. *Physical Review E*, 77(6):066207, 2008.
- [26] V. Flunkert and E. Schöll. Towards easier realization of time-delayed feedback control of odd-number orbits. *Phys. Rev. E*, 84:016214, Jul 2011.
- [27] A. L. Fradkov, R. J. Evans, and B. R. Andrievsky. Control of chaos: methods and applications in mechanics. *Philosophical Transactions of the Royal Society A*, 364:2279–2307, 2006.
- [28] A. Garfinkel, M. L. Spano, W. L Ditto, and J. N. Weiss. Controlling cardiac chaos. *Science*, 257:1230–1235, 1992.
- [29] D. J. Gauthier, D. W. Sukow, H. M. Concannon, and J. E. S. Socolar. Stabilizing unstable periodic orbits in a fast diode resonator using continuous time-delay autosynchronization. *Phys. Rev. E*, 50:2343, 1994.
- [30] M. Golubitsky, D. G. Schaeffer, and I. Stewart. *Singularities and groups in bifurcation theory*, volume 2. Springer New York, 1988.
- [31] J. Guckenheimer and P. Holmes. *Nonlinear oscillations, dynamical systems, and bifurcations of vector fields*, volume 42. Springer, New York, 1983.
- [32] J. K. Hale. *Introduction to functional differential equations*, volume 99. Springer, 1993.
- [33] I. Harrington and J. E. S. Socolar. Limitation on stabilizing plane waves via time-delay feedback. *Phys. Rev. E.*, 64(5):056206, 2001.
- [34] R. B. Hoyle. *Pattern formation: an introduction to methods*. Cambridge University Press, 2006.
- [35] T. Insperger, D.A.W. Barton, and G. Stépán. Criticality of Hopf bifurcation in state-dependent delay model of turning processes. *International Journal of Non-Linear Mechanics*, 43(2):140–149, 2008.
- [36] A. Isidori. *Nonlinear control systems*, volume 2. Springer, London, 1999.
- [37] W. Just, T. Bernard, M. Ostheimer, E. Reibold, and H. Benner. Mechanism of time-delayed feedback control. *Phys. Rev. Lett.*, 78:203–206, Jan 1997.
- [38] W. Just, B. Fiedler, M. Georgi, V. Flunkert, P. Hövel, and E. Schöll. Beyond the odd number limitation: A bifurcation analysis of time-delayed feedback control. *Phys. Rev. E*, 76:026210, 2007.

- [39] W. Just, D. Reckwerth, J. Möckel, E. Reibold, and H. Benner. Delayed feedback control of periodic orbits in autonomous systems. *Phys. Rev. Lett.*, 81(3):562, 1998.
- [40] W. Just, E. Reibold, H. Benner, K. Kacperski, P. Fronczak, and J. Hoyst. Limits of time-delayed feedback control. *Physics Letters A*, 254(34):158 – 164, 1999.
- [41] T. Kalmár-Nagy, G. Stépán, and F.C. Moon. Subcritical Hopf bifurcation in the delay equation model for machine tool vibrations. *Nonlinear Dynamics*, 26(2):121–142, 2001.
- [42] J. L. Kaplan and J. A. Yorke. Preturbulence: a regime observed in a fluid flow model of Lorenz. *Communications in Mathematical Physics*, 67(2):93–108, 1979.
- [43] M. Kim, M. Bertram, M. Pollmann, A. von Oertzen, A. S. Mikhailov, H. H. Rotermund, and G. Ertl. Controlling chemical turbulence by global delayed feedback: pattern formation in catalytic CO oxidation on Pt (110). *Science*, 292(5520):1357–1360, 2001.
- [44] I. Z. Kiss, Z. Kázas, and V. Gáspár. Tracking unstable steady states and periodic orbits of oscillatory and chaotic electrochemical systems using delayed feedback control. *Chaos: An Interdisciplinary Journal of Nonlinear Science*, 16(3):033109–033109, 2006.
- [45] A. Kraft and S. V. Gurevich. The Swift–Hohenberg equation with time delayed feedback. *In preparation*.
- [46] Y. A. Kuznetsov. *Elements of applied bifurcation theory*, volume 112. Springer, New York, 1998.
- [47] Y. N. Kyrychko, K. B. Blyuss, S. J. Hogan, and E. Schöll. Control of spatiotemporal patterns in the Gray–Scott model. *Chaos: An Interdisciplinary Journal of Nonlinear Science*, 19(4):043126, 2009.
- [48] L. D. Landau and V. L. Ginzburg. On the theory of superconductivity. *J. Exp. Theor. Phys. (USSR)*, 20:1064–1082, 1950.
- [49] C. G. Lange and A. C. Newell. A stability criterion for envelope equations. *SIAM Journal on Applied Mathematics*, 27(3):441–456, 1974.
- [50] V. G. LeBlanc. On some secondary bifurcations near resonant Hopf–Hopf interactions. *Dynamics of Continuous, Discrete and Impulsive Systems*, 7(3):405–427, 2000.
- [51] D. J. Leith and W. E. Leithead. Appropriate realization of gain-scheduled controllers with application to wind turbine regulation. *International Journal of Control*, 65(2):223–248, 1996.

- [52] E. N. Lorenz. Deterministic nonperiodic flow. *Journal of the atmospheric sciences*, 20(2):130–141, 1963.
- [53] W. Lu, D. Yu, and R. G. Harrison. Control of patterns in spatiotemporal chaos in optics. *Phys. Rev. Lett.*, 76(18):3316, 1996.
- [54] A. V. Mamaev and M. Saffman. Selection of unstable patterns and control of optical turbulence by Fourier plane filtering. *Phys. Rev. Lett.*, 80(16):3499, 1998.
- [55] MATLAB. *version 7.10.0 (R2011a)*. The MathWorks Inc., Natick, Massachusetts, 2011.
- [56] K. A. Montgomery and M. Silber. Feedback control of travelling wave solutions of the complex Ginzburg–Landau equation. *Nonlinearity*, 17(6):2225, 2004.
- [57] H. Nakajima. On analytical properties of delayed feedback control of chaos. *Physics Letters A*, 232(34):207 – 210, 1997.
- [58] E. Ott, C. Grebogi, and J. A. Yorke. Controlling chaos. *Phys. Rev. Lett.*, 64:2837–2837, 1990.
- [59] P. Parmananda, R. Madrigal, M. Rivera, L. Nyikos, I. Z. Kiss, and V. Gáspár. Stabilization of unstable steady states and periodic orbits in an electrochemical system using delayed-feedback control. *Phys. Rev. E.*, 59(5):5266–5271, 1999.
- [60] B. Peng, V. Petrov, and K. Showalter. Controlling chemical chaos. *The Journal of Physical Chemistry*, 95:4957–4959, 1991.
- [61] V. Petrov, V. Gaspar, J. Masere, and K. Showalter. Controlling chaos in the Belousov–Zhabotinsky reaction. *Nature*, 361(6409):240–243, 1993.
- [62] C. M. Postlethwaite. Stabilization of long-period periodic orbits using time-delayed feedback control. *SIAM J. Appl. Dynam. Syst.*, 8(1):21–39, 2009.
- [63] C. M. Postlethwaite, G. Brown, and M. Silber. Feedback control of unstable periodic orbits in equivariant Hopf bifurcation problems. *Philosophical Transactions of the Royal Society A*, 371, 2013.
- [64] C. M. Postlethwaite and M. Silber. Spatial and temporal feedback control of traveling wave solutions of the two-dimensional complex Ginzburg–Landau equation. *Physica D: Nonlinear Phenomena*, 236(1):65–74, 2007.
- [65] C. M. Postlethwaite and M. Silber. Stabilizing unstable periodic orbits in the Lorenz equations using time-delayed feedback control. *Phys. Rev. E*, 76:056214, 2007.

- [66] A. S. Purewal, C. M. Postlethwaite, and B. Krauskopf. Effect of delay mismatch in Pyragas feedback control. *Physical Review E*, 90(5):052905, 2014.
- [67] A. S. Purewal, C. M. Postlethwaite, and B. Krauskopf. A global bifurcation analysis of the generic subcritical Hopf normal form subject to Pyragas time-delayed feedback control. *SIAM J. Appl. Dynam. Syst.*, 13(4):1879–1915, 2014.
- [68] D. Puzyrev, S. Yanchuk, A. Vladimirov, and S. Gurevich. Stability of plane wave solutions in complex Ginzburg–Landau equation with delayed feedback. *SIAM J. Appl. Dynam. Syst.*, 13(2):986–1009, 2014.
- [69] K. Pyragas. Continuous control of chaos by self-controlling feedback. *Physics Letters A*, 170:421–428, 1992.
- [70] K. Pyragas. Control of chaos via extended delay feedback. *Physics Letters A*, 206:323–330, 1995.
- [71] K. Pyragas. Delayed feedback control of chaos. *Philosophical Transactions of the Royal Society A: Mathematical, Physical and Engineering Sciences*, 364(1846):2309–2334, 2006.
- [72] K. Pyragas and V. Novičenko. Time-delayed feedback control design beyond the odd-number limitation. *Phys. Rev. E*, 88:012903, Jul 2013.
- [73] K. Pyragas and A. Tamaševičius. Experimental control of chaos by delayed self-controlling feedback. *Physics Letters A*, 180(1):99–102, 1993.
- [74] V. Pyragas and K. Pyragas. Adaptive modification of the delayed feedback control algorithm with a continuously varying time delay. *Physics Letters A*, 375(44):3866–3871, 2011.
- [75] I. Ray and M. Toahchoodee. A spatio-temporal role-based access control model. In *Data and Applications Security XXI*, pages 211–226. Springer, 2007.
- [76] D. Roose and R. Szalai. Continuation and bifurcation analysis of delay differential equations. In H. M. Osinga B. Krauskopf and J. Galán-Vioque, editors, *Numerical continuation methods for dynamical systems*, pages 359–399. Springer, 2007.
- [77] R. Roy, T. W. Murphy Jr, T. D. Maier, Z. Gills, and E. R. Hunt. Dynamical control of a chaotic laser: Experimental stabilization of a globally coupled system. *Phys. Rev. Lett.*, 68(9):1259, 1992.
- [78] S. J. Schiff, K. Jerger, D. H. Duong, T. Chang, M. L. Spano, and W. L. Ditto. Controlling chaos in the brain. *Nature*, 370:615–620, 1994.

- [79] S. Schikora, P. Hövel, H. J. Wünsche, E. Schöll, and F Henneberger. All-optical noninvasive control of unstable steady states in a semiconductor laser. *Phys. Rev. Lett.*, 97(21):213902, 2006.
- [80] S Schikora, H. J. Wünsche, and F Henneberger. Odd-number theorem: Optical feedback control at a subcritical Hopf bifurcation in a semiconductor laser. *Phys. Rev. E*, 83:026203, 2011.
- [81] F. W. Schneider, R. Blittersdorf, A. Förster, T. Hauck, D. Lebender, and J. Müller. Continuous control of chemical chaos by time delayed feedback. *The Journal of Physical Chemistry*, 97:12244–12248, 1993.
- [82] E. Schöll, G. Hiller, P. Hövel, and M. A. Dahlem. Time-delayed feedback in neurosystems. *Philosophical Transactions of the Royal Society A: Mathematical, Physical and Engineering Sciences*, 367(1891):1079–1096, 2009.
- [83] E. Schöll and H. G. Schuster. *Handbook of chaos control*. John Wiley & Sons, 2008.
- [84] T. Shinbrot, C. Grebogi, E. Ott, and J. A Yorke. Using small perturbations to control chaos. *Nature*, 363:411–417, 1993.
- [85] J. Sieber. DDE-Biftool version 3.0. http://empslocal.ex.ac.uk/people/staff/js543/research_interests.html.
- [86] J. Sieber. Finding periodic orbits in state-dependent delay differential equations as roots of algebraic equations. *Discrete and Continuous Dynamical Systems - Series A*, 32:2607–2651, 2012.
- [87] J. Sieber, A. Gonzalez-Buelga, S. A. Neild, D. J. Wagg, and B. Krauskopf. Experimental continuation of periodic orbits through a fold. *Phys. Rev. Lett.*, 100:244101, 2008.
- [88] J. Sieber and B. Krauskopf. Control-based continuation of periodic orbits with a time-delayed difference scheme. *International Journal of Bifurcation and Chaos*, 17:2579–2593, 2007.
- [89] J. Sieber and B. Krauskopf. Control based bifurcation analysis for experiments. *Nonlinear Dynamics*, 51:365–377, 2008.
- [90] S. Sinha and N. Gupte. Adaptive control of spatially extended systems: targeting spatiotemporal patterns and chaos. *Phys. Rev. E-Statistical, Nonlinear and Soft Matter Physics*, 58(5):R5221–R5224, 1998.

- [91] H. L. Smith. *An introduction to delay differential equations with applications to the life sciences*. Springer Science, 2011.
- [92] J. E. S. Socolar, D. W. Sukow, and D. J. Gauthier. Stabilizing unstable periodic orbits in fast dynamical systems. *Phys. Rev. E*, 50(4):3245, 1994.
- [93] C. Sparrow. *The Lorenz equations: bifurcations, chaos, and strange attractors*, volume 41. Springer-Verlag New York, 1982.
- [94] G. Stépán, T. Insperger, and R. Szalai. Delay, parametric excitation, and the nonlinear dynamics of cutting processes. *International Journal of Bifurcation and Chaos*, 15(09):2783–2798, 2005.
- [95] E. Stone and S. A. Campbell. Stability and bifurcation analysis of a nonlinear DDE model for drilling. *Journal of Nonlinear Science*, 14(1):27–57, 2004.
- [96] R. Szalai and G. Stépán. Lobes and lenses in the stability chart of interrupted turning. *Journal of computational and nonlinear dynamics*, 1(3):205–211, 2006.
- [97] M. A. Vorontsov and B. A. Samson. Nonlinear dynamics in an optical system with controlled two-dimensional feedback: Black-eye patterns and related phenomena. *Phys. Rev. A.*, 57(4):3040, 1998.
- [98] S. Wu, K. He, and Z. Huang. Controlling spatio-temporal chaos via small external forces. *Physics Letters A*, 260(5):345–351, 1999.
- [99] S. Yanchuk and P. Perlikowski. Delay and periodicity. *Phys. Rev. E*, 79:046221, 2009.